



VYSOKÉ UČENÍ TECHNICKÉ V BRNĚ

Fakulta chemická

Plazmochemické procesy a jejich aplikace

Habilitační práce

Mgr. Věra Mazánková, Ph.D.

Brno 2018

Abstrakt

Předložená práce obsahuje komentovaný soubor patnácti vědeckých prací, které se věnují problematice plazmochemických procesů a reakcí v různých typech výbojů a jejich dohasínání. Práce je logicky rozdělena do tří kapitol. První kapitola je věnována problematice doutnavého výboje za sníženého tlaku a jeho dohasínání. V příložených publikacích jsou rozebrány elementární procesy částic jak v objemu, tak i na stěnách výbojové trubice. Druhá kapitola se věnuje procesům v prebiotických atmosférách a atmosféře měsíce Titanu. Tyto atmosféry jsou simulovány pomocí klouzavého obloukového výboje. Poslední kapitola je věnována studiu generace homogenního plazmatu pomocí dielektrického bariérového výboje a jeho aplikacím.

Klíčová slova

Elektrický výboj, dohasínající plazma, prebiotické atmosféry, diagnostika plazmatu.

Abstract

A compilation of fifteen commented author's publications is presented, dealing with the topic of plasmachemical processes and reactions in different types of discharges and post-discharges. The text is logically divided into three chapters. The first chapter is dedicated to the glow discharge and post-discharge at low pressure. Elementary processes in volume and at surface of discharge tube were studied in presented publications. Second chapter describes processes in prebiotic atmospheres and Titan's and their simulation by gliding arc electric discharge. Last chapter is dedicated to generation of plasma by dielectric barrier discharge and its applications.

Key words

Electrical discharge, post discharge - afterglow, prebiotic atmospheres, plasma diagnostic.

Poděkování

Na tomto místě bych ráda poděkovala všem milým kolegům i studentům, kteří se mnou spolupracovali.

OBSAH

SEZNAM KOMENTOVANÝCH PRACÍ.....	4
1. Úvod	6
2. Plazmochemické procesy v doutnavém výboji a jeho dohasínání	7
2.1 Stav problematiky.....	7
2.2. Komentář k jednotlivým publikacím.....	12
3. Elementární procesy v prebiotických atmosférách zkoumané pomocí klouzavého obloukového výboje	16
3.1 Stav problematiky.....	16
3.2. Komentář k jednotlivým publikacím.....	21
4. Aplikace dielektrického bariérového výboje.....	24
4.1 Stav problematiky.....	24
4.2 Komentáře k jednotlivým publikacím	28
REFERENCE	31
PŘÍLOHY	33

SEZNAM KOMENTOVANÝCH PRACÍ

1. **Mazánková V.**, Trunec D., Navrátil Z., Raud J., Krčma F.: Study of argon-oxygen flowing afterglow. *Plasma Sources Science and Technology*, **25**, 3 (2016), 035008, ISSN: 0963-0252.
2. **Mazánková V.**, Trunec D., Kabeláčová K., Krčma F.: Study of argon afterglow with the air addition. *Plasma Physics and Technology*, **3**, 3 (2016), 136-139, ISSN: 2336-2626.
3. **Mazánková V.**, Trunec D., Krčma F.: Study of argon flowing afterglow with nitrogen injection. *Journal of Chemical Physics*, **139**, 16 (2013), 164311, ISSN: 0021- 9606.
4. **Mazánková V.**, Trunec D., Krčma F.: Study of nitrogen atom recombination by optical emission spectroscopy. *Plasma Physics and Technology*, **2**, 1 (2015), 50-53, ISSN: 2336- 2626.
5. **Mazánková V.**, Trunec D., Krčma F.: Study of nitrogen flowing afterglow with mercury vapor injection. *Journal of Chemical Physics*, **141**, 15 (2014), 154307, ISSN: 0021- 9606.
6. **Mazánková V.**, Krčma F.: Influence of oxygen traces on recombination process in nitrogen post-discharge. *Chemické listy*, **102**, 16 (2008), s1388-s1393, ISSN: 1213-7103.
7. Krčma F., **Mazánková V.**, Soral I, Guerra V.: Power dependence of the pink afterglow in flowing post-discharge in pure nitrogen. *IEEE Transactions on Plasma Science*, **42**, 10 (2014), 2384-2385, ISSN: 0093- 3813.
8. **Mazánková V.**, Töröková L., Krčma F., Mason N., Matejčík Š.: The influence of CO₂ admixtures on the product composition in a nitrogen-methane atmospheric glow discharge used as a prebiotic atmosphere mimic. *Origins of Life and Evolution of the Biosphere*, **46**, 4 (2016), 499-506, ISSN: 0169-6149.
9. Töröková L., **Mazánková V.**, Mason N., Krčma F., Morgan G., Matejčík Š.: The influence of CO₂ admixtures on process in Titan's atmospheric chemistry. *Plasma Physics and Technology*, **3**, 3 (2016), 163-167, ISSN: 2336-2626.
10. Töröková L., **Mazánková V.**, Krčma F., Mason N., Matejčík Š.: The influence of admixtures on the composition of products by nitrogen- methane atmospheric glow discharge. *Plasma Physics and Technology*, **2**, 1 (2015), 88-91, ISSN: 2336- 2626.
11. Töröková L., Watson J., Krčma F., **Mazánková V.**, Mason N., Horváth G., Matejčík Š.: Gas chromatography analysis of discharge products in N₂-CH₄ gas mixture at atmospheric pressure: Study of mimic Titan's atmosphere. *Contributions to Plasma Physics*, **55**, 6 (2015), 470-480, ISSN: 1521- 3986.
12. Töröková L., **Mazánková V.**, Krčma F., Mason N., Matejčík Š.: Atmospheric pressure glow discharge generated in nitrogen-methane gas mixture: PTR- MS

analyzes of the exhaust gas. *European Physical Journal-Applied Physics*, **71** (2015), 20806-20810, ISSN: 1286- 0042.

13. Trunec D., **Mazánková V.**, Mierna J., Manduchová I, Krčma F.: Study of O₂ and O₃ reactions with electrode surface in ozonizer, HAKONE XV (15th High Pressure Low Temperature Plasma Chemistry Symposium), September 11-16, 2016, Brno, Czech Republic, ISBN: 978-80-210-8318-9.
14. Eliáš M., Kloc P., Jašek O., **Mazánková V.**, Trunec D., Hrdý R., Zajíčková L.: Atmospheric pressure barrier discharge at high temperature: Diagnostics and carbon nanotubes deposition. *Journal of Applied Physics*, **117** (2015), 103301, ISSN: 0021-8979.
15. Zajíčková L., Eliáš M., Buršíková V., Studýnková Z., **Mazánková V.**, Michlíček M., Houdková J.: Low pressure plasmachemical processing of multi-walled carbon nanotubes for the production of polyurethane composite films with improved mechanical properties. *Thin Solid Films*, **538** (2013), 7-15, ISSN 0040-6090.

1. Úvod

Předkládaná habilitační práce s názvem „Plazmochemické procesy a jejich aplikace“ je věnována výsledkům experimentů s různými typy výbojů, kterým jsem se věnovala v posledních deseti letech na Fakultě chemické Vysokého učení technického v Brně a ve spolupráci s Přírodovědeckou fakultou Masarykovy univerzity. Práce je logicky rozčleněna do tří kapitol podle typu výbojů a jejich aplikací, se kterými byly experimenty provedeny.

Nízkotlaké výboje jsou specifickou skupinou výbojů a mají své výhody i nevýhody. Nevýhodou je rozhodně nutnost použití rozměrných a drahých vakuových aparatur a složitá je i případná manipulace se substráty, které mohou být v aparatuře plazmově upravovány. Značnou výhodou nízkotlakých vakuových technologií je však možnost dobře definovat pracovní podmínky výbojů včetně čistoty pracovní atmosféry, protože čistota může ovlivnit nejen samotný výboj, ale i plazmochemické reakce probíhající v systému. Proto se nízkotlaké výboje používají zejména pro studium elementárních procesů probíhajících v plazmatu a pomocí vhodných diagnostických metod lze takto získat cenná kinetická data. V předložené práci a příložených publikacích se zabývám doutnavým elektrickým výbojem za nízkého tlaku a jeho využití.

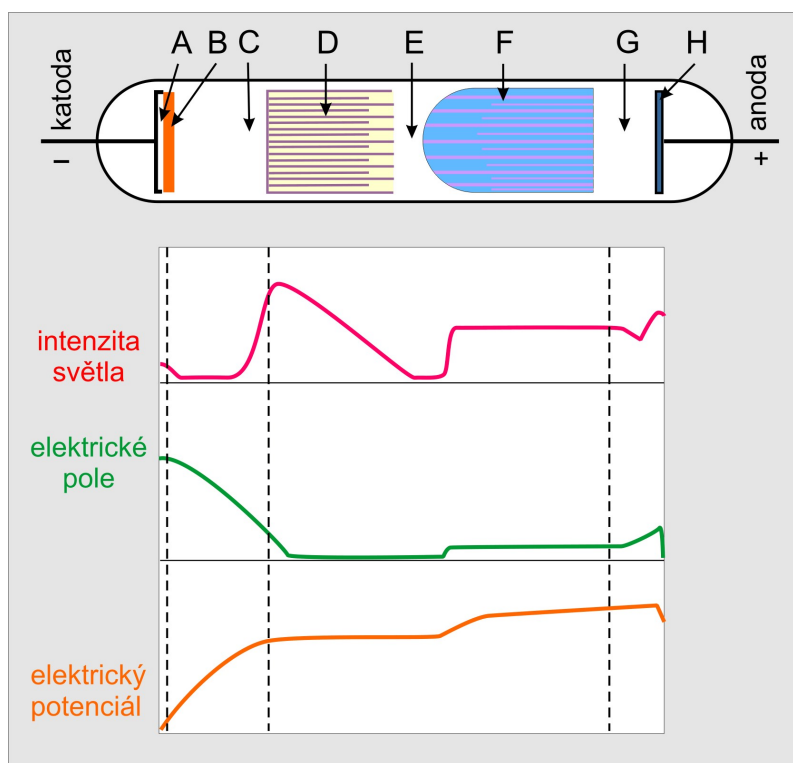
Výboje za atmosférického tlaku jsou pro řadu aplikací velmi zajímavou alternativou nízkotlakých výbojů a v posledních desetiletích je vysoký nárůst zájmu o jejich výzkum. Výhodou je, že nevyžadují nákladný vakuový systém a koncentrace aktivních částic v plazmatu generovaném za atmosférického tlaku může být mnohonásobně vyšší oproti nízkotlakým elektrickým výbojům. Výboje mohou být v různé konfiguraci podle toho, k jaké aplikaci následně slouží. V konfiguraci dielektrického bariérového výboje jsou zejména aparatury pro opracování povrchů různých materiálů, ale také pro růst uhlíkových nanotrubeček nebo pro generaci ozónu. Výboje za atmosférického tlaku mohou být generovány přímo v prostředí laboratoře, nebo v reaktoru, kde lze vytvořit atmosféru z různých směsí plynů.

Zejména jsou zajímavé výboje s nerovnovážným plazmatem, které není v termodynamické rovnováze. V tomto případě bývá teplota elektronů několik desítek tisíc Kelvinů, zatím co teplota iontů a neutrálního plynu je jen o pár desítek stupňů vyšší než pokojová teplota. V takovémto typu plazmatu pak mohou probíhat reakce, které by jinak za nízkých teplot neprobíhaly (např. generace ozónu v dielektrickém bariérovém výboji). Dalšími významnými průmyslovými aplikacemi využívajícími nerovnovážné plazma jsou depozice tenkých vrstev za nízkých teplot a modifikace povrchu polymerů.

2. Plazmochemické procesy v doutnavém výboji a jeho dohasínání

2.1 Stav problematiky

Doutnavý výboj je samostatný typ elektrického výboje vytvářející nízkoteplotní a nerovnovážné plazma (viz. obr. 1). Diagnostika, aplikace i modelování elementárních procesů probíhajících v doutnavém výboji jsou stále aktuální témata v oblasti chemie a fyziky plazmatu (Pintassilgo et al. 2010, Moisan et al. 2013). Doutnavý výboj má svá specifika, je provozován za sníženého tlaku (stovky až tisíce Pa) při relativně malém proudu (desítky až stovky mA). V kladném sloupci doutnavého výboje vzniká neizotermické plazma s teplotou elektronů kolem 10 000 K, teplota iontů a neutrálního plynu není příliš vyšší než laboratorní teplota (300 K). Doutnavý výboj lze generovat také při vyšších tlacích nebo i při tlaku atmosférickém. Tato konfigurace však není běžná a také chování výboje není zcela typické pro tento druh výboje, délka výboje v tomto případě je jen několik milimetrů. Za nízkých tlaků má typická výbojová trubice délku deset až několik desítek centimetrů a průměr v jednotkách centimetrů.



Obr. 1: Charakteristické oblasti doutnavého výboje: A - Astonův tmavý prostor, B - katodová vrstva, C - katodový tmavý prostor, D - záporné světlo, E - Faradayův tmavý prostor, F - kladný sloupec, G - anodový tmavý prostor, H - anodové světlo (Aldebaran).

Doutnavý výboj je zdrojem elektronů, kladných i záporných iontů a radikálů (O, H, N...) a lze ho provozovat ve stacionárním nebo v průtokovém režimu. Průtokový režim má tu výhodu, že produkty vznikající ve výboji jsou unášeny proudem neutrálního plynu do

připojené trubice do prostoru tzv. dohasínání (afterglow). V této části se už nenachází žádný zdroj energie, dochází k relaxaci produktů z aktivního výboje. Pomocí kapilárních trubic je možné do části dohasínání přidávat ještě další reaktanty a studovat probíhající reakce. Tato metoda se nazývá metoda proudové trubice (flow tube). Rychlost proudění neutrálního plynu v trubici je kolem 100 m/s a měření koncentrace částic nebo intenzity vznikajícího záření podél trubice potom umožňuje určit rychlostní konstanty reakcí. Tímto způsobem se převede měření v čase na měření v různých místech trubice. Konfigurace v průtokovém režimu je vhodná zejména pro studium elementárních procesů a získávání kinetických dat. Tímto způsobem lze studovat rekombinaci elektronů a kladných iontů, rekombinaci kladných a záporných iontů a záchyt elektronů na elektronegativních molekulách. V tomto případě se koncentrace elektronů a iontů měří Langmuirovou sondou a tato metoda se pak označuje jako Flowing Afterglow Langmuir Probe (FALP) (Smith et al. 1994). Další modifikace této metody spočívá v tom, že se mezi výboj a proudovou trubicí vloží kvadrupólový filtr, který umožňuje vybrat ze vzniklých iontů pouze jeden a pak studovat jeho reakce s neutrálními částicemi. Tato metoda se nazývá Selected Ion Flow Tube (SIFT) (Smith et al. 2004). SIFT se využívá rovněž ke studiu reakcí iontů H_3O^+ s neutrálními molekulami (tzv. přenos protonu). Reakce s přenosem protonu se nyní využívají v komerčních hmotnostních spektrometrech k analýze stopových množství organických látek.

V doutnavém výboji rovněž vznikají metastabilní částice (např. $\text{Ar}(^3\text{P}_2)$ v argonovém výboji, $\text{N}_2(\text{A})$ v dusíkovém výboji) a radikály (např. O, N), takže v proudové trubici lze studovat jejich reakce s neutrálními částicemi.

Značná část dosud publikovaných prací se zabývá především studiem plazmatu čistého dusíku a jeho dohasínání. V dusíkovém dohasínání jsou totiž přítomné metastabilní molekuly a dusíkové atomy – mluví se o tzv. aktivním dusíku. Přidání příměsí k dusíku ale významně mění kinetické procesy a tím i mechanismy přenosu energie v plazmatu (Ricard 1996). Obvykle jsou v praktických aplikacích přítomny příměsí uhlovodíků, kyslík a vodní páry. Jejich vliv ve stopové úrovni byl detailně studován např. pro uhlíkaté sloučeniny (Krčma 2003). Typický obrázek doutnavého výboje v čistém dusíku s částí dohasínání je na obr. 2.

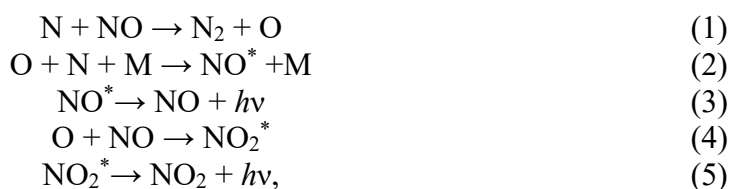


Obr. 2: Doutnavý výboj s dohasínáním v čistém dusíku s viditelným efektem pink afterglow (na obrázku označeno žlutou elipsou) pro průtok plynu 800 sccm a celkový tlak 1000 Pa.

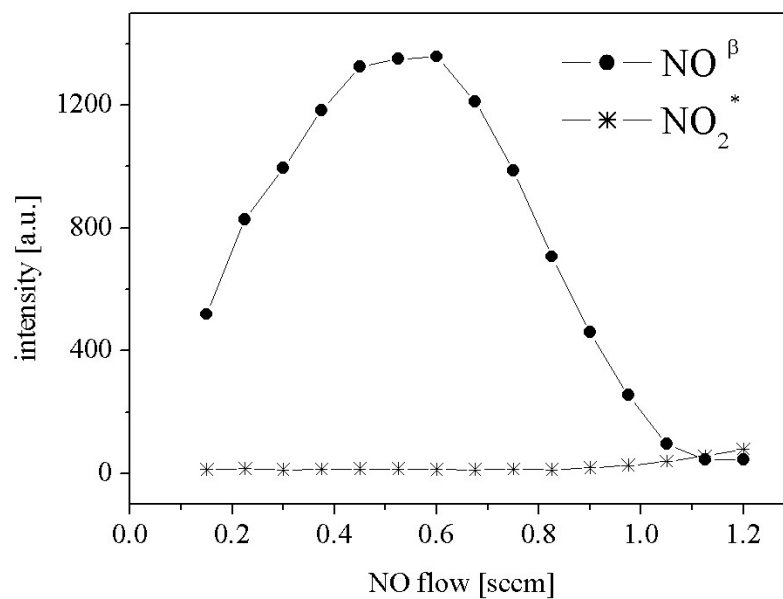
Dohasínání v čistém dusíku je specifické tím, že zde vzniká známý efekt tzv. pink afterglow, který je na obrázku zřetelně vidět.

Vhodnou diagnostickou metodou pro studium elementárních procesů v dohasínajícím plazmatu je optická emisní spektroskopie (OES). Z optických emisních spekter je možné zjistit složení plazmatu a vypočítat elektronovou, rotační a vibrační teplotu (Ricard 1996). Jestliže není spektrometr nakalibrován na absolutní měření, což nebývá, lze z naměřených intenzit lze zjistit pouze relativní koncentrace jednotlivých složek plazmatu. Existují však metody, jak lze i z relativních měření získat absolutní koncentrace určitých částic.

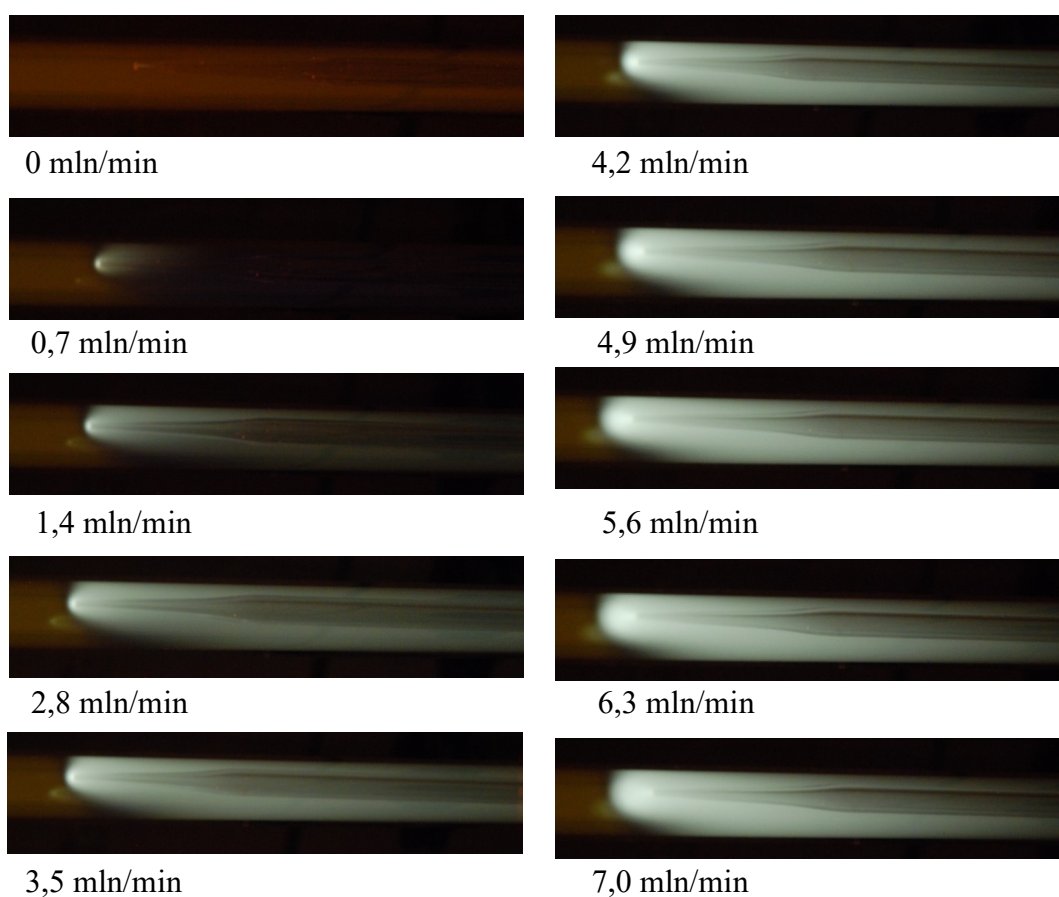
Jedná se zejména o titrační metody (Ricard 1996), kdy do výboje nebo dohasínání přidáváme další složku. Ta reaguje s částicemi v systému a z její známé koncentrace lze stanovit koncentraci částic, se kterými reaguje. Typickým případem je titrace NO do dusíku nebo do směsi dusíku s kyslíkem. Ze známé koncentrace NO (měřené pomocí průtokoměru) lze pak určit koncentraci atomárního dusíku a atomárního kyslíku. Reakce probíhající v systému jsou následující:



kde M je třetí tělelo (např. stěna reaktoru). Reakcí (1) reaguje atomární dusík s přidávaným NO za vzniku atomárního kyslíku a molekulárního dusíku. Reakce (1) je rychlá reakce. Pomalou reakcí (2) z atomárního dusíku a kyslíku vzniká excitovaný stav NO^* a ten vyzáří foton (v oblasti spektrálního pásu NO^β), reakce (3). Reakce (4) je opět pomalá, reaguje atomární kyslík s NO za vzniku excitovaného stavu NO_2^* . Jestliže je koncentrace NO menší než koncentrace atomárního dusíku, tak reakcí (1) vznikne atomární kyslík a dále převáží reakce (2) a ve spektrech se objeví spektrální pás NO^β . Jestliže je koncentrace NO větší než koncentrace atomárního dusíku, tak je veškerý atomární dusík spotřebován v reakci (1) ke vzniku atomárního kyslíku a dále převáží reakce (4). Excitovaný stav NO_2^* pak vyzáří v oblasti zeleného kontinua. Při rovnosti koncentrací NO a N v rovnici (1) není emitováno žádné záření a tento případ se nazývá tzv. dark point. Z naměřených intenzit NO^β a NO_2^* pak v závislosti na průtoku NO lze tento bod stanovit, jak je ukázáno na obr. 3. Jedná se o průsečík závislostí, kde koncentrace NO potom odpovídá koncentraci N. Na obr. 4 je vidět, jak experiment vypadá pro různé koncentrace NO.



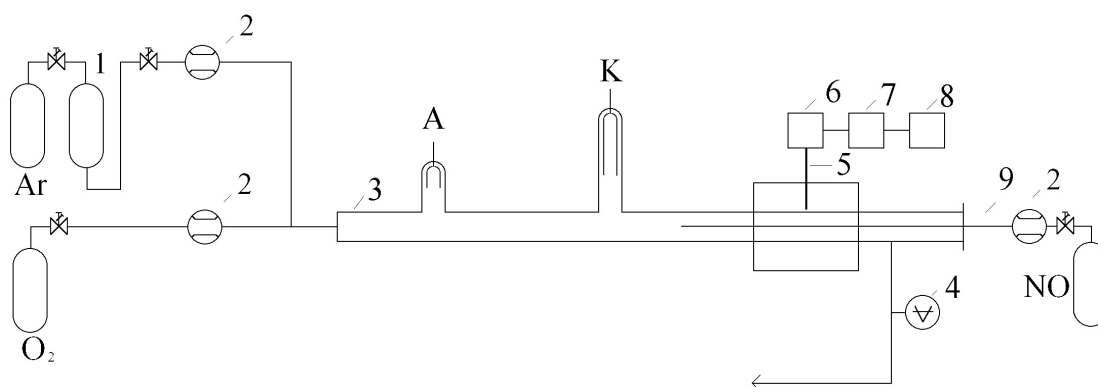
Obr. 3: Průběh intenzit NO^β a NO_2^* v závislosti na průtoku NO pro čistý dusík s titrací NO v čase dohasínání 60 ms.



Obr. 4: Záření při různých průtocích NO kapilární trubici v dohasínání čistého dusíku. Kapilára je zavedena do proudové trubice zprava.

Problematikou dohasínajících výbojů a jejich diagnostikou jsem se zabývala na Fakultě chemické VUT už ve své dizertační práci s názvem „Spektroskopické studium dohasínajících výbojů v dusíku a jeho směsích“. V experimentech jsem pokračovala i dále za účelem studia elementárních procesů v dohasínajícím plazmatu. Experimentální data byla použita pro tvorbu kinetického modelu, který vznikl ve spolupráci s kolegy z Přírodovědecké fakulty Masarykovy Univerzity. Všechny experimenty byly provedeny v aparatuře nacházející se na Fakultě chemické VUT v Brně.

Aparatura je tvořena křemennou trubicí, v jejíž jedné části se nacházejí molybdenové elektrody a následující část tvoří dohasínání (viz obr. 2). Schéma aparatury v konfiguraci se dvěma větvemi jdoucími do aktivního výboje a kapilární trubicí v části dohasínání je na obr. 5. Na elektrody je přiloženo stejnosměrné napětí, jedná se tedy o doutnavý elektrický výboj, který je stručně popsán výše. Měření byla prováděna v průtokovém režimu za různých experimentálních podmínek.



Obr. 5: Schéma experimentální aparatury. 1 – katalyzátor Oxiclear, 2 – průtokoměry, 3 – výbojová trubice z křemene, 4 – tlakoměrka, 5 – optické vlákno, 6 – monochromátor Jobin Yvon Triax 550, 7 – CCD, 8 – počítač, 9 – kapilární trubice ze skla Pyrex

Výsledky výzkumu jsem prezentovala formou ústních prezentací a posterů na mezinárodních konferencích a na stážích v rámci projektů ERASMUS a CEEPUS, kde jsem přednášela na téma dohasínající plazma a jeho diagnostika. Nejvýznamnější výsledky tohoto výzkumu byly postupně publikovány ve vědeckých publikacích č. 1-7 uvedených v podkapitole SEZNAM KOMENTOVANÝCH PRACÍ.

2.2. Komentář k jednotlivým publikacím

Následující tři publikace jsou věnovány studiu dohasínání doutnavého výboje v argonu s různými příměsemi.

1. **Mazánková V.**, Trunec D., Navrátil Z., Raud J., Krčma F.: Study of argon-oxygen flowing afterglow. *Plasma Sources Science and Technology*, **25**, 3 (2016), 035008, ISSN: 0963-0252.

V reakční kinetice hrají významnou roli také procesy na povrchu výbojové trubice. V práci jsme pomocí experimentu a k němu vytvořeného kinetického modelu stanovili pravděpodobnost rekombinace atomárního kyslíku a deaktivace metastabilního molekulárního kyslíku na stěně proudové trubice z křemene. V experimentu bylo využito dohasínání doutnavého výboje v argonu s přidáním kyslíku přímo do aktivního výboje, diagnostickou metodou byla OES. V naměřených optických emisních spektrech byl identifikován atmosférický pás kyslíku (A-band), ze kterého byla stanovena rotační teplota plynu. Teplota na vnější straně trubice v dohasínající části byla měřena termočlánekem a bylo provedeno srovnání průběhu těchto teplot v čase dohasínání. Rotační teplota plynu vykazuje nárůst a po dosažení maxima se snižuje v pozdějších dobách dohasínání. Toto chování je v dobré shodě s teplotní závislostí spočtenou z modelu. Podobný trend byl pozorován i při měření teploty na vnější stěně trubice.

Pomocí NO titrace a OES byla stanovena koncentrace atomárního kyslíku O(P). S přihlédnutím k experimentálním podmínkám byl vytvořen 0-dimenzionální kinetický model, ve kterém bylo zahrnuto celkem 45 kinetických rovnic popisujících chemické reakce probíhající v dohasínání. Na soubor rovnic byla aplikována citlivostní analýza za účelem odhalení nejdůležitějších reakcí v modelu. Analýza ukázala, že v celkové kinetice rekombinace i disociace na stěnách hrají významnou roli. Z modelu nafitované hodnoty pravděpodobnosti rekombinace atomárního kyslíku a deaktivace metastabilního molekulárního kyslíku odpovídají hodnotám publikovaným v literatuře.

2. **Mazánková V.**, Trunec D., Kabeláčová K., Krčma F.: Study of argon afterglow with the air addition. *Plasma Physics and Technology*, **3**, 3 (2016), 136-139, ISSN: 2336-2626.

Oproti předchozí práci byl syntetický vzduch (směs 80% dusíku a 20% kyslíku) přidáván kapilární trubicí přímo do dohasínání argonového výboje. Diagnostickou metodou byla OES, ve spektrech byly detekovány argonové čáry a druhý pozitivní systém dusíku (second positive system – SPS). Tento systém byl tvořen přenosem excitační energie při srážkách argonového metastabilu s molekulami dusíku. Typické pro tento přenos je, že se ve spektrech objevují pouze přechody z hladin nižších než $v=3$. Výsledky kinetického modelu se shodovaly s experimentálními hodnotami a průběhem SPS v čase dohasínání. V publikaci jsou uvedeny průběhy koncentrací jednotlivých částic (elektronů, iontů, neutrálních částic) v závislosti na čase dohasínání vypočtené z modelu. Reakční schéma pak vypadá následovně. V průběhu

prvních stovek mikrosekund se ionty Ar^+ přemění na ionty Ar_2^+ a zároveň oba tyto ionty reagují s atomovým a molekulárním kyslíkem a molekulárním dusíkem za vzniku iontů O^+ , O_2^+ a N_2^+ . Během milisekund dojde k reakcím vedoucím pouze ke vzniku iontů O_2^+ a tyto ionty jsou tak jediné kladné ionty nacházející se v systému v pozdějších časech dohasínání. Dalšími reakcemi pak dochází ke vzniku NO a ozónu.

3. Mazánková V., Trunec D., Krčma F.: Study of argon flowing afterglow with nitrogen injection. *Journal of Chemical Physics*, **139**, 16 (2013), 164311, ISSN: 0021- 9606.

Do argonového dohasínání byl kapilární trubicí přidáván čistý dusík a pomocí OES byla snímána spektra podél proudové trubice v dohasínání. Ve spektrech byl pozorován opět SPS dusíku v závislosti na čase dohasínání. Naměřená závislost SPS na čase dohasínání vykazovala velmi pomalý pokles a rychlost tohoto poklesu nezávisela na koncentraci přidaného dusíku, což se jevílo v rozporu s dříve publikovanými experimentálními výsledky. Toto zvláštní chování bylo vysvětleno pomocí kinetického modelu. Horním stavem pro SPS je stav $\text{N}_2(\text{C})$, který vzniká přenosem excitace z argonového metastabilního stavu. Argonové metastability jsou také produkovány rekombinací iontů Ar_2^+ s elektronem, což vede k pomalému vzniku stavu $\text{N}_2(\text{C})$ a k tvorbě SPS. Tento vznik je pak převážně řízen rychlostí rekombinace iontů Ar_2^+ spíše než rychlostí přenosu excitace. Z modelu vyplývá také to, že rychlostní koeficient pro přenos excitace může být určen pouze při velmi nízkých koncentracích dusíku a pouze v prvních milisekundách dohasínání. Rychlostní koeficient byl tedy určen z měření intenzity SPS dusíku, zatímco v experimentech jiných autorů byl určen z poklesu koncentrace argonových metastabilů, která byla měřena absorpčními metodami.

Následující čtyři publikace jsou věnovány experimentům s dohasínajícím dusíkovým plazmatem. Byly zde studovány vlivy příměsí a dalších experimentálních podmínek na dusíkové dohasínání.

4. Mazánková V., Trunec D., Krčma F.: Study of nitrogen atom recombination by optical emission spectroscopy. *Plasma Physics and Technology*, **2**, 1 (2015), 50-53, ISSN: 2336- 2626.

V pozdějších časech dusíkového dohasínání převládá mezi probíhajícími procesy zejména rekombinace atomárního dusíku. V publikaci byla studována rekombinace atomů dusíku pomocí OES. Ve spektrech byly měřeny intenzity prvního a druhého pozitivního systému a prvního negativního systému dusíku. Spektrům dominoval pás prvního pozitivního systému dusíku, kde byl nejintenzivnější přechod 11-7. Výskyt tohoto pásu je v přímé souvislosti s trojčásticovou rekombinací atomárního dusíku a z jeho intenzity je tedy možné určit jeho relativní koncentraci. Z poklesu intenzity přechodu 11-7 s časem dohasínání bylo možno určit pravděpodobnost rekombinace atomárního dusíku na stěnách trubice.

5. **Mazánková V.**, Trunec D., Krčma F.: Study of nitrogen flowing afterglow with mercury vapor injection. *Journal of Chemical Physics*, **141**, 15 (2014), 154307, ISSN: 0021- 9606.

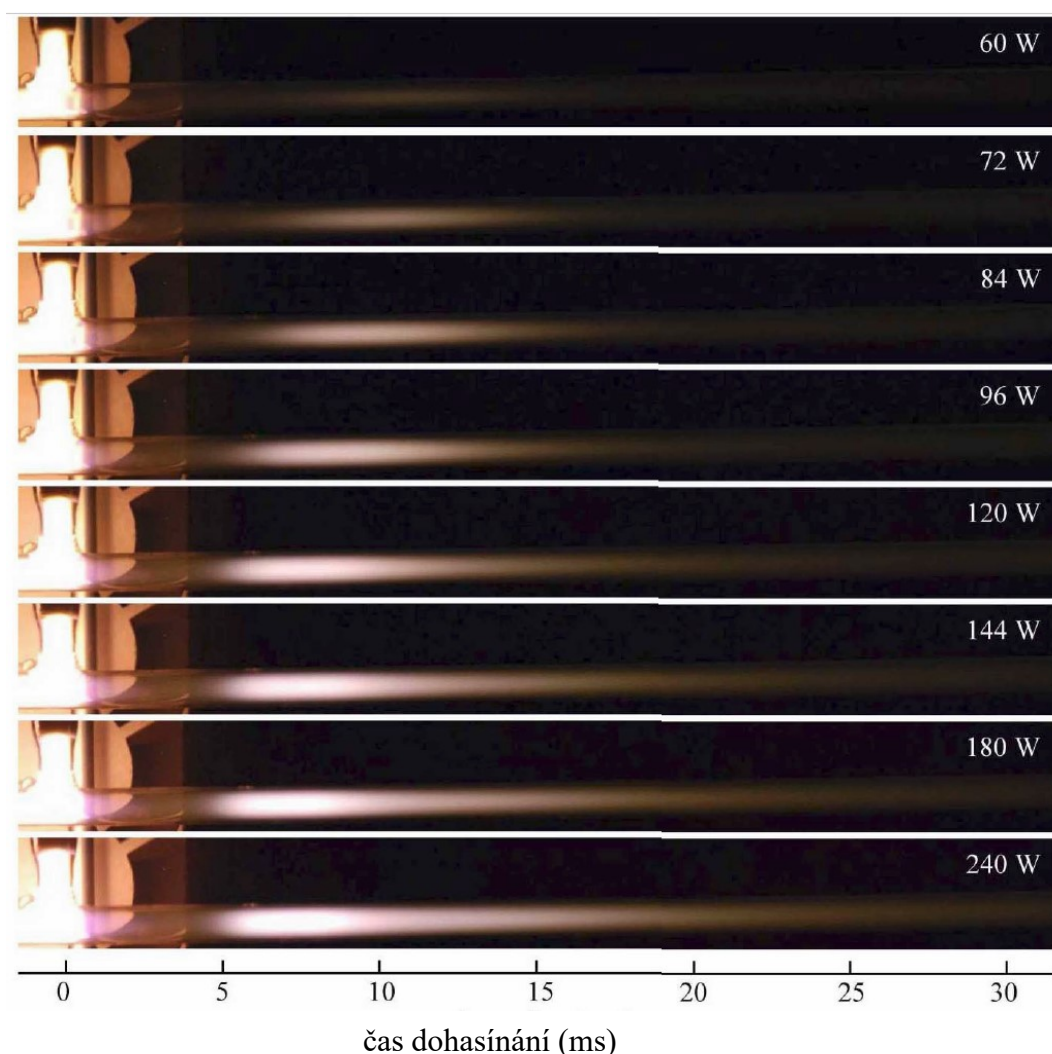
Jestliže přidáme do dusíkového dohasínání rtuť, bude docházet k přenosu energie mezi $N_2(A)$ stavem dusíku a rtuť. Této vlastnosti se využívá v analytické chemii pro stanovování stopového množství rtuti. V experimentu popsáném v publikaci jsme použili aktivní výboj a dohasínání v čistém dusíku a rtuť jsme přiváděli ve formě rtuťových par do dohasínání pomocí kapilární trubice. Při všech měřeních pomocí OES byla zaznamenána spektrální čára rtuti na 254 nm. Intenzita této čáry byla opět měřena podél celé proudové trubice v dohasínání, tedy pro různé časy dohasínání. Naměřená závislost intenzity na čase dohasínání vykazovala pouze pomalý pokles s rostoucím časem a rychlost poklesu nezávisela na koncentraci přidané rtuti. Toto chování bylo vysvětleno pomocí kinetického modelu. Do kinetického modelu bylo zahrnuto 23 chemických reakcí. Na rovnice byla taktéž aplikována citlivostní analýza, ze které vyplynuly tři nejvýznamnější reakce. Jsou to rekombinace atomárního dusíku na stěně, zhášení stavu $N_2(A)$ a objemová rekombinace atomárního dusíku, která vede ke tvorbě molekulárního dusíku ve stavu $N_2(B)$. Stav $N_2(A)$ potom opět vzniká radiačním přechodem ze stavu $N_2(B)$. Dochází tedy k pomalému poklesu tvorby dusíku ve stavu $N_2(A)$ a následně k pomalému poklesu intenzity rtuťové čáry. Pokles intenzity rtuťové čáry je tedy dán rekombinačními procesy atomárního dusíku. Z kinetického modelu byl fitováním určena i pravděpodobnost rekombinace atomárního dusíku na stěně.

6. **Mazánková V.**, Krčma F.: Influence of oxygen traces on recombination process in nitrogen post-discharge. *Chemické listy*, **102**, 16 (2008), s1388-s1393, ISSN: 1213-7103.

Tato publikace byla jedna z prvních, kde jsme prezentovali souhrnné výsledky experimentů s dohasínáním v čistém dusíku pro různé experimentální podmínky. Pomocí OES jsme snímali spektra dusíkového dohasínání ve výbojových trubicích z různých materiálů. Trubice byly vyrobeny ze skla Pyrex nebo z křemenného skla. Později jsme experimenty prováděli už jen v křemenném skle. Dále jsme měnili teplotu v okolí místa snímání spekter. Rychlostní konstanty reakcí probíhajících v dohasínání jsou značně závislé na teplotě, což bylo ověřeno. V další sérii experimentů jsme také přidávali technický vzduch přímo do aktivního výboje a sledovali jsme tak změny v jevu pink afterglow, který se nachází v dohasínání. Tento jev byl v podstatě potlačen díky přítomnosti kyslíku ve výboji. Výsledky těchto přehledových experimentů byly současně prezentovány na konferenci II Central European Symposium on Plasma Chemistry.

7. Krčma F., **Mazánková V.**, Soral I, Guerra V.: Power dependence of the pink afterglow in flowing post-discharge in pure nitrogen. *IEEE Transactions on Plasma Science*, **42**, 10 (2014), 2384-2385, ISSN: 0093- 3813.

Tato publikace vyšla ve speciálním čísle časopisu IEEE Transactions on Plasma Science jako 7th Triennial Special Issue on Images in Plasma Science. Celé číslo časopisu bylo věnováno obrazové prezentaci jevů v plazmatu, proto jsme se zaměřili na jev pink afterglow, který je velmi dobře viditelný a lze ho ovlivnit různými experimentálními podmínkami. V příspěvku je tento jev zaznamenán pro různé výkony dodávané do výboje (60-240 W) a je zde uveden průběh intenzity prvního pozitivního systému dusíku, který je ve spektru pink afterglow pozorován s nejvyšší intenzitou. Na obr. 6 jsou fotografie pink afterglow pro různé výkony.

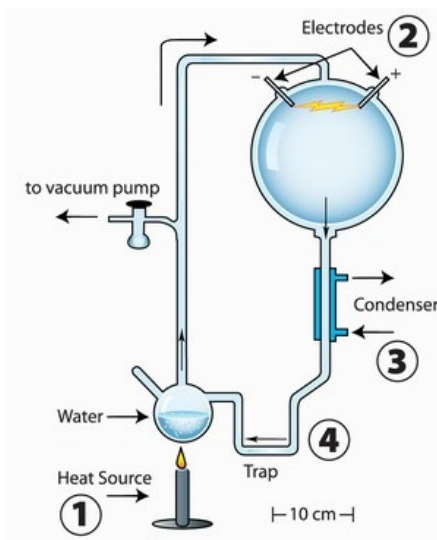


Obr. 6: Závislost intenzity jevu pink afterglow na dodávaném výkonu do aktivního výboje v čistém dusíku.

3. Elementární procesy v prebiotických atmosférách zkoumané pomocí klouzavého obloukového výboje

3.1 Stav problematiky

Teorii o postupném vzniku organických molekul z jednoduchých anorganických látek přítomných na prehistorické Zemi (v době jejího vzniku) vyslovili téměř současně nezávisle na sobě ve 20. letech 20. století vědci Oparin a Haldane (Oparin 1938, Haldane 1928, Haldane 1954). Předpokládali, že před 3,5-4 miliardami let, v období hadaika, byly v zemské atmosféře silně redukční podmínky. A dále předpokládali, že za těchto podmínek se zdrojem energie z UV záření nebo bleskové aktivity mohly anorganické molekuly spontánně vytvářet organické molekuly, jako jsou jednoduché cukry a aminokyseliny. V roce 1953 Stanley Miller a Harold Urey (Miller 1953, Miller and Urey 1959) otestovali tuto hypotézu experimentálně tak, že se snažili simulovat atmosféru na Zemi v době jejího vzniku, tzv. prebiotickou atmosféru, ve skleněné cyklické aparatuře. Schematické znázornění aparatury jejich experimentu je na obr. 7.



Obr. 7: Schéma Miller-Urey experimentu. 1 - ohřev kapalné fáze, 2 - elektrody, 3 - chlazení vodou, 4 - past (Eri's).

V experimentu použili směs plynů složenou z amoniaku (NH_3), metanu (CH_4), vodíku (H_2) a vodní páry (H_2O), která simulovala prebiotickou atmosféru. Za běžných atmosférických podmínek tyto plyny spolu nereagují, takže dodávali do systému energii pomocí jiskrového výboje, který simuloval blesky vyskytující se v atmosféře. Následovalo ochlazení v chladicí pasti a další zahřívání kapaliny, kterou tvořil vodný roztok simulující prehistorický oceán (primordial soup). Z vodného roztoku docházelo k odpařování a tím byl koloběh uzavřen. Takto nechali Miller s Ureyem experiment probíhat jeden týden a pak provedli chemickou analýzu vodného roztoku, který změnil v průběhu experimentu svou barvu z čiré do tmavě hnědé. Tehdejšími analytickými metodami byli schopni detekovat pět aminokyselin a několik

dalších jednoduchých organických sloučenin. Tímto experimentem vzbudili velký zájem o další výzkum prebiotických atmosfér. Originální vzorky z původního experimentu byly uchovány (viz obr. 8) a v nedávné době znovu analyzovány. Díky současným analytickým metodám se podařilo ve vzorcích identifikovat mnohem více organických sloučenin a aminokyselin (Parker et al. 2011, Johnson et al. 2008).



Obr. 8: Vialky se vzorky roztoků pocházejících z Miller-Ureyových experimentů provedených v roce 1958, které jsou popsány samotným Millerem (Phys.org).

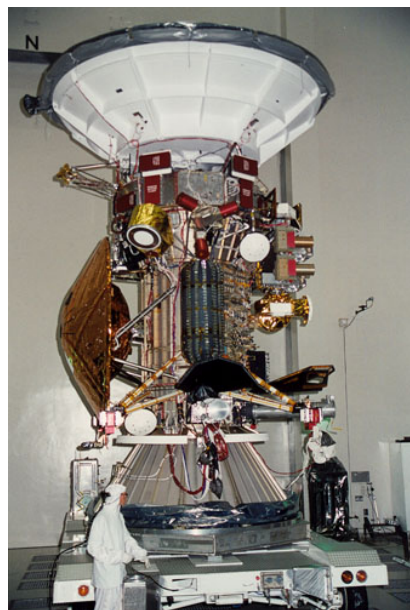
Jak se ale záhy ukázalo, složení atmosféry, které použili Miller s Ureyem ve svém experimentu, bylo velmi redukční a tím pádem nereálné pro vznik života (Cleaves et al. 2008, Mc Colom 2013). V tehdejší atmosféře se vyskytoval také kyslík (O_2) a vznikal oxid uhličitý (CO_2), což dokazují stopy zoxidovaného uranu a železa nacházející se v horninách starých 3,5 miliard let. Od velmi redukční atmosféry $CH_4 + H_2 + NH_3 + H_2O$ se současné teorie modelující atmosféru na Zemi v době jejího vzniku přiklánějí ke složení spíše neutrálnímu – $CO_2 + H_2 + N_2$ s malým množstvím příměsí SO_2 , CH_4 a H_2S .

Od dob prvního experimentu Millera a Ureye bylo provedeno velké množství experimentálních i teoretických simulací prebiotických atmosfér v různých směsích plynů a s různými zdroji energie. Ukázalo se, že těmito simulacemi mohou být syntetizovány rozmanité organické sloučeniny včetně aminokyselin. V neutrálních atmosférách ale dochází k výraznému poklesu v produkci aminokyselin, než při produkci v redukční atmosféře. Z výsledků experimentů vyplynulo, že přítomnost CH_4 a NH_3 je nezbytně nutná právě pro tvorbu aminokyselin. Prekurzorem pro vznik aminokyselin je kyanovodík (HCN), který je meziproduktem v tzv. Streckerově syntéze aminokyselin a je také důležitým prekurzorem pro tvorbu nukleobází (Ferris et al. 1978).

Zásadní roli v procesech probíhajících v prebiotických atmosférách hraje obsah CO_2 . Bylo zjištěno, že vysoký obsah CO_2 a molekul jako CO a N_2 v atmosféře v období hadaika, vedl ke vzniku skleníkového jevu, který ovšem ochránil prehistorický oceán před zamrznutím (Kasting 1993). Sluneční aktivita byla v té době téměř o 70% nižší než v současnosti (Gough 1981) a v atmosféře se nenacházely žádné další plyny způsobující skleníkový jev, takže vysoká koncentrace CO_2 byla důležitá pro udržení teploty na povrchu Země nad bodem mrazu.

Vysvětlení mechanismu syntézy organických sloučenin v neutrálních atmosférách je stále problematické. Tyto stále otevřené otázky jsou také někdy reprezentovány jako důkaz proti evolučním přístupům ke studiu původu života (Wells 2002).

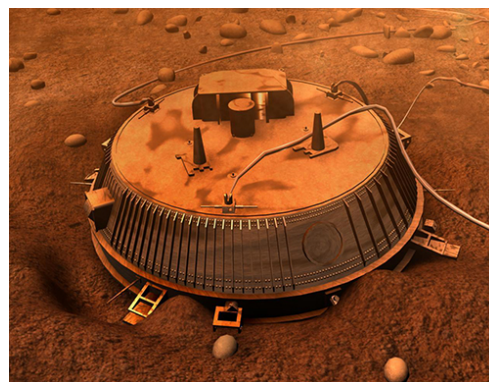
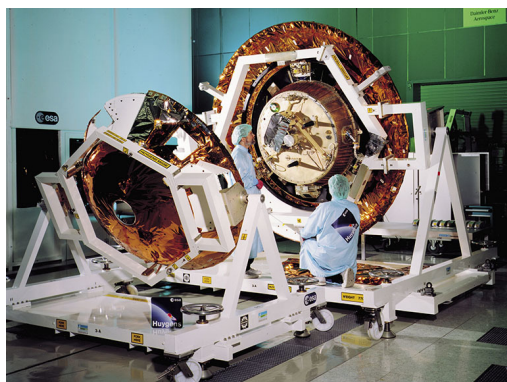
Nový pohled na věc přišel nečekaně z vesmíru. Největší měsíc planety Saturn, kterým je Titan, má atmosféru, jejíž složení je podobné složení prebiotických atmosfér a je tedy podobná atmosféře na prehistorické Zemi. Měsíc Titan byl objeven již v roce 1655 Christiaanem Huygensem. V roce 1979 dorazila k Titanu první vesmírná sonda Pioneer 11, kterou vyslala NASA (National Aeronautics and Space Administration). Podle jeho pozorování byl Titan příliš chladný, než aby na něm mohl existovat život. Pioneer pořídil i několik snímků Titanu. Obrázky získané na počátku 80. let 20. století dvěma sondami Voyager 1 a Voyager 2 byly mnohem vyšší kvality. Pozorování, které sondy provedly, ukázala, že atmosféra Titanu je hustší než zemská a tlak na povrchu dosahuje 1,45 atm. Neprůhledné vrstvy mlhy však zamezují prostupu většiny slunečního světla a zakrývají tak při pohledu z vesmíru povrchové útvary. Díky nižší gravitaci Titanu dosahuje atmosféra do mnohem větší výšky nad povrch než je tomu u Země. Atmosféra je neprůhledná pro značnou část vlnových délek, a proto nebylo možné z orbity získat kompletní spektrum odrazivosti povrchu. Další informace přišly z pozorování pomocí Hubbleova teleskopu v roce 1995, z nichž vyplývala přítomnost kapalného metanu na měsíci, ať již v malých oddělených jezerech nebo ve velkých oceánech. První snímky povrchu a s nimi velké množství dalších informací o Titanu přinesla až roku 2004 vesmírná sonda Cassini-Huygens (viz obr. 9).



Obr. 9: Sonda Casini - Huygens (NASA).

Cassini-Huygens byla americká planetární sonda, určená pro průzkum planety Saturn, jejích prstenců a systému jejích měsíců. Vypuštěna byla 15. října 1997 a byla funkční až do 15. září 2017, tedy téměř 20 let. Její mise byla ukončena řízeným zánikem v atmosféře

planety Saturn. Na jejím přístrojovém vybavení se podílely také evropská organizace pro výzkum vesmíru (European Space Agency-ESA) a italská národní kosmická agentura (Agenzia Spaziale Italiana-ASI). Sonda měla dvě samostatné části: mateřskou sondu Cassini, která nesla jméno italského astronoma Giovanni Domenica Cassiniho, a atmosférickou sondu Huygens pojmenovanou po holandském vědci Christiaanovi Huygensovi. Do Saturnovy sféry gravitačního vlivu vstoupila sonda 9. března 2004. Dne 25. prosince 2004 se od sondy Cassini oddělila sonda Huygens, která 14. ledna 2005 úspěšně přistála na měsíci Titan. Během sestupu atmosférou a po přistání shromáždila sonda Huygens značné množství vědeckých poznatků o tomto tělese. Sonda Cassini sloužila jako retranslační stanice pro předávání vědeckých a technických dat ze sondy Huygens na Zemi (NASA) (viz obr. 10). Sonda Huygens pravděpodobně na povrchu měsíce vydržela pracovat 4 hodiny, avšak Cassini, zprostředkovávající informace, se po dvou hodinách dostala do zákrytu měsíce a přenos byl tedy přerušen. Měsíc Titan se tak stal nejvzdálenějším objektem, na němž kdy přistála lidmi vytvořená sonda.



Obr. 10: Sonda Cassini a její část sonda Huygens (NASA).

Sonda Cassini je pro průzkum vesmíru vybavena zařízeními (viz Tabulka 1) pro měření a monitorování velkého množství fyzikálně chemických vlastností a veličin.

Tabulka 1: seznam zařízení, která nesla sonda Cassini (NASA).

CAPS - Cassini Plasma Spectrometer	RSS - Radio Science Subsystem
CDA - Cosmic Dust Analyzer	MAG - Magnetometer
CIRS - Composite InfraRed Spectrometer	RADAR - Radio Detection and Ranging
INMS - Ion a Neutral Mass Spectrometer	RPWS - Radio and Plasma Wave Science
ISS - Imaging Science Subsystem	MIMI INCA - MIMI Ion and Neutral Camera
VIMS - Visible and Infrared Mapping Spectrometer	MIMI LEMS - MIMI Low Energy Magnetospheric Measurement System
RTG - Radioisotope Thermoelectric Generator	MIMI CHEMS - MIMI Charge-Mass-Energy Spectrometer
UVIS - Ultraviolet Imaging Spectrograph	

Za dobu svého působení v Saturnově sféře se sonda Cassini přiblížila k měsíci Titanu 127 krát a potvrdila přítomnost metanových jezer, objevila pohoří a krátery, které se zde nacházejí. Ze získaných informací o složení atmosféry Titanu byla vyslovena celá řada nových hypotéz o chemických pochodech na Titanu. Ve vrchních vrstvách atmosféry Titanu se uplatňuje vliv slunečního UV záření a elektronů z magnetosféry Saturnu. Jak UV záření, tak i energetické elektrony jsou schopny iniciovat chemické procesy v těchto horních vrstvách atmosféry. Rovněž se spekuluje, že se na Titanu mohou vyskytovat blesky či jiná elektrická aktivita v atmosféře. Tyto jevy však dosud nebyly potvrzeny. Metan může v atmosféře Titanu hrát stejnou roli jako voda v atmosféře Země, může vytvářet mraky a déšť. Metan a další uhlovodíky se nachází na povrchu Titanu ve formě oceánů (Raulin 2007). Zatím je však Titan hlavně zmrzlým světem ve značné vzdálenosti od Slunce, jeho atmosféra obsahuje příliš malé množství oxidu uhličitého a voda se na povrchu vyskytuje jen v pevném skupenství. Proto je analogie s atmosférou prehistorické Země do jisté míry nepřesná.

Chemické procesy na Titanu začínají disociací dusíku a metanu UV zářením nebo elektrony. Reakce radikálů vedou ke vzniku zejména HCN a C₂H₂. Dále mohou vznikat složitější uhlovodíky a nitrily. Rovněž vznikají pevné částice, které byly nazvány tholiny (Raulin 2007). Procesy v atmosféře Titanu je možné simulovat v laboratorních experimentech, které využívají např. elektrické výboje. Při těchto experimentech bylo detekováno mnoho částic, které byly detekovány i v atmosféře Titanu. Při simulacích výboji vznikají i jiné sloučeniny, které zatím v atmosféře Titanu objeveny nebyly. Na tyto sloučeniny se zaměřuje další průzkum atmosféry Titanu pomocí zařízení, které nese sonda Cassini.

Tématem elementárních procesů v prebiotických atmosférách jsem se zabývala v rámci dlouhodobého výzkumu na Fakultě chemické VUT v Brně. Absolvovala jsem také krátkodobé vědecké stáže spojené s tímto tématem v rámci projektů COST CM1401 a TD1308 na Open University v Milton Keynes ve Velké Británii a na Komenského univerzitě v Bratislavě. V rámci projektu CEEPUS jsem se tématem zabývala i na Univerzitě v Innsbrucku v Rakousku. Hlavním cílem celého výzkumu je popis kinetických procesů probíhajících v atmosférách typu CH₄ + N₂. V experimentu máme k dispozici klouzavý obloukový výboj a diagnostické metody jako Infračervenou spektroskopii (Fourier Transform Infrared Spectroscopy – FTIR), plynovou chromatografii spojenou s hmotnostní spektrometrií (Gas Chromatography Mass Spectroscopy – GC-MS), hmotnostní spektrometrii s přenosem protonu (Proton Transfer Reaction Mass Spectrometry – PTR-MS) a OES.

Ve všech našich experimentech s obloukovým klouzavým výbojem jsme používali standardní konfiguraci elektrod. Vzhledem k nízkým průtokům a výkonům se výboj nacházel v režimu, kdy bylo možné pozorovat jeden stojící výbojový kanál mezi elektrodami. Na obr. 11 je ukázána aparatura a elektrody s hořícím výbojem.



Obr. 11: Aparatura pro experimenty s klouzavým obloukovým výbojem (vlevo) a elektrody s výbojovým kanálem (vpravo).

Nejvýznamnější výsledky tohoto výzkumu byly postupně publikovány ve vědeckých publikacích č. 8-12 uvedených v podkapitole SEZNAM KOMENTOVANÝCH PRACÍ.

3.2. Komentář k jednotlivým publikacím

Následující tři publikace byly věnovány experimentům s klouzavým obloukovým výbojem a směsí plynů $N_2 + CH_4 + CO_2$, jejich interpretaci a identifikaci nejdůležitějších reakcí vedoucích k produkci biofyzikálně významných sloučenin.

- 8. Mazánková V., Töröková L., Krčma F., Mason N., Matejčík Š.:** The influence of CO_2 admixtures on the product composition in a nitrogen-methane atmospheric glow discharge used as a prebiotic atmosphere mimic. *Origins of Life and Evolution of the Biosphere*, **46**, 4 (2016), 499-506, ISSN: 0169-6149.

Publikace je zaměřena na studium vlivu CO_2 v reakční směsi $N_2 + CH_4$ pomocí FTIR. Je zde popsán vliv CO_2 na tvorbu HCN a NH_3 . HCN vzniká ve výboji jako hlavní produkt, což bylo FTIR diagnostikou potvrzeno. HCN je velmi důležitý jako prekurzor pro následnou syntézu aminokyselin v probiotických atmosférách (McCollom 2013). Vznik NH_3 je vázán zejména na reakce na povrchu elektrod. Reakční schémata tvorby HCN i NH_3 jsou v publikaci popsána. Z experimentu vyplynulo, že přidávání CO_2 do směsi $N_2 + CH_4$ ovlivnilo produkci HCN, a to tak, že se se zvyšováním koncentrace CO_2 se zvýšila produkce HCN. Zajímavé bylo porovnání s experimenty Fleuryho et al. (Fleury et al., 2014), kde do směsi $N_2 + CH_4$ byl přidáván oxid uhelnatý (CO). Bylo tím dosaženo opačného efektu – poklesu koncentrace HCN. V našich experimentech došlo ke zvýšení produkce NH_3 s přidáváním CO_2 došlo pouze v případě nižších koncentrací CH_4 (1 % a 2 %) v reakční směsi. Pro vyšší koncentrace CH_4 (4 % a 5 %) nemělo přidávání CO_2 na tvorbu NH_3 zásadní vliv.

9. Töröková L., **Mazánková V.**, Mason N., Krčma F., Morgan G., Matejčík Š.: The influence of CO₂ admixtures on process in Titan' s atmospheric chemistry. *Plasma Physics and Technology*, **3**, 3 (2016), 163-167, ISSN: 2336-2626.

V této publikaci jsou výsledky FTIR doplněné o výsledky z další analýzy a to GC-MS. Analýza GC-MS byla provedena pro vybrané experimentální podmínky a byla provedena v rámci stáže na Open University ve Velké Británii. Analýzu nebylo možné provádět in-situ, ale za použití kryopasti. Do kryopasti byly zachyceny stabilní produkty chemických reakcí probíhajících ve výboji. Následně byla kryopast zahřáta na pokojovou teplotu a zachycené plyny byly odebrány přes vyměnitelné chromatografické septum plynotěsnou stříkačkou (Hamilton 1 ml). Plyný vzorek byl ze stříkačky vstříknut do injektoru plynového chromatografu a pak byla spuštěna analýza přístrojem GC-MS. Tato metoda byla použita opakovaně a za daných podmínek byla dobře reprodukovatelná. Analýza GC-MS také potvrdila, že HCN je nejvíce koncentrovaný produkt a zároveň byly detekovány i produkty, které se ve FTIR analýze neobjevily. Hlavními uhlovodíky, které se podařilo spolehlivě detekovat, byly etan (C₂H₆), acetylén (C₂H₂) a ethen (C₂H₄). V případě nitrilů to jsou to HCN, acetonitril (CH₃CN), akrylonitril (C₂H₃CN) a propionitrile (C₂H₅CN). Výsledky experimentů jsou v dobrém souladu s daty získanými o složení atmosféry měsíce Titanu pomocí sondy Cassini. Tato skutečnost jasně demonstruje použitelnost laboratorních experimentů s klouzavým obloukovým výbojem pro simulaci atmosféry Titanu.

10. Töröková L., **Mazánková V.**, Krčma F., Mason N., Matejčík Š.: The influence of admixtures on the composition of products by nitrogen- methane atmospheric glow discharge. *Plasma Physics and Technology*, **2**, 1 (2015), 88-91. ISSN: 2336- 2626.

Jedná se o naši první publikaci se souhrnnými výsledky z experimentů s klouzavým obloukovým výbojem v reakční směsi N₂ + CH₄ + CO₂. Je zaměřená na sledování změny koncentrace HCN v závislosti na výbojovém proudu, koncentraci CH₄ a CO₂. Koncentrace HCN byla určována pomocí absorpčního měření metodou FTIR. Mezi další minoritní produkty v našich experimentech se řadí zejména C₂H₂, NH₃, CO₂ a CO. Bohužel nebyly detekovány žádné další oxidy např. formaldehyd nebo ethylenoxid, i když vznik těchto sloučenin byl předpovězen teoretickým modelem (Dobrijevic et al., 2014).

Následující dvě publikace jsou věnovány experimentálním výsledkům se směsí plynů N₂ + CH₄. Publikace vznikly s cílem porovnání našich experimentálních výsledků s výsledky ostatních skupin zabývajících se také simulací atmosféry měsíce Titanu a také porovnání výsledků získaných ze sondy Cassini.

11. Töröková L., Watson J., Krčma F., **Mazánková V.**, Mason N., Horváth G., Matejčík Š.: Gas chromatography analysis of discharge products in N₂-CH₄ gas mixture at atmospheric pressure: Study of mimic Titan's atmosphere. *Contributions to Plasma Physics*, **55**, 6 (2015), 470-480, ISSN: 1521- 3986.

Jedná se o naši první publikaci věnovanou experimentální simulaci procesů, které by mohly probíhat v atmosféře měsíce Titanu. Pro iniciaci chemických procesů byl zvolen klouzavý obloukový výboj ve směsi N₂ + CH₄ a produkty z výboje byly analyzovány pomocí GC-MS. Experimenty byly provedeny bez dalších příměsí, ale pro různé experimentální podmínky. Byl studován vliv velikosti výkonu ve výboji a také vliv velikosti průtoku reakční směsi výbojem. Analýzou GC-MS bylo detekováno více než dvacet různých produktů, přičemž některé produkty již byly pozorovány při předchozích experimentech jiných autorů a některé produkty byly v našich experimentech detekovány poprvé. V publikaci je uvedeno srovnání s výsledky uvedených v článcích jiných autorů. Dále jsou zde uvedeny reakční mechanismy vedoucí ke vzniku pozorovaných produktů. Výsledkem měření byly relativní koncentrace jednotlivých produktů, ze kterých vyplynulo, že relativní koncentrace vyšších uhlovodíků a nitrilů klesá. Výtěžky produktů lze zapsat v následujících poměrech:

Uhlovodíky: C₂H₂ > C₂H₄ > C₂H₆ > C₃H₆ > C₃H₈ > C₃H₄ > C₃H₄ > další uhlovodíky s C₄
Nitrily: HCN > CH₃CN > C₂H₅CN > C₂H₃CN > C₂N₂ > C₃H₅CN > C₃H₇CN.

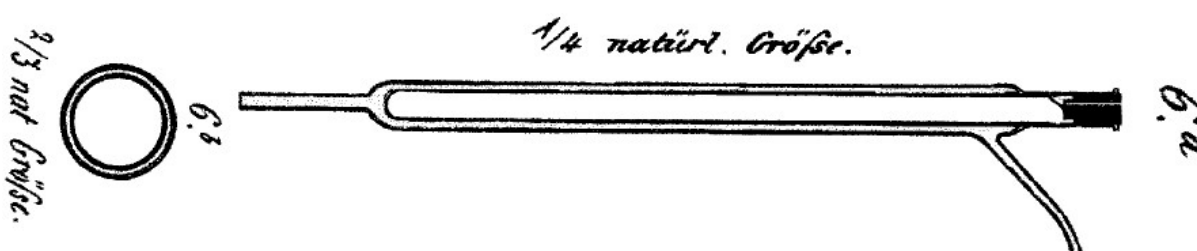
12. Töröková L., **Mazánková V.**, Krčma F., Mason N., Matejčík Š.: Atmospheric pressure glow discharge generated in nitrogen-methane gas mixture: PTR-MS analyzes of the exhaust gas. *European Physical Journal- Applied Physics*, **71** (2015), 20806-20810, ISSN: 1286- 0042.

Stejně jako předchozí publikace je i tato věnována simulaci procesů v atmosféře měsíce Titanu. V tomto článku jsou produkty klouzavého obloukového výboje analyzovány in-situ metodou PTR-MS. Tato metoda je citlivější než GC-MS a protože byla provedena in-situ, tak bylo pomocí ní detekováno více druhů produktů, zejména vyšších uhlovodíků a nitrilů. Poměry relativních koncentrací zůstaly zachovány jako při použití metody GC-MS.

4. Aplikace dielektrického bariérového výboje

4.1 Stav problematiky

Historie dielektrického bariérového výboje (dielectric barrier discharge - DBD) je popsána v přehledovém článku dr. Kogelschatze (Kogelschatz 2003), kde se zmiňují počátky studia dielektrických bariérových výbojů. Jejich historie sahá až do roku 1857, kdy Werner von Siemens sestrojil ozonizátor pomocí dvou skleněných trubic, které byly protékány vzduchem (viz obr. 12). Konfigurace byla originální v tom, že kovové elektrody nebyly v přímém kontaktu s plazmatem, jak tomu bylo u různých výbojů doposud. Rozsáhlejší výzkum DBD byl proveden na počátku 20. století a zaměřoval se zejména na konstrukci průmyslových ozonizátorů.



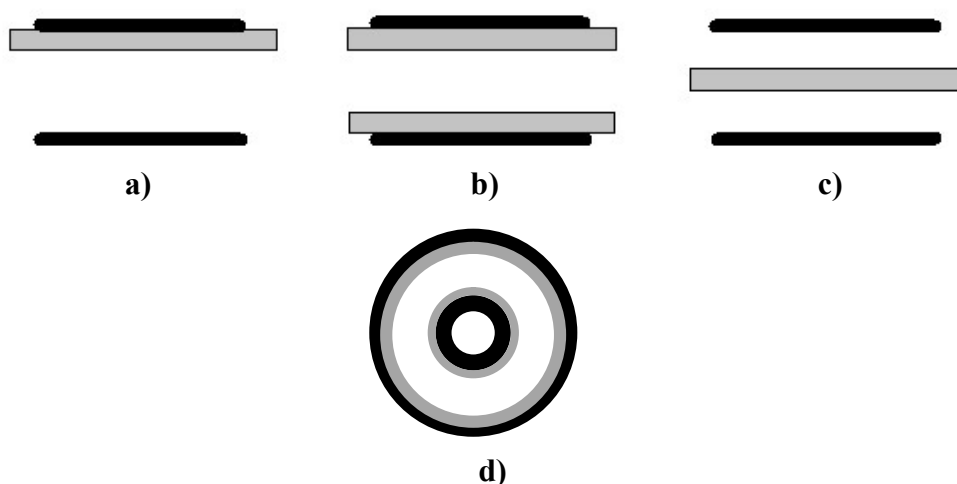
Obr. 12: Siemensův ozonizátor (Kogelschatz 2003).

Ve 30. letech 20. století bylo zjištěno, že běžný DBD je filamentární – je tvořen mikrovýboji (filamenty), což je základní mód hoření bariérových výbojů (Kogelschatz 2003). Prostorové a časové rozložení jednotlivých filamentů je obvykle náhodné a nerovnoměrné. Typický průměr filamentu je 100 μm a doba trvání filamentu je 1-10 ns (výboje ve vzduchu). V 60. letech byly objeveny homogenní bariérové výboje v heliu (Bartnikas 1968). Tyto výboje nejsou tvořeny jednotlivými filamenty, ale homogenním plazmatem. Později bylo dosaženo homogenního výboje i v dusíku. Výzkum homogenního DBD dále pokračoval v 80. letech 20. století, kdy prof. Okazaki nazvala tento typ výboje „atmospheric-pressure glow discharge“ (APGD) (Okazaki 1993).

Díky své technické jednoduchosti je DBD jedním z nejrozšířenějších výbojů používaných v zařízeních pro generaci teplotně nerovnovážného plazmatu při atmosférickém tlaku. Ve výbojovém prostoru tohoto výboje je umístěná elektroizolační bariéra z vhodného dielektrika, která zabezpečuje trvání elektrického průrazu (doby trvání mikrofilamentu) v jednotkách nanosekund. Tento krátký čas stačí lehkým elektronům k tomu, aby získaly v elektrickém poli dostatečnou energii k ionizačním srážkám, díky nimž začnou exponenciálně zvyšovat svůj počet. Zároveň je tato doba příliš krátká na to, aby tyto elektrony stačily významně ohřát okolní plyn. Výsledkem je nerovnovážný stav plazmatu s teplotou řádově jednotky eV a teplotou iontů a neutrálního plynu kolem 300 K. Díky tomu nachází DBD uplatnění

v mnohých aplikacích, jako je výroba ozónu, rozklad organických prchavých látek, modifikace povrchu polymerů nebo depozice tenkých vrstev.

Z hlediska konfigurace rozeznáváme několik typů DBD. Ve všech případech jsou elektrody odděleny alespoň jednou dielektrickou vrstvou. Podle konfigurace elektrod a dielektrika lze rozdělit bariérové výboje na objemové a povrchové. V případě objemového výboje mohou být elektrody cylindrické, jak tomu bylo u Siemensova ozonizátoru nebo planární navzájem rovnoběžné (viz obr. 13). U povrchových DBD plazma nevzniká v objemu v mezielektrodovém prostoru, ale přímo na povrchu dielektrika, takže je umožněn volný přístup k ploše pokryté plazmatem. Elektrodový systém povrchového bariérového výboje je tvořen planární elektrodou, která je pokryta dielektrikem. Druhá elektroda je umístěna z druhé strany dielektrika a může mít prakticky jakýkoli tvar, nejčastěji se setkáváme s elektrodou ve formě pásky nebo válečku. Povrchové výboje mohou být také v tzv. koplanární konfiguraci. Elektrodový systém koplanárního povrchového DBD je tvořen dvěma a více paralelními elektrodami, které jsou umístěny přímo uvnitř dielektrika (viz obr. 14).



Obr. 13: Verze objemového DBD, a) planární s jedním dielektrikem, b) planární se dvěma dielektriky, c) planární s dielektrikem uprostřed, d) cylindrický. Černá plocha zobrazuje elektrody a šedá dielektrikum.



Obr. 14: Verze povrchového DBD, a) planární, b) koplanární. Černá plocha zobrazuje elektrody a šedá dielektrikum.

Jako dielektrikum se nejčastěji používají materiály typu sklo, keramika, slída či různé polymery. Skutečnost, že systém obsahuje jedno nebo více dielektrik si vynucuje buzení pomocí střídavého zdroje napětí. Když napětí dosáhne dostatečně velké hodnoty, dojde k

průrazu pracovního plynu, kde vlastnosti dielektrika a frekvence omezují průměrnou proudovou hustotu ve výbojovém prostoru.

Významnou aplikací DBD je výroba ozónu v ozonizátorech s cylindrickou konfigurací elektrod. Pro tyto aplikace je možné bez obav využívat filamentární mód DBD. Ozón je zejména účinné oxidační činidlo a význam jeho použití v různých průmyslových odvětvích je stále větší. Využívá se zejména pro čištění vody, ovzduší a pro odbarvování látek. Má také široké uplatnění ve zdravotnictví a potravinářském průmyslu díky svým sterilizačním účinkům. Ozón efektivně ničí většinu známých bakterií a plísní. Nezanechává žádné vedlejší produkty a v atmosféře se rozkládá volně na kyslík. Je ekologicky přijatelnějším a účinnějším prostředkem v porovnání s chlórem nebo brómem např. při úpravě vody. Při konstrukci ozonizátorů je ale nutné brát v úvahu, že ozón reaguje s plasty a kovy a může ovlivňovat jejich fyzikálně-chemické vlastnosti a přispívat k jejich degradaci.

Ozón je alotropická modifikace kyslíku schopná existovat ve všech třech látkových skupenstvích. Za standartních podmínek je to nestálý, velmi reaktivní modrý diamagnetický plyn s charakteristickým ostrým zápachem, podle kterého ho v roce 1840 pojmenoval Christian Friedrich Schönbein.

Ozón je velmi nestabilní látka, kterou není možné dlouhodobě skladovat nebo uchovávat. Proto jsou pro jeho produkci konstruovány ozonizátory, ve kterých se vyrobený ozón okamžitě používá k danému účelu. Ve výboji dochází nárazem elektronu k disociaci molekuly kyslíku. Vzniklé kyslíkové atomy jsou velmi reaktivní a reagují s molekulami kyslíku za vzniku ozónu:



kde M je třetí částice (většinou molekula kyslíku).

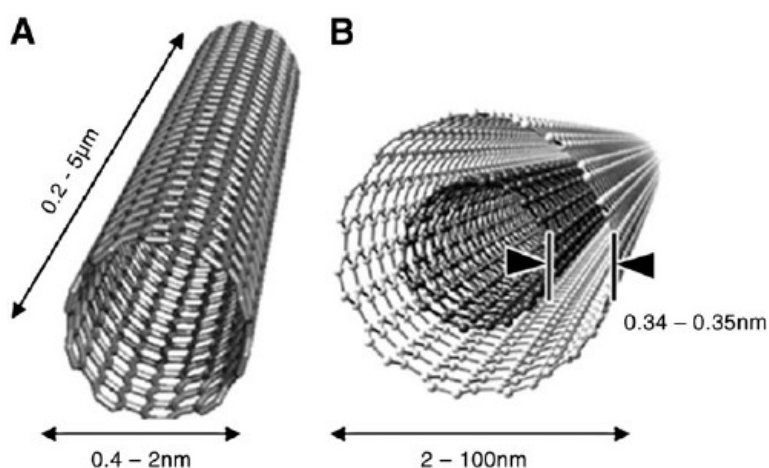
Při výrobě ozónu i jeho aplikacích v průmyslu je velmi důležité měření jeho koncentrace. Nejběžnějšími metodami pro stanovení koncentrace ozónu jsou fotometrická a titrační. Fotometrická metoda spočívá ve spektroskopickém měření absorpce UV záření v ozónu, je vhodná zejména pro kontinuální měření. Jako titrační metoda se nejčastěji používá jodometrická titrace thiosíranem.

Pro aplikace, kde dochází ke kontaktu plazmatu s povrchem substrátu, je výhodné použít homogenního módu DBD, aby nedošlo k nežádoucímu poškození substrátu filamenti DBD. Homogenní mód DBD lze také použít pro depozici tenkých vrstev. Jedním z materiálů, který lze vyrábět pomocí DBD, jsou uhlíkové nanotrubičky (carbon nanotubes – CNT). CNT jsou novým materiálem s vysokým potenciálem využití v rozmanitých průmyslových i vědních oborech. CNT jsou unikátní alotropickou modifikací uhlíku. Na existenci těchto nanotrubeček se přišlo v průběhu studia fullerenu v roce 1991.

Za objev fullerenu v roce 1996 dostali Nobelovu cenu za chemii Robert F. Curl, Sir Harold W. Kroto a Richard E. Smalley. Fullereny představují třetí alotropickou modifikaci uhlíku

vedle grafitu a diamantu. Jde o kondenzované polycyklické klecovité struktury, složené ze sudého počtu uhlíkových atomů, poskládaných přednostně z pěti a šestiúhelníků. Studium jejich struktury vedlo k formulování pravidla o izolovaných pětiúhelnících. Toto pravidlo říká, že stabilní jsou pouze ty fullereny, u nichž se ve struktuře nachází dva pětiúhelníky vedle sebe. Zároveň předpokládá minimum násobných vazeb v těchto pětiúhelnících. Nejmenším systémem splňujícím toto pravidlo je právě ikosahedrální struktura C_{60} . Pomocí obloukového výboje s uhlíkovými elektrodami používaného k výrobě fullerenů byly vyrobeny v roce 1991 první CNT (Iijima 1991).

Svůj název získaly CNT díky svému tvaru. Jsou to trubice tvořené z šestiúhelníků. Mohou být otevřené, ale i uzavřené. Aby mohla být CNT uzavřena, musí obsahovat kromě šestiúhelníků, které tvoří vlastní trubici, také pětiúhelníky, které tuto trubici uzavřou. Poměr délky k průměru CNT bývá okolo 1000. CNT mohou být jednovrstvé (také označované jako jednostěnné – single-walled nanotubes – SWNT) nebo vícevrstvé (vícestěnné – multi-walled nanotubes – MWNT) (viz obr. 15). Typická SWNT má vnitřní průměr 1 - 2 nm, přičemž délka může dosahovat až několika μm .



Obr. 15: CNT, A - jednostěnné – single-walled nanotubes – SWNT, B - vícestěnné – multi-walled nanotubes – MWNT).

Uhlíkové nanotrubičky mají řadu výjimečných vlastností, které je předurčují k budoucím aplikacím. Jsou chemicky reaktivní, i když tato reaktivita je velmi nízká. Mohou tedy být kovalentně modifikovány, a to buď přímo na povrchu trubky, nebo také na jejím uzavřeném konci. Modifikace může být také prováděna v elektrických výbojích. Jejich modifikace zvyšuje jejich rozpustnost v řadě organických rozpouštědel. K dalším důležitým vlastnostem uhlíkových nanotrubiček patří elektrická vodivost. Tyto vlastnosti jsou ovlivněny průměrem nanotrubičky – ty s malým průměrem jsou polovodivé. Kromě toho se vyznačují optickou aktivitou a nabízí uplatnění v optice. Jejich důležitou vlastností je také velmi dobrá

mechanická odolnost. Na druhé straně jsou velmi flexibilní, což nabízí využití v kompozitních materiálech (Harris 2009).

Výzkumem s DBD jsem se zabývala v rámci projektu GA ČR (GAP205/10/1374 Syntéza uhlíkových nanotrubelek plazmochemickou metodou a studium jejich funkčních vlastností) na Přírodovědecké fakultě Masarykovy univerzity. Pomocí DBD za různých experimentálních podmínek byly vyráběny CNT. Další aplikací DBD byly experimenty s generací ozónu, které probíhaly na Fakultě chemické VUT v Brně. Nejvýznamnější výsledky tohoto výzkumu byly postupně publikovány ve vědeckých publikacích č. 13-15 uvedených v podkapitole SEZNAM KOMENTOVANÝCH PRACÍ.

4.2 Komentáře k jednotlivým publikacím

Reakcím kyslíku a ozónu na povrchu elektrod v DBD je věnována následující publikace.

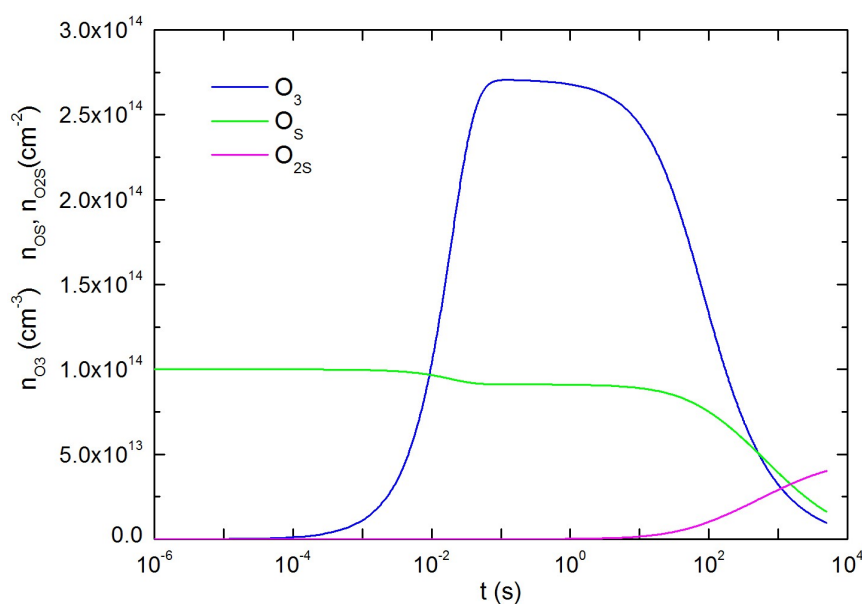
13. Trunec D., **Mazánková V.**, Mierna J., Manduchová I, Krčma F.: Study of O₂ and O₃ reactions with electrode surface in ozonizer, HAKONE XV (15th High Pressure Low Temperature Plasma Chemistry Symposium), September 11-16, 2016, Brno, Czech Republic.

Práce se zabývá experimenty s generací ozónu v ozonizátorech s cylindrickou konfigurací elektrod DBD. Elektrody byly vyrobeny z nerezové oceli a vnější elektroda byla pokryta dielektrikem z korundové keramiky. V experimentech byl použit kyslík čistoty 6.0, který byl do ozonizátorů přiváděn ještě přes zeolitové síto. Pomocí experimentů s generovaným ozónem byly studovány procesy probíhající na povrchu elektrod.

Povrchové procesy jsou důležitými mechanismy při tvorbě, ale i při zániku ozónu v DBD. Při generování ozónu v DBD v čistém kyslíku lze po několika hodinách pozorovat pokles koncentrace ozónu a až téměř nulovou produkci, tzv. ozone zero effect (Murayama et al. 2008). Pomocí experimentů v pulzním kyslíkovém výboji a výrazným zvětšením plochy povrchu stěn reaktoru pomocí nanovláken lze také sledovat změnu produkce ozónu (Marinov et al. 2013). Výsledkem je výrazný nárůst tvorby ozónu v časech do 50 ms, pak dochází k poklesu koncentrace ozónu. V případě produkce ozónu bez přidaných nanovláken do reaktoru je také pozorován nárůst, koncentrace je však o třetinu nižší než v předchozím případě. Nárůst je možno pozorovat do času 150 ms, pak už je koncentrace ozónu konstantní.

Na základě těchto poznatků jsme provedli experimenty, kdy jsme pomocí absorpční spektroskopie byli schopni in-situ určit koncentraci ozónu. První sada experimentů byla provedena tak, že se v ozonizátoru nechal po dobu 5 minut generovat ozón. Výboj byl potom vypnut a zbylý ozón byl z ozonizátoru vyfouknut argonem. Pak byl do ozonizátoru přiveden kyslík, bez zapnutí výboje. Kyslík reagoval s atomárním kyslíkem vázaným na povrchu za reakční čas (0,1-5 min) za vzniku ozónu. Se zvyšujícím se reakčním časem stoupala produkce ozónu. Druhá sada experimentů byla provedena obdobně, jen zbylý ozón po vypnutí výboje nebyl vyfouknut argonem, ale byl v ozonizátoru ponechán. V tomto případě se ukázalo, že délka reakčního času nemá vliv na hodnotu koncentrace ozónu, který je v ozonizátoru.

Abychom si potvrdili naši teorii se vznikem ozónu na povrchu, vytvořili jsme jednoduchý kinetický model. Analogickou situaci řešil Guerra et al. (Guerra et al. 2014) ve své práci, kde se zabýval reakcemi plynného NO s atomárním kyslíkem vázaným na povrchu reaktoru z Pyrexového skla. V našem modelu jsme využili stejnou úvahu o reakcích s povrchem a určili jsme nutné rychlostní konstanty vzhledem k našim experimentálním podmínkám. O výsledcích modelu a porovnání s experimentem budeme podrobněji referovat v připravované publikaci. Na následujícím obrázku (obr. 16) je znázorněn výsledek vypočtený z modelu. Výsledek se kvalitativně shoduje s experimentálními výsledky uvedenými v naší publikaci.



Obr. 16: Průběh koncentrací jednotlivých částic vypočtený z modelu.

Následující dvě publikace shrnují experimentální výsledky depozic a funkcionalizace CNT v DBD a v radiofrekvenčním (RF) výboji za nízkého tlaku za různých experimentálních podmínek.

14. Eliáš M., Kloc P., Jašek O., **Mazánková V.**, Trunec D., Hrdý R., Zajíčková L.: Atmospheric pressure barrier discharge at high temperature: Diagnostics and carbon nanotubes deposition. *Journal of Applied Physics*, **117** (2015), 10330, ISSN: 0021- 8979.

Práce je zaměřena na diagnostiku DBD ve směsi Ar + H₂ s příměsemi C₂H₂ a CH₄ pomocí OES, rychlé kamery a elektrických měření. Diagnostika byla prováděna při různých teplotách. Jednak pro laboratorní teplotu a dále pro teplotu 680 °C, kdy byla spodní dielektrická destička vyhřívána. Reaktor byl směsí plynů napuštěn na atmosférický tlak a ten byl díky průtokovému režimu během experimentů stále udržován na konstantní hodnotě. Ze snímků z rychlé kamery je vidět, že při pokojové teplotě je výboj v módu APGD, zatímco pro vysokou teplotu se výboj každou půlperiodu mění z APGD módu do módu Townsendova výboje za atmosférického tlaku. Diagnostika výboje byla prováděna s ohledem na experimentální podmínky, při kterých dochází ve výboji k depozici CNT na křemíkovém vzorku

s 5nm vrstvou železa jako katalyzátorem. CNT se podařilo deponovat ve směsi s C₂H₂, v případě směsi s CH₄ byl deponován pouze amorfni uhlík. Jako podstatný se ukázal také vliv vodíku, jehož příměs zvyšovala kvalitu deponovaných CNT. CNT byly diagnostikovány pomocí SEM, TEM a Ramanovy spektroskopie. Bylo zjištěno, že vzniklé CNT jsou vícestěnné o průměru 15 nm až 30 nm s tloušťkou stěny 3 nm až 7 nm. Přínosem této práce bylo, že se podařilo deponovat CNT bez předchozího žihání katalytické vrstvy, za atmosférického tlaku a při použití argonu jako pracovního plynu. Dřívější práce využívaly dražšího helia.

15. Zajíčková L., Eiaš M., Buršíková V., Studýnková Z., **Mazánková V.**, Michlíček M., Houdková J.: Low pressure plasmachemical processing of multi-walled carbon nanotubes for the production of polyurethane composite films with improved mechanical properties. *Thin Solid Films*, **538** (2013), 7-15, ISSN 0040-6090.

Těžištěm práce byla funkcionalizace vícestěnných CNT pomocí kapacitně vázaného RF výboje a následně jejich použití jako plnidlo při přípravě polyuretanových (PU) materiálů metodou in-situ polymerace. Funkcionalizované CNT byly komerční výrobky Nanocyl-3100 a Nanocyl-3150. Do reaktoru, ve kterém probíhala funkcionalizace CNT, byly vpouštěny různé směsi plynů při různých experimentálních podmínkách, čímž bylo dosaženo různé aktivace CNT. Směsi plynů byly zejména argon s kyslíkem, etanolem, vodou nebo argon s amoniakem. CNT byly diagnostikovány pomocí rentgenové fotoelektronové spektroskopie (X-ray photoelectron spectroscopy – XPS) a pomocí FTIR. XPS byla aplikována přímo na CNT prášek a byla provedena prvková analýza. Aby bylo možné použít diagnostiku pomocí FTIR, byl CNT prášek zalisován spolu s bromidem draselným (KBr) do tablet a ty pak byly analyzovány. XPS metoda ukázala, že na povrchu CNT se váže kyslík, zatímco dusík se na povrch nevázal. Mechanické vlastnosti připravených PU materiálů byly určeny indentančním měřením. Bylo prokázáno významné zlepšení tvrdosti a modulu pružnosti, když jako plnidlo byly použity funkcionalizované CNT s vysokým obsahem navázaného kyslíku.

REFERENCE

- Aldebaran: dostupné z: http://www.aldebaran.cz/bulletin/2012_42_pla.php
- Bartnikas R.: Note on discharges in helium under a.c. conditions. *British Journal of Applied Physics (Journal of Physics D: Applied Physics)*, **1**, 5 (1968), 659-661.
- Cleaves H. J., Chalmers J. H., Lazcano A., Miller S. L., Bada J. L.: A reassessment of prebiotic organic synthesis in neutral planetary atmospheres. *Origins of Life and Evolution of Biospheres*, **38**, 2 (2008), 105-115.
- Dobrijevic M., Hebrard E., Loison J. C., Hickson K. M.: Coupling of oxygen, nitrogen, and hydrocarbon species in the photochemistry of Titan's atmosphere. *Icarus*, **228**, (2014), 324–346.
- Eri's: dostupné z: <http://blog.canacad.ac.jp/wpmu/15matser/2011/11/23/12-1-history-of-life-on-earth/>
- Ferris J. P., Joshi P. C., Edelson E. H., Lawless J. G.: HCN: A plausible source of purines, pyrimidines and amino acids on the primitive earth. *Journal of Molecular Evolution*, **11**, 4 (1978), 293-311.
- Fleury B., Carrasco N., Gautier T., Mahjoub A., Hec J., Szopa C., Hadamcik E., Buch A., Cernogora G.: Influence of CO on titan atmospheric reactivity. *Icarus*, **238**, (2014), 221–229.
- Gough D. O.: Solar interior structure and luminosity variations. *Solar Physics*, **74**, 1 (1981), 21-34.
- Guerra V., Marinov D., Guaitella O., Rousseau A.: NO oxidation on plasma pretreated Pyrex: the case for a distribution of reactivity of adsorbed O atoms. *Journal of Physics D: Applied Physics*, **47**, 22 (2014), 224012.
- Haldane J. B. S.: Possible Worlds. Hugh & Bros, New York (1928).
- Haldane J. B. S.: The Origin of Life. *New Biology*, **16**, 12 (1954).
- Harris P. J. F.: Carbon Nanotube Science - Synthesis, properties and applications. Cambridge University Press, London, (2009), ISBN 978-0-521-53585-4.
- Iijima S.: Helical microtubules of graphitic carbon. *Nature* **354**, 56 (1991).
- Johnson A. P., Cleaves H. J., Dworkin J. P., Glavin D. P., Lazcano A., Bada J. L.: The Miller Volcanic Spark Discharge Experiment. *Science*, **322**, 5900 (2008), 404.
- Kasting J. F.: Earth's early atmosphere. *Science*, **259**, 5097 (1993), 920-926.
- Kogelschatz U.: Dielectric-barrier Discharges: Their History, Discharge Physics, and Industrial Applications, *Plasma Chemistry and Plasma Processing*, **23**, 1 (2003).
- Krčma F., Protasevich E. T.: Post-discharges in Pure Nitrogen and in Nitrogen Containing Halogenated Hydrocarbon Traces, 1st ed. Tomsk: Tomsk Polytechnic University publishing, (2003).
- Marinov D., Guaitella O., Booth J. P., Rousseau A.: Direct observation of ozone formation on SiO₂ surfaces in O₂ discharges. *Journal of Physics D: Applied Physics*, **46**, 3 (2013) 032001.

- McCollom T.: Miller-Urey and Beyond: What Have We Learned About Prebiotic Organic Synthesis Reactions in the Past 60 Years? *Annual Review of Earth and Planetary Sciences*, **41**, (2013), 207-229.
- Miller S. L.: A Production of Amino Acids under Possible Primitive Earth Conditions. *Science, New Series*, **117**, 3046 (1953), 528-529.
- Miller S. L., Urey C. H.: Organic Compound Synthesis on the Primitive Earth. *Science, New Series*, **130**, 3370 (1959), 245-251.
- Moisan M., Boudam K., Carignan D., Keroack D., Levif P., Barbeau J., Seguin J., Kutasi K., Elmoualij B., Thellin O., Zorzi W.: Sterilization/disinfection of medical devices using plasma: the flowing afterglow of the reduced-pressure N₂-O₂ discharge as the inactivating medium. *European Physical Journal Applied Physics*, **63** (2013), 10001.
- Murayama K., Matsumura N., Taguchi M., Kato Y., Teranishi K., Suzuki S., Itoh H.: Experimental investigation of ozone zero phenomenon. Contribution papers, HAKONE XI, Oleron Island, France (2008).
- NASA: dostupné z : <https://www.nasa.gov/>
- Okazaki S., Kogoma M., Uehara M., Kimura Y.: Appearance of stable glow discharge in air, argon, oxygen and nitrogen at atmospheric pressure using a 50 Hz source. *Journal of Physics D: Applied Physics*, **26** (1993), 889-892.
- Oparin A. I.: Origin of Life. Macmillan, New York (1938).
- Parker E. T., Cleaves H. J., Dworkin J. P., Glavin D. P., Callahan M., Aubrey A., Lazcano A., Bada J. L.: Primordial synthesis of amines and amino acids in a 1958 Miller H₂S-rich spark discharge experiment. Proceedings of the National Academy of Sciences of the United States of America, **108**, 14 (2011), 5526–5531.
- Phys.org : dostupné z : <https://phys.org/news/2014-06-stanley-miller-forgotten.html>
- Pintassilgo C. D., Guerra V., Guaitella O., Rousseau A.: Modelling of an afterglow plasma in air produced by a pulsed discharge. *Plasma Sources Science and Technology*, **19** (2010), 055001.
- Raulin F.: Astrobiology and habitability of Titan. *Space Science Reviews*, **135**, 1 (2008), 37-48.
- Ricard A.: Reactive plasmas. Societe Francaise du Vide, Paris, (1996).
- Smith D. Spanel P.: Studies of electron-attachment at thermal energies using the flowing afterglow Langmuir probe technique. *Advances In Atomic Molecular and Optical Physics*, **32**, (1994), 307-343.
- Smith D. Spanel P.: Selected ion flow tube mass spectrometry (SIFT-MS) for on-line trace gas analysis. *Mass Spectrometry Reviews*, **24**, 5 (2004), 661-700.
- Wells J.: Icons of Evolution. Regnery Publishing, Washington, D. C. (2002) ISBN 0-89526-200-2.

PŘÍLOHY

Study of argon–oxygen flowing afterglow

This content has been downloaded from IOPscience. Please scroll down to see the full text.

2016 Plasma Sources Sci. Technol. 25 035008

(<http://iopscience.iop.org/0963-0252/25/3/035008>)

View [the table of contents for this issue](#), or go to the [journal homepage](#) for more

Download details:

IP Address: 147.229.91.138

This content was downloaded on 06/04/2016 at 14:26

Please note that [terms and conditions apply](#).

Study of argon–oxygen flowing afterglow

V Mazánková¹, D Trunec², Z Navrátil², J Raud² and F Krčma¹

¹ Institute of Physical and Applied Chemistry, Faculty of Chemistry, Brno University of Technology, Purkyňova 118, 612 00 Brno, Czech Republic

² Department of Physical Electronics, Faculty of Science, Masaryk University, Kotlářská 2, 611 37 Brno, Czech Republic

E-mail: mazankova@fch.vutbr.cz

Received 17 December 2015, revised 2 March 2016

Accepted for publication 10 March 2016

Published 6 April 2016



Abstract

The reaction kinetics in argon–oxygen flowing afterglow (post-discharge) was studied using NO titration and optical emission spectroscopy. The flowing DC post-discharge in argon–oxygen mixture was created in a quartz tube at the total gas pressure of 1000 Pa and discharge power of 90 W. The O(³P) atom concentration was determined by NO titration at different places along the flow tube. The optical emission spectra were also measured along the flow tube. Argon spectral lines, oxygen lines at 777 nm and 844.6 nm and atmospheric A-band of O₂ were identified in the spectra. Rotational temperature of O₂ was determined from the oxygen atmospheric A-band and also the outer wall temperature of the flow tube was measured by a thermocouple and by an IR thermometer. A zero-dimensional kinetic model for the reactions in the afterglow was developed. This model allows the time dependencies of particle concentrations and of gas temperature to be calculated. The wall recombination probability for O(³P) atoms $\gamma_{O(P)} = (1.63 \pm 0.06) \times 10^{-3}$ and wall deactivation probability for O₂(b ¹Σ_g⁺) molecules $\gamma_{O_2(b)} = (1.7 \pm 0.1) \times 10^{-3}$ were determined from the fit of model results to experimental data. Sensitivity analysis was applied for the analysis of kinetic model in order to reveal the most important reactions in the model. The calculated gas temperature increases in the afterglow and then decreases at later afterglow times after reaching the maximum. This behavior is in good agreement with the spatial rotational temperature dependence. A similar trend was also observed at outer wall temperature measurement.

Keywords: argon–oxygen afterglow, wall recombination probability, kinetic model

(Some figures may appear in colour only in the online journal)

1. Introduction

Afterglow systems containing oxygen have a wide range of applications in different fields due to the presence of reactive oxygen species (oxygen atoms and excited metastable oxygen molecules). For example, Ar–O₂ afterglows were used for surface treatment [1], sterilization [2] and thin film deposition [3]. The afterglow of Ar–O₂ plasmas have been studied experimentally or theoretically by numerous groups. The published studies mainly aimed to determine the concentrations of reactive species in the treatment area. An afterglow of RF driven DBD-like atmospheric pressure plasma jet in Ar + 2% O₂ mixture was studied by Zhang *et al* [4] and ozone concentration was measured by UV absorption. A gas temperature increase at a distance of about 7 mm from the jet nozzle

was found in this study. A zero-dimensional kinetic model in Ar–O₂ surface-wave microwave discharges was developed by Kutasi *et al* [5–8] to investigate electron and heavy particle kinetics and dissociation of O₂ molecules in the discharge and the flowing afterglow. The O atom concentration in the afterglow has been the most frequently determined by NO titration. This method was used by Ricard *et al* [9–12] and Mafra *et al* [1] in the afterglow of discharges generated under different discharge conditions and gas mixture compositions. The total gas pressure in these studies was in range 100–1200 Pa and the measured O atom concentrations were between 2×10^{14} cm⁻³ and 2.25×10^{15} cm⁻³. The error (including systematic errors) of the NO titration method was estimated to be ±30%. Mafra *et al* [1] also determined the O₂ dissociation degree ($[O]/2[O_2]$) to be in the range 5–14% at different gas pressures

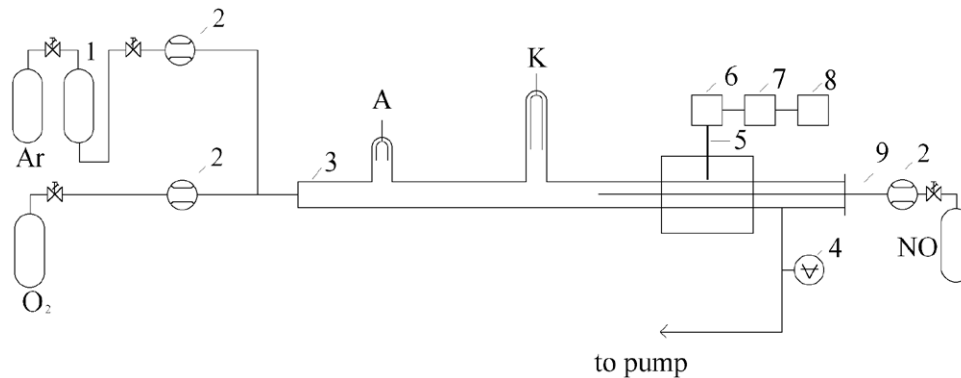
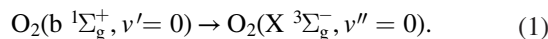


Figure 1. Scheme of the experimental setup. 1—catalyzer oxiclear; 2—mass flow controllers; 3—quartz discharge tube; 4—capacitance gauge; 5—quartz optical fiber; 6—monochromator Jobin Yvon Triax 550; 7—CCD; 8—PC; 9—movable Pyrex titration capillary tube.

in an Ar – 10% O₂ mixture. The local concentration of the O atoms in the post-discharge reactor can be determined also by two recently developed techniques. The first technique is based on the measurement of intensity of O₂ atmospheric A-band [1]



The second technique is the probe method that relies on the temperature rise of a catalytic probe due to the atomic oxygen recombination on the probe surface [13, 14]. Important factor in performed experiments is a reactor surface material which has an influence on surface recombination probability of O atoms. This was discussed in detail by Kutasi and Loureiro [15]. Owing to the large variety of conditions under which the experiments were realized, namely regarding the nature of the surface and the shape of the reactor, it is not easy to draw any conclusion about the predicted particle densities in the reactor. For Pyrex and total gas pressure of 300 Pa the surface recombination probability of O atoms was reported in range from 4×10^{-4} to 2×10^{-3} [16–18].

The present work is focused on the experimental study of an argon–oxygen flowing afterglow with the aim to determine the wall reaction probabilities for O(³P) atoms in ground state and O₂(b ¹Σ_g⁺) molecules. The concentration of atomic oxygen was determined by NO titration along the flow tube. Also the spectra of atmospheric band of molecular oxygen were recorded along the flow tube and the intensity of this band and the rotational temperature were calculated from these measurements. A kinetic model was developed in order to explain the experimental results. The fit of calculated concentrations to experimental data allows to determine the wall recombination probability for oxygen atoms and the wall deactivation probability for O₂(b ¹Σ_g⁺) excited molecules. The calculation of gas temperature in the afterglow was also performed.

2. Experimental set-up

The flowing configuration of argon DC discharge with oxygen admixture was used for this experimental study. The experimental set-up was already used for our previous studies of argon afterglow with nitrogen admixture [19] and nitrogen afterglow with mercury vapor admixture [20]. A simplified schematic drawing of the experimental set-up is given in

figure 1. The active discharge was created in a quartz discharge tube with the inner diameter of 12 mm at the constant total gas pressure of 1000 Pa and the discharge power of 90 W. Hollow molybdenum electrodes were placed in the side arms (at the interelectrode distance of 120 mm) of the main discharge tube to minimize their sputtering and also to minimize the influence of the light emitted in the electrode regions. The active discharge part of the flow tube was cooled by a ventilator. The argon gas was of 99.99% purity and it was further cleaned by Oxiclear column. The reactor system was pumped continuously by a rotary oil pump. The argon flow of 1400 sccm and oxygen flow of 10 sccm were automatically controlled by the Bronkhorst mass flow controllers and mixed together. The total gas pressure in the discharge tube was measured by a capacitance gauge connected to the end of the discharge tube. The input gas temperature was 300 K. The moveable capillary tube for NO titration was made of Pyrex and it was immersed upstream from the discharge into the quartz tube at its axis. Its external diameter was 2 mm, the inner diameter was 0.5 mm and the length was 400 mm. NO titration method was performed as described elsewhere [21–23].

The flow analysis was performed in the same way as in previous studies on argon metastable quenching [24, 25]. The bulk flow velocity v_g of argon in the tube was calculated from the continuity equation and the state equation. The calculated velocity v_g was 21 m s⁻¹. The distance d needed to develop a full parabolic velocity profile is given by $d = 0.277R \text{ Re}$, where R is the flow tube radius (0.6 cm) in cm and Re is the Reynolds number. For our experimental conditions, the Reynolds number Re is equal to 150, which gives $d = 25$ cm. Furthermore, our experimental setup introduced perturbations into the flow pattern at the side arms with discharge electrodes. So, the flow will be in transition between plug and parabolic flow and in this case the bulk flow velocity can be used for the calculation of the decay time. This approach was found to be correct in previous study [24]. In our experiment, the line intensities (which are proportional to excited particle concentrations) were collected from the whole diameter of the flow tube. Bolden *et al* [26] have experimentally demonstrated that this is equivalent to monitoring the concentration at the center of the tube for fully developed parabolic flow conditions. Kolts and Setser [24] measured the argon metastable concentration across the diameter of the flow tube by

Table 1. Argon and argon–oxygen reactions and their rate coefficients considered in the model.

No.	Reaction	Rate coefficient	Reference
R101	$\text{Ar}^* + \text{Ar}^* \rightarrow \text{e} + \text{Ar}^+ + \text{Ar}$	1.5×10^{-11}	[5]
R102	$\text{Ar}^* + \text{Ar} + \text{Ar} \rightarrow \text{Ar}_2^* + \text{Ar}$	1.0×10^{-32}	[28]
R103	$\text{Ar}_2^* \rightarrow \text{Ar} + \text{Ar} + h\nu$	2.4×10^7	[28]
R104	$\text{Ar}^+ + \text{Ar} + \text{Ar} \rightarrow \text{Ar}_2^+ + \text{Ar}$	2.5×10^{-31}	[27]
R105	$\text{Ar}_2^+ + \text{e} \rightarrow \text{Ar}^* + \text{Ar}$	1.0×10^{-6}	[28]
R151	$\text{Ar}^* + \text{O}_2 \rightarrow \text{Ar} + \text{O(P)} + \text{O(P)}$	$0.46 \times 2.1 \times 10^{-10}$	[5]
R152	$\text{Ar}^* + \text{O}_2 \rightarrow \text{Ar} + \text{O(P)} + \text{O(D)}$	$0.52 \times 2.1 \times 10^{-10}$	[5]
R153	$\text{Ar}^* + \text{O} \rightarrow \text{Ar} + \text{O(3p P)}$	7.6×10^{-11}	[5]
R154	$\text{Ar}^+ + \text{O}^- \rightarrow \text{Ar} + \text{O(P)}$	2.8×10^{-7}	[5]
R155	$\text{Ar} + \text{O}_2 + \text{O(P)} \rightarrow \text{Ar} + \text{O}_3$	$3.9 \times 10^{-34} \times (300/T_g)^{1.9}$	[5]
R156	$\text{Ar} + \text{O(P)} + \text{O(P)} \rightarrow \text{Ar} + \text{O}_2$	$5.2 \times 10^{-35} \times \exp(900/T_g)$	[5]
R157	$\text{Ar} + \text{O}_2(\text{b}) \rightarrow \text{Ar} + \text{O}_2$	1.5×10^{-17}	[5]
R158	$\text{Ar} + \text{O(D)} \rightarrow \text{Ar} + \text{O(P)}$	3.0×10^{-13}	[5]
R159	$\text{Ar}^+ + \text{O(P)} \rightarrow \text{Ar} + \text{O}^+$	6.4×10^{-12}	[5]
R160	$\text{Ar}^+ + \text{O}_2 \rightarrow \text{Ar} + \text{O}_2^+$	$4.9 \times 10^{-11} \times (300/T_g)^{0.78}$	[5]
R161	$\text{Ar}_2^+ + \text{O}_2 \rightarrow \text{Ar} + \text{Ar} + \text{O}_2^+$	7.4×10^{-11}	[29]
R162	$\text{Ar}_2^* + \text{O}_2 \rightarrow \text{Ar} + \text{Ar} + \text{O} + \text{O}$	2.53×10^{-10}	[30]
R163	$\text{Ar}_2^+ + \text{O(P)} \rightarrow \text{Ar} + \text{Ar} + \text{O}^+$	7.4×10^{-11}	[29]

Note: The values of rate coefficients are for $T_g = 300$ K, also the electron temperature for reaction R105 is $T_e = 300$ K. The rate coefficient units are s^{-1} , $\text{cm}^3 \text{s}^{-1}$ and $\text{cm}^6 \text{s}^{-1}$ for reactions of the first, second and third order, respectively.

the optical absorption spectroscopy in the case of plug flow. They found that no correction is necessary in order to obtain correct values of quenching rate coefficients. Therefore no correction was applied also at our measurement.

The optical spectra were measured by Jobin Yvon monochromator TRIAX 550 with 1200 gr mm^{-1} grating and with CCD detector. The spectra were measured in the range from 750 nm to 850 nm. The emitted light was led to the entrance slit of the monochromator by the multimode quartz optical fiber movable along the discharge tube.

3. Kinetic model

A zero-dimensional kinetic model for the argon–oxygen afterglow was developed. The following particles were considered in the kinetic model—electrons, Ar^+ , Ar_2^+ , O_2^+ and O^- ions, excited (metastable) argon species $\text{Ar}^*(^3\text{P}_2)$ and Ar_2^* , oxygen atoms in ground state $\text{O}(^3\text{P})$ and in excited states $\text{O}(^1\text{D})$ and $\text{O}(3\text{p } ^3\text{P})$, electronically excited states of molecular oxygen $\text{O}_2(\text{a } ^1\Delta_g)$, $\text{O}_2(\text{b } ^1\Sigma_g^+)$ (hereafter labeled as O(P) , O(D) , O(3p P) , $\text{O}_2(\text{a})$ and $\text{O}_2(\text{b})$) and ozone O_3 . The initial concentrations of argon $[\text{Ar}]_0$ and molecular oxygen $[\text{O}_2]_0$ in ground states were calculated from the equation of state for ideal gas for $T = 300$ K and from corresponding flow rates. The concentration of argon ground state was considered to be constant. Forty five reactions concerning these particles were included in the kinetic model, see tables 1 and 2.

The rate coefficients for these reactions were taken from recent papers [5, 27–30]. The rate coefficients for Ar_2^+ and O_2^+ ions recombination with electrons (reactions R105, R226 and R227) depend on the electron temperature [5, 27]. At our experimental conditions, the electrons are thermalized due to

collisions mainly with argon atoms. The time needed for the electron temperature decrease down to 1.1 multiple of neutral gas temperature was calculated using data published by Trunec *et al* [31]. This time calculated for estimated initial electron energy of 4 eV was 1.2 ms, which corresponds to the distance of 2.5 cm in the flow tube. So the electron temperature was equal to neutral gas temperature (300 K) in our experiment and this electron temperature was also used in the kinetic model.

Besides the homogeneous gas-phase reactions, a crucial role has also the surface reactions, such as heterogeneous recombination of O atoms or deactivation of metastable particles at the surface. The wall loss process of species (reactions R233, R234, R235 and R236) was considered as a first order reaction with a characteristic time τ_i [32]

$$\tau_i = \frac{1}{D_i} \left(\frac{R}{2.405} \right)^2 + \frac{2R(1 - \gamma_i/2)}{\gamma_i \bar{v}_i}, \quad (2)$$

where i denotes the different species, D_i is the diffusion coefficient of specie i , γ_i is the deactivation or recombination probability at the wall, \bar{v}_i is the mean velocity, $\bar{v}_i = \sqrt{8k_B T / \pi m_i}$ and R is the flow tube radius. This relation was derived by Chantry [32] and it was used in recent studies of discharges and afterglows [5, 33, 34]. Note that $\tau_i^{-1} \simeq \gamma_i \bar{v}_i / 2R$ when $\gamma_i \ll 1$ and $\tau_i^{-1} \simeq D_i (2.405/R)^2$ when $\gamma_i \rightarrow 1$. The values of γ_i depend on many wall parameters, e.g. the type of material, cleanliness, morphology, temperature and surface coverage. Numerous works dealing with the determination of the wall recombination probabilities of O atoms can be found in the literature. However, there is quite a large discrepancy (of several orders of magnitude) between the results obtained by different authors, which could stem from different reasons [15].

Table 2. Oxygen reactions and their rate coefficients considered in the model.

No.	Reaction	Rate coefficient	Reference
R201	$O(P) + O_2 + O \rightarrow O_3 + O$	$2.1 \times 10^{-34} \times \exp(345/T_g)$	[5]
R202	$O^- + O_2(a) \rightarrow O_3 + e$	$0.75 \times 1.9 \times 10^{-10}$	[5]
R203	$O_2(a) + O_2 \rightarrow O_2 + O_2$	$2.2 \times 10^{-18} \times (T_g/300)^{0.8}$	[5]
R204	$O_2(a) + O \rightarrow O_2 + O$	7.0×10^{-17}	[5]
R205	$O_2(b) + O \rightarrow O_2 + O$	4.0×10^{-14}	[5]
R206	$O_2(b) + O \rightarrow O_2(a) + O$	4.0×10^{-14}	[5]
R207	$O_2 + O_2 + O(P) \rightarrow O_3 + O_2$	$6.4 \times 10^{-35} \times \exp(663/T_g)$	[5]
R208	$O_2(a) + O_3 \rightarrow O_2 + O_2 + O(P)$	$5.2 \times 10^{-11} \times \exp(-2840/T_g)$	[5]
R209	$O_2(b) + O_3 \rightarrow O_2 + O_2 + O(P)$	1.5×10^{-11}	[5]
R210	$O(P) + O_3 \rightarrow O_2 + O_2$	$0.5 \times 1.8 \times 10^{-11} \times \exp(-2300/T_g)$	[5]
R211	$O(P) + O_3 \rightarrow O_2(a) + O_2$	$0.33 \times 1.8 \times 10^{-11} \times \exp(-2300/T_g)$	[5]
R212	$O(P) + O_3 \rightarrow O_2(b) + O_2$	$0.17 \times 1.8 \times 10^{-11} \times \exp(-2300/T_g)$	[5]
R213	$O_2(a) + O_2(a) \rightarrow O_2(b) + O_2$	$1.81 \times 10^{-18} \times \exp(700/T_g) \times (T_g/300)^{3.8}$	[5]
R214	$O(P) + O(P) + O_2 \rightarrow O_2 + O_2$	$0.5 \times 3.81 \times 10^{-30} \times \exp(-170/T_g)/T_g$	[5]
R215	$O(P) + O(P) + O_2 \rightarrow O_2(a) + O_2$	$0.33 \times 3.81 \times 10^{-30} \times \exp(-170/T_g)/T_g$	[5]
R216	$O(P) + O(P) + O_2 \rightarrow O_2(b) + O_2$	$0.17 \times 3.81 \times 10^{-30} \times \exp(-170/T_g)/T_g$	[5]
R217	$O(P) + O(P) + O(P) \rightarrow O_2 + O(P)$	$3.6 \times 10^{-32} \times (1/T_g)^{0.63}$	[5]
R218	$O(P) + O_2 + O_3 \rightarrow O_3 + O_3$	$1.66 \times 10^{-34} \times \exp(T_g/300)$	[5]
R219	$O(D) + O(P) \rightarrow O(P) + O(P)$	8.0×10^{-12}	[5]
R220	$O(D) + O_2 \rightarrow O(P) + O_2$	$7.0 \times 10^{-12} \times \exp(67/T_g)$	[5]
R221	$O(D) + O_2 \rightarrow O(P) + O_2(a)$	1.0×10^{-12}	[5]
R222	$O(D) + O_2 \rightarrow O(P) + O_2(b)$	$2.56 \times 10^{-11} \times \exp(67/T_g)$	[5]
R223	$O(D) + O_3 \rightarrow O_2 + O_2$	1.2×10^{-10}	[5]
R224	$O(D) + O_3 \rightarrow O_2 + O(P) + O(P)$	1.2×10^{-10}	[5]
R225	$O(3p P) \rightarrow O(3s S) + h\nu$	3.22×10^7	[5]
R226	$e + O_2^+ \rightarrow O(P) + O(P)$	$2.0 \times 10^{-7} \times (300/T_e)$	[5]
R227	$e + O_2^+ \rightarrow O(P) + O(D)$	$1.95 \times 10^{-7} \times (300/T_e)^{0.7}$	[5]
R228	$O^+ + O_2 \rightarrow O(P) + O_2^+$	$2.0 \times 10^{-11} \times (300/T_g)^{0.5}$	[5]
R229	$O^+ + O_2(a) \rightarrow O(P) + O_2^+$	$2.0 \times 10^{-11} \times (300/T_g)^{0.5}$	[5]
R230	$O^+ + O_3 \rightarrow O_2^+ + O_2$	1.0×10^{-10}	[5]
R231	$O^+ + O^- \rightarrow O(P) + O(P)$	2.8×10^{-7}	[5]
R232	$O^- + O_2^+ \rightarrow O(P) + O_2$	$9.6 \times 10^{-8} \times (300/T_g)^{0.5}$	[5]
R233	$O(P) + \text{wall} \rightarrow 1/2 O_2$	See text	
R234	$O(D) + \text{wall} \rightarrow O(P)$	$\gamma = 1$	[5]
R235	$O_2(a) + \text{wall} \rightarrow O_2(X)$	$\gamma = 2 \times 10^{-5}$	[5]
R236	$O_2(b) + \text{wall} \rightarrow O_2(X)$	See text	

Note: The values of rate coefficients are for $T_g = 300$ K, also the electron temperature for reaction R226 and R227 is $T_e = 300$ K. The rate coefficient units are s^{-1} , $cm^3 s^{-1}$ and $cm^6 s^{-1}$ for reactions of the first, second and third order, respectively.

So in this study, the wall recombination probability for O(P) atoms $\gamma_{O(P)}$ and wall deactivation probability for O₂(b) molecules $\gamma_{O_2(b)}$ were considered as free parameters, the values of which were varied in order to obtain the best fit to the measured data. Furthermore, the wall deactivation probabilities of O(D) and O₂(a) were taken to be 1 and 2×10^{-5} , respectively [5].

The diffusion losses of all charged species are negligible in comparison with volume recombination losses at the argon pressure used in the experiment. Only the diffusion losses of electrons and O₂⁺ ions become important at the end of afterglow, when their concentrations decrease below 5×10^8 cm⁻³ and therefore the diffusion of charged particles was not considered in the kinetic model.

The resulting system of differential equations was solved numerically. A Fortran program, which used the RADAU5 procedure [35] for the intrinsic integration of the differential equation system, was written for this purpose. So only the inputs and outputs for the RADAU5 procedure and the right hand side of differential equation system had to be programmed.

4. Results and discussion

4.1. Experimental results

The concentration of atomic oxygen was determined by NO titration method along the flow tube. The results are shown

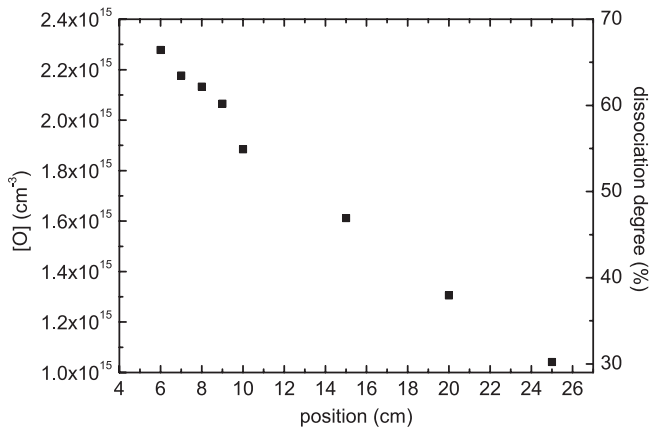


Figure 2. The dependence of atomic oxygen concentration and dissociation degree $[O]/2[O_2]_0$ on the distance from active discharge.

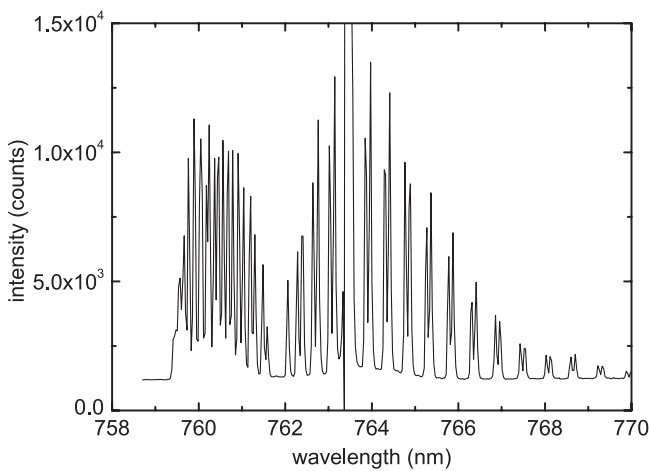


Figure 3. The atmospheric band of molecular oxygen in the post-discharge at the distance of 10 cm from active discharge. The emission spectrum has a doublet-like structure in the long wavelength region. This is because the oxygen atmospheric band is both a magnetic dipole transition and an intercombination transition, and the band has four branches, $^R R$, $^R Q$, $^P Q$ and $^P P$ based on two sets of selection rules [37, 38]. An argon line appears at 763.5 nm.

in figure 2. The O concentration was in the range 1.0×10^{15} – 2.3×10^{15} cm^{-3} and the dissociation degree was in the range 30–67% in the afterglow. Such high dissociation degree was also predicted by Kutasi *et al* [7] for low oxygen content in Ar–O₂ mixture and higher gas pressures. The optical emission spectra were measured also along the flow tube. Argon spectral lines, oxygen lines at 777 nm and 844.6 nm and atmospheric band of O₂ were identified in the spectra. An example of the typical recorded oxygen atmospheric band spectrum is shown in figure 3. The dependence of the integrated intensity of atmospheric band and O₂(b) state rotational temperature on the distance from the active discharge is shown in figure 4. The concentration of O₂(b) state is proportional to the atmospheric band integrated intensity. When the oxygen was added to the Ar afterglow instead to the active discharge, no atmospheric band was observed. The rotational temperature was calculated from resolved $^P Q$ branch of atmospheric A-band $b^1\Sigma_g^+$

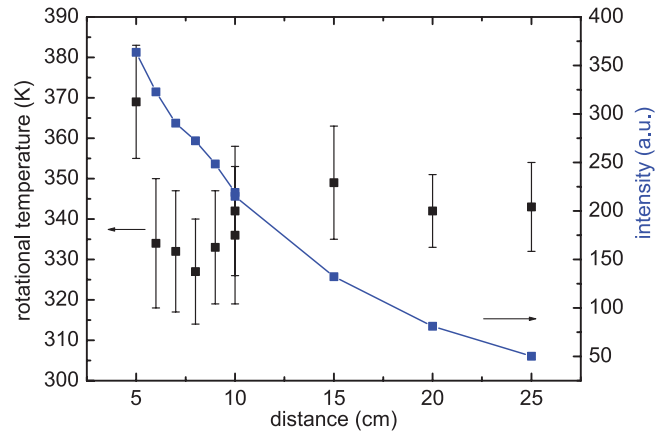


Figure 4. The dependence of the integrated intensity of atmospheric A-band and rotational temperature of O₂(b) on the distance from active discharge.

($v' = 0$) \rightarrow X $^3\Sigma_g^-$ ($v'' = 0$), $J' = 4$ –20 at 761–766 nm. The intensities of the rotational lines were plotted in the Boltzmann plot and the temperature was calculated from the fit. The rotational temperature of O₂(b) state is generally considered as a good approximation of the kinetic temperature of O₂ molecules in the ground state [39]. The dependence of rotational (hence also gas) temperature on the distance from the active discharge shows a rapid decrease at the distance of first 5 cm which is due to cooling of the flow tube by ventilator in the active discharge area. After reaching the minimum at the distance of 8 cm, the temperature again rises up 20 K at 15 cm distance. A slow temperature decrease then follows. To confirm this temperature course the temperature of outer wall of the flow tube was measured by a thermocouple and an IR thermometer. The results are shown in figure 5. The dependence of outer wall temperature exhibits the same spatial dependence as the gas temperature. However, the values of outer wall temperature are lower than the values of gas temperature due to cooling by surrounding air. The minimum and maximum are shifted to shorter distances from active discharge.

4.2. Results from kinetic model

The experimental data shown in the section 4.1 can be explained by the results of the kinetic model described in section 3. The calculation started at the time $t = 0$ which corresponds to the beginning of afterglow. The initial concentrations of particles were calculated for presented experimental conditions (as discharge voltage and current, gas pressure, tube radius, ...) using code LoKI (LisbOn KInetics) [40]. The so obtained initial values are: concentration of electrons -6.076×10^{11} cm^{-3} , Ar⁺ ions -3.385×10^{11} cm^{-3} , Ar₂⁺ ions -8.882×10^{10} cm^{-3} , argon metastables Ar* -4.387×10^{11} cm^{-3} , O⁺ ions -1.258×10^{11} cm^{-3} and O₂⁺ ions -5.777×10^{10} cm^{-3} . The initial values of oxygen neutral particles are: concentration of atomic oxygen -2.051×10^{15} cm^{-3} , excited molecular oxygen O₂ (a) -5.156×10^{13} cm^{-3} , excited molecular oxygen O₂ (b) -3.909×10^{13} cm^{-3} , metastable atomic oxygen O(D) -3.840×10^{13} cm^{-3} and ozone O₃ -2.537×10^{13} cm^{-3} .

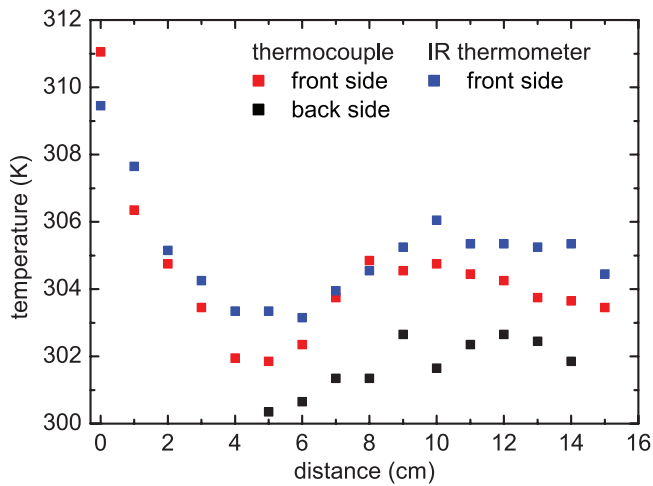


Figure 5. The dependence of outer wall temperature on the distance from the active discharge. The temperature was measured at the back side of the flow tube (side cooled by ventilator) and at front side (side turned away from ventilator).

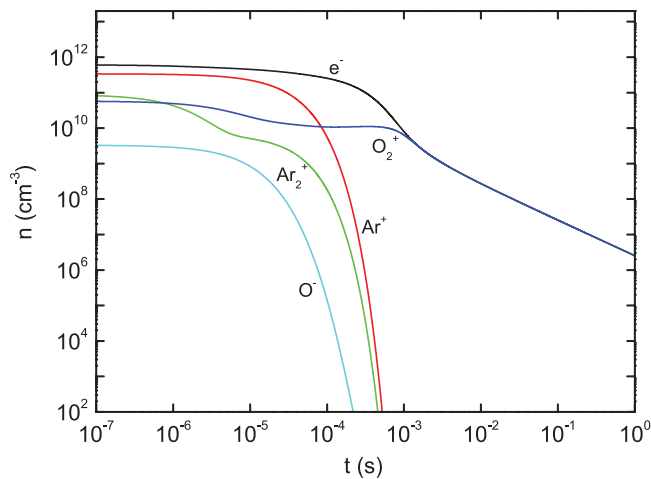


Figure 6. The calculated time dependence of electron and ion concentrations in the afterglow.

However, exact initial values of electron and ion concentrations are not important, because all positive ions are converted very quickly to O_2^+ ions and O^- are destroyed very quickly by recombination with positive ions and by collisions with $O_2(a)$ molecules as it is shown below. Furthermore, the initial ion concentrations and argon metastable concentration are two orders lower than the initial concentrations of O atoms and $O_2(a)$ and $O_2(b)$ molecules, so the ions and metastables do not influence the concentrations of oxygen particles in the late afterglow. The initial concentration of $O(P)$ atoms was adjusted to the value $2.9 \times 10^{15} \text{ cm}^{-3}$ so that the calculated O atom concentrations in later afterglow fit the values of O atom concentrations measured by the NO titration. Simultaneously, the concentration of $O_2(X)$ was proportionally decreased. The initial value calculated by LoKI $2.051 \times 10^{15} \text{ cm}^{-3}$ is within 30% error range of this value (estimated error of NO titration method).

The results of the kinetic model are shown in figures 6 and 7. The figure 6 shows the time dependence of electron and ion concentrations. During the first hundred μs , the Ar^+ ions are converted to Ar_2^+ molecular ions (reaction R104), however

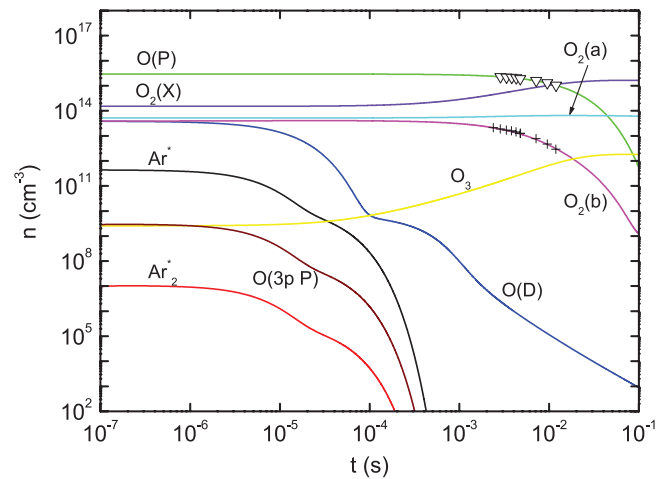


Figure 7. The calculated time dependence of neutral particle concentrations in the afterglow. The points are experimental results: triangles— $O(P)$ atom concentration determined by NO titration; crosses—concentrations of $O_2(b)$ proportional to integrated atmospheric A-band intensities.

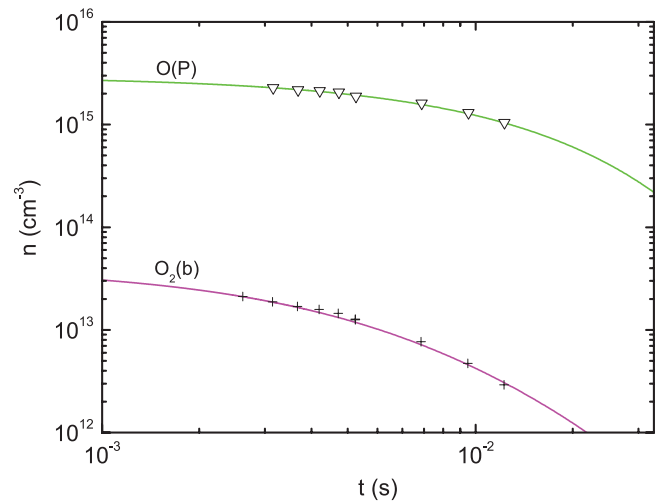


Figure 8. The detailed comparison of calculated time dependence of $O(P)$ and $O_2(b)$ concentrations with the experimental data. The points are experimental results: triangles— $O(P)$ atom concentration determined by NO titration; crosses—concentrations of $O_2(b)$ proportional to integrated atmospheric A-band intensities.

both these ions react with atomic and molecular oxygen in charge transfer reactions producing O^+ and O_2^+ ions (reactions R159, R160, R161 and R163). Thereafter the O^+ ions are converted to O_2^+ ions by exothermic charge transfer reaction R228. So, after the first millisecond all positive ions are converted to O_2^+ ions. Also O^- negative ions are destroyed very quickly by recombination with O_2^+ ions (reaction R232) and by collisions with $O_2(a)$ molecules (reaction R202) and again after the first millisecond the concentration of O^- ions is negligibly small. Thus, after the first millisecond only electrons and O_2^+ ions are the remaining charged particles, which recombine mutually and their concentrations further decrease.

The figure 7 shows the time dependence of neutral particle concentrations. The Ar^* metastables produced in the discharge are converted to excimer Ar_2^* molecules (reaction R102), both

Table 3. Normalized sensitivity coefficients for oxygen particles in the afterglow.

No.	O(P)	O(D)	O ₂ (a)	O ₂ (b)	O ₃
R155	-3.8×10^{-4}	-1.1×10^{-3}	-8.6×10^{-4}	-4.5×10^{-2}	9.9×10^{-1}
R156	-9.8×10^{-3}	-1.8×10^{-3}	-3.9×10^{-4}	7.6×10^{-3}	-1.4×10^{-3}
R157	6.4×10^{-5}	-1.0×10^{-4}	-2.0×10^{-3}	-3.6×10^{-2}	9.3×10^{-3}
R158	1.7×10^{-4}	-5.8×10^{-1}	-7.2×10^{-3}	-3.3×10^{-2}	1.3×10^{-2}
R205	1.7×10^{-3}	-2.7×10^{-3}	-5.3×10^{-2}	-7.9×10^{-1}	2.2×10^{-1}
R206	-4.2×10^{-3}	-2.3×10^{-3}	1.5×10^{-1}	-7.8×10^{-1}	2.1×10^{-1}
R207	-2.1×10^{-6}	-5.2×10^{-6}	-2.4×10^{-6}	-1.8×10^{-4}	4.9×10^{-3}
R208	3.8×10^{-7}	6.4×10^{-7}	-1.2×10^{-5}	2.6×10^{-5}	-8.6×10^{-4}
R209	1.8×10^{-4}	3.3×10^{-4}	-8.0×10^{-4}	-3.0×10^{-2}	-3.7×10^{-1}
R222	-2.4×10^{-4}	-2.6×10^{-1}	8.7×10^{-3}	4.4×10^{-2}	-1.7×10^{-2}
R226	9.7×10^{-7}	-1.0×10^0	-3.8×10^{-5}	-1.9×10^{-4}	7.4×10^{-5}
82.33	-8.6×10^{-1}	-1.4×10^{-1}	-2.8×10^{-2}	5.7×10^{-1}	-1.1×10^{-1}
R236	1.1×10^{-3}	-1.8×10^{-3}	-3.4×10^{-2}	-6.3×10^{-1}	1.6×10^{-1}

Note: The sensitivity coefficients with the highest absolute values for each particle are in bold.

Ar* and Ar₂* react with molecular oxygen producing atomic oxygen in ground or excited state (reaction R151, R152 and R162). After the first millisecond, the concentrations of argon excited species are negligibly small. So after the first millisecond the remaining neutral particles with significant concentrations in afterglow are atomic oxygen in ground state O(P), metastable molecular oxygen states O₂(a) and O₂(b) and ozone together with argon and molecular oxygen in ground states. The concentration of metastable atomic oxygen O(D) is very low (around 10⁴ cm⁻³). The reactions among these particles in afterglow after first millisecond were analyzed using sensitivity analysis, see section 4.4.

4.3. Comparison of theoretical and experimental results

As it was written in section 3, wall recombination probability for O(P) atoms $\gamma_{O(P)}$ and wall deactivation probability for O₂(b) molecules $\gamma_{O_2(b)}$ were considered as free parameters in the kinetic model. The least squares method was used to fit the calculated results to the experimental data. During the fitting procedure the relative values of integrated atmospheric A-band intensities have been also fitted to calculated absolute values of O₂(b) concentration by multiplication of these relative values by a suitable real constant. The values $\gamma_{O(P)} = (1.63 \pm 0.06) \times 10^{-3}$ and $\gamma_{O_2(b)} = (1.7 \pm 0.1) \times 10^{-3}$ were obtained from this method for quartz tube walls. Since the fitted value of $\gamma_{O(P)}$ does not depend on the absolute values of O(P) concentration (due to the exponential dependence of O(P) concentration on time (reaction R233)), the statistical uncertainty of $\gamma_{O(P)}$ determined from the fit is lower than the error of O density measurement using NO titration. The details of these fits are shown in figure 8. The obtained value for $\gamma_{O(P)}$ is in good agreement with values obtained by other authors for Pyrex and $T = 300$ K (Gordiets et al [17], Dilecce et al [16] -2×10^{-3} ; Macko et al [18] $(2 \pm 0.5) \times 10^{-3}$). The obtained value for $\gamma_{O_2(b)}$ is one order lower than the value 2×10^{-2} used by Pinheiro et al [41] for Pyrex.

4.4. Sensitivity analysis

Sensitivity analysis [42–44] was applied for the analysis of kinetic model in order to find the most important reactions. Normalized local concentration sensitivity coefficients S_{ij} were calculated according to the following equation [43]

$$S_{ij} = \frac{k_j}{n_i} \frac{\partial n_i}{\partial k_j}, \quad (3)$$

where n_i is the concentration of i th particle kind and k_j is the rate coefficient for j th reaction (see table 1). The coefficients S_{ij} were calculated numerically using the finite difference approximation. The central difference with the step Δk_j was used for this calculation. The step Δk_j has been decreasing until the estimated error of sensitivity coefficients was below 1%. This method is also called indirect method (or brute force method) [42]. The calculated sensitivity coefficients with highest absolute values for oxygen atoms and molecules in different states for $t = 10$ ms are shown in table 3. The sensitivity coefficients not shown in table 3 have absolute values one or more orders lower than the sensitivity coefficients shown in bold in this table. The sensitivity coefficients with highest absolute values can show the main channels for the creation and losses of each particle kind and they also can show the most important reactions in the kinetic model. These most important reactions influence the concentrations of many kinds of particles directly or indirectly via other reactions. The table 3 shows that the most important reactions in the argon–oxygen afterglow under our experimental conditions are: the wall recombination of O(P) atoms (reaction R233), which has the influence (direct or indirect) on all oxygen particle concentrations, the wall deactivation of O₂(b) states (reaction R236), the quenching of O₂(b) states by O(P) atoms (reactions R205 and 206), the destruction of ozone by O₂(b) states (reaction R209) and the ozone creation by three body reaction of O(P) atom with O₂ and Ar (reaction R155). At later afterglow times, the wall reactions become more important (higher sensitivity coefficients) for O(P) atoms and O₂(b) metastable states.

Table 4. Normalized sensitivity coefficients for initial concentrations for oxygen particles in the afterglow.

n_{j0}	O(P)	O(D)	O ₂ (a)	O ₂ (b)	O ₃
e	4.9×10^{-19}	1.2×10^{-51}	7.0×10^{-19}	-6.8×10^{-20}	9.0×10^{-19}
Ar +	-8.9×10^{-6}	-2.4×10^{-36}	8.6×10^{-5}	9.6×10^{-6}	2.4×10^{-5}
Ar ₂ ⁺	6.8×10^{-7}	1.6×10^{-15}	1.3×10^{-5}	2.0×10^{-6}	5.5×10^{-6}
Ar*	-4.6×10^{-6}	-4.6×10^{-6}	-1.1×10^{-6}	4.1×10^{-6}	3.4×10^{-7}
O(P)	3.4×10^{-1}	-1.4×10^{-1}	3.3×10^{-2}	-5.7×10^{-1}	7.6×10^{-1}
O(D)	-1.6×10^{-3}	5.2×10^{-4}	-1.4×10^{-3}	-3.0×10^{-3}	-1.3×10^{-3}
O ₂ (a)	-1.3×10^{-6}	-3.7×10^{-2}	9.9×10^{-1}	1.3×10^{-4}	-2.8×10^{-4}
O ₂ (b)	2.2×10^{-5}	5.5×10^{-5}	-7.8×10^{-4}	-3.9×10^{-3}	1.3×10^{-3}
O ₃	2.6×10^{-4}	-2.0×10^{-3}	-2.1×10^{-3}	-2.4×10^{-2}	9.4×10^{-2}
O ₂ ⁻	8.0×10^{-18}	-1.1×10^{-21}	-3.1×10^{-18}	-1.3×10^{-17}	1.7×10^{-17}
O ⁻	-4.6×10^{-8}	-6.2×10^{-4}	-5.9×10^{-7}	9.3×10^{-7}	-3.9×10^{-6}
O ₂	-2.0×10^{-3}	-9.5×10^{-1}	6.9×10^{-2}	2.1×10^{-1}	1.3×10^0
O ⁺	-1.1×10^{-5}	4.1×10^{-22}	5.3×10^{-5}	1.3×10^{-5}	-4.1×10^{-6}
Ar	-1.0×10^{-2}	-5.9×10^{-1}	-1.0×10^{-2}	-1.1×10^{-1}	1.0×10^0

The sensitivity coefficients show that the O(P) atom concentration decreases mainly due to wall recombination (reaction R233) and it increases due to reaction of ozone with O₂(b) state (reaction R209). The O(P) atoms are also lost by three body reactions with O or O₂ and Ar (reactions R155 and R156).

The O₂(a) states are mainly destroyed at wall deactivation (reaction R235) and they are created at the quenching of O₂(b) states by O atoms (reaction R206).

The O₂(b) states are mainly destroyed at wall deactivation (reaction R236) and at the quenching by O atoms and ozone (reactions R205, R206 and R209). They are created in reactions of O(P) with ozone (reaction R212).

Ozone is created mainly by three body reaction of O(P), O₂ and Ar (reaction R155) and it is destroyed by collisions with excited oxygen molecules O₂(b) (reaction R209). Ozone is also destroyed by collisions with O(P) atoms (reactions R210–R212), these reactions are less important. The reactions that change significantly concentrations of O(P) and O₂(b) (e.g. wall reactions) are also important for ozone concentrations, see the sensitivity coefficients in table 3.

Finally, normalized local concentration sensitivity coefficients $S_{ij}^{(c)}$ for initial concentrations were calculated according to the following equation

$$S_{ij}^{(c)} = \frac{n_{j0}}{n_i} \frac{\partial n_i}{\partial n_{j0}}, \quad (4)$$

where n_i is the concentration of i th particle kind and n_{j0} is the initial concentration of the j th particle kind. These coefficients show how the concentration of i th particle kind depends on the values of initial concentrations. The coefficients $S_{ij}^{(c)}$ were calculated in the same way as the coefficients S_{ij} . These sensitivity coefficients $S_{ij}^{(c)}$ calculated for oxygen atoms and molecules in different states for $t = 10$ ms are shown in table 4. The sensitivity coefficients $S_{ij}^{(c)}$ in this table show that concentrations of oxygen particles do not depend on initial concentration of any charged particle and on initial concentration of excited argon species at our experimental conditions. On the other hand, the

concentration of O₂(a) particles depends almost only on their initial concentration. The ozone concentration depends on initial concentrations of O(P), O₂ and Ar, because ozone is produced in ternary collisions of these particles.

4.5. Calculation of gas temperature

The radially averaged gas temperature $T_g(t)$ in the flow tube under assumption of parabolic radial temperature profile is described by equation [36]

$$n_m c_p \frac{\partial T_g}{\partial t} = \frac{8\lambda_g(T_w - T_g)}{R^2} + Q_{in}, \quad (5)$$

where n_m is the gas molar density, c_p is the molar heat capacity at constant pressure, λ_g is the gas thermal conductivity, T_w is the gas temperature at the inner wall and R is the flow tube radius. The term Q_{in} is the total power per unit volume transferred into gas heating from the energy release after volume and wall reactions. The thermal conductivity of argon is $\lambda_{Ar} = 7.31 \times 10^{-3} + 3.71 \times 10^{-5} T_g \text{ W m}^{-1} \text{ K}^{-1}$, the thermal conductivity of quartz is $\lambda_{quartz} = 1.46 \text{ W m}^{-1} \text{ K}^{-1}$. The specific heat of argon is $c_p = 20.79 \text{ J mol}^{-1} \text{ K}^{-1}$.

The chemical reactions between species A and B in the volume (including electron–ion recombination) lead to the energy release

$$Q_{chem} = [A][B]k\Delta E_{chem}, \quad (6)$$

where ΔE_{chem} is the available energy after a given reaction with a rate coefficient k , that occurs in the gas phase of Ar–O₂ mixture between two species A and B , is transferred to the gas heating. This term accounts for the enthalpies of all volume reactions considered in the model.

Recombination of O atoms at the wall leads to the energy release

$$Q_{wall}^O = \frac{1}{2}[O]\nu_O\Delta E_O(1 - \beta), \quad (7)$$

where ν_O is given by $\gamma_{O(P)}\bar{v}_{O(P)}/2R$. β is the thermal accommodation coefficient, describing the fraction β of released

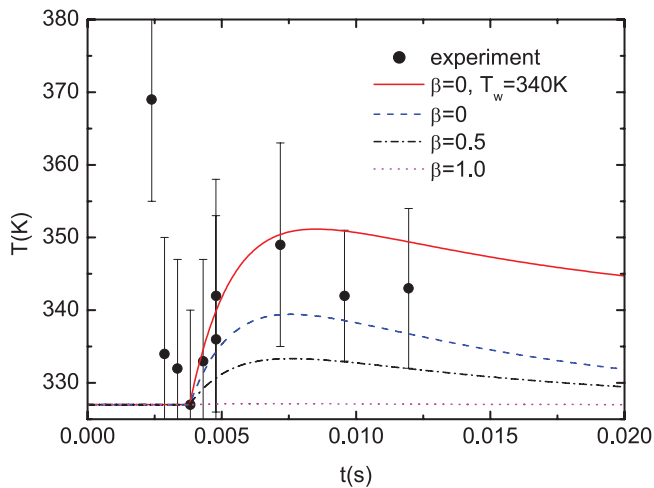


Figure 9. The calculated time dependences of gas temperature in afterglow for different values of accommodation coefficient β . The calculations were performed for wall temperature $T_w = 327$ K except the red line for which $T_w = 340$ K. The points are the values of rotational temperature determined from the measured spectra of oxygen atmospheric band.

energy that is dissipated in wall heating. The remaining fraction $(1 - \beta)$ of released energy contributes to gas heating. Since the energy of molecular oxygen is lower than that of two O atoms, this process contributes to gas and/or wall heating (depending on the value of accommodation coefficient β) with energy $\Delta E_O = 5.12$ eV. The energy release due to metastable deactivation at the wall was calculated similarly.

The time dependence of the gas temperature in the afterglow was calculated using equation (5). Initially, the gas temperature was calculated for the case with no internal heating, i.e. for $Q_{in} = 0$. Because the thermal conductivity of quartz is much larger than the thermal conductivity of argon, the temperature of inner tube wall T_w is almost equal to the temperature of outer tube wall, i.e. ~ 300 K (see figure 5). In this case the gas temperature decays exponentially with a decay constant $8\lambda_{Ar}/(n_m c_p R^2) = 492$ s $^{-1}$. Because in this case the gas temperature reaches 300 K for $t \rightarrow \infty$, the time needed for gas temperature decrease from initial gas temperature of 400 K (in the active discharge) to 301 K was calculated. It was found that the gas temperature decreases to 301 K in 10 ms. Because the gas temperature determined from spectroscopic measurement at 10 ms is higher (see figure 4), there is an internal heating in the gas.

So the equation (5) was solved with nonzero term Q_{in} containing the terms Q_{chem} and Q_{wall}^O (see equations (6) and (7)). The initial gas temperature T_g was set to 327 K (the minimum temperature at $t = 3.8$ ms obtained from the spectroscopic measurement). At the calculation, T_g was kept constant to $t = 3.8$ ms and its calculation started after this time. In this case, the inner tube wall is heated mostly by oxygen atoms recombining on the wall (see below) and its temperature increases. The preliminary temperature calculations showed that the temperature increase in the afterglow can be observed only if the temperature of inner tube wall is not more than 15 K lower the gas temperature, otherwise the temperature decay prevails. So, for the gas temperature calculation T_w was set

also to 327 K and it was kept constant. There is no knowledge about the actual value of accommodation coefficient β . So, the calculation of temperature dependence was performed for β equal 0, 0.5 and 1. The value 0.5 was also used in previous calculation of temperature [36]. The results of calculations are shown in figure 9. The calculation with $\beta = 1$ did not show any significant gas temperature increase. In this case, the wall processes do not contribute to the gas heating and the energy released at volume processes is negligible. The calculations with $\beta = 0$ and $\beta = 0.5$ reveal the significant temperature increase. The maximum of calculated temperature corresponds to the position of maximum temperature obtained from experiment. So the energy which heats the gas is released at the wall processes and it was found by switching on/off the different wall reactions, that almost all energy is released at the wall recombinations of O(P) atoms. The gas temperature strongly depends on the value of T_w . The gas temperature calculated with $T_w = 340$ K and $\beta = 0$ reaches the maximum value which is in agreement with experiment. However, the following gas temperature decrease is too slow in comparison with the experiment. This is caused by the assumed constant wall temperature T_w in the calculation, whereas the wall temperature changes in experiment as it was shown by the outer wall temperature measurement (see figure 5). For this reason it is not possible to determine the accommodation coefficient from this experiment.

5. Conclusion

The flowing argon–oxygen afterglow was studied using optical emission spectroscopy and NO titration. The NO titration method was used to determine the O atom concentration along the axis of the flow tube. The optical emission spectroscopy was used to measure the oxygen atmospheric A-band also along the flow tube. The integral intensity of this atmospheric A-band and rotational temperature of $O_2(b)$ molecule were then determined from these spectroscopic measurements. The zero-dimensional kinetic model was used for the calculation of time dependences of particle concentrations. It was found out using sensitivity analysis that wall recombination and deactivation processes play important role in the kinetic model and the wall recombination probability for O(P) atoms and wall deactivation probability for $O_2(b)$ states were determined. The best fit of the calculated data to the experimental ones was obtained for the wall recombination probability $\gamma_{O(P)} = (1.63 \pm 0.06) \times 10^{-3}$ and wall deactivation probability $\gamma_{O_2(b)} = (1.7 \pm 0.1) \times 10^{-3}$. The gas temperature calculation showed that the wall recombination of O(P) atoms produces sufficient amount of energy which can heat the gas in the afterglow and rises the gas temperature up twenty kelvins, in the agreement with the experiment.

Acknowledgments

We thank V Guerra for providing us the particle density calculations in the Ar– O_2 DC discharge obtained from the numerical code LoKI. This work results within the collaboration

of the COST Action TD 1308 and CM 1401. This research has been supported by the project CZ.1.05/2.1.00/03.0086 funded by European Regional Development Fund, by the projects LO1411 (NPU I) and LD15010 funded by Ministry of Education, Youth and Sports of Czech Republic and by the Czech Science Foundation, contract No. 13-24635S. JR has been supported by the program ‘Employment of newly graduated doctors of science for scientific excellence’ (CZ.1.07/2.3.00/30.0009) cofinanced by the European Social Fund and the state budget of the Czech Republic.

References

- [1] Mafra M, Belmonte T, Poncin-Epaillard F, Maliska A and Cvelbar U 2009 *Plasma Process. Polym.* **6** S198
- [2] Lerouge S, Wertheimer M R and Yahia L’H 2001 *Plasma Polym.* **6** 175
- [3] Belmonte T, Czerwiec T, Gavillet J and Michel H 1997 *Surf. Coat. Technol.* **97** 642
- [4] Zhang S, van Gaens W, van Gessel B, Hofmann S, van Veldhuizen E, Bogaerts A and Bruggeman P 2013 *J. Phys. D: Appl. Phys.* **46** 205202
- [5] Kutasi K, Guerra V and Sá P 2010 *J. Phys. D: Appl. Phys.* **43** 175201
- [6] Kutasi K, Guerra V and Sá P 2011 *Plasma Sources Sci. Technol.* **20** 035006
- [7] Kutasi K, Sá P and Guerra V 2012 *J. Phys. D: Appl. Phys.* **45** 195205
- [8] Kutasi K, Zaplotnik R, Primc G and Mozetic M 2014 *J. Phys. D: Appl. Phys.* **47** 025203
- [9] Ricard A, Gaillard M, Monna V, Vesel A and Mozetic M 2001 *Surf. Coat. Technol.* **142–4** 333
- [10] Ricard A and Monna V 2002 *Plasma Sources Sci. Technol.* **11** A150
- [11] Ricard A, Monna V and Mozetic M 2003 *Surf. Coat. Technol.* **174–5** 905
- [12] Czerwiec T, Gavillet J, Belmonte T, Michel H and Ricard A 1998 *Surf. Coat. Technol.* **98** 1411
- [13] Mozetic M and Zalar A 2000 *Appl. Surf. Sci.* **158** 263
- [14] Mozetic M, Ricard A, Babic D, Poberaj I, Levaton J, Monna V and Cvelbar U 2003 *J. Vac. Sci. Technol. A* **21** 369
- [15] Kutasi K and Loureiro J 2007 *J. Phys. D: Appl. Phys.* **40** 5612
- [16] Dilecce S and De Benedictis S 1999 *Plasma Sources Sci. Technol.* **8** 266
- [17] Gordiets B, Ferreira C M, Nahorny J, Pagnon D, Touzeau M and Vialle M 1996 *J. Phys. D: Appl. Phys.* **29** 1021
- [18] Macko P, Veis P and Cernogora G S 2004 *Plasma Sources Sci. Technol.* **13** 251
- [19] Mazankova V, Trunec D and Krcma F 2013 *J. Chem. Phys.* **139** 164311
- [20] Mazankova V, Trunec D and Krcma F 2014 *J. Chem. Phys.* **141** 154307
- [21] Ricard A, Moisan M and Moreau S 2001 *J. Phys. D: Appl. Phys.* **34** 1203
- [22] Vasina P, Kudrle V, Talsky A, Botos P, Mrazkova M and Mesko M 2004 *Plasma Sources Sci. Technol.* **13** 668
- [23] Zerrouki H, Ricard A and Sarrette J P 2014 *Contrib. Plasma Phys.* **54** 827
- [24] Kolts J H and Setser D W 1978 *J. Chem. Phys.* **68** 4848
- [25] Piper L G, Velazco J E and Setser D W 1973 *J. Chem. Phys.* **59** 3323
- [26] Bolden R C, Hemsworth R S, Shaw M J and Twiddy N D 1970 *J. Phys. B: At. Mol. Phys.* **3** 45
- [27] Shneider M N, Baltuška A and Zheltikov A M 2011 *J. Appl. Phys.* **110** 083112
- [28] Loiseau J F, Pignolet P and Held B 1992 *J. Phys. D: Appl. Phys.* **25** 745
- [29] Shul R J, Upschulte B L, Passarella R, Keesee R G and Castleman A W Jr 1987 *J. Phys. Chem.* **91** 2556
- [30] Oka T, Kogoma M, Imamura M, Arai S and Watanabe T 1979 *J. Chem. Phys.* **70** 3384
- [31] Trunec D, Spanel P and Smith D 2003 *Chem. Phys. Lett.* **372** 728
- [32] Chantray P J 1987 *J. Appl. Phys.* **62** 1141
- [33] Roufflet B, Gaboriau F and Sarrette J P 2010 *J. Phys. D: Appl. Phys.* **43** 185203
- [34] Oinuma G, Inanaga Y, Tanimura Y, Kuzumoto M, Tabata Y and Watanabe K 2010 *J. Phys. D: Appl. Phys.* **43** 255202
- [35] Hairer E and Wanner G 1996 *Solving Ordinary Differential Equations II. Stiff and Differential-Algebraic Problems* (Berlin: Springer)
- [36] Pintassilgo C D, Guerra V, Guaitella O and Rousseau A 2014 *Plasma Sources Sci. Technol.* **23** 025006
- [37] Miller J H, Boese R W and Giver L P 1969 *J. Quant. Spectrosc. Radiat. Transfer* **9** 1507
- [38] Childs W H J and Mecke R 1931 *Z. Phys.* **68** 344
- [39] Touzeau M, Vialle M, Zellagui A, Gousset G and Lefevre M 1991 *J. Phys. D: Appl. Phys.* **24** 41
- [40] Guerra V 2015 private communication
- [41] Pinheiro M J, Gousset G, Granier A and Ferreira C M 1998 *Plasma Sources Sci. Technol.* **7** 524
- [42] Turanyi T 1990 *J. Math. Chem.* **5** 203
- [43] Turanyi T 1997 *Reliab. Eng. Syst. Saf.* **57** 41
- [44] Saltelli A, Ratto M, Tarantola S and Campolongo F 2005 *Chem. Rev.* **105** 2811

STUDY OF ARGON AFTERGLOW WITH THE AIR ADDITION

MAZÁNKOVÁ V.^{a,*}, TRUNEC D.^b, PETROVÁ K.^a, KRČMA F.^a

^a Faculty of Chemistry, Brno University of Technology, Purkyňova 118, 612 00 Brno, Czech Republic

^b Faculty of Science, Masaryk University, Kotlářská 2, 611 37 Brno, Czech Republic

* mazankova@fch.vut.cz

Abstract. The reaction kinetics in argon flowing afterglow (post-discharge) with the air addition was studied by optical emission spectroscopy. The optical emission spectra were measured along the post-discharge flow tube. A zero-dimensional kinetic model for the reactions in the afterglow was developed. This model allows to calculate the time dependencies of particle concentrations.

Keywords: argon afterglow, optical emission spectroscopy, kinetic model.

1. Introduction

Besides different types of plasma argon plasma generated by electrical discharges has an exceptional position for its exploitation. A lot of treatment techniques and production of thin films and multilayer systems are arranged in argon plasma atmosphere [1]. Special position has also argon afterglows containing different impurities. Afterglow systems containing oxygen or nitrogen have a wide range of applications in different fields due to the presence of reactive oxygen or nitrogen species (oxygen atoms, excited metastable oxygen and nitrogen molecules) [2, 3]. The afterglows of Ar-O₂ or Ar-N₂ plasmas have been studied experimentally or theoretically by numerous groups. The published studies mainly aimed to determine the concentrations of reactive species in the treatment area. Theoretical kinetic model of Ar-N₂ flowing afterglow was developed by Loiseau et al. [4] and recently a model for Ar-N₂ mixture was also developed by Shneider et al. [5] in order to study population inversion in this gas mixture. A zero dimensional kinetic model in Ar-O₂ surface-wave microwave discharges was developed by Kutasi et al [6, 7] to investigate electron and heavy particle kinetics and dissociation of O₂ molecules in the discharge and the flowing afterglow. The present work is focused on the experimental study of air addition directly to the argon flowing afterglow. The intensity of the arising nitrogen second positive system (SPS) was measured in dependence on decay time by optical emission spectroscopy. A simple kinetic model was developed in order to explain the experimental results.

2. Experimental setup

The flowing configuration of argon DC discharge with the air admixture was used for this experimental study. The experimental set-up was already used for our previous studies of argon afterglow with nitrogen admixture [8] and nitrogen afterglow with mercury vapour admixture [9]. A simplified schematic drawing of the experimental set-up is given in Figure 1. The active

discharge was created in a quartz discharge tube with the inner diameter of 12 mm at the constant total gas pressure of 1000 Pa and the discharge power of 50 W. Hollow molybdenum electrodes were placed in the side arms (at the interelectrode distance of 120 mm) of the main discharge tube. The argon gas was of 99.99 % purity and it was further cleaned by Oxiclear. The reactor system was pumped continuously by a rotary oil pump. The argon flow of 1400 sccm was automatically controlled by the Bronkhorst mass flow controller. The synthetic air was prepared by mixing of nitrogen and oxygen (8 sccm N₂ + 2 sccm O₂) and flow was also automatically controlled by the Bronkhorst mass flow controllers. The moveable capillary tube for air addition was made of Pyrex and it was immersed upstream from the discharge into the quartz tube at its axis. Its external diameter was 2 mm, the inner diameter was 0.5 mm and the length was 400 mm. The position of the output end of capillary tube was fixed at 50 mm from the end of the active discharge (nearest edge of the side arm with cathode). The flow analysis was performed in the same way as in previous study on argon metastable quenching [8]. The input gas temperature was 300 K.

The optical spectra were measured by Jobin Yvon monochromator TRIAX 550 with 300 gr/mm and 1200 gr/mm grating and with CCD detector. The emitted light was led to the entrance slit of the monochromator by the multimode quartz optical fibre movable along the discharge tube.

3. Results and Discussion

The optical emission spectra were measured in the active discharge with grating 1200 gr/mm and in the afterglow with grating 300 gr/mm. The argon metastable concentration in the active discharge was determined from the spectra using the self-absorption method [10]. However, no self-absorption was observed, so the mean (across the tube diameter) metastable concentration was below 10⁹ cm⁻³. Only the SPS and argon lines were found in the spectra. The N₂(C) state, which is the upper state of SPS, is

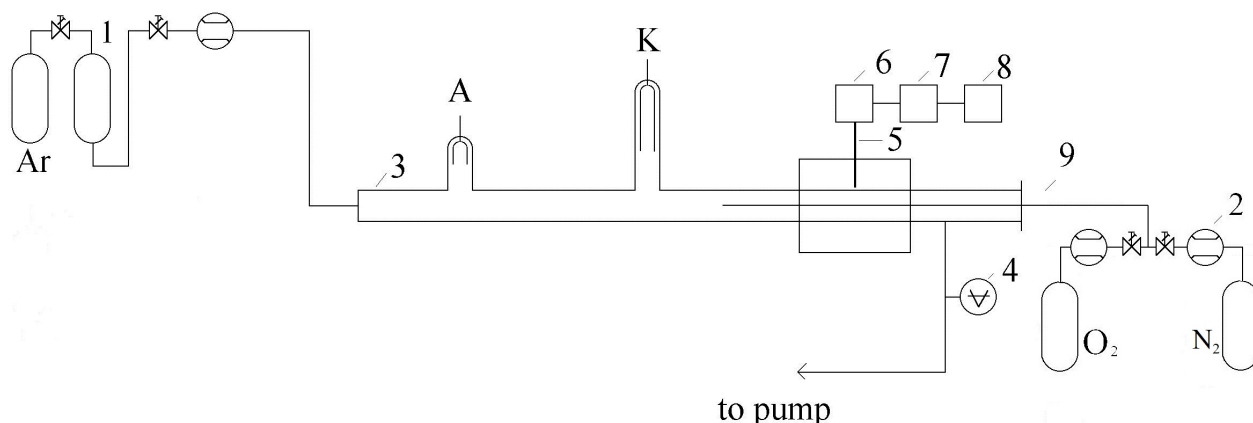


Figure 1. Scheme of the experimental setup. 1 — catalyzer Oxiclear; 2 — mass flow controllers; 3 — quartz discharge tube; 4 — capacitance gauge; 5 — quartz optical fibre; 6 — monochromator Jobin Yvon Triax 550; 7 — CCD; 8 — PC; 9 — movable Pyrex capillary tube.

produced by excitation transfer in collisions of argon metastable $\text{Ar}(^3\text{P}_2)$ with nitrogen molecules.

As it can be seen from Figure 2, no transitions from the upper state with $v > 2$ were observed, which is typical for the population of $\text{N}_2(\text{C})$ state by excitation transfer from $\text{Ar}(^3\text{P}_2)$ state. The SPS intensity was measured as a function of position along the flow tube. The SPS was identified 20 millimeters before the addition point. An example of the recorded post-discharge spectrum after air addition is shown in Figure 2. The dependence of SPS intensity on the distance from active discharge is shown in Figure 3. This dependence can be divided into two parts. The first part represents a rapid increase of SPS intensity to the maximal value due to the mixing of air with flowing argon.

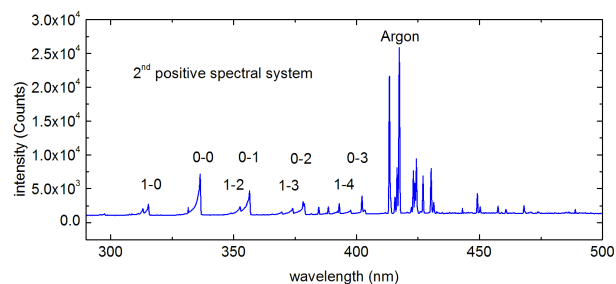


Figure 2. Overview spectrum of argon post-discharge with air titration.

In the second part the SPS intensity decreases due to the decrease of argon metastable concentration and thus due to the decrease of excitation transfer rate. A zero-dimensional kinetic model for the argon — air afterglow was developed. The initial concentrations of argon $[\text{Ar}]_0$, molecular oxygen $[\text{O}_2]_0$ and molecular nitrogen $[\text{N}_2]_0$ in ground states were calculated from the equation of state for ideal gas for $T = 300$ K and from corresponding flow rates. The concentration of argon ground state was considered to be constant. At our experimental conditions the electrons are thermal-

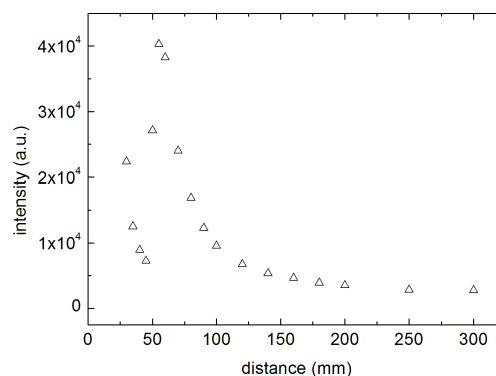


Figure 3. The dependence of SPS intensity (0-1 transition) on distance from active discharge.

ized due to collisions with argon atoms. The time needed for the electron temperature decrease within 10% of neutral gas temperature was calculated using data published by Trunec et al. [11]. This calculated time for estimated initial electron energy of 4 eV was 1.2 ms, which corresponds to the distance of 2.4 cm in the flow tube. So, the electron temperature was equal to neutral gas temperature (300 K) in our experiment and this electron temperature was also used in the kinetic model. The reactions involved in the model and their rate coefficients were taken from [8, 9, 12]. The resulting system of differential equations was solved numerically. The results of the kinetic model are shown in Figures 4, 5 and 6.

The Figure 4 shows the time dependence of electron and ion concentrations. During the first hundred μs , the Ar^+ ions are converted to Ar_2^+ molecular ions, however both these ions react with atomic and molecular oxygen and also with molecular nitrogen in charge transfer reactions producing O^+ , O_2^+ and N_2^+ ions. Thereafter the O^+ ions and all nitrogen ions are

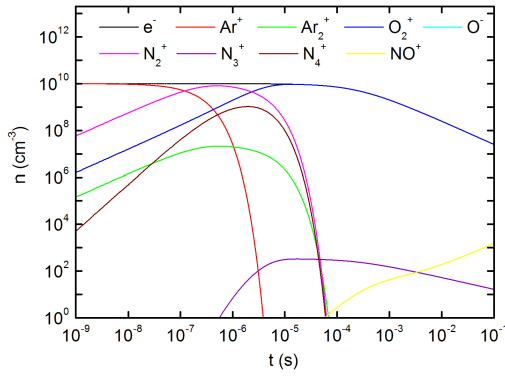


Figure 4. The calculated time dependence of electron and ion concentrations in the afterglow.

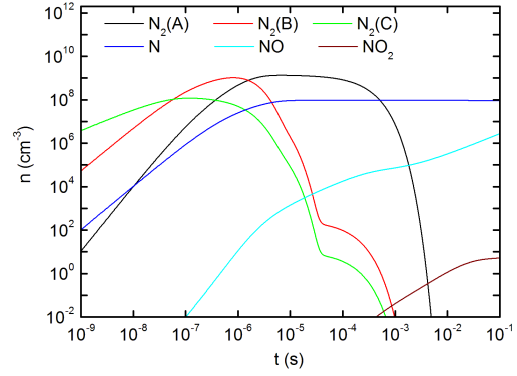


Figure 6. The calculated time dependence of nitrous oxides concentrations in the afterglow.

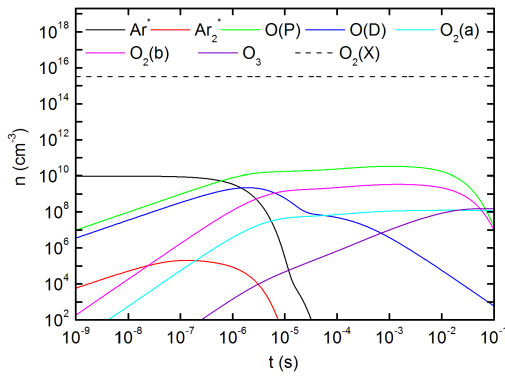


Figure 5. The calculated time dependence of neutral particle concentrations in the afterglow.

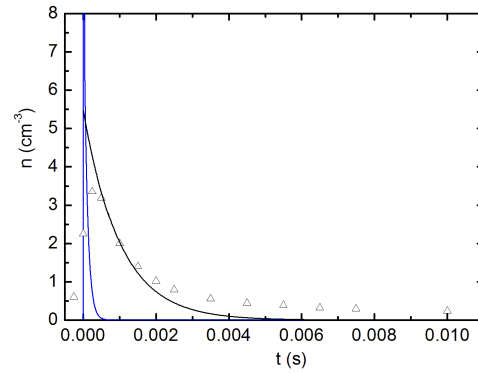


Figure 7. The comparison of calculated $N_2(C)$ concentration with measured SPS intensity. Blue line – calculated $N_2(C)$ concentration, black line – convolution of calculated $N_2(C)$ concentration with apparatus function, triangles – measured SPS intensities.

converted to O_2^+ ions by exothermic charge transfer reaction. So, after the first millisecond all positive ions are converted to O_2^+ ions. Thus, after the first millisecond only electrons and O_2^+ ions are the remaining charged particles, which recombine mutually and their concentrations further decrease and also the O_2^+ ions react again in exothermic charge transfer reaction with arising NO.

The Figure 5 shows the time dependence of neutral oxygen species and excited argon and oxygen species concentrations. The Ar^* metastables produced in the discharge are converted to excimer Ar_2^* molecules, both Ar^* and Ar_2^* react with molecular oxygen producing atomic oxygen in ground or excited state. After the first millisecond, the concentrations of argon excited species are negligibly small. Mutual reactions of O and O_2 produce ozone and metastable oxygen molecules $O_2(a)$ and $O_2(b)$. So after the first millisecond the remaining neutral particles with significant concentrations in afterglow are atomic oxygen in ground state O(P), metastable molecular oxygen states $O_2(a)$ and $O_2(b)$ and ozone together with argon and molecular oxygen in ground states. The concentration of metastable atomic oxygen O(D) is very low

(around 10^4 cm^{-3}).

The Figure 6 shows the time dependence of nitrogen and nitrous oxides species concentrations. The $N_2(C)$ states produced in excitation transfer reaction decays to $N_2(B)$ which decays further to $N_2(A)$. All these three nitrogen excited states are also quenched by O_2 producing oxygen atoms. The nitrogen atoms are produced in collisions of two $N_2(A)$ molecules. The atomic oxygen and nitrogen then react and nitrous oxides are produced.

The results from the kinetic model are compared with measured SPS intensities in Figure 7.

In order to compare directly the results of model with experimental results the convolution of kinetic model results with an apparatus function of experimental setup was calculated [8]. The apparatus function accounts for the light propagation in flow tube wall. This light propagation in the wall leads to the slower decrease of SPS intensity in the experiment. So calculated SPS intensity decay is in good agreement with experimental data except the times longer than 5 ms, when there is still very low nonzero experimentally

measured SPS intensity. The origin of this very low SPS intensity is not clear.

4. Conclusions

The flowing argon afterglow with air addition was studied using optical emission spectroscopy. The optical emission spectroscopy was used to measure the nitrogen SPS along the flow tube, which arises in excitation transfer between argon metastables and nitrogen molecules. The kinetic model shows time dependences of different species in the afterglow. The argon and nitrogen excited states decay very quickly mainly by quenching with molecular oxygen. Also the argon and nitrogen ions decay very quickly due to charge transfer reactions to molecular oxygen. So after first millisecond only oxygen species are important. Then atomic oxygen reacts with atomic nitrogen producing NO and further NO₂.

Acknowledgements

The research was supported by Czech Ministry of Education, Youth and Sports, project No. COST CZ LD15010 and within the collaboration of the COST Action CM 1401.

References

- [1] S. Saloum, M. Naddaf, and B. Alkhaled. Diagnostics of N₂-Ar plasma mixture excited in a 13.56 MHz hollow cathode discharge system: application to remote plasma treatment of polyamide surface. *J. Phys. D: Appl. Phys.*, 41(4):045205, 2008.
- [2] M. Mafra, T. Belmonte, F. Poncin-Epaillard, A. Maliska, and U. Cvelbar. Treatment of hexatriacontane by Ar-O₂ remote plasma: Formation of the active species. *Plasma Process. Polym.*, 6(S):S198–S203, 2009.
- [3] S. Lerouge, M. R. Wertheimer, and L'H. Yahia. Plasma sterilization: a review of parameters, mechanisms, and limitations. *Plasma Polym.*, 6(3):175–188, 2001.
- [4] J. F. Loiseau, P. Pignolet, and B. Held. Numerical simulation of Ar-N₂ excitation transfer in flowing afterglow. *J. Phys. D: Appl. Phys.*, 25(5):745–750, 1992.
- [5] M. N. Shneider, A. Baltuška, and A. M. Zheltikov. Population inversion of molecular nitrogen in an Ar: N₂ mixture by selective resonance-enhanced multiphoton ionization. *J. Appl. Phys.*, 110(8):083112, 2011.
- [6] K. Kutasi, P. Sá, and V. Guerra. O₂ dissociation in Ar-O₂ surface-wave microwave discharges. *J. Phys. D: Appl. Phys.*, 45(19):195205, 2012.
- [7] K. Kutasi, R. Zaplotnik, G. Primc, and M. Mozetic. Controlling the oxygen species density distributions in the flowing afterglow of O₂/Ar-O₂ surface-wave microwave discharges. *J. Phys. D: Appl. Phys.*, 47(2):025203, 2014.
- [8] V. Mazánková, D. Trunec, and F. Krčma. Study of argon flowing afterglow with nitrogen injection. *J. Chem. Phys.*, 139(3):164311, 2013.
- [9] V. Mazánková, D. Trunec, and F. Krčma. Study of nitrogen flowing afterglow with mercury vapor injection. *J. Chem. Phys.*, 141(3):154307, 2014.
- [10] M. Schulze, A. Yanguas-Gil, A. von Keudell, and Awakowicz P. A robust method to measure metastable and resonant state densities from emission spectra in argon and argon-diluted low pressure plasmas. *J. Phys. D: Appl. Phys.*, 41(3):065206, 2008.
- [11] D. Trunec, P. Spanel, and D. Smith. The influence of electron-electron collisions on electron thermalization in He and Ar afterglow plasmas. *Chem. Phys. Lett.*, 372:728–732, 2003.
- [12] C. D. Pintassilgo, J. Loureiro, G. Cernogora, and M. Touzeau. Methane decomposition and active nitrogen in a N₂-CH₄ glow discharge at low pressures. *Plasma Sources Sci. Technol.*, 8:463–478, 1999.

Study of argon flowing afterglow with nitrogen injection

V. Mazánková, D. Trunec, and F. Krčma

Citation: *J. Chem. Phys.* **139**, 164311 (2013); doi: 10.1063/1.4826650

View online: <http://dx.doi.org/10.1063/1.4826650>

View Table of Contents: <http://jcp.aip.org/resource/1/JCPSA6/v139/i16>

Published by the [AIP Publishing LLC](#).

Additional information on *J. Chem. Phys.*

Journal Homepage: <http://jcp.aip.org/>

Journal Information: http://jcp.aip.org/about/about_the_journal

Top downloads: http://jcp.aip.org/features/most_downloaded

Information for Authors: <http://jcp.aip.org/authors>



Re-register for Table of Content Alerts

Create a profile.



Sign up today!



Study of argon flowing afterglow with nitrogen injection

V. Mazánková,^{1,a)} D. Trunec,² and F. Krčma¹

¹*Institute of Physical and Applied Chemistry, Faculty of Chemistry, Brno University of Technology, Purkyňova 118, 612 00 Brno, Czech Republic*

²*Department of Physical Electronics, Faculty of Science, Masaryk University, Kotlářská 2, 611 37 Brno, Czech Republic*

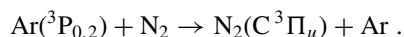
(Received 11 July 2013; accepted 10 October 2013; published online 28 October 2013)

In this work, the reaction kinetics in argon flowing afterglow with nitrogen addition was studied by optical emission spectroscopy. The DC flowing post-discharge in pure argon was created in quartz tube at the total gas pressure of 1000 Pa and discharge power of 60 W. The nitrogen was added into the afterglow at the distance of 9 cm behind the active discharge. The optical emission spectra were measured along the flow tube. The argon spectral lines and after nitrogen addition also nitrogen second positive system (SPS) were identified in the spectra. The measurement of spatial dependence of SPS intensity showed a very slow decay of the intensity and the decay rate did not depend on the nitrogen concentration. In order to explain this behavior a kinetic model for reaction in afterglow was developed. This model showed that $C^3\Pi_u$ state of molecular nitrogen, which is the upper state of SPS emission, is produced by excitation transfer from argon metastables to nitrogen molecules. However, the argon metastables are also produced at Ar_2^+ ion recombination with electrons and this limits the decay of argon metastable concentration and it results in very slow decay of SPS intensity.

© 2013 AIP Publishing LLC. [<http://dx.doi.org/10.1063/1.4826650>]

I. INTRODUCTION

Plasmas generated in Ar-N₂ mixtures have been widely studied for different conditions (pressure, concentration, discharge kind, etc.) during the last decades with respect to the broad applications.^{1–3} A lot of treatment techniques and production of thin films and multilayer systems are arranged in argon plasma atmosphere.^{4,5} The use of discharge plasmas in the applications often requires the understanding of the kinetics in this environment, where the different pathways of production and loss of active species exist. Among them, the energy transfer process from argon metastable states to molecular nitrogen is important. This energy transfer process is due to the reaction



The excited $N_2(C^3\Pi_u)$ nitrogen state is then the origin state of the nitrogen second positive spectral system (SPS). Many papers have been devoted to the investigation of the electronic energy transfer from metastable argon atoms $Ar(^3P_{0,2})$ to molecular nitrogen.^{6–11} Le Calve and Bourene studied the SPS induced by the transfer of energy to nitrogen by metastable argon atoms obtained by the pulsed radiolysis of argon-nitrogen mixtures using optical emission spectroscopy.⁶ The obtained rate coefficient was $(3 \pm 0.3) \times 10^{-11} \text{ cm}^3 \text{ s}^{-1}$. Piper *et al.*⁸ used flowing afterglow technique with absorption spectroscopy for determination of metastable concentration and they reported a value of $3.3 \times 10^{-11} \text{ cm}^3 \text{ s}^{-1}$. Theoretical kinetic model of Ar-N₂ flowing afterglow was developed by Loiseau *et al.*⁹ and recently a model for Ar-N₂ mixture was also developed by

Shneider *et al.*¹⁰ in order to study population inversion in this gas mixture. $Ar(^3P_0)$ is less efficient than $Ar(^3P_2)$ in excitation transfer to $N_2(C^3\Pi_u)$.^{12,13} In addition, $Ar(^3P_0)$ concentration is smaller than $Ar(^3P_2)$ concentration,^{13,14} then almost all the excitation transfer is produced by $Ar(^3P_2)$.

The present work is focused on the experimental study of nitrogen titration directly to the argon flowing afterglow. The intensity of the arising SPS was measured in dependence on decay time by optical emission spectroscopy. A simple kinetic model was developed in order to explain the experimental results.

II. EXPERIMENTAL SETUP

The DC flowing configuration of argon discharge was used for the experimental study. A simplified schematic drawing of the experimental setup is given in Figure 1. The active discharge was created in a quartz discharge tube with inner diameter of 12 mm at the constant total gas pressure of 1000 Pa and discharge power of 60 W. Hollow molybdenum electrodes were placed in the side arms (at interelectrode distance of 120 mm) of the main discharge tube to minimize their sputtering and also to minimize scattering of the light emitted in the electrode regions. The reactor system was pumped continuously by a rotary oil pump separated from the discharge tube by a LN₂ trap. The gas flow of 1400 sccm was automatically controlled by Bronkhorst mass flow controller. The total gas pressure in the discharge tube was measured by a capacitance gauge connected to the end of the discharge tube. The gas temperature was 300 K.

The moveable titration capillary tube was made of Pyrex and it was immersed upstream from the discharge into the quartz tube at its axis. Its external diameter was 2 mm,

^{a)}Electronic mail: mazankova@fch.vutbr.cz

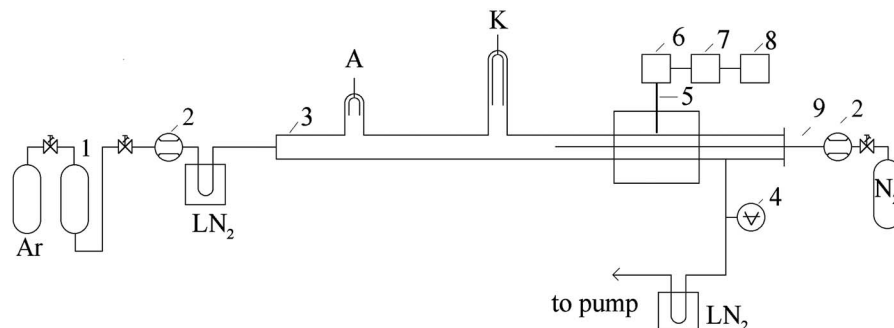


FIG. 1. Scheme of the experimental setup. 1 – catalyzer Oxiclear; 2 – mass flow controller; 3 – quartz discharge tube; 4 – capacitance gauge; 5 – quartz optical fiber; 6 – monochromator Jobin Yvon Triax 550; 7 – CCD; 8 – PC; 9 – movable Pyrex titration capillary tube.

inner diameter was 0.5 mm, and the length was 400 mm. The position of the output end of capillary tube was fixed at 90 mm from the active discharge which corresponded to the decay time of 4.5 ms in this experiment. The nitrogen of 99.999% purity with flow of 0.15–0.8 sccm (again controlled by Bronkhorst mass flow controller) was used for the titration.

The bulk flow velocity v_g of argon in the tube was calculated from the continuity equation and the state equation. The calculated velocity v_g was 20 m s^{-1} in the mainstream and 3 m s^{-1} in the capillary tube. The flow analysis was performed in the same way as in previous studies on argon metastable quenching.^{7,8} The distance d needed to develop a full parabolic velocity profile is given by $d = 0.277aR$, where a is the flow tube radius (0.6 cm) in cm and R is the Reynolds number. For our experimental conditions, the Reynolds number R is equal to 150, which gives $d = 25 \text{ cm}$. Furthermore, our experimental setup introduced perturbations into the flow pattern at the side arms and at the nitrogen inlet. So, the flow will be in transition between plug and parabolic flow and in this case the bulk flow velocity can be used for the calculation of the decay time. This approach was found to be correct in previous study.⁷ In our experiment the line intensities (which are proportional to excited particle concentrations) were measured across the diameter of the flow tube. Bolden *et al.*¹⁵ have experimentally demonstrated that this is equivalent to monitoring the concentration at the center of the tube for fully developed parabolic flow conditions. Kolts and Setser⁷ measured the argon metastable concentration across the diameter of the flow tube by the optical absorption spectroscopy in the case of plug flow. They found that no correction is necessary in order to obtain correct values of quenching rate coefficients. So, again no correction was applied at our measurement.

The optical spectra were measured by Jobin Yvon monochromator TRIAX 550 with CCD detector. A 1200 g/mm grating was used for spectra acquisition in the range of 300–500 nm. The emitted light was led to the entrance slit of the monochromator by the multimode quartz optical fiber movable along the discharge tube. The integration time for spectra measurement in the afterglow was 120 s due to very low intensity of SPS. The SPS of nitrogen $\text{N}_2(\text{C } ^3\Pi_u) \rightarrow \text{N}_2(\text{B } ^3\Pi_g)$ was recorded in all spectra. For the determination of SPS intensity the 0-1 transition at wavelength 357.69 nm was chosen. Argon spectral lines

around 400 nm were also recognized. No other atomic or molecular emissions were observed.

III. KINETIC MODEL

The following particles were considered in the kinetic model – atomic argon ion Ar^+ , molecular argon ion Ar_2^+ , argon metastable Ar^* ($^3\Pi_2$ state), argon excimer molecule Ar_2^* , and excited nitrogen $\text{N}_2(\text{C})$ ($\text{C } ^3\Pi_u$ state). The concentrations of argon and nitrogen in ground states were calculated from equation of state for $T = 300 \text{ K}$ and they were considered constant. Six reactions concerning these particles were included in the kinetic model, see Table I. The rate coefficients for these reactions were taken from recent papers.^{9,10} The rate coefficient for molecular argon ion recombination depends on electron temperature.¹⁰ At our experimental conditions the electrons are thermalized due to collisions with argon atoms. The time needed for the electron temperature decrease within 10% of neutral gas temperature was calculated using data published by Trunec *et al.*¹⁶ This calculated time for estimated initial electron energy of 4 eV was 1.2 ms, which corresponds to the distance of 2.4 cm in the flow tube. So, the electron temperature was equal to neutral gas temperature (300 K) in our experiment and this electron temperature was also used in the kinetic model. The reactions which are known to be negligible (the radiative decay of Ar^* , the $\text{Ar}^* + \text{Ar}$ two-body quenching, and the quenching of $\text{N}_2(\text{C})$ by collision with Ar or N_2) were not included. The diffusion losses of all considered species are also negligible at argon pressure used in the experiment.

TABLE I. Reactions and their rate coefficients considered in the model. The values of rate coefficients are for $T = 300 \text{ K}$, also the electron temperature for reaction 2 is $T_e = 300 \text{ K}$. The symbols in brackets show the marking for corresponding rate coefficients used in the following text.

No.	Reaction	Rate coefficient ^{9,10}
1.	$\text{Ar}^+ + \text{Ar} + \text{Ar} \rightarrow \text{Ar}_2^+ + \text{Ar}$	$2.5 \times 10^{-31} \text{ cm}^6 \text{ s}^{-1}$
2.	$\text{Ar}_2^+ + e^- \rightarrow \text{Ar}^* + \text{Ar}$	$1 \times 10^{-6} \text{ cm}^3 \text{ s}^{-1} (k_d)$
3.	$\text{Ar}^* + \text{Ar} + \text{Ar} \rightarrow \text{Ar}_2^* + \text{Ar}$	$1 \times 10^{-32} \text{ cm}^6 \text{ s}^{-1}$
4.	$\text{Ar}_2^* \rightarrow \text{Ar} + \text{Ar} + h\nu$	$2.4 \times 10^7 \text{ s}^{-1}$
5.	$\text{Ar}^* + \text{N}_2 \rightarrow \text{Ar} + \text{N}_2(\text{C})$	$3 \times 10^{-11} \text{ cm}^3 \text{ s}^{-1} (k_r)$
6.	$\text{N}_2(\text{C}) \rightarrow \text{N}_2(\text{B}) + h\nu$	$2.74 \times 10^7 \text{ s}^{-1} (k_r)$

Let us consider the production of SPS by reactions 5 and 6 only. These reactions are described by following equations

$$\frac{dn_m}{dt} = -k_q n_m n_2, \quad (1)$$

$$\frac{dn_C}{dt} = k_q n_m n_2 - k_r n_C, \quad (2)$$

where n_m is the concentration of argon metastable Ar^* , n_C is the concentration of nitrogen $\text{N}_2(\text{C})$ state, n_2 is the concentration of nitrogen N_2 in ground state, k_q is the rate coefficient for excitation transfer, and k_r is the rate coefficient for SPS emission from $\text{N}_2(\text{C})$ state. Reaction 5 is a second order reaction and it was assumed that $n_2 \gg n_m$ for its solution. So the concentration n_2 was considered as constant during the reaction. At $t = 0$, when the plasma starts to decay, the initial concentration n_m is equal n_{m0} and the initial concentration $n_C = 0$. Then the solution of Eq. (2) is

$$n_C(t) = \frac{k_q n_2 n_{m0}}{k_q n_2 - k_r} (\exp(-k_q n_2 t) - \exp(-k_r t)). \quad (3)$$

The density n_C can be determined from the intensity of SPS, I , which is proportional to the second term on the right side of Eq. (2)

$$I \sim n_C. \quad (4)$$

If $k_r > k_q n_2$, the intensity decays exponentially and it is the first exponential term in Eq. (3) which governs the intensity decay. So the k_q could be determined from the intensity decay.

However, if the metastables are also simultaneously produced in other collisional processes (e.g., in dissociative recombination of Ar_2^+ ions with electrons) in the afterglow, Eq. (1) has to be corrected and all reactions from Table I must be taken into account. The resulting system of differential equations was solved numerically using RADAU5 procedure.¹⁷ For initial conditions for this system a glow discharge in pure argon, producing electrons, Ar^+ ions and Ar^* metastables was assumed. The concentrations of these particles n_{e0} , $n_{i0} = n_{e0}$ and n_{m0} were taken as the initial values for the system of differential equations describing the kinetic model.

IV. RESULTS AND DISCUSSION

A. Experimental results

The optical emission spectra were measured in the active discharge and in the afterglow. The argon metastable concentration in the active discharge was determined from the spectra using the self-absorption method.^{18,19} However, no self-absorption was observed, so the mean (across the tube diameter) metastable concentration was below 10^9 cm^{-3} .

As described in Sec. II, the SPS intensity was measured as a function of position along the flow tube. The SPS was identified a few millimeters before the titration point. An example of the recorded post-discharge spectrum after nitrogen addition is shown in Figure 2. As it can be seen from Figure 2, no transitions from the upper state with $v > 2$ were observed, which is typical for the population of $\text{N}_2(\text{C})$ state by excitation transfer from $\text{Ar}(^3\text{P}_2)$ state. The dependence of

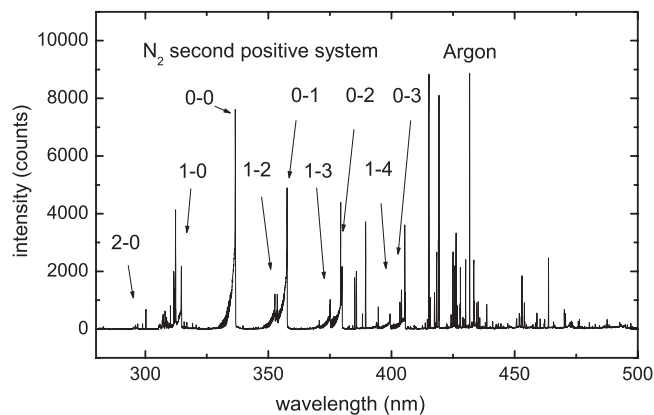


FIG. 2. Overview spectrum of argon post-discharge with nitrogen titration.

SPS intensity on the distance from active discharge is shown in Figure 3. This dependence can be divided into two parts. The first part represents a rapid increase of SPS intensity to the maximal value due to the mixing of nitrogen with flowing argon. After that reaction 5 prevails and the decrease of intensity can be observed in the second part. However, the decay time constant is greater than that expected from the reaction rate of reaction 5. Also, as can be seen from Figure 3, higher concentration of nitrogen does not result in a steeper decay of the SPS intensity, the decay rate almost does not depend on nitrogen concentration. This is in contradiction with Eq. (3).

B. Results from kinetic model

The experimental data can be explained by the results of kinetic model described in Sec. III. The results of the kinetic model are shown in Figure 4. The rapid conversion of atomic Ar^+ ions to molecular Ar_2^+ ions takes place in first millisecond. Also Ar^* metastables are converted to Ar_2^* excimer molecules, however, Ar_2^* concentration at pressure of 1000 Pa remains low (several orders below Ar^* concentration). Then, at $t = 4.5 \text{ ms}$ the nitrogen was injected. The calculated time dependence of $\text{N}_2(\text{C})$ concentration can be seen in the detail

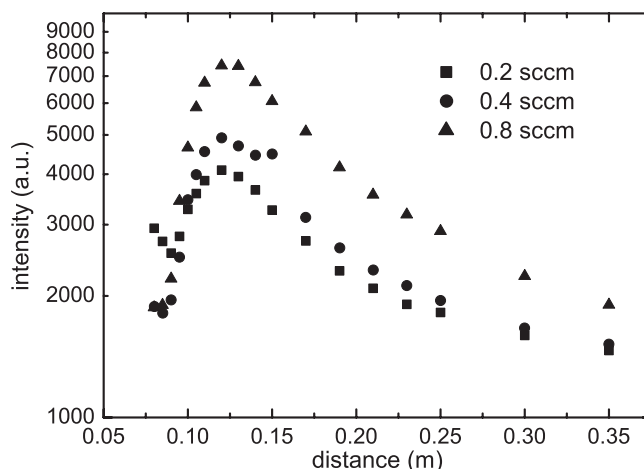


FIG. 3. The dependence of SPS intensity (0-1 transition) on distance from active discharge for different nitrogen flow rates.

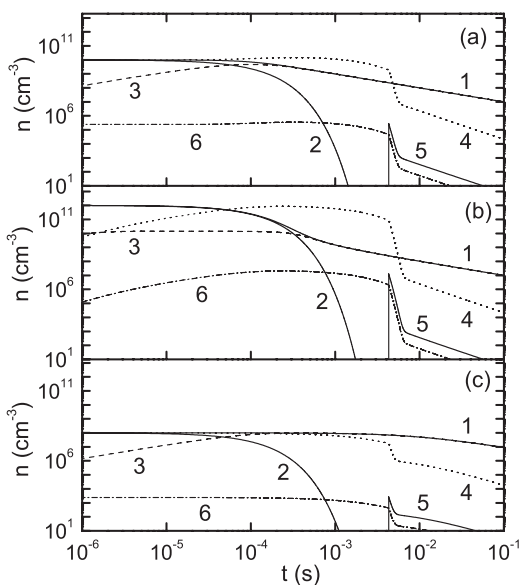


FIG. 4. The time dependence of particle concentrations for different initial conditions. Concentrations: 1 – electrons, 2 – Ar^+ , 3 – Ar_2^+ , 4 – Ar^* , 5 – $\text{N}_2(\text{C})$, 6 – Ar_2^* . Initial concentrations: (a) $n_{e0} = 10^{10} \text{ cm}^{-3}$, $n_{m0} = 10^{10} \text{ cm}^{-3}$, nitrogen flow rate 0.8 sccm; (b) $n_{e0} = 10^{12} \text{ cm}^{-3}$, $n_{m0} = 10^8 \text{ cm}^{-3}$, nitrogen flow rate 0.8 sccm; (c) $n_{e0} = 10^8 \text{ cm}^{-3}$, $n_{m0} = 10^8 \text{ cm}^{-3}$, nitrogen flow rate 0.8 sccm.

in Figure 5. This dependence consists of three parts: an initial very steep increase – part A, a steep decrease – part B, and much slower decrease – part C (see again Figure 5). These parts are discussed in detail below.

1. Part A

After nitrogen injection, the $\text{N}_2(\text{C})$ concentration increases very rapidly to maximum value. The maximum of

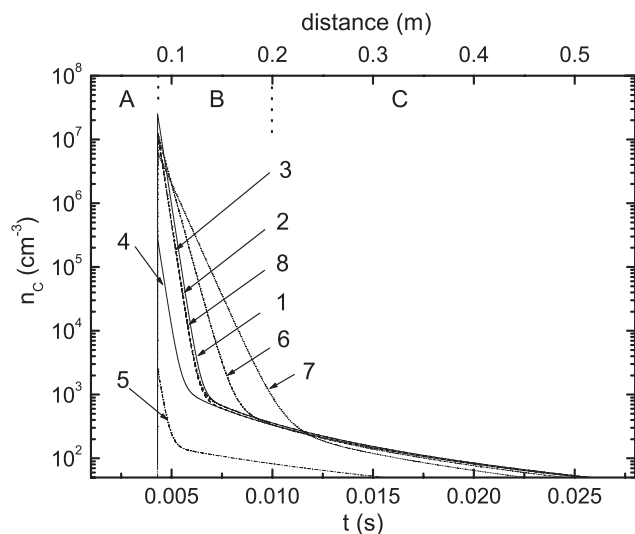


FIG. 5. The time dependence of $\text{N}_2(\text{C})$ concentration for different initial conditions. 1 – $n_{e0} = 10^{12} \text{ cm}^{-3}$, $n_{m0} = 10^{12} \text{ cm}^{-3}$, $q_{\text{N}_2} = 0.8 \text{ sccm}$; 2 – $n_{e0} = 10^{12} \text{ cm}^{-3}$, $n_{m0} = 10^{10} \text{ cm}^{-3}$, $q_{\text{N}_2} = 0.8 \text{ sccm}$; 3 – $n_{e0} = 10^{12} \text{ cm}^{-3}$, $n_{m0} = 10^8 \text{ cm}^{-3}$, $q_{\text{N}_2} = 0.8 \text{ sccm}$; 4 – $n_{e0} = 10^{10} \text{ cm}^{-3}$, $n_{m0} = 10^{10} \text{ cm}^{-3}$, $q_{\text{N}_2} = 0.8 \text{ sccm}$; 5 – $n_{e0} = 10^8 \text{ cm}^{-3}$, $n_{m0} = 10^8 \text{ cm}^{-3}$, $q_{\text{N}_2} = 0.8 \text{ sccm}$; 6 – $n_{e0} = 10^{12} \text{ cm}^{-3}$, $n_{m0} = 10^{12} \text{ cm}^{-3}$, $q_{\text{N}_2} = 0.4 \text{ sccm}$; 7 – $n_{e0} = 10^{12} \text{ cm}^{-3}$, $n_{m0} = 10^{12} \text{ cm}^{-3}$, $q_{\text{N}_2} = 0.2 \text{ sccm}$; 8 – $n_{e0} = 10^{10} \text{ cm}^{-3}$, $n_{m0} = 10^{12} \text{ cm}^{-3}$, $q_{\text{N}_2} = 0.8 \text{ sccm}$.

the peak increases with increasing nitrogen concentration, and decreases when initial argon metastable concentration and initial electron concentration are both decreased, compare curves 1, 4, and 5 in Figure 5.

2. Part B

The Ar^* concentration decreases rapidly in part B and this leads also to the decrease of $\text{N}_2(\text{C})$ concentration. The steep decrease is caused by depopulation of Ar^* by reaction 5 and the decay rate depends on nitrogen concentration, compare curves 1, 6, and 7 in Figure 5. The rate coefficient for reaction 5 can be determined from this part of the dependence. At the end of this part the Ar^* concentration decreases to a very low value and further the production of argon metastables in argon molecular ions recombination with electrons becomes substantial. This metastable production balances the losses due to reaction 5 which leads to much slower decrease of $\text{N}_2(\text{C})$ concentration. The shape of $\text{N}_2(\text{C})$ concentration time dependencies for different initial metastable concentration is the same, since the metastable concentrations at the time of nitrogen injection are similar due to metastable production in the first millisecond, compare curves 1–3 in Figure 5. The rate coefficient for reaction 5 can be determined in our experiment only for very low nitrogen flow (0.15 sccm) and it follows from the model that the decay curve only in range from 0.10 to 0.14 m has to be considered. The measured SPS intensity dependence for above mentioned nitrogen flow and distance range has exponential form, see Figure 6. So Eq. (3) can be used for the rate coefficient determination. The value of rate coefficient obtained from exponential fit is $(1.4 \pm 0.4) \times 10^{-11} \text{ cm}^3 \text{ s}^{-1}$.

3. Part C

For times longer than 12 ms all curves merge together, except of the curve for lowest values of initial electron and metastable concentrations (curve 5). In this part, the decay rate does not depend on nitrogen concentration. The $\text{N}_2(\text{C})$ concentration is slightly decreased and it also decays slightly

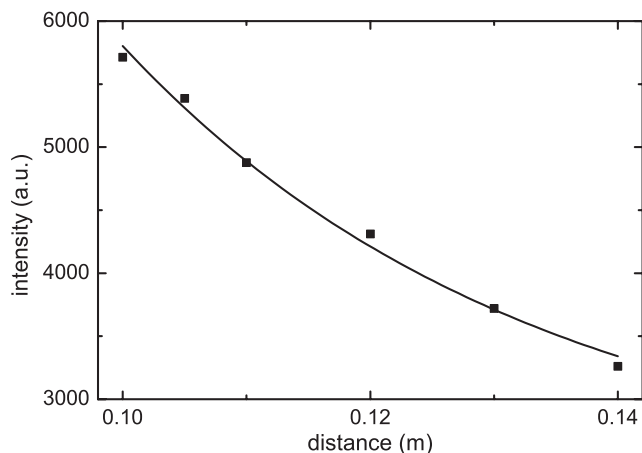


FIG. 6. The dependence of SPS intensity on distance from active discharge. Nitrogen flow $q_{\text{N}_2} = 0.15 \text{ sccm}$.

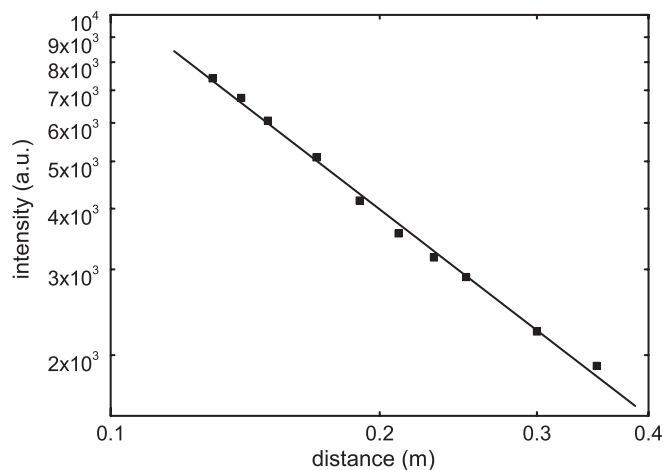


FIG. 7. The dependence of SPS intensity on distance from active discharge. Nitrogen flow $q_{N_2} = 0.8$ sccm.

more slowly with decreasing initial electron concentration n_{e0} . This effect is more dominant at very low initial electron concentration n_{e0} , see curve 5 in Figure 5.

The measurement presented in Subsection IV A mostly covered this part of the dependence. Therefore, the experimental dependencies did not change with nitrogen concentration. It is not possible to determine the rate coefficient for reaction 5 from this part of $N_2(C)$ concentration dependence. Both measured and theoretical dependencies are not exponential, having the form $n_C \sim t^\alpha$. The coefficient α has the value of -2.1 and -1.2 for theoretical curves 1 and 5 in Figure 5, respectively, and the value of -1.4 for the experimental data with nitrogen flow of 0.8 sccm in Figure 3. This experimental dependence has a linear form in log-log plot as it can be seen in Figure 7. It also follows from the kinetic model that the decay of $N_2(C)$ concentration in this part depends mainly on rate coefficient for molecular argon ion recombination k_d , which also suggests the form of its time dependence. The influence of the value of k_d on the $N_2(C)$ concentration is shown in Figure 8. As can be seen from this figure the changes of k_d do not change significantly the slope of $N_2(C)$ concentration curves in part B and they have significant influence on these curves in part C.

C. Comparison of theoretical and experimental results

In order to compare directly the results of model with experimental results the convolution of kinetic model results with an apparatus function of experimental setup was calculated by following equation

$$I_m(x) = \int_{-\infty}^{\infty} I_c(y/v_g) \exp(-k|x-y|) dy, \quad (5)$$

where I_m and I_c are the measured and calculated SPS intensity, respectively. The apparatus function was taken in the form $\exp(-k|x-y|)$, this form of apparatus function represents an exponential decay of the light intensity along the tube observed in an independent experiment. The best fit to measured

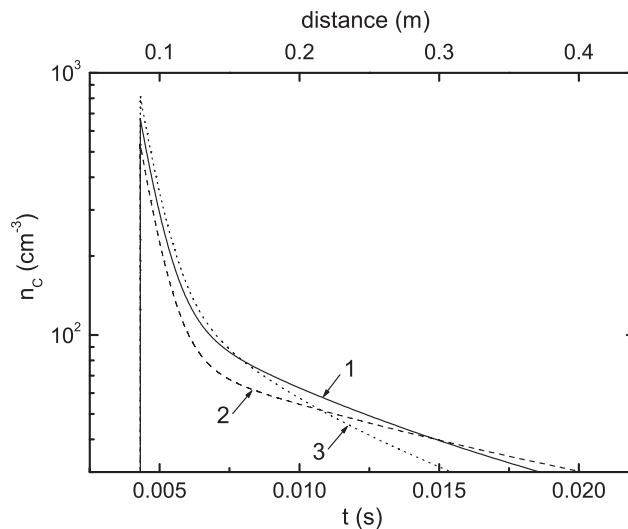


FIG. 8. The influence of value of rate coefficient for molecular argon ion recombination k_d on $N_2(C)$ concentration. Initial concentrations $n_{e0} = 10^8 \text{ cm}^{-3}$, $n_{m0} = 10^8 \text{ cm}^{-3}$; nitrogen flow $q_{N_2} = 0.2$ sccm. 1 – $k_d = 1 \times 10^{-6} \text{ cm}^3 \text{ s}^{-1}$; 2 – $k_d = 0.5 \times 10^{-6} \text{ cm}^3 \text{ s}^{-1}$; 3 – $k_d = 2 \times 10^{-6} \text{ cm}^3 \text{ s}^{-1}$.

data was obtained for $k = 50 \text{ m}^{-1}$. The comparison of convoluted theoretical SPS intensity profiles with experimental ones is shown in Figure 9. The calculated profiles were divided by the factor of 800 in order to obtain the best fit to experimental intensity profiles (the SPS intensities were measured only relatively). As can be seen in the figure the maxima of calculated profiles are shifted to shorter distances and they are also higher in comparison with experimental profiles. This is caused by the slow mixing of added nitrogen with flowing afterglow plasma which is not taken into account in the calculation. In the decaying part of profiles there is a good agreement of calculated and measured profiles for the value of electron and metastable concentrations equal to 10^8 cm^{-3} ,

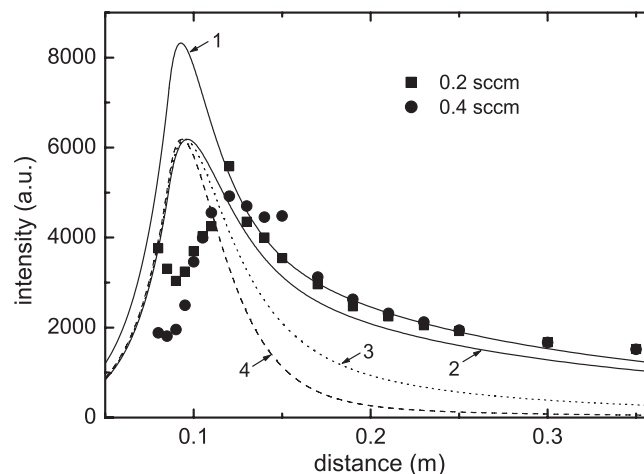


FIG. 9. The dependence of SPS intensity on the distance from active discharge – the comparison of experimental and theoretical results. Experimental results – points; results of calculations – lines: 1 – $n_{e0} = 10^8 \text{ cm}^{-3}$, $n_{m0} = 10^8 \text{ cm}^{-3}$, $q_{N_2} = 0.4$ sccm; 2 – $n_{e0} = 10^8 \text{ cm}^{-3}$, $n_{m0} = 10^8 \text{ cm}^{-3}$, $q_{N_2} = 0.2$ sccm; 3 – $n_{e0} = 10^9 \text{ cm}^{-3}$, $n_{m0} = 10^8 \text{ cm}^{-3}$, $q_{N_2} = 0.2$ sccm; 4 – $n_{e0} = 10^{10} \text{ cm}^{-3}$, $n_{m0} = 10^8 \text{ cm}^{-3}$, $q_{N_2} = 0.2$ sccm.

see lines 1 and 2 in Figure 9. On the other hand, the profiles calculated for the value of electron concentrations equal to 10^9 cm^{-3} and 10^{10} cm^{-3} do not fit the experimental data, see lines 3 and 4 in Figure 9. The value of 10^8 cm^{-3} for initial electron and metastable concentration is also indicated by the value of α exponent of the time dependence, see above. So this measurement may be used for the indication of electron and metastable concentrations in the discharge.

The different rates of $\text{N}_2(\text{C})$ concentration decay were also observed in experiment by Le Calve and Bourene⁶ at argon pressures below 200 Torr. They also proposed that this effect is caused by metastable production at recombination of argon molecular ions. However, the kinetic model was not developed in their work.

V. CONCLUSION

The SPS of nitrogen was observed in optical spectra after nitrogen addition to argon flowing afterglow plasma at neutral gas pressure of 1000 Pa. The SPS intensity was measured at different positions along the flow tube (and hence at different times of afterglow). The measured spatial dependence exhibited very slow decrease only and the decrease rate does not depend on the concentration of added nitrogen which was in contradiction with previous experiments done by other authors. This peculiar behavior was explained by kinetic model. The upper state of SPS is $\text{N}_2(\text{C})$ state which is produced by excitation transfer from argon metastable state $^3\text{P}_2$ to nitrogen ground state. The argon metastables are also produced in afterglow at Ar_2^+ ion recombination with electron, which leads to slow decay of $\text{N}_2(\text{C})$ states and also of SPS intensity. This slow decay is then mainly controlled by the rate of Ar_2^+ ion recombination rather than by the rate of excitation transfer. It follows also from the model that the rate coefficient for excitation transfer can be determined only at very low nitrogen concentrations and only in the first few milliseconds.

The rate coefficient obtained in such way was $(1.4 \pm 0.4) \times 10^{-11} \text{ cm}^3 \text{ s}^{-1}$. This value is two times lower than the value obtained by Le Calve and Bourene.⁶

ACKNOWLEDGMENTS

The present work was supported by the project “R&D center for low-cost plasma and nanotechnology surface modifications” (Grant No. CZ.1.05/2.1.00/03.0086) funding by European Regional Development Fund and by Czech Science Foundation, Contract No. 13-24635S.

- ¹S. G. Belostotskiy, T. Ouk, V. M. Donnelly, D. J. Economou, and N. Sadeghi, *J. Appl. Phys.* **107**, 053305 (2010).
- ²F. Krčma and M. Žáková, *Eur. Phys. J. D* **54**, 369 (2009).
- ³N. Kang, S. Oh, and A. Ricard, *J. Korean Phys. Soc.* **58**, 776 (2011).
- ⁴U. Ikhlāqa, R. Ahmada, S. Saleema, M. S. Shaha, U. Kalsooma, N. Khana, and N. Khalida, *Eur. Phys. J.: Appl. Phys.* **59**, 20801 (2012).
- ⁵S. Saloum, M. Naddaf, and B. Alkhaled, *J. Phys. D: Appl. Phys.* **41**, 045205 (2008).
- ⁶J. Le Calve and M. Bourene, *J. Chem. Phys.* **58**, 1446 (1973).
- ⁷J. H. Kolts and D. W. Setser, *J. Chem. Phys.* **68**, 4848 (1978).
- ⁸L. G. Piper, J. E. Velazco, and D. W. Setser, *J. Chem. Phys.* **59**, 3323 (1973).
- ⁹J. F. Loiseau, P. Pignolet, and B. Held, *J. Phys. D: Appl. Phys.* **25**, 745 (1992).
- ¹⁰M. N. Shneider, A. Baltuška, and A. M. Zheltikov, *J. Appl. Phys.* **110**, 083112 (2011).
- ¹¹L. Isola, M. Lopez, and B. J. Gomez, *J. Phys. D: Appl. Phys.* **44**, 375204 (2011).
- ¹²N. Sadeghi, M. Cheaib, and D. W. Setser, *J. Chem. Phys.* **90**, 219 (1989).
- ¹³V. Mazankova, F. Krčma, and M. Zakova, in *Proceedings of the 18th Symposium on Physics of Switching Arc, Brno, 2009*, edited by V. Aubrecht and M. Bartlova (Brno University of Technology, 2009), p. 250.
- ¹⁴V. Mazankova and F. Krčma, *Chem. Listy* **102**, S1388 (2008).
- ¹⁵R. C. Bolden, R. S. Hemsworth, M. J. Shaw, and N. D. Twiddy, *J. Phys. B* **3**, 45 (1970).
- ¹⁶D. Trunec, P. Španel, and D. Smith, *Chem. Phys. Lett.* **372**, 728 (2003).
- ¹⁷E. Hairer and G. Wanner, *Solving Ordinary Differential Equations II. Stiff and Differential-Algebraic Problems* (Springer, 1996).
- ¹⁸M. Schulze, A. Yanguas-Gil, A. von Keudell, and P. Awakowicz, *J. Phys. D: Appl. Phys.* **41**, 065206 (2008).
- ¹⁹Z. Navrátil, L. Dosoudilová, J. Hnilica, and T. Bogdanov, *J. Phys. D: Appl. Phys.* **46**, 295204 (2013).

Study of Nitrogen Atom Recombination by Optical Emission Spectroscopy

Mazánková V.¹, Trunec D.², Krčma F.¹

1Faculty of Chemistry, Brno University of Technology, Purkyňova 118, Brno 612 00, Czech Republic, mazankova@fch.vutbr.cz, krcma@fch.vutbr.cz

2 Masaryk University, Kotlářská 2, 611 37 Brno, Czech Republic, trunec@physics.muni.cz

The reaction kinetics in nitrogen flowing afterglow was studied by optical emission spectroscopy. The DC flowing post-discharge in pure nitrogen was created in a quartz tube at the total gas pressure of 1000 Pa. The optical emission spectra were measured along the flow tube. It was found that N atoms are the most important particles in the late nitrogen afterglow. In order to explain the decrease of N atom concentration, it was also necessary to include the surface recombination of N atoms to the model.

Keywords: optical emission spectroscopy, nitrogen afterglow, surface recombination coefficient

1 INTRODUCTION

In flowing nitrogen afterglows (post-discharges) at low pressure, a large number of nitrogen atoms is created in the discharge or in the short-lived (pink) afterglow during collisions of nitrogen molecules with electrons, vibrationally excited nitrogen molecules and metastable states. The nitrogen atoms are lost by volume and wall recombination [1]. The probability of volume recombination (a three-body collision) tends to be lower than the wall recombination probability γ . The probability γ is the ratio between the number of atoms effectively recombining at the surface over the number of atom-wall collisions [2]. Nitrogen late afterglow is characterized by a visible emission in the yellow part of the spectrum, associated with the recombination of the nitrogen atoms in the gas phase.

Nitrogen post-discharges are widely used for various industrial applications such as nitriding [3], plasma surface modification [4] or plasma sterilization [5]. Besides laboratory and technological plasmas, the nitrogen post-discharge is studied also in connection with the kinetics of the upper Earth atmosphere (corona borealis [6]) and the processes occurring in nitrogen post-discharges are also taken into account in some extraterrestrial systems, for example in the Titan atmosphere [7].

This paper presents a method for obtaining the atomic nitrogen recombination probability (γ). It is based on the measurement of 11-7 transition intensity in first positive nitrogen spectral system (FPS).

2 EXPERIMENTAL SET-UP

The flowing configuration of nitrogen DC discharge was used for the experimental study. This experimental set-up was already used for our previous study with nitrogen [8, 9]. A simplified schematic drawing of the experimental set-up is given in Fig. 1. The active discharge was created in a quartz discharge tube with the inner diameter of 12 mm at the constant total gas pressure of 1000 Pa and the discharge power of 130 W. Hollow molybdenum electrodes were placed in the side arms (at the interelectrode distance of 120 mm) of the main discharge tube to minimize their sputtering and also to minimize the influence of the light emitted in the electrode regions. The nitrogen gas was of 99.9999 % purity and it was further cleaned by Oxiclear and LN₂ traps. The reactor system was pumped continuously by a rotary oil pump separated from the discharge tube by another LN₂ trap. The gas flow of 800 sccm was automatically controlled by the Bronkhorst mass flow controller. The total gas pressure in the discharge tube was measured by a capacitance gauge connected to the end of the discharge tube. The gas temperature was 300 K.

The bulk flow velocity v_g of nitrogen in the tube was calculated from the continuity equation and the state equation for ideal gas. The calculated velocity v_g was 12 ms⁻¹. The flow analysis was performed in the same way as in previous studies using flowing afterglow [10, 11].

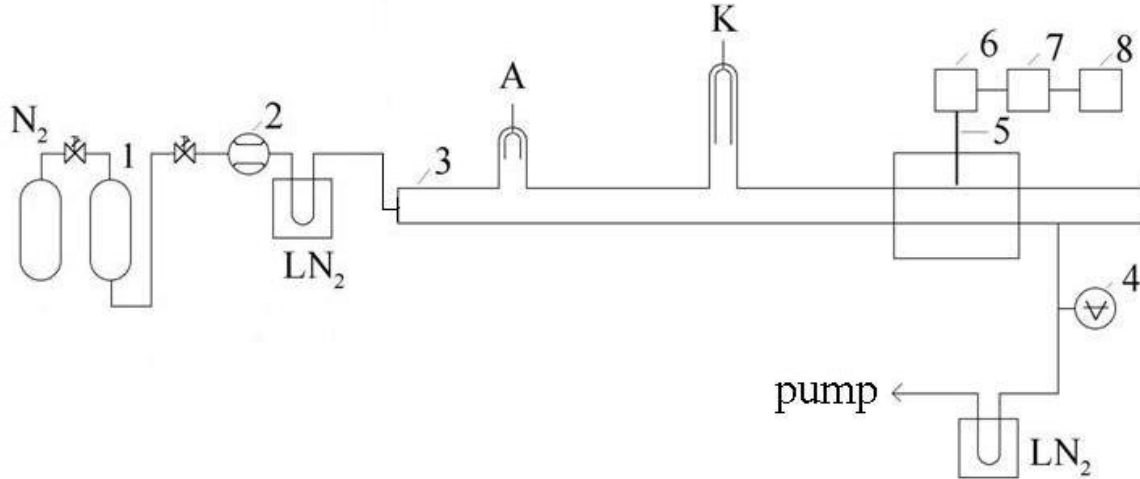


Fig. 1: Scheme of the experimental setup. 1- catalyzer Oxiclear; 2- mass flow controller; 3- quartz discharge tube; 4-capacitance gauge; 5-quartz optical fiber; 6-monochromator Jobin Yvon Triax 550; 7- CCD; 8-PC

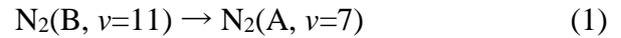
The distance d needed to develop a full parabolic velocity profile is given by $d = 0.277 a R$, where a is the flow tube radius (0.6 cm) in cm and R is the Reynolds number. For our experimental conditions, the Reynolds number R is equal to 184, which gives $d = 31$ cm. Furthermore, our experimental setup introduced perturbations into the flow pattern at the side arms and at the nitrogen inlet. So, the flow will be in transition between plug and parabolic flows and in this case the bulk flow velocity can be used for the calculation of the decay time. This approach was found to be correct in previous studies [8-10]. In present experiment the line intensities (which are proportional to the excited particle concentrations) were measured across the diameter of the flow tube. Bolden et al. [12] have experimentally demonstrated that this is equivalent to monitoring the concentration at the center of the tube for fully developed parabolic flow conditions.

The optical spectra were measured by Jobin Yvon monochromator TRIAX 550 with CCD detector. The 300 gr/mm grating was used for overview spectra in the range from 300 nm to 600 nm. The emitted light was led to the entrance slit of the monochromator by the multimode quartz optical fiber movable along the discharge tube.

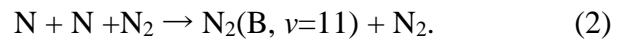
3 RESULTS

The optical spectra were measured as a

function of position along the flow tube in the distances 30 – 52 cm from the active discharge. An example of the typical recorded post-discharge spectrum is shown in Fig. 2. The nitrogen late afterglow emission is dominated by the



band of the first positive system at 580 nm [13], see also Fig. 2. This band is correlated with the three-body recombination process with the rate constant $k_{\text{vol}} = 4.4 \times 10^{-33} \text{ cm}^6 \text{ s}^{-1}$ taken from [14]



As the $\text{N}_2(\text{B}, \nu=11)$ state can de-excite either radiatively to the A state with a global frequency ν_{rad} or collisionally by quenching with the nitrogen molecules (k_{q}), the emitted intensity can be written as

$$I_{11-7} \propto [\text{N}_2(\text{B}, \nu=11)] \propto \frac{k_{\text{vol}}[\text{N}]^2[\text{N}_2]}{\nu_{\text{rad}} + k_{\text{q}}[\text{N}_2]} \quad (3)$$

where the values $\nu_{\text{rad}} = 1.7 \times 10^5 \text{ s}^{-1}$ and $k_{\text{q}} = 5 \times 10^{-11} \text{ cm}^3 \text{ s}^{-1}$ were taken from [15]. So it appears that the evolution of the N atom concentration can be followed monitoring I_{11-7} . For pressures higher than 133 Pa is $k_{\text{q}}[\text{N}_2] \gg \nu_{\text{rad}}$ and equation (3) reduces to

$$[N] \propto \sqrt{I_{11-7}} . \quad (4)$$

The N atom concentration determined from equation (4) is shown in Fig. 3 as a function of decay time. These N atom concentrations were

multiplied by a constant so that they can be coincident at $t = 0$ s (distance 30 cm from active discharge) with absolute N atom concentration determined in previous study by NO titration [16].

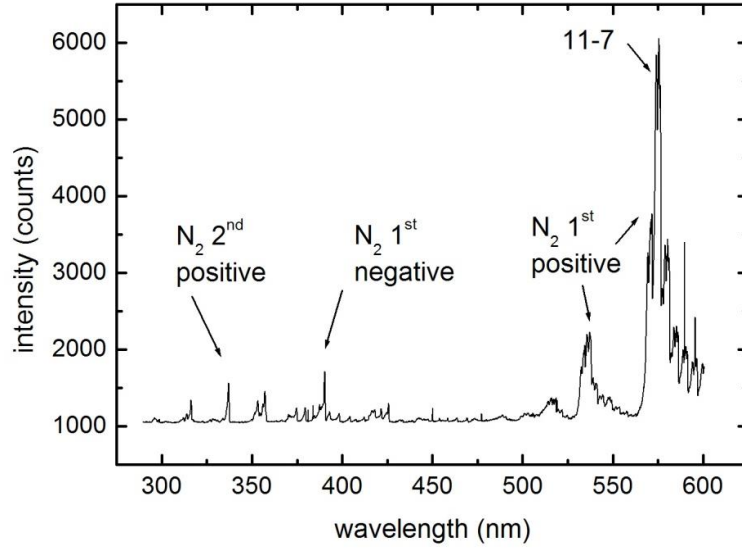


Fig. 2: Overview spectrum of nitrogen post-discharge

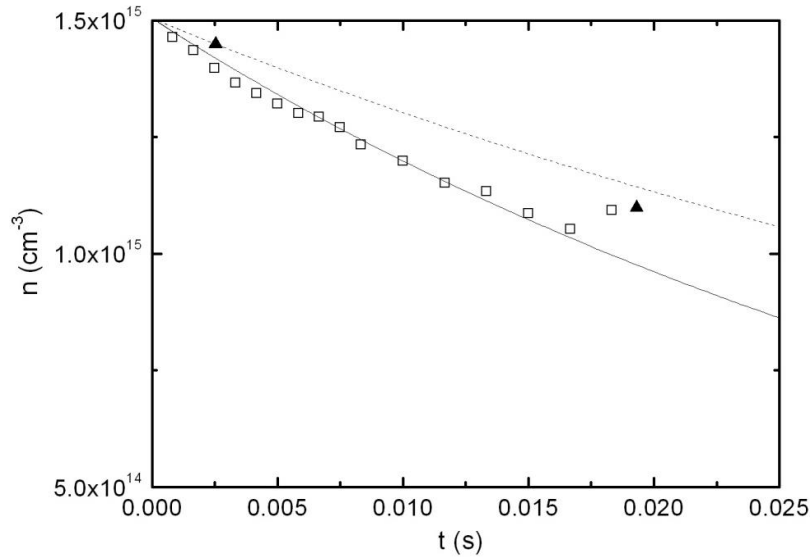


Fig. 3: Time dependence of nitrogen atom concentration. Squares – concentrations determined from Eq. (4); triangles – concentrations determined by NO titration [16]; full line – calculation from the model with $\gamma = 2.16 \times 10^{-6}$; dashed line – calculation from the model with $\gamma = 1.35 \times 10^{-6}$

The kinetic model of nitrogen late afterglow developed previously [9] was used to fit measured data using least square method. The value $\gamma = (2.16 \pm 0.07) \times 10^{-6}$ was obtained

from this method. However, the N atom concentrations determined from measurement of FPS intensity decreases faster than the N atom concentration determined by NO titration and also faster than calculated N atom concentration from the model in previous study [9] with the value $\gamma = 1.35 \times 10^{-6}$. This discrepancy could be caused by incorrect determination of 11-7 transition intensity in FPS due to overlap of this band with neighbouring vibrational bands.

4 CONCLUSION

The recombination of N atoms in nitrogen late afterglow was studied in flowing afterglow experiment at pressure of 1000 Pa. The optical emission spectra were measured at different positions along the quartz flow tube (and hence at different times of afterglow). The spectra were dominated by 11-7 band of the nitrogen first positive system. This band is correlated with three body (volume) recombination of atomic nitrogen and thus it is possible to determine the relative concentration of N atoms from band intensity. Then the wall recombination probability γ for N atoms was calculated from the decrease of N atom concentration along the flow tube and the value $\gamma = (2.16 \pm 0.07) \times 10^{-6}$ was obtained.

Acknowledgements

The present work was supported by the project "R&D center for low-cost plasma and nanotechnology surface modifications" (CZ.1.05/2.1.00/03.0086) funding by the European Regional Development Fund and by the Czech Science Foundation, contract No. 13-24635S.

REFERENCES

- [1] Guerra V, Sa P A, Loureiro, J Eur. Phys. J. - Appl. Phys. 28 (2004) 125.
- [2] Rouffet B, Gaboriau F, Sarrette J P, J. Phys. D: Appl. Phys. 43 (2010) 185203.
- [3] Bockel S, Belmonte T, Michel H, Ablitzer D, Surf. Coat. Technol. 97 (1997) 618.
- [4] Junkar I, Vesel A, Cvelbar U, Mozetic M, Strnad S, Vacuum 84 (2009) 83.
- [5] Kutasi K, Pintassilgo C D, Coelho P J, Loureiro J, J. Phys. D: Appl. Phys. 39 (2006) 3978.
- [6] Ashrafi M, Lanchester B S, Lummerzheim D, Ivchenko N, Jokiahho O, Ann. Geophys. 27 (2009) 2545.
- [7] Horvath G, Krcma F, Polachova L, Klohnova K, Mason N J, Zahoran M, Matejcek S, Eur. J. Phys. D: Appl. Phys. 53 (2011) 11001.
- [8] Mazankova V, Trunec D, Krcma F, J. Chem. Phys. 139 (2013) 164311.
- [9] Mazankova V, Trunec D, Krcma F, J. Chem. Phys. 141 (2014) 154307.
- [10] Kolts J H, Setser D W, J. Chem. Phys. 68 (1978) 4848.
- [11] Piper L G, Velazco J E, Setser D W, J. Chem. Phys. 59 (1973) 3323.
- [12] Bolden R C, Hemsworth R S, Shaw M J, Twiddy N D, J. Phys. B 3 (1970) 45.
- [13] Noxon J F, J. Chem. Phys. 36 (1962) 926.
- [14] Krivonosova O E, Losev S A, Nalivaiko V P, Mukoseev Y K, Shatalov O P, Reviews of Plasma Chemistry vol. 1 (Ed. Smirnov B M). New York: Consultants Bureau, 1991, 9.
- [15] Gordiets B, Ricard A, Plasma Sources Sci. Technol. 2 (1993) 158.
- [16] Mazankova V, Polachova L, Krcma F, Horvath G, Mason N J, In: Proceedings, 19th Symposium on Physics of Switching Arc, Brno, (Ed. Aubrecht V and Bartlova M). Brno University of Technology, 2011, 283.

Study of nitrogen flowing afterglow with mercury vapor injection

V. Mazánková, D. Trunec, and F. Krčma

Citation: *The Journal of Chemical Physics* **141**, 154307 (2014); doi: 10.1063/1.4898367

View online: <http://dx.doi.org/10.1063/1.4898367>

View Table of Contents: <http://scitation.aip.org/content/aip/journal/jcp/141/15?ver=pdfcov>

Published by the [AIP Publishing](#)

Articles you may be interested in

[Study of argon flowing afterglow with nitrogen injection](#)

J. Chem. Phys. **139**, 164311 (2013); 10.1063/1.4826650

[Flowing afterglow measurements of the density dependence of gas-phase ion-ion mutual neutralization reactions](#)

J. Chem. Phys. **138**, 204302 (2013); 10.1063/1.4803159

[Experimental study of the asymmetric charge transfer reaction between Ar⁺ ions and Fe atoms](#)

J. Chem. Phys. **134**, 064308 (2011); 10.1063/1.3548657

[Surface loss probabilities of H and N radicals on different materials in afterglow plasmas employing H₂ and N₂ mixture gases](#)

J. Appl. Phys. **107**, 103310 (2010); 10.1063/1.3372750

[Characteristics of C₃ radicals in high-density C₄F₈ plasmas studied by laser-induced fluorescence spectroscopy](#)

J. Appl. Phys. **88**, 6201 (2000); 10.1063/1.1321029



2014 Special Topics

PEROVSKITES

2D MATERIALS

MESOPOROUS MATERIALS

BIOMATERIALS/
BIOELECTRONICS

METAL-ORGANIC
FRAMEWORK
MATERIALS

AIP | APL Materials

Submit Today!

Study of nitrogen flowing afterglow with mercury vapor injection

V. Mazánková,^{1,a)} D. Trunec,² and F. Krčma¹

¹*Institute of Physical and Applied Chemistry, Faculty of Chemistry, Brno University of Technology, Purkyňova 118, 612 00 Brno, Czech Republic*

²*Department of Physical Electronics, Faculty of Science, Masaryk University, Kotlářská 2, 611 37 Brno, Czech Republic*

(Received 19 June 2014; accepted 5 October 2014; published online 17 October 2014)

The reaction kinetics in nitrogen flowing afterglow with mercury vapor addition was studied by optical emission spectroscopy. The DC flowing post-discharge in pure nitrogen was created in a quartz tube at the total gas pressure of 1000 Pa and discharge power of 130 W. The mercury vapors were added into the afterglow at the distance of 30 cm behind the active discharge. The optical emission spectra were measured along the flow tube. Three nitrogen spectral systems – the first positive, the second positive, and the first negative, and after the mercury vapor addition also the mercury resonance line at 254 nm in the spectrum of the second order were identified. The measurement of the spatial dependence of mercury line intensity showed very slow decay of its intensity and the decay rate did not depend on the mercury concentration. In order to explain this behavior, a kinetic model for the reaction in afterglow was developed. This model showed that the state $\text{Hg}(6^3\text{P}_1)$, which is the upper state of mercury UV resonance line at 254 nm, is produced by the excitation transfer from nitrogen $\text{N}_2(\text{A } ^3\Sigma_u^+)$ metastables to mercury atoms. However, the $\text{N}_2(\text{A } ^3\Sigma_u^+)$ metastables are also produced by the reactions following the N atom recombination, and this limits the decay of $\text{N}_2(\text{A } ^3\Sigma_u^+)$ metastable concentration and results in very slow decay of mercury resonance line intensity. It was found that N atoms are the most important particles in this late nitrogen afterglow, their volume recombination starts a chain of reactions which produce excited states of molecular nitrogen. In order to explain the decrease of N atom concentration, it was also necessary to include the surface recombination of N atoms to the model. The surface recombination was considered as a first order reaction and wall recombination probability $\gamma = (1.35 \pm 0.04) \times 10^{-6}$ was determined from the experimental data. Also sensitivity analysis was applied for the analysis of kinetic model in order to reveal the main control parameters in the model. © 2014 AIP Publishing LLC. [<http://dx.doi.org/10.1063/1.4898367>]

I. INTRODUCTION

Nitrogen discharges and post-discharges (afterglows) have been intensively studied since the beginning of discharge physics research. Despite this long interest there are still various open problems in the understanding of N_2 discharge and post-discharge kinetics. Nitrogen post-discharges are widely used for various industrial applications such as nitriding,¹ plasma surface modification,² or plasma sterilization.^{3,4} Besides laboratory and technological plasmas, the nitrogen post-discharge is also studied in connection with the kinetics of the upper Earth atmosphere (corona borealis⁵) and the processes occurring in nitrogen post-discharges are also taken into account in some extraterrestrial systems, for example, in the Titan atmosphere.^{6,7}

Lewis⁸ showed that traces of mercury vapor in active nitrogen gave strong emission of the $\text{Hg}(6^3\text{P}_1 \rightarrow 6^1\text{S}_0)$ resonance line at 253.7 nm. In nitrogen, mercury atoms are excited by $\text{N}_2(\text{A } ^3\Sigma_u^+)$ ⁹



The rate coefficient for this deactivation of $\text{N}_2(\text{A})$ is $2.90 \times 10^{-10} \text{ cm}^3 \text{ s}^{-1}$ and 80% of the quenching collisions of

$\text{N}_2(\text{A})$ with Hg populate $\text{Hg}(6^3\text{P}_1)$ either directly or via the higher metastable state $\text{Hg}(6^3\text{P}_2)$, which is then rapidly relaxed to $\text{Hg}(6^3\text{P}_1)$.¹⁰ The remaining 20% of the quenching collisions populate the lower metastable state $\text{Hg}(6^3\text{P}_0)$. Reaction (1) was studied by many authors. Callear and Wood studied this reaction using the flash technique for excitation of nitrogen.^{10,11} Thrush and Wild studied this reaction using flowing afterglow system.¹² They also proposed that the $\text{N}_2(\text{A})$ states are produced in three body recombination of nitrogen atoms and that the $\text{N}_2(\text{A})$ states are quenched by N atoms, other species and at the wall. This reaction mechanism was used to analyze their results in steady-state approximation. Klopovsky *et al.* proposed another reaction mechanism in order to study the kinetics of metastable states in high-pressure nitrogen plasma with Hg admixture pumped by a high-current electron beam.¹³ They proposed that the main sources of $\text{N}_2(\text{A})$ states under their conditions are dissociative recombination of N_4^+ ions and cascade quenching of states $\text{N}_2(\text{B } ^3\Pi_g)$ and $\text{N}_2(\text{C } ^3\Pi_u)$.

The $\text{Hg}(6^3\text{P}_1)$ state could also be excited by vibrationally excited ground state $\text{N}_2(\text{X } ^1\Sigma_g^+)$. However, it is generally accepted that the $\text{N}_2(\text{A})$ state is responsible for excitation of levels requiring more than 4.5 eV (which is the case of Hg excitation) while the vibrationally excited ground state might participate in the excitation of lower energy levels.¹⁴

^{a)}Electronic mail: mazankova@fch.vutbr.cz

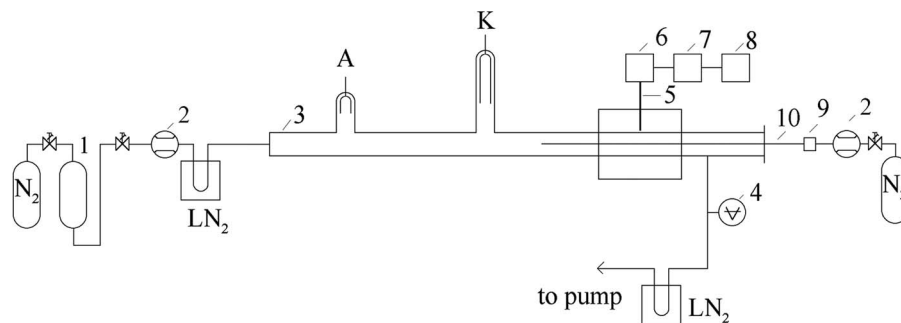


FIG. 1. Scheme of the experimental setup. 1-catalyzer Oxiclear; 2-mass flow controller; 3-quartz discharge tube; 4-capacitance gauge; 5-quartz optical fiber; 6-monochromator Jobin Yvon Triax 550; 7-CCD; 8-PC; 9-vessel with mercury; 10-movable Pyrex titration capillary tube.

It was proposed by many authors that this excitation energy transfer between $N_2(A)$ and Hg or some metal atoms can be used for analytical techniques.^{14,15}

The present work is focused on the experimental study of mercury vapor titration directly into the nitrogen flowing afterglow. The intensity of the arising Hg resonance line was measured in dependence on decay time by optical emission spectroscopy. A simple kinetic model was developed in order to explain the experimental results.

II. EXPERIMENTAL SETUP

The flowing configuration of nitrogen DC discharge was used for the experimental study. This experimental setup was already used for our previous study of argon afterglow with nitrogen admixture.¹⁶ A simplified schematic drawing of the experimental setup is given in Figure 1. The active discharge was created in a quartz discharge tube with the inner diameter of 12 mm at the constant total gas pressure of 1000 Pa and the discharge power of 130 W. Hollow molybdenum electrodes were placed in the side arms (at the interelectrode distance of 120 mm) of the main discharge tube to minimize their sputtering and also to minimize the influence of the light emitted in the electrode regions. The nitrogen gas was of 99.9999% purity and it was further cleaned by Oxiclear and LN_2 traps. The reactor system was pumped continuously by a rotary oil pump separated from the discharge tube by another LN_2 trap. The gas flow of 800 sccm was automatically controlled by the Bronkhorst mass flow controller. The total gas pressure in the discharge tube was measured by a capacitance gauge connected to the end of the discharge tube. The gas temperature was 300 K.

The moveable titration capillary tube was made of Pyrex and it was immersed upstream from the discharge into the quartz tube at its axis. Its external diameter was 2 mm, the inner diameter was 0.5 mm, and the length was 400 mm. The position of the output end of the capillary tube was fixed at axis at 30 cm from the active discharge which corresponded to the decay time of 25 ms in this experiment. The liquid mercury was placed in a vessel at the entrance to the capillary and it was flowed by auxiliary nitrogen flow. The nitrogen of 99.999% purity with flow (again controlled by the Bronkhorst mass flow controller) up to 20 sccm was used for this titration flow. The mercury concentration in capillary tube flow was measured by Advanced Mercury Analyzer AMA 254

(ALTEC). The bulk flow velocity v_g of nitrogen in the tube was calculated from the continuity equation and the state equation. The calculated velocity v_g was 12 m s^{-1} . The flow analysis was performed in the same way as in previous studies using flowing afterglow.^{17,18} The distance d needed to develop a full parabolic velocity profile is given by $d = 0.277aR$, where a is the flow tube radius (0.6 cm) in cm and R is the Reynolds number. For our experimental conditions, the Reynolds number R is equal to 184, which gives $d = 31 \text{ cm}$. Furthermore, our experimental setup introduced perturbations into the flow pattern at the side arms and at the nitrogen inlet. So, the flow will be in transition between plug and parabolic flows and in this case the bulk flow velocity can be used for the calculation of the decay time. This approach was found to be correct in previous studies.^{16,17} In present experiment, the line intensities (which are proportional to the excited particle concentrations) were measured across the diameter of the flow tube. Bolden *et al.*¹⁹ have experimentally demonstrated that this is equivalent to monitoring the concentration at the center of the tube for fully developed parabolic flow conditions.

The optical spectra were measured by Jobin Yvon monochromator TRIAX 550 with CCD detector. The 300 gr/mm grating was used for overview spectra in the range from 300 nm to 600 nm. The emitted light was led to the entrance slit of the monochromator by the multimode quartz optical fiber movable along the discharge tube.

III. KINETIC MODEL

A kinetic model for the late nitrogen afterglow was developed. The following particles were considered in the kinetic model – electrons, N_2^+ , N_3^+ , and N_4^+ ions, electronically excited states of molecular nitrogen $N_2(A^3\Sigma_u^+)$, $N_2(B^3\Pi_g)$, and $N_2(C^3\Pi_u)$, nitrogen atoms N and electronically excited states of mercury atoms $Hg(6^3P_0)$ and $Hg(6^3P_1)$. The concentration of molecular nitrogen in ground state $N_2(X^1\Sigma_g^+)$ was calculated from the equation of state for ideal gas for $T = 300 \text{ K}$. The concentration of molecular nitrogen in ground state and the concentration of mercury in ground state $Hg(6^1S_0)$ were considered to be constant. Twenty-three reactions concerning these particles were included in the kinetic model, see Table I. The rate coefficients for these reactions were taken from recent papers.^{10,13,20} The rate coefficients for N_2^+ , N_3^+ , and N_4^+ ions recombination with electrons (reactions R12, R22, and

TABLE I. Reactions and their rate coefficients considered in the model. The values of rate coefficients are for $T = 300$ K, also the electron temperature for reaction R12, R22, and R23 is $T_e = 300$ K. The units are s^{-1} , $\text{cm}^3 \text{s}^{-1}$, and $\text{cm}^6 \text{s}^{-1}$ for reactions of first, second, and third order, respectively.

No.	Reaction	Rate coefficient	Ref.
R1	$\text{N}_2(\text{A}) + \text{N}_2(\text{A}) \rightarrow \text{N}_2(\text{X}) + \text{N}_2(\text{B})$	7.7×10^{-11}	20
R2	$\text{N}_2(\text{A}) + \text{N}_2(\text{A}) \rightarrow \text{N}_2(\text{X}) + \text{N}_2(\text{C})$	1.5×10^{-10}	20
R3	$\text{N}_2(\text{A}) + \text{N}_2(\text{A}) \rightarrow \text{N}_2(\text{X}) + \text{N} + \text{N}$	3×10^{-11}	20
R4	$\text{N}_2(\text{A}) + \text{N}_2 \rightarrow \text{N}_2 + \text{N}_2(\text{X})$	3×10^{-16}	20
R5	$\text{N}_2(\text{A}) + \text{N} \rightarrow \text{N}_2(\text{X}) + \text{N}$	4.2×10^{-11}	20
R6	$\text{N}_2(\text{B}) + \text{N}_2 \rightarrow \text{N}_2 + \text{N}_2(\text{A})$	2.85×10^{-11}	20
R7	$\text{N}_2(\text{B}) + \text{N}_2 \rightarrow \text{N}_2 + \text{N}_2(\text{X})$	1.5×10^{-12}	20
R8	$\text{N}_2(\text{B}) \rightarrow \text{N}_2(\text{A}) + h\nu$	2.4×10^5	20
R9	$\text{N} + \text{N} + \text{N}_2 \rightarrow \text{N}_2(\text{B}) + \text{N}_2$	4.4×10^{-33}	20
R10	$\text{N} + \text{wall} \rightarrow \frac{1}{2} \text{N}_2(\text{X})$	$\gamma = 1.35 \times 10^{-6}$	see text
R11	$\text{N}_2(\text{C}) \rightarrow \text{N}_2(\text{B}) + h\nu$	2.74×10^7	20
R12	$\text{N}_2^+ + \text{e} \rightarrow \text{N}_2(\text{C}) + \text{N}_2(\text{X})$	2.3×10^{-6}	20
R13	$\text{N}_2(\text{A}) + \text{Hg}(6^1\text{S}_0) \rightarrow \text{N}_2(\text{X}) + \text{Hg}(6^3\text{P}_1)$	2.3×10^{-10}	10
R14	$\text{N}_2(\text{A}) + \text{Hg}(6^1\text{S}_0) \rightarrow \text{N}_2(\text{X}) + \text{Hg}(6^3\text{P}_0)$	6×10^{-11}	10
R15	$\text{Hg}(6^3\text{P}_0) + \text{N}_2 \rightarrow \text{N}_2 + \text{Hg}(6^3\text{P}_1)$	3×10^{-11}	13
R16	$\text{Hg}(6^3\text{P}_1) + \text{N}_2 \rightarrow \text{N}_2 + \text{Hg}(6^3\text{P}_0)$	3.5×10^{-12}	13
R17	$\text{Hg}(6^3\text{P}_1) \rightarrow \text{Hg}(6^1\text{S}_0) + h\nu$	8×10^6	13
R18	$\text{N}_2^+ + \text{N}_2 + \text{N}_2 \rightarrow \text{N}_4^+ + \text{N}_2$	5.2×10^{-29}	20
R19	$\text{N}_2^+ + \text{N} + \text{N}_2 \rightarrow \text{N}_3^+ + \text{N}_2$	3.4×10^{-29}	20
R20	$\text{N}_3^+ + \text{N} \rightarrow \text{N}_2^+ + \text{N}_2$	6.6×10^{-11}	20
R21	$\text{N}_4^+ + \text{N} \rightarrow \text{N}_3^+ + \text{N}_2$	1.0×10^{-9}	20
R22	$\text{N}_2^+ + \text{e} \rightarrow \text{N} + \text{N}$	1.8×10^{-7}	20
R23	$\text{N}_3^+ + \text{e} \rightarrow \text{N} + \text{N}_2$	2.0×10^{-7}	20

R23) depend on electron temperature.²⁰ At our experimental conditions, the electrons are thermalized due to collisions with nitrogen molecules. The time needed for the electron temperature decrease within 10% of neutral gas temperature was estimated using the data published by Trunec *et al.*²¹ Although these data were calculated for argon, they provide an upper estimate for molecular nitrogen. This is because the mass of molecular nitrogen is lower than the mass of argon atom, and the electrons besides energy loss at elastic collisions lose their energy at inelastic collisions with molecular nitrogen at low electron energies around 0.1 eV. This calculated time for argon and for the estimated initial electron energy of 4 eV was 1.2 ms, which corresponds to the distance of 1.4 cm in the flow tube and this time and distance is even lower for nitrogen. So the electron temperature was equal to neutral gas temperature (300 K) in our experiment and this electron temperature was also used in the kinetic model. The diffusion losses of all considered species are also negligible at the nitrogen pressure used in the experiment. The reaction R10 was considered as a first order reaction with rate coefficient k_w ²²

$$k_w = \gamma \frac{v_a S}{4V}, \quad (2)$$

where γ is the wall recombination probability, v_a is the mean velocity of N atoms, $v_a = \sqrt{8k_b T / \pi m}$, S and V are the inner surface and volume of the flow tube, respectively. S/V is equal to $2/r$ in our case (r is the inner radius of the flow tube). This relation was derived by Chantrý²² and it was used in recent studies of nitrogen discharges and afterglows.^{23–25}

The value of γ depends on many wall parameters, e.g., the type of material, cleanliness, morphology, temperature, and surface coverage. In the literature, it can be found numerous works dealing with the determination of the wall recombination probabilities of N atoms. However, there is quite a large discrepancy (of several orders of magnitude) between the results obtained by different authors, which could stem from different reasons.²³ So in this study γ was considered as a free parameter, the value of which was varied in order to obtain the best fit to the measured data.

The resulting system of differential equations was solved numerically. A Fortran program, which used the RADAU5 procedure²⁶ for the intrinsic integration of the differential equation system, was written for this purpose. So only the inputs and outputs for the RADAU5 procedure and the right hand side of differential equation system had to be programmed.

IV. RESULTS AND DISCUSSION

A. Experimental results

The optical emission spectra were measured in the active discharge and in the afterglow. The first positive $\text{N}_2(\text{B } ^3\Pi_g \rightarrow \text{A } ^3\Sigma_u^+)$, the second positive $\text{N}_2(\text{C } ^3\Pi_u \rightarrow \text{B } ^3\Pi_g)$, and the first negative $\text{N}_2^+(\text{B } ^2\Sigma_u^+ \rightarrow \text{X } ^2\Sigma_g^+)$ nitrogen spectral systems were recorded in all spectra. If the mercury vapor was added to the afterglow using auxiliary nitrogen flow through the capillary tube, mercury spectral line at 254 nm was observed in the spectrum of the second order at the wavelength of 508 nm. If the auxiliary nitrogen flow above liquid mercury was switched off, the mercury line disappeared in few seconds. No other atomic or molecular emissions were observed. As described in Sec. II, the Hg resonance line intensity was measured as a function of position along the flow tube. This line was identified a few millimeters before the titration point. An example of the typical recorded post-discharge spectrum after mercury vapor addition is shown in Figure 2. As it can be seen from this figure, the first positive system is the most intensive, the intensities of the second positive and the first negative systems are four times lower. The dependence of Hg resonance line intensity on the distance from active discharge is shown in Figure 3 for two different Hg vapor concentrations. This dependence can be divided into two parts. The first part represents a rapid increase of Hg line intensity to the maximum value due to the mixing of Hg vapor with flowing nitrogen. After that the reactions R13 and R17 prevail and the decrease of intensity can be observed in the second part. The intensity of Hg line is linearly dependent on Hg vapor concentration, the small deviations from this can be attributed to the difficulty to obtaining saturated Hg vapor in nitrogen flow through the capillary. Also, as it can be seen from Figure 3, the slope of Hg line intensity decrease almost does not depend on Hg vapor concentration. The mercury concentrations in the afterglow were determined as follows. The mercury concentration in the capillary flow was measured by Advanced Mercury Analyzer AMA 254. The obtained concentration was $1.7 \times 10^{13} \text{ cm}^{-3}$ and this value does not change with the flow rate above mercury surface. The mercury concentration in the

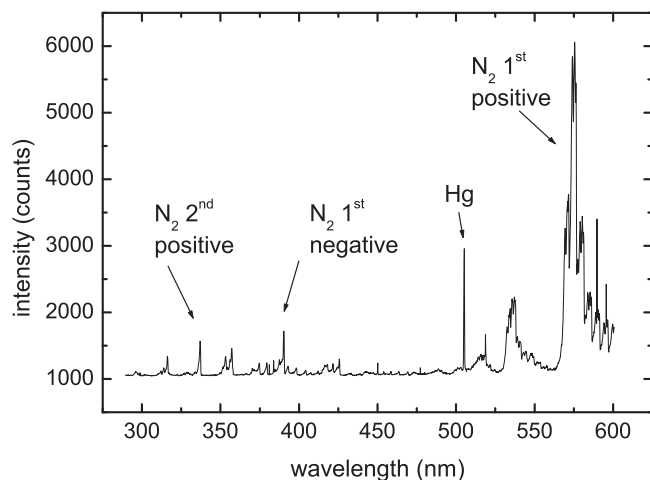


FIG. 2. Overview spectrum of nitrogen post-discharge with mercury vapor addition at the distance of 32 cm.

flow tube was then obtained by multiplication of this value $1.7 \times 10^{13} \text{ cm}^{-3}$ by the ratio of flow rates in the capillary and in the flow tube.

In the last experiment, the mercury vapor was added in the nitrogen flow before the active discharge and the optical spectra were measured directly from the active discharge through the region of pink afterglow. The significant increase of Hg resonant line intensity was observed in the pink afterglow region, the spatial dependence of Hg line intensity is identical with the spatial dependence of the first negative system intensity, see Figure 4. In this figure, the Hg line intensities were multiplied by a constant, so that the Hg line intensity and the first negative system intensity can have the same value at the maximum in the pink afterglow region. Because the Hg resonant line acts an indicator of $\text{N}_2(\text{A})$ state due to the fast excitation energy transfer reaction R13, this result also shows the spatial dependence of the relative concentration of $\text{N}_2(\text{A})$. This spatial dependence is therefore the same as spatial dependence of $\text{N}_2^+(\text{B } ^2\Sigma_u^+)$ concentration. The $\text{N}_2^+(\text{B } ^2\Sigma_u^+)$ state is produced in the collisions of molecular

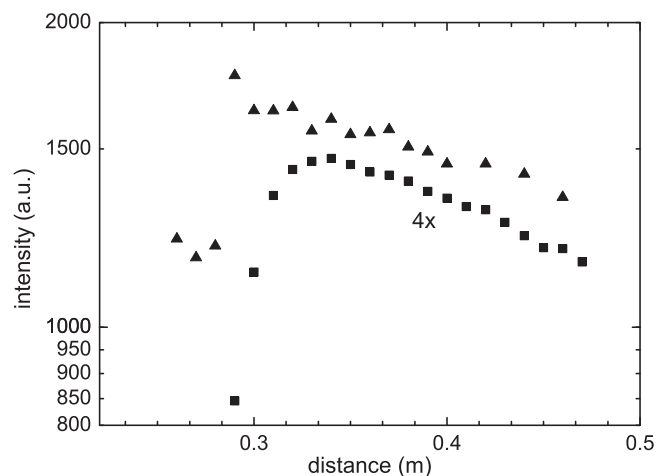


FIG. 3. The dependence of Hg resonance line (253.7 nm) intensity on distance from active discharge. Hg vapor concentration: triangles – $4.1 \times 10^{11} \text{ cm}^{-3}$, squares – $1.1 \times 10^{11} \text{ cm}^{-3}$.

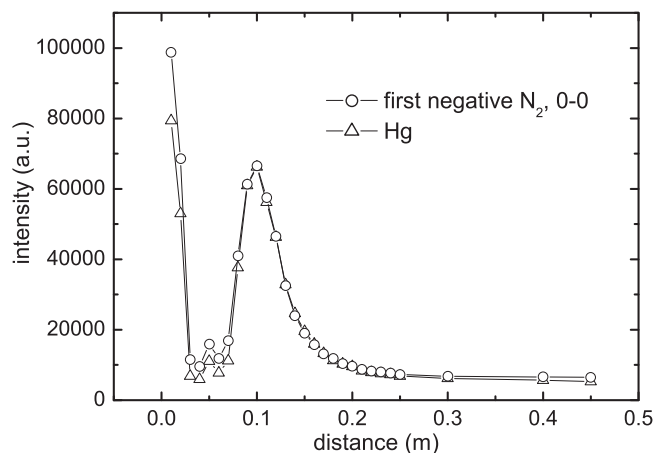


FIG. 4. The dependence of Hg resonance line (253.7 nm) and first negative N_2 , 0-0 intensities on the distance from the active discharge in the region of pink afterglow.

nitrogen ion in ground state $\text{N}_2^+(\text{X } ^2\Sigma_g^+)$ with vibrationally excited ground state of nitrogen $\text{N}_2(\text{X } ^1\Sigma_g^+, v > 11)$.²⁰

B. Results from kinetic model

The experimental data can be explained by the results of the kinetic model described in Sec. III. The calculation started at the time $t = 0$ which corresponds to the time of mercury vapor injection to the afterglow. The initial concentrations of electrons n_{e0} and N_2^+ ions n_{i0} , $n_{i0} = n_{e0} = 10^{14} \text{ cm}^{-3}$, the initial concentration of $\text{N}_2(\text{A})$ metastables $n_{A0} = 10^{11} \text{ cm}^{-3}$, and the initial concentration of N atoms $n_{N0} = 1.37 \times 10^{15} \text{ cm}^{-3}$ were taken as the initial values for kinetic equations. These initial values were taken from the theoretical model²⁰ and the initial concentration of N atoms was adjusted so that the N atom concentrations in later afterglow fit the values of N atom concentrations taken from previous measurement²⁷ of their concentration by the NO titration method.²⁸ The mercury vapor concentration was set to $4.1 \times 10^{11} \text{ cm}^{-3}$, which correspond to the mercury concentration used in the experiment. The results of the kinetic model are shown in Figure 5. During the first $10 \mu\text{s}$ the ion-molecular reactions R18 and R19 take place, converting N_2^+ ions to N_3^+ and N_4^+ ions. After $t = 10 \mu\text{s}$ the N_3^+ ions prevail over N_4^+ and N_2^+ ions, the ratios of concentrations $[\text{N}_2^+] : [\text{N}_3^+] : [\text{N}_4^+]$ are 1 : 31 : 2 (at $t = 1 \text{ ms}$). These ratios remain constant until $t = 10 \text{ ms}$. This can be interpreted as a consequence of the equilibrium achieved by ionic mixing reactions R18–R21. The dominance of N_3^+ ions is in agreement with results of previous study.²⁰ During the first 100 ns the recombination of electrons and N_4^+ ions also takes place, producing $\text{N}_2(\text{C})$ state. The $\text{N}_2(\text{C})$ state is also produced at the collision of two $\text{N}_2(\text{A})$ metastables (reaction R2). The $\text{N}_2(\text{C})$ state after the photon emission turns to the $\text{N}_2(\text{B})$ state. The $\text{N}_2(\text{B})$ state then after the photon emission or quenching changes to $\text{N}_2(\text{A})$ state. So, the sequential concentration increase of these states can be observed, see Figure 5. After $t = 2 \times 10^{-7} \text{ s}$ the electron and N_4^+ ion concentrations decrease and the loss processes of $\text{N}_2(\text{C})$ and $\text{N}_2(\text{B})$ states prevail and the concentrations of

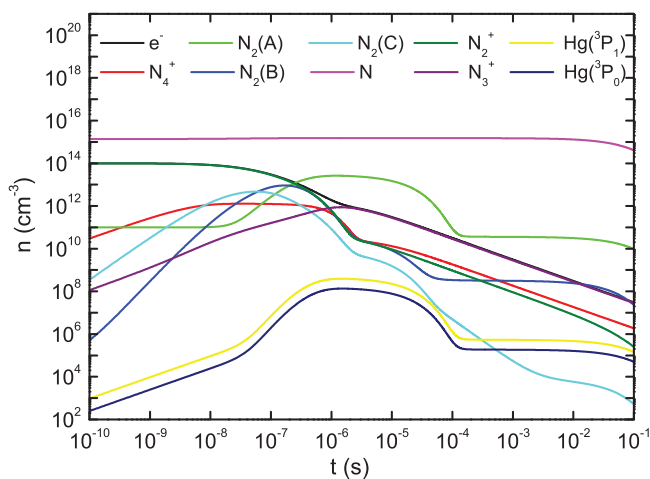


FIG. 5. The calculated time dependence of particle concentrations in the afterglow.

these states start to decrease. The fast dissociative recombination reactions of N_2^+ and N_3^+ ions with electrons (reactions R22 and R23) produce N atoms, which leads to increase of N atom concentration up to $1.5 \times 10^{15} \text{ cm}^{-3}$ at $t = 2 \times 10^{-7} \text{ s}$. After this time the concentrations of N_2^+ and N_3^+ ions decrease to low values so that the production of N atoms from these dissociative recombination reactions is negligible. The initial N atom concentration increase due to nitrogen ions recombination can be seen clearly in Figure 10.

After $t = 10^{-4} \text{ s}$ the reactions connected with N atoms prevails. The N atoms are the most important among all the long lived particles due to their high concentration and low losses. The reactions starting with N atom volume recombination produce other excited states of molecular nitrogen existing in the afterglow, they do not produce electrons and nitrogen ions. The dissociative recombination of N_2^+ and N_3^+ ions increases the N atom concentration only up to $t = 2 \times 10^{-7} \text{ s}$. The contribution from the initial concentrations of $N_2(A)$ molecules is not significant and their initial concentration can be set to zero without any changes in the resulting particle concentrations in later afterglow times. This can be seen in Figure 6, where the results of the calculation with only N atom nonzero initial concentration is shown. The initial concentration of N atoms was set to $1.5 \times 10^{15} \text{ cm}^{-3}$, which corresponds to N concentration after its increase due to dissociative recombination of nitrogen ions. The concentrations of all particles (except electrons and nitrogen ions, which are not present in this case) reach the same value at times longer than 0.2 ms as in the previous case with non-zero initial concentrations of electrons, N_2^+ ions, and $N_2(A)$ metastables. The concentration of N atoms decreases due to volume and surface recombination. The volume recombination produces $N_2(B)$ molecules. The quenching of $N_2(B)$ molecules by nitrogen molecules is then the main source of $N_2(A)$ molecules. The main loss of $N_2(A)$ molecules is their quenching by N atoms, the quenching of $N_2(A)$ molecules by Hg atoms is not important due to low Hg concentration. So it follows from the model that the concentration of $Hg(6^3P_1)$ state (and also the intensity of mercury lines at 253.7 nm) is proportional to

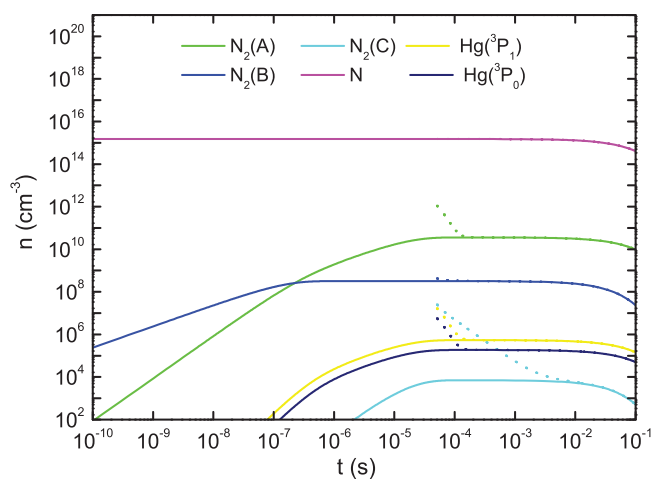


FIG. 6. The calculated time dependence of particle concentrations in the afterglow. Initial concentration of N atoms $n_{N0} = 1.5 \times 10^{15} \text{ cm}^{-3}$, other initial particle concentrations are equal to zero. The dotted lines show the time dependence of particle concentration from Figure 5.

the product of concentrations $[N][Hg][N_2]$, as it was observed in experiments.¹⁰ This is shown in Figure 7. The curves in Figure 7 were always calculated successively for initial concentrations of Hg, N, and N_2 2× and 4× higher and 2× and 4× lower than the initial concentrations given at the beginning of this section. The dependence of $Hg(6^3P_1)$ concentration on $Hg(6^1S_0)$ concentration is perfectly linear, the linearity gets worsens at higher initial Hg concentrations (not shown here). The dependence of $Hg(6^3P_1)$ concentration on N and N_2 concentrations is not so perfectly linear, the deviations are higher at higher concentrations of N and N_2 .

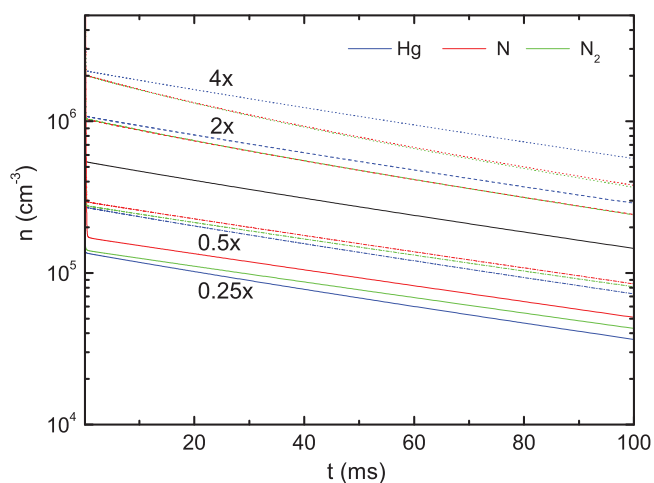


FIG. 7. The calculated time dependence of $Hg(6^3P_1)$ concentration for different initial concentrations of Hg, N, and N_2 . Full black line – result of calculation for initial values given at the beginning of this section – $n_{Hg} = 4.1 \times 10^{11} \text{ cm}^{-3}$, $n_{N0} = 1.37 \times 10^{15} \text{ cm}^{-3}$, $n_{N_2} = 2.41 \times 10^{17} \text{ cm}^{-3}$ (neutral nitrogen pressure 1000 Pa). Blue lines – calculation with different Hg initial concentrations; red lines – calculation with different N atom initial concentrations; green lines – calculation with different initial $N_2(X)$ concentrations; dotted lines – 4× higher initial concentrations; dashed lines – 2× higher initial concentrations; dotted-dashed lines – 2× lower initial concentrations; full lines – 4× lower initial concentrations.

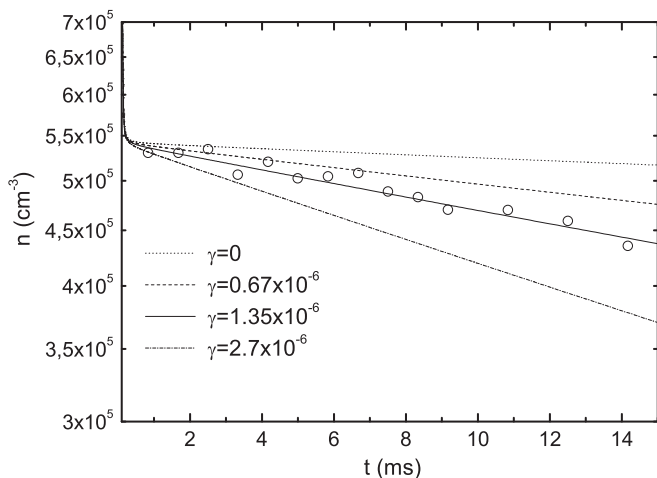


FIG. 8. The time dependence of $\text{Hg}(6\ ^3\text{P}_1)$ state concentration for different γ values. Lines – results of calculation; open circles – measured intensities of Hg line.

C. Comparison of theoretical and experimental results

As it was written in Sec. III, the wall recombination probability γ was considered as a free parameter in the kinetic model. The influence of γ value on the time dependence of $\text{Hg}(6\ ^3\text{P}_1)$ state concentration is shown in Figure 8. It can be seen from this figure that the time dependence of $\text{Hg}(6\ ^3\text{P}_1)$ state concentration calculated for $\gamma = 0$ exhibits a very slow decrease which is not in accordance with the experimental results. So the recombination of N atoms at the flow tube wall (reaction R10) has to be included in the kinetic model. The least squares method was used to fit the calculated results to experimental data. The value $\gamma = (1.35 \pm 0.04) \times 10^{-6}$ was obtained from this method. The influence of γ value is also shown in Figure 8 for γ values two times higher and lower than the value obtained from the best fit. The value of 1.35×10^{-6} obtained for γ is one order smaller than the values of γ for quartz obtained by Rouffet *et al.*²⁴ However, Guerra *et al.*²⁹ used for modelling of low-pressure nitrogen afterglow the value $\gamma = 3 \times 10^{-6}$, which is only $2.2 \times$ higher than our γ value. The calculated time dependence of the $\text{N}_2(\text{B})$ state concentration and its comparison with the experimental results is shown in Figure 9. A good agreement of calculated and experimental results, which also confirm the used γ value, can be seen. Further comparison of the calculated and experimental data can be seen in Figure 10, where the calculated time dependence of N atom concentration is compared with the N atom concentration measured by NO titration from previous study²⁷ of nitrogen afterglow. Again, good agreement between the calculated and the experimental data was obtained. Without the surface recombination of N atoms, the decrease of N atom concentration with time is too slow, which shows the necessity of including of the reaction R10 in the kinetic model and confirms the value of γ used.

D. Sensitivity analysis

Sensitivity analysis^{30–32} was applied for the analysis of kinetic model. Normalized local concentration sensitivity

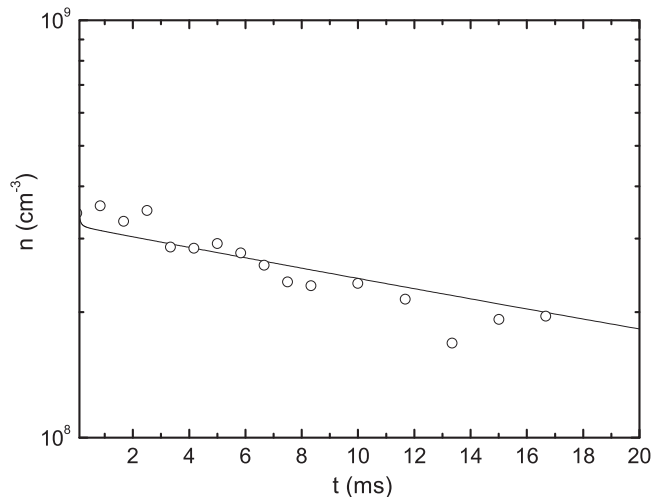


FIG. 9. The time dependence of $\text{N}_2(\text{B})$ state concentration. Full line – result of calculation; open circles – experimentally measured intensities of first positive system (0–0 transition).

coefficients S_{ij} were calculated according to the following equation:³¹

$$S_{ij} = \frac{k_j}{n_i} \frac{\partial n_i}{\partial k_j}, \quad (3)$$

where n_i is the concentration of i th particle kind and k_j is the rate coefficient for j th reaction (see Table I). The coefficients S_{ij} were calculated numerically using the finite difference approximation. The central difference with the step Δk_j was used for this calculation. The step Δk_j has been decreasing until the estimated error of sensitivity coefficients was below 1%. This method is also called indirect method (or brute force method).³⁰ The calculated sensitivity coefficients are shown in Tables II and III. The sensitivity coefficients show that N atom concentration decreases mainly due to wall and volume recombination (reactions R9 and R10), the wall recombination being more important. At higher nitrogen ion concentrations, the N atom concentration decreases due to reaction with nitrogen ions (reactions R20 and R21) and increases due to dissociative recombination reactions R22 and

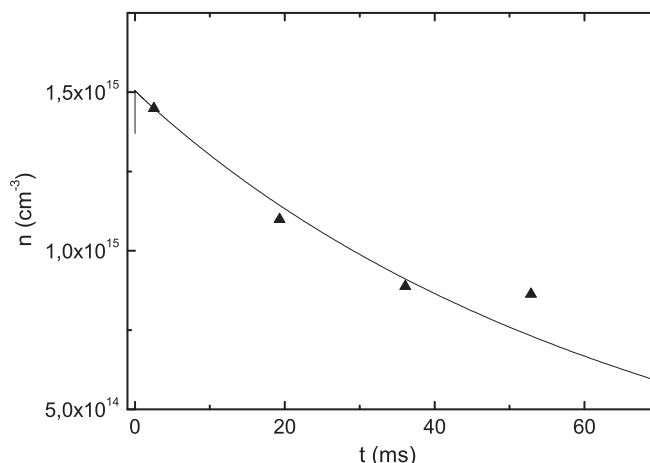


FIG. 10. The time dependence of N atom concentration. Full line – result of calculation; triangles – N atom concentrations measured by NO titration.

TABLE II. Normalized sensitivity coefficients S_{ij} .

j^i	e	N_4^+	$N_2(A)$	$N_2(B)$	$N_2(C)$
	1	2	3	4	5
1	-8.3×10^{-9}	-2.8×10^{-8}	-5.0×10^{-5}	3.3×10^{-5}	-9.8×10^{-5}
2	4.2×10^{-7}	-4.9×10^{-7}	-9.7×10^{-5}	6.3×10^{-5}	9.9×10^{-1}
3	2.2×10^{-6}	-5.5×10^{-7}	1.6×10^{-4}	3.9×10^{-4}	3.2×10^{-4}
4	-3.2×10^{-7}	3.2×10^{-7}	-4.2×10^{-3}	-1.5×10^{-6}	-8.3×10^{-3}
5	-1.1×10^{-6}	-4.4×10^{-7}	-1.0	-6.3×10^{-4}	-2.0
6	-1.0×10^{-6}	1.2×10^{-6}	4.7×10^{-2}	-9.3×10^{-1}	9.4×10^{-2}
7	-1.1×10^{-6}	9.3×10^{-7}	-4.8×10^{-2}	-4.8×10^{-2}	-9.6×10^{-2}
8	9.6×10^{-7}	-9.6×10^{-7}	1.6×10^{-3}	-3.2×10^{-2}	3.2×10^{-3}
9	-6.7×10^{-4}	7.8×10^{-4}	8.4×10^{-1}	6.8×10^{-1}	1.7
10	-3.5×10^{-3}	6.2×10^{-3}	-1.1	-2.1	-2.1
11	-3.6×10^{-7}	3.6×10^{-7}	1.1×10^{-7}	2.2×10^{-7}	-1.0
12	-4.3×10^{-1}	-4.3×10^{-1}	4.3×10^{-4}	8.4×10^{-4}	2.2×10^{-3}
13	4.4×10^{-7}	-4.5×10^{-7}	-5.5×10^{-3}	-1.9×10^{-6}	-1.1×10^{-2}
14	6.4×10^{-7}	-6.4×10^{-7}	-1.4×10^{-3}	-5.0×10^{-7}	-2.9×10^{-3}
15	1.2×10^{-7}	-1.2×10^{-7}	4.0×10^{-11}	8.0×10^{-11}	8.0×10^{-11}
16	-5.3×10^{-7}	5.3×10^{-7}	-1.8×10^{-10}	-3.7×10^{-10}	-3.7×10^{-10}
17	-1.2×10^{-6}	1.2×10^{-6}	-4.2×10^{-10}	-8.4×10^{-10}	-8.4×10^{-10}
18	-8.5×10^{-3}	1.1×10^{-3}	-2.0×10^{-2}	-3.9×10^{-2}	-3.9×10^{-2}
19	7.9×10^{-4}	-2.3×10^{-4}	-7.0×10^{-5}	-1.4×10^{-4}	-1.3×10^{-4}
20	-3.6×10^{-1}	5.7×10^{-1}	-2.2×10^{-3}	-4.4×10^{-3}	-2.4×10^{-3}
21	3.7×10^{-1}	-5.8×10^{-1}	-1.3×10^{-3}	-2.6×10^{-3}	-4.5×10^{-3}
22	-8.9×10^{-3}	-9.0×10^{-3}	2.1×10^{-2}	4.1×10^{-2}	4.1×10^{-2}
23	-5.7×10^{-1}	-5.7×10^{-1}	1.9×10^{-3}	3.8×10^{-3}	-6.8×10^{-3}

R23. However, sufficiently high nitrogen ion concentrations are only at the beginning of afterglow up to $t = 2 \times 10^{-7}$ s, after this time reactions R20–R23 are not significant. The $N_2(A)$ metastables are mainly produced at the quenching of

$N_2(B)$ state by N_2 and destroyed by the quenching by N atoms (reactions R6 and R5). Their concentration is also sensitive to the rate coefficients of reactions which involves the precursors of $N_2(A)$, namely, $N_2(B)$ states and N atoms. This

TABLE III. Normalized sensitivity coefficients S_{ij} . Continuation of Table II.

j^i	N	$Hg(^3P_1)$	$Hg(^3P_0)$	N_2^+	N_3^+
	6	7	8	9	10
1	-4.3×10^{-6}	-5.0×10^{-5}	-5.0×10^{-5}	-4.3×10^{-6}	-3.2×10^{-8}
2	-8.4×10^{-6}	-9.7×10^{-5}	-9.7×10^{-5}	-8.8×10^{-6}	-5.0×10^{-7}
3	2.0×10^{-4}	1.6×10^{-4}	1.6×10^{-4}	1.9×10^{-4}	-3.7×10^{-7}
4	-2.2×10^{-7}	-4.2×10^{-3}	-4.2×10^{-3}	9.5×10^{-8}	3.2×10^{-7}
5	-1.9×10^{-4}	-1.0	-1.0	-1.9×10^{-4}	-6.3×10^{-7}
6	1.9×10^{-5}	4.7×10^{-2}	4.7×10^{-2}	2.1×10^{-5}	1.2×10^{-6}
7	-1.9×10^{-5}	-4.8×10^{-2}	-4.8×10^{-2}	-1.8×10^{-5}	9.2×10^{-7}
8	6.7×10^{-7}	1.6×10^{-3}	1.6×10^{-3}	-2.8×10^{-7}	-9.6×10^{-7}
9	-1.6×10^{-1}	8.4×10^{-1}	8.4×10^{-1}	-1.6×10^{-1}	6.3×10^{-4}
10	-1.1	-1.1	-1.1	-1.1	5.2×10^{-3}
11	1.1×10^{-7}	1.1×10^{-7}	1.1×10^{-7}	4.7×10^{-7}	3.6×10^{-7}
12	4.2×10^{-4}	4.3×10^{-4}	4.3×10^{-4}	-4.3×10^{-1}	-4.3×10^{-1}
13	-2.9×10^{-7}	7.9×10^{-1}	2.6×10^{-1}	-7.4×10^{-7}	-4.5×10^{-7}
14	-7.6×10^{-8}	2.1×10^{-1}	7.3×10^{-1}	-7.2×10^{-7}	-6.4×10^{-7}
15	4.0×10^{-11}	-5.4×10^{-7}	-1.0	-1.2×10^{-7}	-1.2×10^{-7}
16	-1.8×10^{-10}	1.8×10^{-7}	3.4×10^{-1}	5.3×10^{-7}	5.3×10^{-7}
17	-4.2×10^{-10}	-1.0	-3.4×10^{-1}	1.2×10^{-6}	1.2×10^{-6}
18	-1.9×10^{-2}	-2.0×10^{-2}	-2.0×10^{-2}	-1.0	-4.0×10^{-5}
19	-6.9×10^{-5}	-7.0×10^{-5}	-7.0×10^{-5}	-3.0×10^{-4}	8.7×10^{-4}
20	-2.2×10^{-3}	-2.2×10^{-3}	-2.2×10^{-3}	5.7×10^{-1}	-4.3×10^{-1}
21	-1.3×10^{-3}	-1.3×10^{-3}	-1.3×10^{-3}	4.3×10^{-1}	4.3×10^{-1}
22	2.0×10^{-2}	2.1×10^{-2}	2.1×10^{-2}	1.1×10^{-2}	-9.0×10^{-3}
23	1.9×10^{-3}	1.9×10^{-3}	1.9×10^{-3}	-5.7×10^{-1}	-5.7×10^{-1}

TABLE IV. Overall sensitivity coefficients B_j .

Rj	R1	R2	R3	R4	R5	R6	R7
B_j	1.8×10^{-8}	9.8×10^{-1}	4.1×10^{-7}	1.2×10^{-4}	7.0	8.8×10^{-1}	1.8×10^{-2}
Rj	R8	R9	R10	R11	R12	R13	R14
B_j	1.0×10^{-3}	5.5	1.5×10	1.0	7.4×10^{-1}	6.9×10^{-1}	5.8×10^{-1}
Rj	R15	R16	R17	R18	R19	R20	R21
B_j	1.0	1.2×10^{-1}	1.1	1.0	1.6×10^{-6}	9.6×10^{-1}	8.4×10^{-1}
Rj	R22	R23					
B_j	5.4×10^{-3}	1.3					

confirms the conclusions about main reaction mechanism from Subsection IV B.

The sensitivity coefficients for N atom concentrations and reactions R13 and R14 are very small. Reactions R13 and R14 are only two reactions, where mercury atoms in ground state are involved, therefore at concentrations used in the experiment the mercury atoms have no influence on N atom concentration (this was also proved by the direct solution of kinetic equation with zero mercury concentration).

Furthermore, the overall sensitivities B_j were calculated according to the equation³¹

$$B_j = \sum_i \left(\frac{k_j}{n_i} \frac{\partial n_i}{\partial k_j} \right)^2. \quad (4)$$

The calculated overall sensitivities are shown in Table IV. The values of overall sensitivities again show that the most important reactions are reactions R10 (wall recombination of N atoms), R5 (quenching of $N_2(A)$ metastable by nitrogen atom), and R9 (volume recombination of N atoms). On the other hand, the reactions R1, R3, and R4 have the lowest overall sensitivities, so these reactions could be removed from the reaction set.

V. CONCLUSION

The mercury resonance line at 254 nm was observed after mercury vapor addition to nitrogen flowing plasma at the neutral gas pressure of 1000 Pa. The intensity of this mercury line was measured at different positions along the quartz flow tube (and hence at different times of afterglow). The measured spatial dependence exhibited a very slow decrease only and the decrease rate does not depend on the concentration of added mercury vapor. This behavior was explained by the kinetic model. The Hg (6^3P_1) state, which is the upper state for mercury resonance line, is produced by the excitation transfer from nitrogen metastable state $N_2(A)$. The $N_2(A)$ state is also produced by the $N_2(B)$ state quenching and the $N_2(B)$ state is produced at the N atoms recombination. This leads to the slow decay of the $N_2(A)$ state and subsequently also of the Hg (6^3P_1) state and mercury resonance line intensity. This slow decay is therefore controlled by the N atom concentration decay, which is due to the volume and surface recombination. The best fit of the calculated data to the experimental ones was obtained for the wall recombination probability $\gamma = (1.35$

$\pm 0.04) \times 10^{-6}$. The above described reaction mechanism was confirmed by sensitivity analysis.

ACKNOWLEDGMENTS

The present work was supported by the project “R&D center for low-cost plasma and nanotechnology surface modifications” (CZ.1.05/2.1.00/03.0086) funding by the European Regional Development Fund and by the Czech Science Foundation, Contract No. 13-24635S. The authors wish to thank Mr. K. Štefka for his technical assistance in conducting the experiments.

- S. Bockel, T. Belmonte, H. Michel, and D. Ablitzer, *Surf. Coat. Technol.* **97**, 618 (1997).
- I. Junkar, A. Vesel, U. Cvelbar, M. Mozetic, and S. Strnad, *Vacuum* **84**, 83 (2009).
- M. K. Boudam, B. Saoudi, M. Moisan, and A. Ricard, *J. Phys. D: Appl. Phys.* **40**, 1694 (2007).
- K. Kutasi, C. D. Pintassilgo, P. J. Coelho, and J. Loureiro, *J. Phys. D: Appl. Phys.* **39**, 3978 (2006).
- M. Ashrafi, B. S. Lanchester, D. Lummerzheim, N. Ivchenko, and O. Joki-aho, *Ann. Geophys.* **27**, 2545 (2009).
- G. Horvath, Y. Aranda-Gonzalvo, N. J. Mason, M. Zahoran, and S. Matejcik, *Eur. J. Phys. D: Appl. Phys.* **49**, 13105 (2010).
- G. Horvath, F. Krčma, L. Polachova, K. Klohnova, N. J. Mason, M. Zahoran, and S. Matejcik, *Eur. J. Phys. D: Appl. Phys.* **53**, 11001 (2011).
- E. P. Lewis, *Astrophys. J.* **12**, 8 (1900).
- W. R. Brennen and G. B. Kistiakowsky, *J. Chem. Phys.* **44**, 2695 (1966).
- A. B. Callear and P. M. Wood, *Trans. Faraday Soc.* **67**, 272 (1971).
- A. B. Callear and P. M. Wood, *Chem. Phys. Lett.* **5**, 128 (1970).
- B. A. Thrush and A. H. Wild, *J. Chem. Soc. - Faraday Trans.* **68**, 2023 (1972).
- K. S. Klopovsky, A. V. Mukhovatova, A. M. Popov, N. A. Popov, O. B. Popovicheva, and T. V. Rakhimova, *J. Phys. D: Appl. Phys.* **27**, 1399 (1994).
- H. C. Na and T. M. Niemczyk, *Anal. Chem.* **54**, 1839 (1982).
- J. E. Melzer, J. L. Jordon, and D. G. Sutton, *Anal. Chem.* **52**, 348 (1980).
- V. Mazankova, D. Trunec, and F. Krčma, *J. Chem. Phys.* **139**, 164311 (2013).
- J. H. Kolts and D. W. Setser, *J. Chem. Phys.* **68**, 4848 (1978).
- L. G. Piper, J. E. Velazco, and D. W. Setser, *J. Chem. Phys.* **59**, 3323 (1973).
- R. C. Bolden, R. S. Hemsworth, M. J. Shaw, and N. D. Twiddy, *J. Phys. B* **3**, 45 (1970).
- J. Levaton, J. Amorim, A. R. Souza, D. Franco, and A. Ricard, *J. Phys. D: Appl. Phys.* **35**, 689 (2002).
- D. Trunec, P. Spáňal, and D. Smith, *Chem. Phys. Lett.* **372**, 728 (2003).
- P. J. Chantry, *J. Appl. Phys.* **62**, 1141 (1987).
- K. Kutasi and J. Loureiro, *J. Phys. D: Appl. Phys.* **40**, 5612 (2007).
- B. Rouffet, F. Gaboriau, and J. P. Sarrette, *J. Phys. D: Appl. Phys.* **43**, 185203 (2010).
- G. Oinuma, Y. Inanaga, Y. Tanimura, M. Kuzumoto, Y. Tabata, and K. Watanabe, *J. Phys. D: Appl. Phys.* **43**, 255202 (2010).
- E. Hairer and G. Wanner, “Solving ordinary differential equations II,” *Stiff and Differential-Algebraic Problems* (Springer, 1996).

- ²⁷V. Mazankova, L. Polachova, F. Krcma, G. Horvath, and N. J. Mason, in *Proceedings of the 19th Symposium on Physics of Switching Arc, Brno, 2011*, edited by V. Aubrecht and M. Bartlova (Brno University of Technology, 2011), p. 283.
- ²⁸P. Vasina, V. Kudrle, A. Talsky, P. Botos, M. Mrazkova, and M. Mesko, *Plasma Sources Sci. Technol.* **13**, 668 (2004).
- ²⁹V. Guerra, P. A. Sa, and J. Loureiro, *Eur. Phys. J. - Appl. Phys.* **28**, 125 (2004).
- ³⁰T. Turanyi, *J. Math. Chem.* **5**, 203 (1990).
- ³¹T. Turanyi, *Reliab. Eng. Syst. Safety* **57**, 41 (1997).
- ³²A. Saltelli, M. Ratto, S. Tarantola, and F. Campolongo, *Chem. Rev.* **105**, 2811 (2005).

INFLUENCE OF OXYGEN TRACES ON RECOMBINATION PROCESSES IN NITROGEN POST-DISCHARGE

VĚRA MAZÁNKOVÁ and FRANTIŠEK KRČMA

*Institute of Physical and Applied Chemistry, Faculty of Chemistry, Brno University of Technology, Purkyňova 118, Brno 612 00, Czech Republic
mazankova@fch.vutbr.cz*

Introduction

Kinetic processes in nitrogen post-discharges have been a subject of many studies because nitrogen and nitrogen based plasmas are used in a huge number of applications like hard films deposition¹ or plasma sterilization². Besides the use of an active discharge nowadays the post-discharge is one of the most favorite research directions because it can be applied for the treatment of various temperature sensitive materials³.

The neutral nitrogen molecule can form many electronic states. Due to its symmetry, all vibrational levels of the ground state and also the first eight levels of the first electronically excited state are metastables. Besides them, there are some other strongly metastable highly excited states. All these states conserve the excitation energy for a long time. The excitation energy transfer during collisions among these species as well as atomic recombination processes lead to the formation of some radiative states and the visible light emission can be observed up to one second after switching off an active discharge depending on the experimental conditions, mainly on pressure. Kinetic modeling of pure nitrogen was given for example in *Guerra's* work⁴. It is interesting that oxygen concentration has strong influence on kinetic processes. This study extends our recent experiments by the changes in nitrogen post-discharge kinetics caused by oxygen impurity. Paper compares the influences of reactor wall material and its temperature on the post-discharge kinetics with respect to the three body recombination of nitrogen ground state atoms. This process populates mainly the $N_2(B^3\Pi_g)$ state⁵ at its vibrational levels 10–12 but all the kinetics is much more complex and thus some other observations are also briefly described in this paper.

Experimental set up

The DC flowing post-discharge was used for the experimental study. The schematic drawing of the experimental set up is given in Fig. 1. The active discharge was created in Pyrex or Quartz discharge tube with a 120 mm electrode distance at current of 200 mA and pressure of 1000 Pa. Hollow molybdenum electrodes were placed in the side arms of the main discharge tube to minimize their sputtering and also to suppress the light emitted in the electrode regions. Nitrogen was of 99.999 % purity and it was further cleaned by Oxy-clear and LN_2 traps. No oxygen or carbon traces were detectable in the pure nitrogen discharge and post-discharge

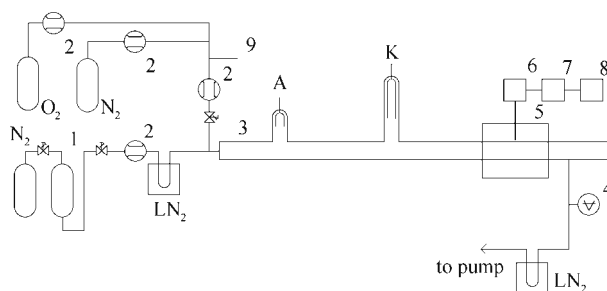


Fig. 1. **Scheme of the experimental set up.** 1 – catalyzer BASF R-3-11; 2 – mass flow controller; 3 – Pyrex discharge tube (900 mm long, inner diameter 13 mm); 4 – capacitance gauge; 5 – quartz optical fiber; 6 – monochromator Jobin Yvon Triax 550; 7 – CCD; 8 – PC; 9 – outlet of synthetic air

(concentrations under 1 ppm or 0.01 ppm, resp.⁶). The reactor system was pumped continuously by a rotary oil pump separated from the discharge tube by another LN_2 trap.

The oxygen traces were added into the main pure nitrogen flow just before the active discharge using the low range mass flow controller (MFC). To reach concentrations less than 1000 ppm synthetic air was prepared continuously using another set of MFCs. Also in this case, nitrogen of 99.999 % purity was used and the purity of oxygen was the same. Thus concentrations of other impurities, containing mainly carbon, were kept low enough to have no disturbing effect on the studied processes.

The post-discharge optical emission spectra were measured by Jobin Yvon monochromator TRIAX 550 with the 1200 grooves per mm grating coupled with CCD detector. The emitted light was lead to the entrance slit of the monochromator by the multimode quartz optical fiber movable along the discharge tube. The optical fiber holder (length of 6 cm with optical fiber mounted at its center) had to be filled by liquid nitrogen. Thus the reactor wall temperature was kept at 300 K or 77 K around (± 3 cm) the optical spectra observation point. Temperature of decaying plasma at 77 K wall temperature was calculated at about 100 K (ref.⁷) using the simulated nitrogen 1st positive ($N_2(B^3\Pi_g) \rightarrow (A^3\Sigma_u^+)$) 2–0 band spectrum. Nitrogen 1st ($N_2(B^3\Pi_g) \rightarrow (A^3\Sigma_u^+)$) and 2nd ($N_2(C^3\Pi_u) \rightarrow (B^3\Pi_g)$) positive and nitrogen 1st negative ($N_2^+(B^2\Sigma_u^+) \rightarrow (X^2\Sigma_g^+)$) systems were recorded in all spectra. The bands of NO^+ system ($NO(B^2\Pi) \rightarrow NO(A^2\Sigma^+)$) dominantly originating from vibrational level 0 were observed, too. The bands of NO^+ system dominantly originating also from vibrational level 0 were observed only in the Quartz tube. No other molecular emissions were observed. The relative vibrational populations at the selected nitrogen levels were calculated using all measurable emission band intensities. The transition probabilities and wavelengths of the transitions were taken from *Gilmore's* tables⁸.

Results and discussion

The examples of measured spectra are shown in the Figs. 1 and 2 in Pyrex and Quartz discharge tube at the decay time of 42 ms and for two wall temperatures mentioned

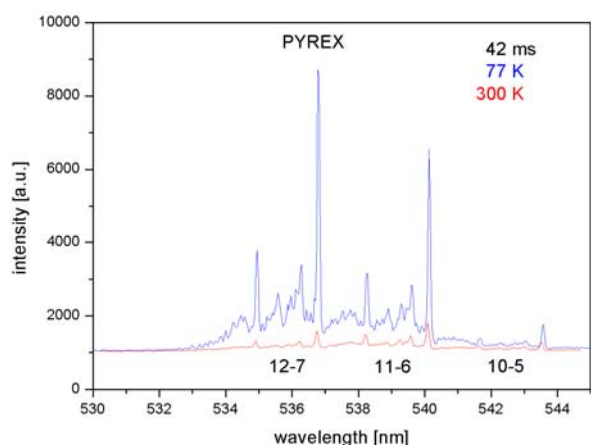


Fig. 2. Example of nitrogen recombination spectrum in Pyrex tube at decay time of 42 ms and wall temperatures of 77 K and 300 K. Concentration of oxygen traces was 1 871 ppm

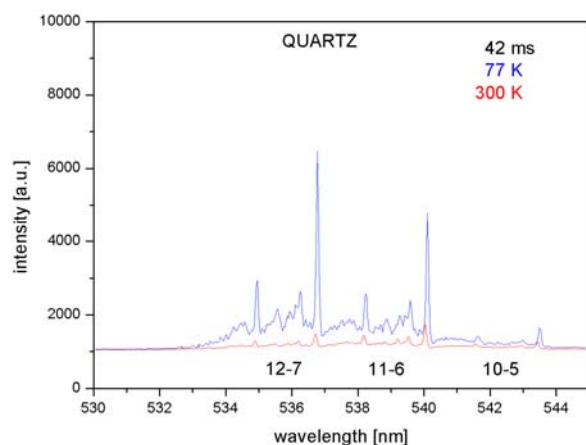


Fig. 3. Example of nitrogen recombination spectrum in Quartz tube at decay time of 42 ms and wall temperatures of 77 K and 300 K. Concentration of oxygen traces was 1 871 ppm.

above. The shown bands are dominantly populated by the three body recombination of nitrogen ground state atoms. It can be seen that at the given decay time there is no great difference between observation in Pyrex and Quartz but there is a strong effect of the wall temperature. At the lower wall temperature, the 12–7 band is much more intensive than at ambient wall temperature and its maximal intensity is even higher than the intensity of 11–6 band. The same effect was observed more times before⁹ and it reflects the recombination mechanism that was reported in *Partridge's* work⁵ and that is briefly described below.

The post-discharge in Pyrex tube is shown in Fig. 4. The relatively strong light is emitted at all oxygen concentrations. In pure nitrogen a pink afterglow effect (a part of the post-discharge where the pink light emission is dominant) is well visible and this effect is quenched by oxygen traces as it is shown in Fig. 4 and as it was reported in details recently¹⁰. The pink afterglow effect in pure nitrogen is also well observ-

able in Quartz discharge tube but the light emission outside this region is significantly lower in comparison to the post-discharge in Pyrex. The light emission in Quartz significantly increases with the increase of oxygen concentration and at oxygen concentrations higher than 1000 ppm the post-discharge in Quartz looks visually as post-discharge in Pyrex.

This visual observation is described more exactly in Figs. 5 and 6 where the relative populations of $N_2(B^3\Pi_g)$ state at levels 10–12 are shown and compared at different conditions. It can be seen from these figures that the populations at all these three levels are significantly lower in pure nitrogen in Quartz discharge tube than in Pyrex one at all post-discharge times. Oxygen added into the discharge in low concentration up to about 500 ppm enhances all the populations and the difference given by the wall material is nearly negligible at higher oxygen concentrations. This well corresponds to the direct visual observation, as it was shown before. It should be also pointed out that the oxygen increase over 500 ppm has nearly no effect on the populations at given vibrational levels.

There are two main processes populating vibrational levels of $N_2(B^3\Pi_g)$ state. Besides the ground state atoms recombination, the pooling of lower energy metastables can play a significant role in the population of the studied levels. To verify the significance of pooling contribution to the populations the ratio of band head intensities of 11–7 band and 2–0 band from the nitrogen first positive system ($N_2(B^3\Pi_g) \rightarrow (A^3\Sigma_u^+)$) was calculated. We can suppose that the $N_2(B^3\Pi_g, v=2)$ level is populated mainly by the pooling and the contribution of recombination can be neglected at this level. Thus the I_{11-7}/I_{2-0} ratio can reflect the effectiveness of the recombination process.

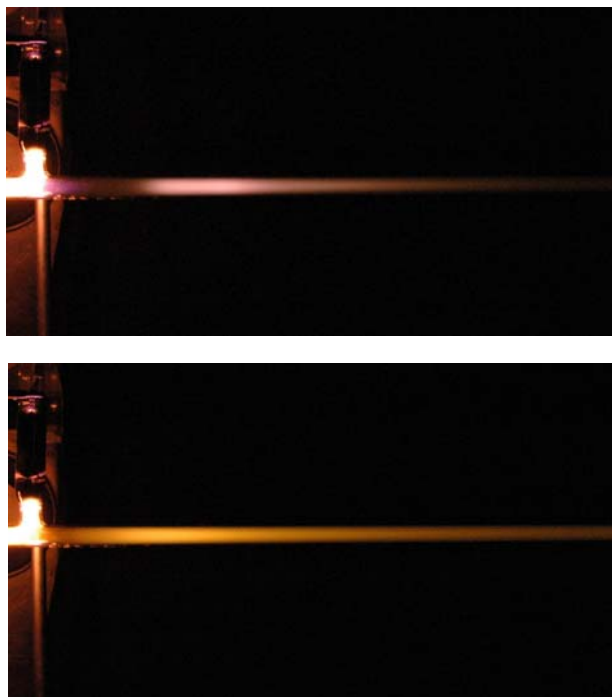


Fig. 4. Post-discharge in pure nitrogen (top) and in nitrogen containing 1 870 ppm of oxygen (bottom) in Pyrex discharge tube at the ambient wall temperature

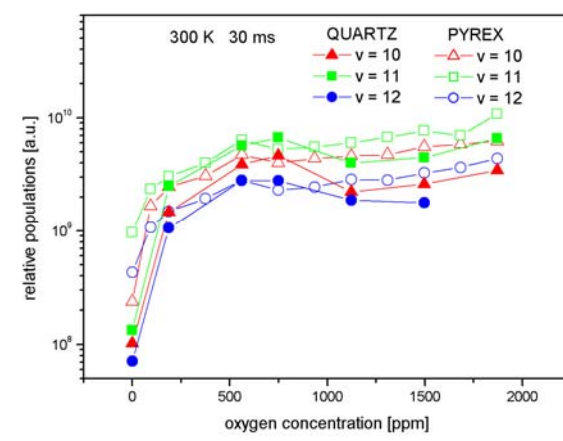
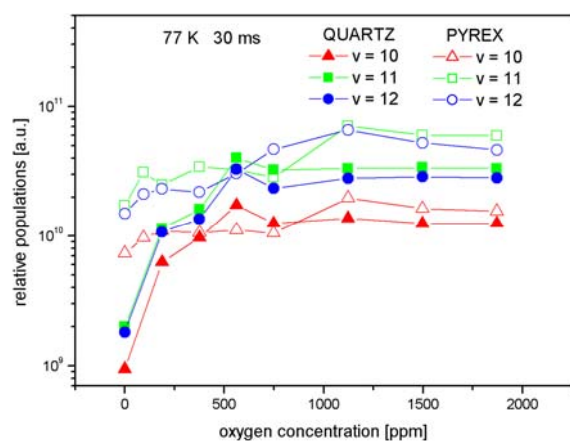
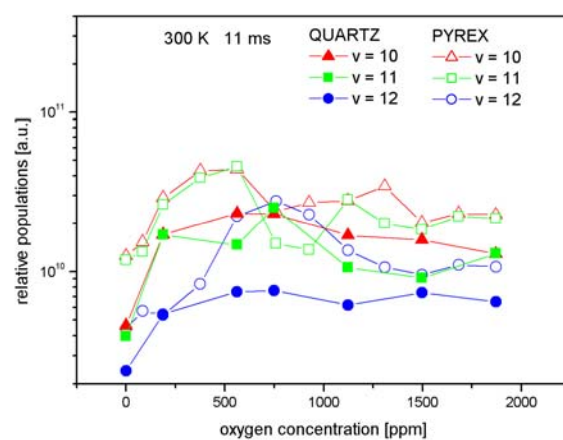
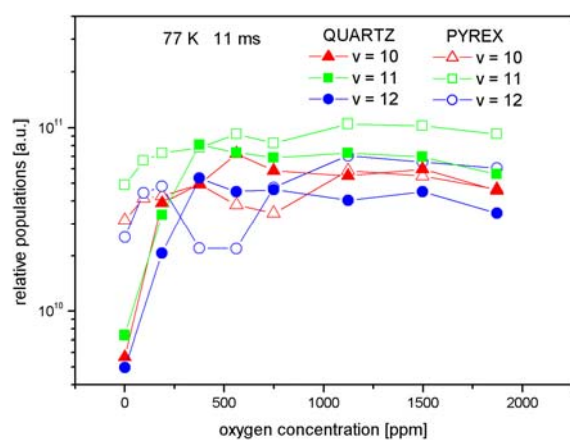
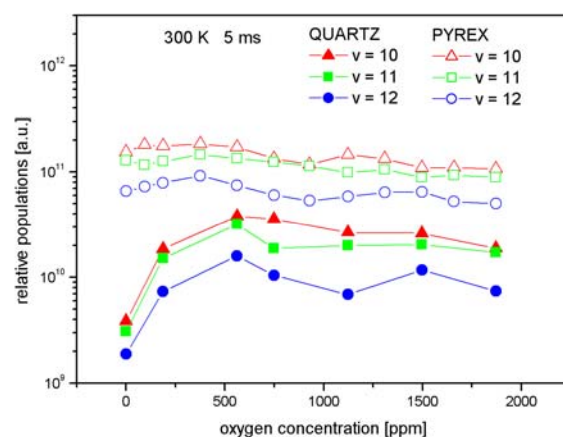
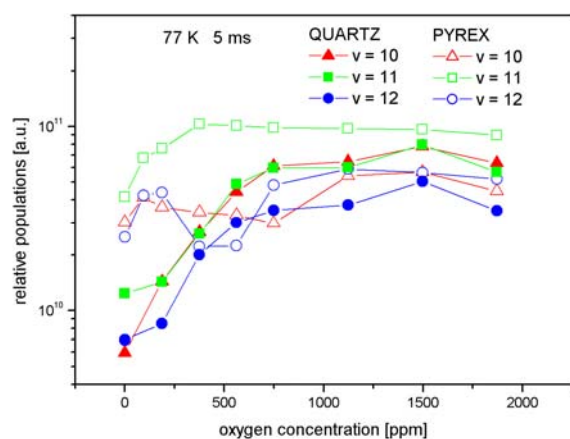


Fig. 5. Dependencies of $N_2(B^3\Pi_g, v=10-12)$ relative populations on oxygen concentration at selected decay times and at wall temperature of 77 K

Fig. 6. Dependencies of $N_2(B^3\Pi_g, v=10-12)$ relative populations on oxygen concentration at selected decay times and at wall temperature of 300 K

The experimental results are shown in Figs. 7–10 during the post-discharge in dependencies on wall material and wall temperature at selected oxygen concentrations. The nearly linear increase of the ratio can be seen during the post discharge at decay times later than 10 ms. This time corresponds

to the maximum emission of pink afterglow effect (see Fig. 4 and details in references¹⁰).

The figures also demonstrate the increase of intensity ratio with the increase of oxygen concentration. This effect is observable in all cases but it is more visible in Quartz tube,

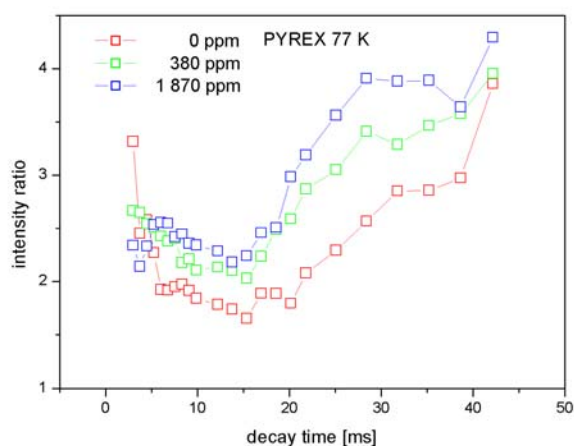


Fig. 7. Band head intensities ratio of 11-7 and 2-0 bands of nitrogen 1st positive system during the post-discharge in Pyrex tube at wall temperature of 77 K

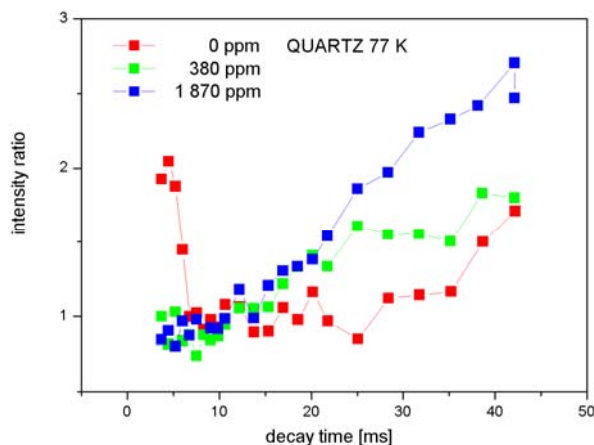


Fig. 9. Band head intensities ratio of 11-7 and 2-0 bands of nitrogen 1st positive system during the post-discharge in Quartz tube at wall temperature of 77 K

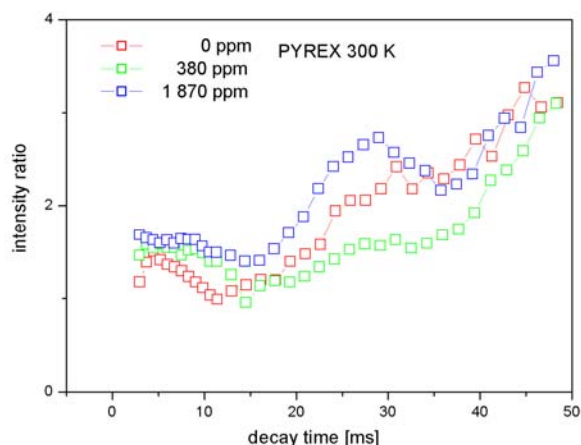


Fig. 8. Band head intensities ratio of 11-7 and 2-0 bands of nitrogen 1st positive system during the post-discharge in Pyrex tube at wall temperature of 300 K

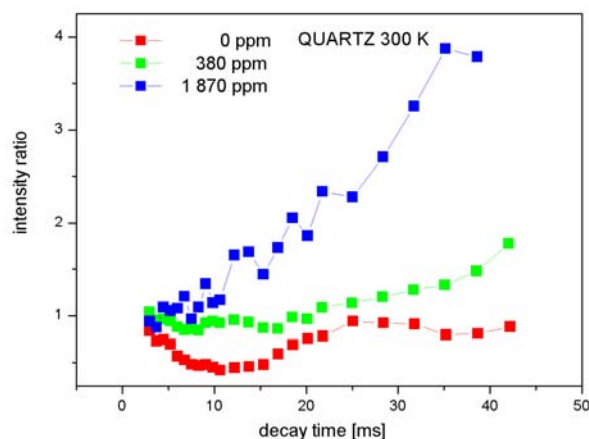


Fig. 10. Band head intensities ratio of 11-7 and 2-0 bands of nitrogen 1st positive system during the post-discharge in Quartz tube at wall temperature of 300 K

especially at the ambient wall temperature.

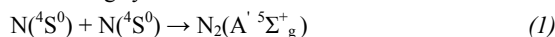
It is known that the recombination is the main process at the later decay times (during so called Lewis-Rayleigh afterglow¹¹) and thus the pooling efficiency is decreasing and the I_{11-7}/I_{2-0} ratio increases. To describe the oxygen influence in more detail, the I_{11-7}/I_{2-0} ratio is shown in Figs. 11 and 12 as a function of oxygen concentration at two selected decay times at all reactor wall conditions. It can be seen the ratio of intensities increases with the increase of oxygen concentration at all wall conditions at shorter decay time (Fig. 11). The situation at later decay time is not such simple. There is no clear dependence in the Pyrex. The ratio of intensities strongly increases in the Quartz at the ambient wall temperature but its dependence on oxygen concentration at wall temperature of 77 K shows different behavior but generally it is also increasing.

The last experimental results that must be mentioned before the kinetic description of the observed processes are

the following. The pink afterglow effect is strongly quenched by oxygen and it disappears at oxygen concentrations over about 1000 ppm¹⁰. The NO^β and NO^γ emission is directly proportional to the oxygen concentration and it is nearly directly proportional to the decay time at given oxygen concentration. Based on these all experimental results the following kinetic description can be proposed.

Kinetic processes

Atomic recombination in nitrogen is known for a long time¹¹. A detailed theory of the three body recombination of two nitrogen ground state atoms was presented in Partridge's work⁵. The mechanism of the recombination can be described by the following system of reactions



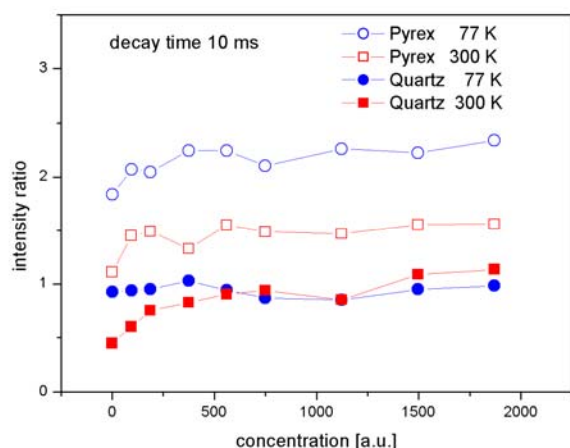


Fig. 11. Band head intensities ratio of 11-7 and 2-0 bands of nitrogen 1st positive system as a function of oxygen concentration at decay time of 10 ms

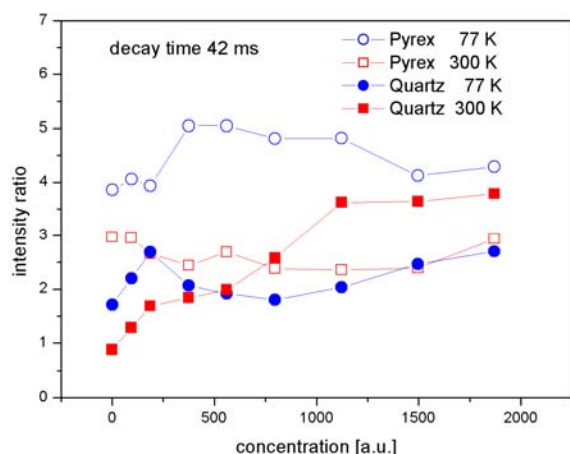
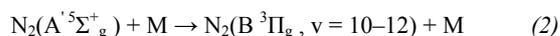
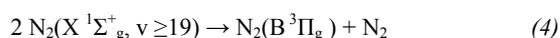
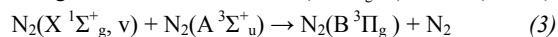


Fig. 12. Band head intensities ratio of 11-7 and 2-0 bands of nitrogen 1st positive system as a function of oxygen concentration at decay time of 42 ms



where M is the third body, mainly any nitrogen molecule. The first of these reactions represented the equilibrium between concentrations of nitrogen atoms and weakly bonded molecules. Usually it is presented in complex with the second reaction. Thus this recombination has a three body form. The rate coefficient of this process is $8.3 \cdot 10^{-34} \exp(500/T) \text{ cm}^6 \text{ s}^{-1}$ as it was reported in ref.¹². As it has a negative temperature dependence, the recombination increases with decreasing temperature as it was presented in the Results.

Other process that contributes to $\text{N}_2(\text{B}^3\Pi_g)$ population is the pooling of lower metastables $\text{N}_2(\text{X}^1\Sigma_g^+, v)$ and $\text{N}_2(\text{A}^3\Sigma_u^+)$.

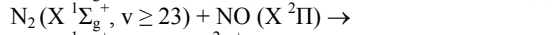
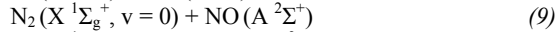
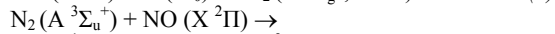
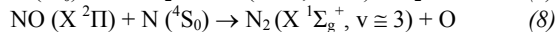
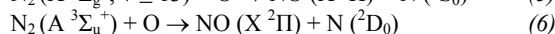


The $\text{N}_2(\text{A}^3\Sigma_u^+)$ state is again created by the pooling of

ground state molecules (the process similar to the reaction 4). Vibrationally excited ground state molecules are created during the post-discharge period mainly by a well known v-v process⁴. As the $\text{N}_2(\text{A}^3\Sigma_u^+)$ state concentration at the end of an active discharge is low¹³, the main energy source in the afterglow besides the atoms is vibrationally excited nitrogen ground state molecules.

The same molecules that are precursors for the $\text{N}_2(\text{B}^3\Pi_g)$ state creation are also the precursors for molecular ion creation. This process is known as a step-wise ionization¹⁴. The highly excited neutral metastable molecules (excited both electronically and vibrationally) can have energy sufficient for the ionization during their mutual collisions. After molecular ion creation, the excitation to the radiative $\text{N}_2^+(\text{B}^2\Sigma_u^+)$ state is done by the collisionally induced energy transfer from the vibrationally excited neutral ground state molecules, namely $\text{N}_2(\text{X}^1\Sigma_g^+, v \geq 12)$ ^{6,10}. This mechanism is responsible for the pink afterglow creation.

If some other species are added the reaction scheme become more complicated and it is significantly different. Small addition of oxygen traces lead to form NO. The oxygen influence can be described by the following main reactions



The reactions 5 and 10 have a strong influence on the v-v process in nitrogen ground state. Highly excited molecular states are thus formed with a lower probability and the pooling creation of electronically excited states is strongly decreased. Moreover, the concentration of $\text{N}_2(\text{A}^3\Sigma_u^+)$ state is quenched by atomic oxygen as it is described by the reactions 6 and 9. On the other hand, these processes increase the populations at lower vibrationally excited ground state levels and thus the pooling processes involving only these levels are more efficient. Reactions 7 and 8 describe the NO species formation and backward dissociation. The reactions 6 and 7 lead also to the increase of atomic nitrogen concentration. This description itself is not sufficient for the experimental results explanation. Thus the nitrogen molecular ion must be included in the model.

The formation of nitrogen molecular ion is strongly dependent on the oxygen concentration. Its formation by the step-wise ionization process is strongly decreased because the reactions 5 and 6 strongly decrease the production of high energetic metastables. Thus the ion formation efficiency is significantly lower and there are not enough ionic species that could be populated by energy transfer from the vibrationally excited nitrogen ground state. That reaction has a high rate coefficient and at low temperature, it has a strongly resonant character^{6,10}. Thus if the molecular ion is created, the strong depopulation of $\text{N}_2(\text{X}^1\Sigma_g^+, v \geq 12)$ vibrational levels is observed.

When oxygen is added, the process of the step-wise ionization creating molecular ion is blocked and thus higher ground state vibrational levels can be significantly populated.

Besides the higher electronic states creation by pooling of these states, the dissociation can be observed, too. It means the concentration of nitrogen ground state atoms can be increased in the afterglow if the oxygen traces are added. Similar effect was recently directly observed in Vašina's work¹⁵. This process has a reflection in the increase of populations at $N_2(B^3\Pi_g, v=10-12)$ levels as it was observed. The same process is also reflected in the observed dependences of NO emission bands.

High vibrationally excited ground state nitrogen molecules (over $v=22$) play a minor role in the direct formation of electronically excited states. Thus the reaction (10) has only the slight effect, mainly on the population of $N_2(B^3\Pi_g)$ levels laying above the predissociation limit.

Conclusions

The recombination of nitrogen ground state atoms was observed through the emission of nitrogen first positive system spectral bands in pure nitrogen containing the traces of oxygen. The observations were carried out in Pyrex and Quartz discharge tubes at wall temperatures of 300 and 77 K. The significant increase of the bands originating at level $N_2(B^3\Pi_g, v=12)$ was observed at decreased wall temperature. The oxygen traces increased the light emission during the post-discharge period; this effect was significantly stronger in Quartz tube. Simultaneously, the nitrogen pink afterglow effect was strongly quenched by oxygen. The detail study showed that low oxygen concentration up to 500 ppm significantly increased the populations at $N_2(B^3\Pi_g, v=10-12)$ levels and this effect was higher in the Quartz tube. The kinetic model showed that oxygen traces were responsible for the NO creation that consequently decreased the populations of highly excited nitrogen molecular metastables. Thus the step-wise ionization was quenched and finally this influence resulted in the increase of atomic nitrogen concentration in the afterglow. To verify this model experimentally the NO titration during the post-discharge in nitrogen-oxygen mixtures will be carried out.

This work was supported by the Czech Science Foundation under projects No. 202/05/0111 and No. 202/08/1106.

REFERENCES

- Pierson J. F., Belmonte T., Michel H.: *Appl. Surf. Sci.* **172**, 285 (2001).
- Pintassilgo C. D., Loureiro J., Guerra V.: *J. Phys. D: Appl. Phys.* **38**, 417 (2005).
- Mezerette D., Belmonte T., Hugon R., Czerwiec T., Henrion G., Michel H.: *Surf. Coat. Technol.* **142-144**, 761 (2001).
- Guerra V., Sa P. A., Loureiro J.: *Eur. Phys. J. – Appl. Phys.* **28**, 125 (2004).
- Partridge H., Langhoff S. R., Bauschlicher C. W., Schwenke D. W.: *J. Chem. Phys.* **84**, 6901 (1986).
- Krčma F., Protasevich E. T.: *Post-discharges in Pure Nitrogen and Nitrogen Containing Halogenated Hydrocarbon Traces*, Tomsk Polytechnic University 2003.
- Krčma F., Mazánková V., Soral I., Šimek M.: *Proceedings of ICPIG XXVIII, 1722 Praha 2007*.
- Gilmore F. R., Laher R. R., Espy P. J.: *J. Phys. Chem. Ref. Data* **21**, 1005 (1992).
- Kumar V., Kumar A.: *Physica* **132 C**, 273 (1985).
- Krčma F., Mazánková V., Soral I.: *Publ. Astronom. Observatory of Belgrade* **82**, 133 (2007).
- Kistiakowski G. B., Warneck P.: *J. Chem. Phys.* **27**, 417(1957).
- Klopovsky K. S., Mukhovatova A. V., Popov A. M., Popov N. A., Popovicheva O. B., Rakhimova T. V.: *J. Phys. D: Appl. Phys.* **27**, 1399 (1994).
- Sadeghi N., Foissac C., Supiot P.: *J. Phys. D: Appl. Phys.* **34**, 1779 (2001).
- Paniccia F., Gorse C., Cacciatore M., Capitelli M.: *J. Phys.* **61**, 3123 (1987).
- Vašina P., Kudrle V., Tálský A., Botoš P., Mrázková M., Meško M.: *Plasma Source Sci. Technol.* **13**, 668 (2005).

Power Dependence of the Pink Afterglow in Flowing Postdischarge in Pure Nitrogen

František Krčma, Věra Mazánková, Ivo Soural, and Vasco Guerra

Abstract—The nitrogen short-lived postdischarge, also known as nitrogen pink afterglow, was studied in the flowing regime as a function of the applied power. The maximal emission intensity of this afterglow shifts to shorter times proportionally to the applied power. The images demonstrate that the pink afterglow creation is due to kinetic processes in volume, although heterogeneous surface reactions may contribute significantly to the overall kinetics.

Index Terms—Glow discharge, plasma diagnostics, plasma properties.

THE study of nitrogen discharges and afterglows is a rather complex problem, due to the strong interplay between different kinetics. The nitrogen pink afterglow is known for many decades [1], but, despite the many experimental and theoretical investigations carried out along the years [1]–[6], it is not yet fully explained [3]. Our work demonstrates its strong dependence on the applied power.

The afterglow of pure nitrogen (99.9999%) dc discharge is studied at a fixed pressure of 1000 Pa, the discharge currents 50–200 mA, and an applied voltage of 1200 V. The discharge is created in a Pyrex tube (i.d. of 12 mm) with molybdenum electrodes placed in the side arms. A gas flow of 800 sccm allows the direct observation of the postdischarge up to decay times of about 50 ms. The postdischarge images were taken by a Nikon D80 camera with a Nikkor AF-S DX 18-55/1:3.5-5.6 6 VR objective, using an exposure time of 1/6 s. Optical emission spectroscopy using a Jobin Yvon Triax 550 spectrometer with 1200 gr/mm grating and CCD detector is used for detailed observations of the nitrogen first positive, second positive and first negative systems.

The light emission during the postdischarge is hardly visible in the first image of the series shown on Fig. 2. A weak yellow–orange emission can be recognized using longer exposure times (not shown here). This emission corresponds to the long-lived afterglow (also known as the Lewis–Rayleigh afterglow) and originates mainly from the atomic three-body

Manuscript received November 22, 2013; revised January 9, 2014; accepted February 11, 2014. Date of publication March 11, 2014; date of current version October 21, 2014. This work was supported by the Czech Science Foundation under Project 202/08/1106. The work of V. Guerra was supported by FCT under Grant Pes-OE/SADG/LA0010/2011.

F. Krčma, V. Mazánková, and I. Soural are with the Faculty of Chemistry, Brno University of Technology, Brno 612 00, Czech Republic (e-mail: krma@fch.vutbr.cz; mazankova@fch.vutbr.cz; ivo.soural@mendelu.cz).

V. Guerra is with the Instituto de Plasmas e Fusão Nuclear, Instituto Superior Técnico, Universidade de Lisboa, Lisbon 1049-001, Portugal (e-mail: vguerra@tecnico.ulisboa.pt).

Color versions of one or more of the figures in this paper are available online at <http://ieeexplore.ieee.org>.

Digital Object Identifier 10.1109/TPS.2014.2307611

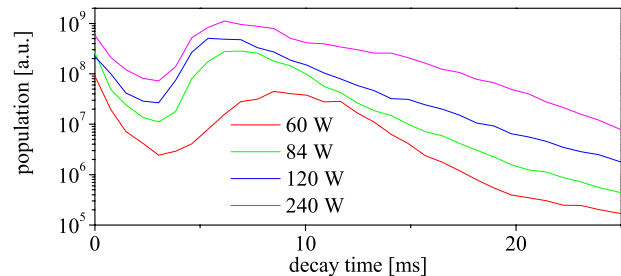


Fig. 1. Profile of N_2^+ ($B, v = 0$) relative population during afterglow.

recombination processes. A significant emission starts to be visible at a discharge power of 72 W and for an afterglow time ~ 10 ms, as it is shown in second picture on Fig. 2. It has a pink color (hence the term pink afterglow), coming from the characteristic emission of the molecular ion bands. By increasing the applied power, the pink afterglow emission becomes much brighter and its maximal intensity shifts to shorter decay times, as it is demonstrated by the remaining pictures of the series, as well as on Fig. 1. This is the result of a combination of various effects, namely the higher gas temperature in the beginning of the afterglow and in the discharge, and the higher vibrational temperature at the end of the discharge.

The axial profile of the pink afterglow is characterized by decrease of the emissions at the discharge end, followed by a rapid increase of intensity at the discharge tube axis and by a much slower decay after the maximum. The radial profile reveals much lower intensities near the reactor walls. This means that heterogeneous reactions play a negative role in the pink emission creation (such reactions quench the precursors for the pink afterglow formation [2]).

Numeric simulations have shown that vibration–vibration up-pumping processes in the nitrogen electronic ground state are at the origin of the pink afterglow [2]. In fact, they lead to a significant increase of the population of molecules in very high v -levels, followed by vibrational electronic transfers that form various electronic states, which then participate in associative/Penning ionization [2], [3], [5], [6].

The discharge tube wall is kept at ambient temperature (~ 360 K at the pink afterglow maximum at the highest power). The temperature profile of the gas flow is nearly parabolic, so that the flow is laminar [4]. The shape of the pink afterglow confirms this statement and implies that the temperature must play a significant role in the postdischarge kinetics, as it was also pointed in [5]. A detailed numeric simulation, including the temperature profiles is needed in

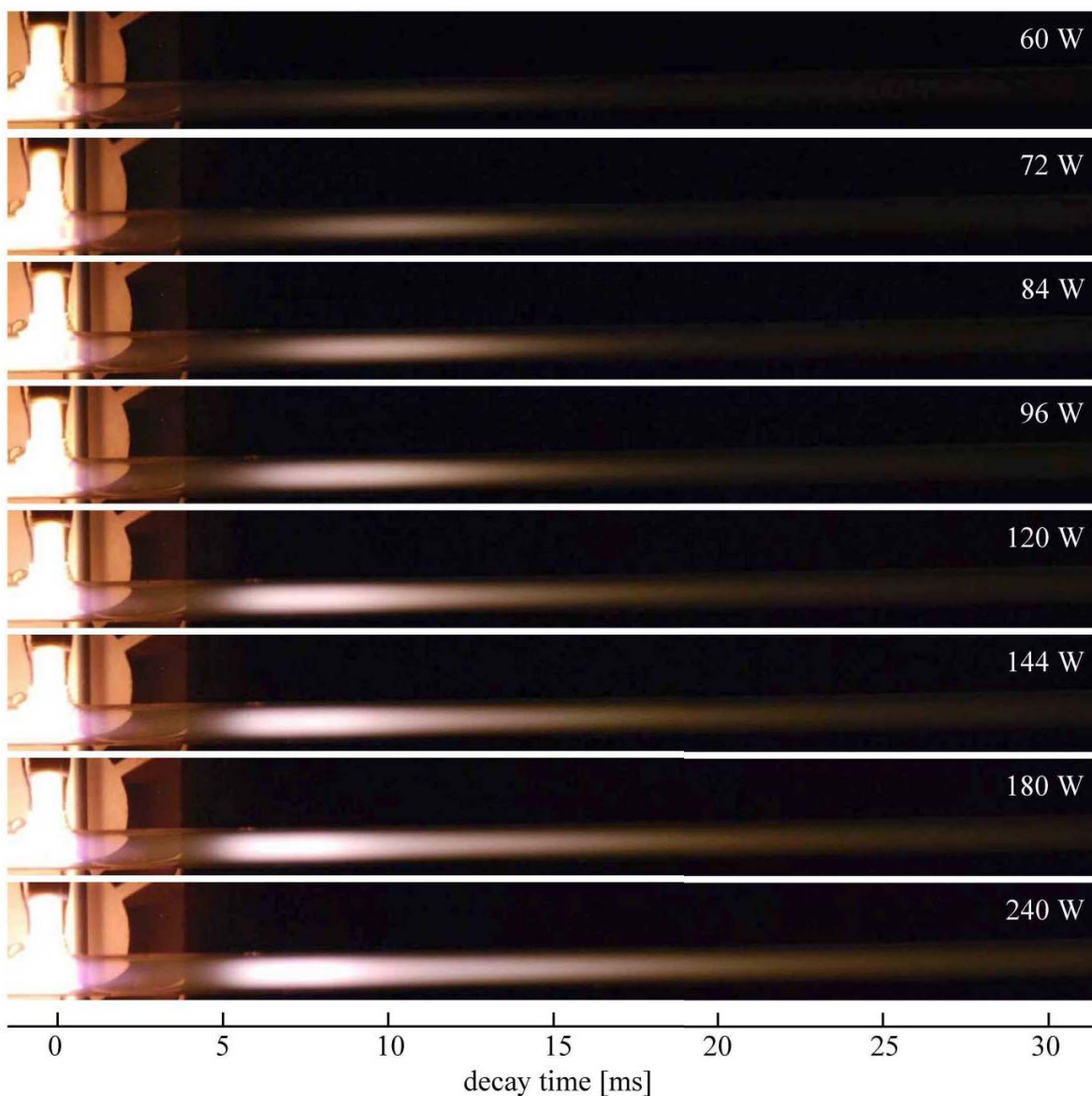


Fig. 2. Nitrogen flowing afterglow at selected applied powers indicated in the pictures.

order to clarify and characterize more precisely the influence of the gas temperature and power in the formation of the pink afterglow. Work is in progress in this direction.

REFERENCES

- [1] G. E. Beale and H. P. Broida, "Spectral study of a visible, short-duration afterglow in nitrogen," *J. Chem. Phys.*, vol. 31, no. 4, pp. 1030–1034, 1959.
- [2] J. Loureiro, V. Guerra, P. A. Sá, C. D. Pintassilgo, and M. L. da Silva, "Non-equilibrium kinetics in N_2 discharges and post-discharges: A full picture by modelling and impact on the applications," *Plasma Source Sci. Technol.*, vol. 20, no. 2, p. 024007, 2011.
- [3] V. Guerra, P. A. Sá, and J. Loureiro, "Nitrogen pink afterglow: The mystery continues," *J. Phys. Conf. Ser.*, vol. 63, no. 1, p. 012007, 2007.
- [4] V. Mazánková, D. Trunec, and F. Krčma, "Study of argon flowing afterglow with nitrogen injection," *J. Chem. Phys.*, vol. 139, no. 16, p. 164311, 2013.
- [5] P. A. Sá, V. Guerra, J. Loureiro, and N. Sadeghi, "Self-consistent kinetic model of the short-lived afterglow in flowing nitrogen," *J. Phys. D, Appl. Phys.*, vol. 37, no. 2, pp. 221–231, 2004.
- [6] J. Levaton and J. Amorim, "Metastable atomic species in the N_2 flowing afterglow," *Chem. Phys.*, vol. 397, pp. 9–17, Mar. 2012.

The Influence of CO₂ Admixtures on the Product Composition in a Nitrogen-Methane Atmospheric Glow Discharge Used as a Prebiotic Atmosphere Mimic

V. Mazankova¹ · L. Torokova^{1,2} · F. Krcma¹ ·
N. J. Mason² · S. Matejcik³

Received: 26 August 2015 / Accepted: 30 March 2016 /
Published online: 11 April 2016
© Springer Science+Business Media Dordrecht 2016

Abstract This work extends our previous experimental studies of the chemistry of Titan's atmosphere by atmospheric glow discharge. The Titan's atmosphere seems to be similarly to early Earth atmospheric composition. The exploration of Titan atmosphere was initiated by the exciting results of the Cassini-Huygens mission and obtained results increased the interest about prebiotic atmospheres. Present work is devoted to the role of CO₂ in the prebiotic atmosphere chemistry. Most of the laboratory studies of such atmosphere were focused on the chemistry of N₂ + CH₄ mixtures. The present work is devoted to the study of the oxygenated volatile species in prebiotic atmosphere, specifically CO₂ reactivity. CO₂ was introduced to the standard N₂ + CH₄ mixture at different mixing ratio up to 5 % CH₄ and 3 % CO₂. The reaction products were characterized by FTIR spectroscopy. This work shows that CO₂ modifies the composition of the gas phase with the detection of oxygenated compounds: CO and others oxides. There is a strong influence of CO₂ on increasing concentration other products as cyanide (HCN) and ammonia (NH₃).

Keywords Prebiotic atmosphere · Atmospheric glow discharge · FTIR spectroscopy

Paper presented at the conference: Habitability in the Universe: From the Early Earth to Exoplanets 22–27 March 2015, Porto, Portugal

✉ V. Mazankova
mazankova@fch.vutbr.cz

¹ Faculty of Chemistry, Brno University of Technology, Purkynova 119, 612 00 Brno, Czech Republic

² Department of Physics and Astronomy, Open University, Walton Hall, Milton Keynes MK7 6AA, UK

³ Department of Experimental Physics, Comenius University, Mlynska dolina F-2, 842 48 Bratislava, Slovakia

Introduction

The Miller-Urey spark-discharge experiments in the early 1950s inspired a strong interest in experimental studies of prebiotic organic chemistry that continues today. The prebiotic synthesis in the mixtures of $N_2 + CH_4 + CO/CO_2$ was studied by (Schlesinger and Miller 1983a; Schlesinger and Miller 1983b). Different types of discharges were used to mimic the influence of lightning in prebiotic atmospheres or the influence of solar VUV radiation. Also the atmospheric pressure glow discharge can be used for such purposes.

The atmospheric pressure glow discharges are of significant interest for a wide range of applications such as pollution control, material processing or surface treatment. Among the many different types of atmospheric pressure discharges the glow discharge is one of the most deeply studied (Kloc et al. 2010; Machala et al. 2004). The gliding arc configuration of atmospheric pressure discharge has been shown to be a good mimic of processes in the prebiotic atmospheres (Torokova et al. 2015b) being used to replicate physical and chemical conditions on Titan. It is the only lunar body with significant quantities of methane (CH_4) and nitrogen (N_2) in its atmosphere (Coustenis et al. 2010; Horst and Tolbert 2014). The chemical composition of the Titan's atmosphere is considered to be similar to the atmosphere of early Earth and is favorable for formation of complex molecules containing C, N and H. The solar ultraviolet radiation and magnetospheric electrons are responsible for the generation of primary radicals and other neutral species, which initiate chains of chemical reactions that finally result in the formation of various organic molecules in the Titan atmosphere. This makes Titan as planetary-scale laboratory for the synthesis of complex organic molecules (Raulin et al. 2012). The composition of early Earth atmosphere was deeply discussed in many studies (Kasting and Howard 2006; Kasting and Ono 2006; Olson et al. 2013).

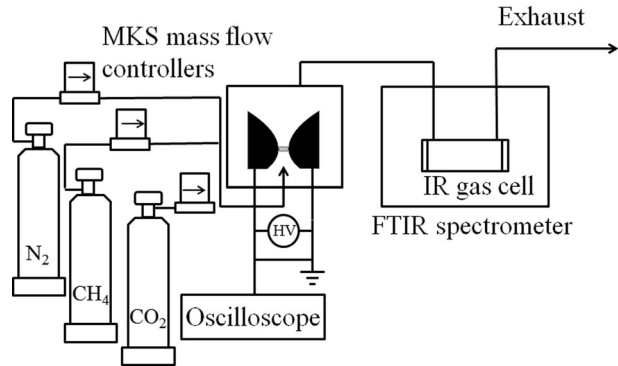
The present work is focused on the experimental study of gaseous products produced in the atmospheric pressure glow discharge fed by $N_2 + CH_4$ gas mixtures with CH_4 concentrations in the range from 1 % to 5 % and admixture of the carbon dioxide (CO_2) from 1 % to 3 %. The atmospheric DC glow discharge is a source of electrons, ions and neutral radicals. All these species initiate a complex chemical processes under laboratory conditions, which are similar to the processes which may occur in the prebiotic atmosphere.

The neutral products generated in the discharge were identified and quantified by the means of the Fourier-Transform-Infra-Red spectroscopy (FTIR). In more detail the influence of the CO_2 admixture on production of the major neutral product detected HCN and on the formation of NH_3 has been studied.

Experimental Apparatus

The experimental set-up was detail described in our previous studies (Torokova et al. 2015a; Torokova et al. 2015b). A simplified schematic diagram of the experimental set up is presented in Fig. 1. An atmospheric pressure DC glow discharge was created between two stainless steel electrodes separated by a 2 mm gap. The electrode system used the standard configuration of the gliding arc discharge but due to the low applied power as well as low gas velocity the discharge is not moving along the electrodes. The discharge was operated at an applied voltage of 350 V and discharge current in range 15 to 40 mA in pure nitrogen enriched by 1–5 % of CH_4 (both gases having quoted purity of 99.995 %) with admixture of 1 and 3 % of CO_2 at the total flow rate of 50 sccm. Flow rates of all gases through the reactor were regulated using

Fig 1 Schematic diagram of the experimental setup used for FTIR analysis of gaseous products of a DC glow discharge fed by various mixtures of N₂ + CH₄ + CO₂



mass flow controllers (MKS, Flow Measurement & Control Products). These values of CH₄ and CO₂ concentration were chosen with the aim to enhance the reactions with CO₂, that possibly allow to detect oxides compounds produced in larger amounts in the plasma reactor.

The exhaust gas was analyzed in-situ by FTIR spectroscopy using IR multipath cell with total absorption length of 3 m. Compositions of the different gaseous mixtures studied here are given in Table 1. The discharge was formed in the stable abnormal glow regime with a plasma channel of 1 mm diameter. The discharge is contained in a stainless steel vacuum chamber (1 l volume). Before starting the experiments, the discharge chamber was pumped down to 1 Pa for 1 h and then filled with the investigated gas mixture up to the pressure of 101 kPa. Atmospheric pressure during the experiments was maintained by a slight pumping through the needle valve.

The high-resolution transmission (HITRAN) database (Rothman et al. 2009) was used to identify specific compounds in the measured spectra. Concentration of the gaseous products were calculated using the Beer-Lambert formula (1)

$$A = n \cdot l \cdot \sigma \quad (1)$$

where A is the absorbance measured experimentally, n (cm⁻³) is the concentration of detected compound, l (cm) is the length of the absorption path in IR cell and σ (cm²) is the IR absorption

Table 1 Compositions of the studied gas mixtures

Mixture	CO ₂ (%)	CH ₄ (%)	N ₂ (%)
1	0	1	99
2	0	2	98
3	0	4	96
4	0	5	95
5	1	1	98
6	1	2	97
7	1	4	95
8	1	5	94
9	3	1	96
10	3	2	95
11	3	4	93
12	3	5	92

cross-section drawn from the HITRAN database (Rothman et al. 2009). The uncertainty in the determination of concentration was estimated about 20 %. All experiments were done at room temperature.

Results and Discussion

A typical FTIR spectrum showing the products formed in the nitrogen discharge fed by 1 % of CH_4 and 1 % of CO_2 is shown in Fig. 2. Similar spectra were observed for all other $\text{N}_2 + \text{CH}_4 + \text{CO}_2$ gas mixture composition. Hydrogen cyanide (HCN) was identified at wavenumbers of 1430 cm^{-1} and of 720 cm^{-1} and it was recognized as the most abundant product. Ammonia (NH_3) was identified at 966 cm^{-1} which was surprising because ammonia was not detected in our previous experimental studies (Torokova et al. 2015a; Torokova et al. 2015b). Bernard et al. 2003 observed NH_3 production at their experiments in low pressure discharge in the mixture $\text{N}_2 + \text{CH}_4 + \text{CO}$. NH_3 production was explained by the chain of ion-molecular reactions (Bernard et al. 2003).

The other major products in our experiments were acetylene (C_2H_2) as well as carbon monoxide (CO) and water (H_2O). These products were recognized in all $\text{N}_2 + \text{CH}_4 + \text{CO}_2$ gas mixtures. The products concentrations are strongly dependent on the gas mixtures composition Legrand et al. 1999 reported typical values of obtained hydrocarbons from their experiments in nitrogen/methane gas mixture: C_2H_2 (22 %), C_2H_6 (18 %), C_2H_4 (14 %), C_3H_8 (4 %), C_4H_{10} (less than 0.5 %). Pintassilgo and Loureiro (2009) in their comparative study report the most abundant hydrocarbons C_2H_6 and C_3H_4 .

Figure 3 shows the quantitative analysis of HCN at 1430 cm^{-1} formed under different experimental conditions. The increase of the initial CH_4 concentration from 1 % to 5 % leads to increase in the product yield of this compound. The admixture of 1 % CO_2 had a little influence on HCN production up to 4 % CH_4 . However, there is visible effect of CO_2 addition to nitrogen methane mixtures with 5 % methane with the yield of HCN increasing with increasing CO_2 concentrations. This is in contrast to earlier study (Fleury et al. 2014) that suggested that the kinetics of HCN formation slows down at the presence of CO, showing an inhibiting role of CO on HCN formation.

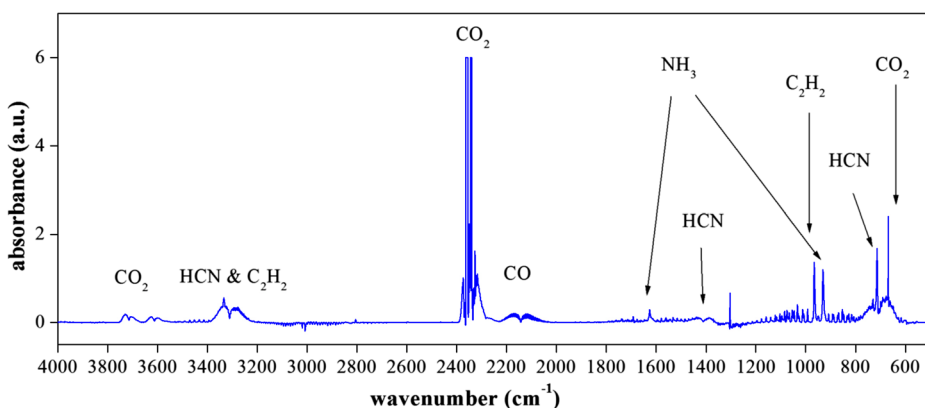


Fig 2 FTIR spectrum of analysed products formed in a gas mixture 1 % of $\text{CH}_4 + 1$ % of CO_2 in N_2 , discharge current 30 mA and gas flow 50 sccm

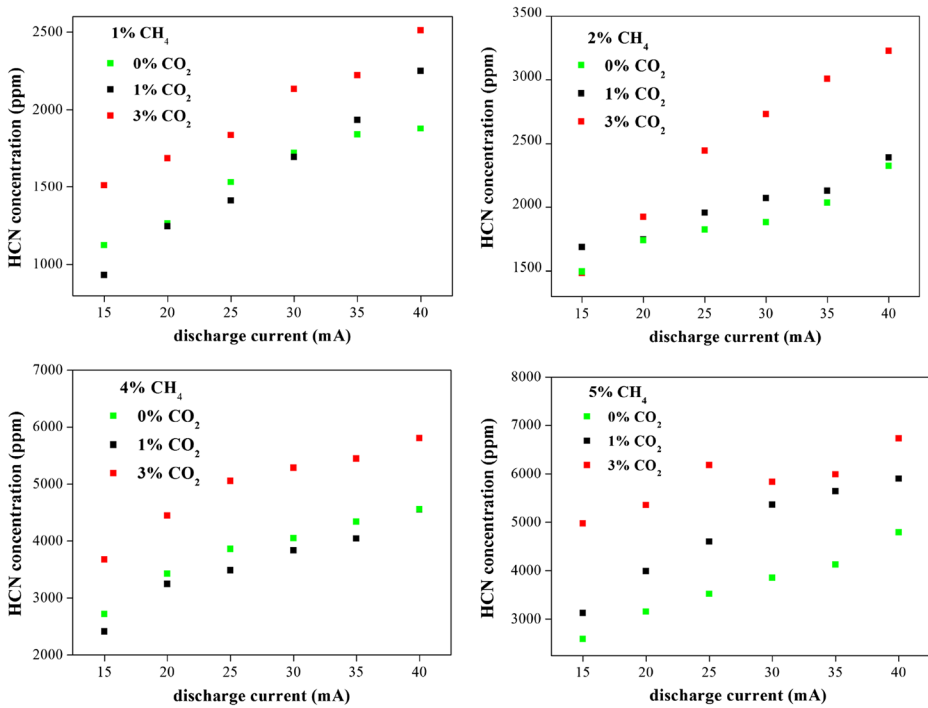


Fig 3 The dependence of hydrogen cyanide (HCN) concentration on discharge current for different initial concentrations of methane and carbon dioxide

Similar analysis is shown in Fig. 4 for NH₃. The concentration of the ammonia increases with the increase of CH₄ concentration. The effect of CO₂ admixture is ambivalent. For lower CH₄ concentrations (1 and 2 %) it can be seen that the admixture of CO₂ promotes formation of the NH₃ in whole range of discharge currents, while in the case of higher CH₄ concentrations it occurs only for higher discharge currents (above 30 mA). At lower discharge currents and CH₄ concentrations there is no increase of the NH₃ formation with increasing CO₂ concentration.

The discharge current increase is connected with the increase of the electron concentration and also the rates of reaction induced by electrons (dissociation, ionisation) increases. This leads to the increase of radical concentration and thus to the increase of the final products concentrations. This can be seen in all dependencies in Figs. 3 and 4.

These effects are related to the complex kinetics of the discharge and detailed explanation of the processes associated with it should be an object of the further experimental work and computer simulation of the discharge kinetics.

The formation of various nitriles is assigned to a complex plasma-physical chemistry. The nitrogen and methane are dissociated in the discharge by the electron impact producing the radicals CH_x ($x = 1, 2, 3$) and N atoms. Also the metastable molecules N₂(A) are produced in the discharge, these metastables can again produce CH_x radicals in the afterglow. The concentrations of ions are lower than concentrations of radicals, so the ion-molecule reactions are not important.

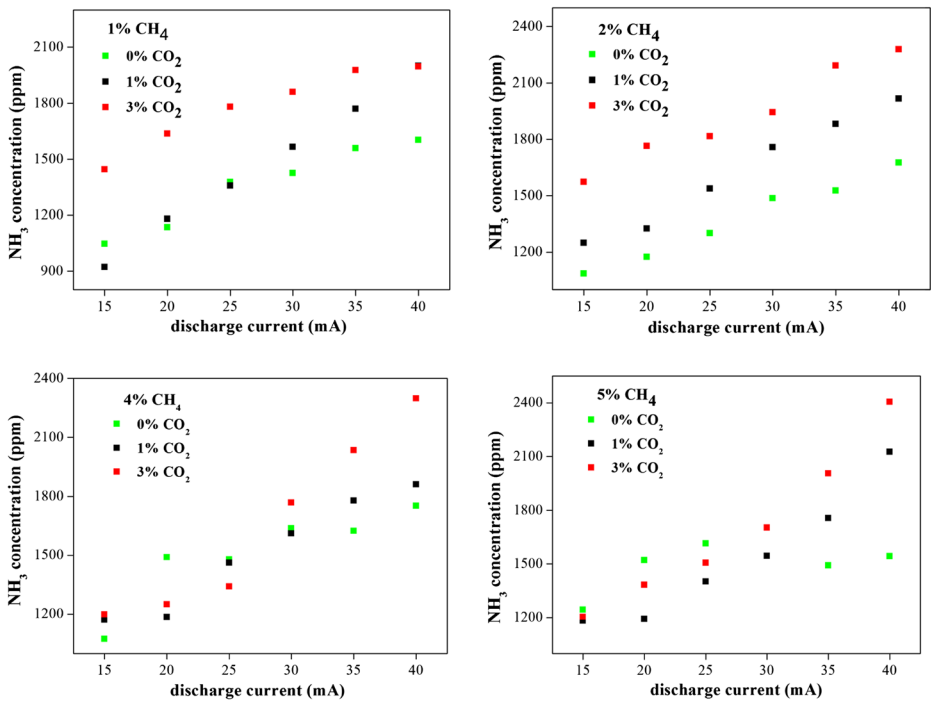


Fig 4 The dependence of ammonia (NH_3) concentration on discharge current for different initial concentrations of methane and carbon dioxide

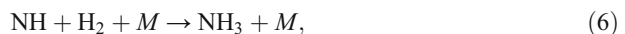
The radicals then react and produce new molecules. Hydrogen cyanide formation can be described by the direct reaction:



or/and indirect by a two-step process through a highly unstable intermediate product, H_2CN (Pintassilgo and Loureiro 2010).



The formation of ammonia may proceed via reactions (Dove and Nip 1979):



where M is a third particle. Formation of above mentioned radicals CH_3 , N , NH in the discharge is discussed in (Pintassilgo and Loureiro 2010). At the atmospheric pressure, reaction (6) is important, whereas at low pressure this reaction can be neglected. This fact can explain why ammonia was not observed at some low pressure experiments (Pintassilgo and Loureiro 2009).

If CO₂ is added into the discharge, the O atoms are produced by CO₂ dissociation or CO₂⁺ recombination with electrons. These O atoms can then react with CH₄ via reaction (Baulch et al. 1992; Baulch et al. 1994):



So, reaction (7) is responsible for the increase of the concentrations HCN precursors (see reactions (2) and (3)) and also for the consequent increase of HCN concentration as it was observed experimentally.

Conclusion

The gaseous phase products formed in the atmospheric glow discharge fed by different mixtures of N₂ + CH₄ (1, 2, 4 and 5 %) and admixture of CO₂ (1 and 3 %) were determined by in situ FTIR analysis. The discharge was operated in the flowing regime at different discharge currents at laboratory temperature. An in-situ FTIR technique for the exhaust gas phase sampling was successfully used for chemical analysis to deduce the gas composition in the N₂ + CH₄ + CO₂ reactive gas mixture.

The nitrile compounds and hydrocarbon were observed in all experiments. HCN was identified as the major gas phase product in all measurements. HCN is important compound for subsequent synthesis of nucleobases at early Earth (McCullom 2013). Other minor products detected were C₂H₂, NH₃, CO₂, CO. The nitrile oxides, formaldehyde, ethylene oxide were not observed in our experiments, although creation of oxygenated compounds was predicted by theoretical model (Dobrijevic et al. 2014). Fleury et al. 2014 reported only creation of N₂O and CO₂ from the mixture N₂ + CH₄ + CO. The absence of formaldehyde in the gaseous phase has been previously observed in an electrical discharge by Bernard et al. 2003 where the gaseous phase composition was studied by GC-MS and Infrared spectroscopy. So there is disagreement of our experiments with theoretical models which predict important production of formaldehyde. The absence of formaldehyde or other aldehydes is a serious problem for subsequent production of amino acids in liquid phase via Strecker synthesis (Miller and Urey 1959).

The addition of CO₂ increases the production of HCN, however the addition of CO decreases the production of HCN. All above mentioned facts show that further experimental and theoretical studies of coupling between nitrogen chemistry and oxygen chemistry are necessary.

Acknowledgments This work results within the collaboration of the COST Actions TD 1308 and CM 1401. The research was supported by Czech Ministry of Education, Youth and Sports, projects No. COST CZ LD15010 and COST CZ LD15011, CEEPUS network AT-0063 and partially by the Slovak Research and Development Agency, project Nr. APVV-0733-11.

References

- Baulch DL, Cobos CJ, Cox RA, Esser C, Frank P, Just T, Kerr JA, Pilling MJ, Troe J, Walker RW, Warnatz J (1992) Evaluated kinetic data for combustion modeling. *J Phys Chem Ref Data* 21:411–734
- Baulch DL, Cobos CJ, Cox RA, Frank P, Hayman G, Just T, Kerr JA, Murrells T, Pilling MJ, Troe J, Walker RW, Warnatz J (1994) Evaluated kinetic data for combustion modeling supplement-i. *J Phys Chem Ref Data* 23: 847–1033

- Bernard JM, Coll P, Coustenis A, Raulin F (2003) Experimental simulation of Titan's atmosphere: detection of ammonia and ethylene oxide. *Planet Space Sci* 51:1003–1011
- Coustenis A, Jennings DE, Nixon CA, Achterberg RK, Lavvas P, Vinatier S, Teanby NA, Bjoraker GL, Carlson RC, Piani L, Bampasidis G, Flasar FM, Romani PN (2010) Titan trace gaseous composition from CIRS at the end of the Cassini-Huygens prime mission. *Icarus* 207:461–476
- Dobrijevic M, Hebrard E, Loison JC, Hickson KM (2014) Coupling of oxygen, nitrogen, and hydrocarbon species in the photochemistry of Titan's atmosphere. *Icarus* 228:324–346
- Dove JE, Nip WS (1979) A shock-tube study of ammonia pyrolysis. *Can J Chem* 57:689–701
- Fleury B, Carrasco N, Gautier T, Mahjoub A, Hec J, Szopa C, Hadamcik E, Buch A, Cernogora G (2014) Influence of CO on titan atmospheric reactivity. *Icarus* 238:221–229
- Horst SM, Tolbert MA (2014) The effect of carbon monoxide on planetary haze formation. *Astrophys J* 781:53. doi:10.1088/0004-637X/781/1/53
- Kasting JF, Howard MT (2006) Atmospheric composition and climate on the early earth. *Philos Trans R Soc Lond B Biol Sci* 361:1733–1741
- Kasting JF, Ono S (2006) Palaeoclimates: the first two billion years. *Philos Trans R Soc Lond B Biol Sci* 361: 917–929
- Kloc, P., Wagner, H. E., Trunec, D., Navratil, Z., Fedoseev, G., 2010. An investigation of dielectric barrier discharge in Ar and Ar/NH₃ mixture using cross-correlation spectroscopy. *J Phys D Appl Phys* 43
- Legrand JC, Diany AM, Hrach R, Hrachova V (1999) Mechanisms of methane decomposition in nitrogen afterglow plasma. *Vacuum* 52:27–32
- Machala Z, Marode E, Laux CO, Kruger CH (2004) DC glow discharges in atmospheric pressure air. *Journal of Advanced Oxidation Technologies* 7:133–137
- McCollom TM (2013) Miller-Urey and beyond: what have we learned about prebiotic organic synthesis reactions in the past 60 years? *Annu Rev Earth Planet Sci* 41(41):207–229
- Miller SL, Urey HC (1959) Organic compound synthesis on the primitive earth. *Science* 130:245–251
- Olson SL, Kump LR, Kasting JF (2013) Quantifying the areal extent and dissolved oxygen concentrations of Archean oxygen oases. *Chem Geol* 362:35–43
- Pintassilgo CD, Loureiro J (2009) Production of hydrocarbons and nitriles using a N₂-CH₄ afterglow plasma for simulation of Titan's atmosphere. *Planet Space Sci* 57:1621–1630
- Pintassilgo CD, Loureiro J (2010) Kinetic study of a N₂-CH₄ afterglow plasma for production of N-containing hydrocarbon species of Titan's atmosphere. *Adv Space Res* 46:657–671
- Raulin F, Brasse C, Poch O, Coll P (2012) Prebiotic-like chemistry on titan. *Chem Soc Rev* 41:5380–5393
- Rothman LS, Gordona IE, Barbeb A, Chris Bennecr D, Bernathd PF, Birke M, Boudonf V, Browng LR, Campargueh A, Championf J-P, Chancea K, Couderti LH, Danaj V, Devic VM, Fallyk S, Flaudi J-M, Gamachel RR, Goldmann A, Jacquemartin D, Kleineri I, Lacomn N, Laffertyo WJ, Mandinj J-Y, Massiep ST, Mikhailenkoq SN, Millerg CE, Moazzen-Ahmadir N, Naumenkoq OV, Nikiting AV, Orphali J, Perevalovq VI, Perrini A, Predoi-Crosss A, Rinslandt CP, Rotgerb M, Šimečková M, Smitht MAH, Sungg K, Tashkunq SA (2009) The HITRAN 2008 molecular spectroscopic database. *J Quant Spectrosc Radiat Transf* 110:533–572
- Schlesinger G, Miller SL (1983a) Prebiotic synthesis in atmospheres containing CH₄, CO, and CO₂. 1. Amino-acids. *J Mol Evol* 19:376–382
- Schlesinger G, Miller SL (1983b) Prebiotic synthesis in atmospheres containing CH₄, CO, and CO₂. 2. Hydrogen-cyanide, formaldehyde and ammonia. *J Mol Evol* 19:383–390
- Torokova L., Mazankova V., Krcma F., Mason, N. J., Matejcik, S., 2015a. Atmospheric pressure glow discharge generated in nitrogen-methane gas mixture: PTR-MS analyzes of the exhaust gas EPJ Applied Physics 71
- Torokova L, Watson J, Krcma F, Mazankova V, Mason NJ, Horvath G, Matejcik S (2015b) Gas chromatography analysis of discharge products in N₂-CH₄ gas mixture at atmospheric pressure: study of mimic Titan's atmosphere. *Contrib Plasma Phys* 55:470–480

THE INFLUENCE OF CO₂ ADMIXTURES ON PROCESS IN TITAN'S ATMOSPHERIC CHEMISTRY

TOROKOVA L.^{a,*}, MAZANKOVA V.^a, MASON N. J.^b, KRCMA F.^a, MORGAN G.^b,
MATEJCIK S.^c

^a Faculty of Chemistry, Brno University of Technology, Purkynova 118, 612 00 Brno, Czech Republic

^b Department of Physical Sciences, Open University, Milton Keynes MK7 6AA, United Kingdom

^c Faculty of Mathematics, Physics and Informatics, Comenius University, 842 48 Bratislava, Slovakia

* torokova@fch.vutbr.cz

Abstract. The exploration of planetary atmosphere is being advanced by the exciting results of the Cassini-Huygens mission to Titan. The complex chemistry revealed in such atmospheres leading to the synthesis of bigger molecules is providing new insights into our understanding of how life on Earth developed. In our experiments Titan's atmosphere is simulated in a glow discharge formed from a mixture of N₂:CH₄:CO₂ gas. Samples of the discharge gas were analysed by GC-MS and FTIR. The major products identified in spectra were: hydrogen cyanide, acetylene and acetonitrile. The same compounds were detected in the FTIR: hydrogen cyanide, acetylene and ammonia. Whilst many of these compounds have been predicted and/or observed in the Titan atmosphere, the present plasma experiments provide evidence of both the chemical complexity of Titan atmospheric processes and the mechanisms by which larger species grow prior to form the dust that should cover much of the Titan's surface.

Keywords: atmosphere of Titan, glow discharge, GC-MS analysis and FTIR spectroscopy.

1. Introduction

Simple organic molecules play an important role in the formation of complex organics in planetary atmospheres. On the last decade, several lower hydrocarbons and nitriles have been confirmed in the atmosphere of Titan, the largest satellite of the Saturn. The first detailed information was brought by Voyager space mission in 1980. More important complex information about Titan atmosphere was obtained from Cassini-Huygens mission in 2005. Its atmosphere composition is principally nitrogen with 2-6 % methane and some trace gases as nitriles (HCN, HC₃N, HC₅N, and C₂N₂) and lower molecule hydrocarbons (C₂H₂, C₂H₄, C₂H₆, C₃H₈, C₃H₄) as well as hydrogen [1, 2]. These compounds can be produced by low power discharges in the methane clouds [3, 4] or by dissociation of nitrogen and methane either by solar induced photolysis, photodissociation or by electron impact. The same processes generate also charged particles that are transported through the atmospheric clouds. Neutralization of these charged particles leads to high power discharges like lightning within the clouds which can induce other chemical reactions in the troposphere [5]. Organic radicals produced by electron impact could also supply a significant fraction of Titan's haze and surface material [6]. Lightning activity is one of the most probable initiators of organic molecules formation on Titan lower atmosphere and has also been suggested as a mechanism for triggering the prebiotic chemistry on Earth [7], for which the lower atmosphere of Titan may be a good mimic [8–11].

The possibility of lightning on Titan is supported by theoretical models and observations of Titan's troposphere during the last decade, which indicate that methane droplets may suddenly condense and undergo vertical motions in the Titan's atmosphere [12]. Most of the experiments reproduce a gas mixture close to the Titan's atmosphere, or at least to a part of its atmosphere, and then supply energy into this gas mixture to induce chemical reactions. Different plasma discharges have been shown to be good mimics to a planetary atmosphere providing insights into both physical and chemical processes of such atmosphere. Various studies of electron-molecule and ion-molecule reactions in the planetary atmosphere were presented recently. Namely results obtained by corona discharge were presented in [9–13], by DBD discharge in [14], by glow discharge in [15–17], by microwave discharge in [18], and by RF discharges in [10, 19, 20]. However, the mechanisms of such organic chemistry are still unclear.

2. Experiment

The experimental setup schematic drawing is shown in Figure 1. The special high vacuum stainless steel reactor was constructed for our experiments to prevent any oxygen contamination during the experiments. Nitrogen and methane flows were automatically controlled by Bronkhorst controllers. The measurements were carried out at total gas flows 100 sccm at atmospheric pressure and laboratory temperature. The discharge electrode system had the standard config-

uration of the gliding arc discharge. The discharge was formed in the stable abnormal glow regime, and plasma was occurred between the electrodes at their shortest distance of 2 mm in the form of a plasma channel of 1 mm in its diameter. The reactor chamber volume was 0.5 l. The discharge was supplied by a DC stabilized HV source. Discharge breakdown voltage was 5500 V, a stable plasma channel was operating at 400 V at current of 30 mA during all presented experiments. The measurements were performed for different $N_2:CH_4$ ratios in the range from 1 % to 3 % of methane in nitrogen (both gases having quoted purities of 99.995 %) and admixture 1, 2 and 3 % of carbon dioxide (CO_2). The exhaust gas was sampled using the cold trap technique. The liquid nitrogen stainless steel trap (diameter of 15 mm, length of 165 mm, the total volume of 116 cm³) was mounted at the outlet of the reactor, as it is shown in Figure 1, as a side removable arm. The sampling time was 5 min and all gas products were subsequently analysed by GC-MS. The sampling efficiency closed to 100 % was confirmed by in situ FTIR done behind the sampling point (see description of experimental device). Sampling time was adjusted based on preliminary experiments to avoid saturation at GC-MS measurements.

3. Results

The chromatogram given in Figure 2 corresponding to experiment at nitrogen, methane and carbon dioxide are shown as typical examples. All the peaks have been identified using their retention time in the sequence and their mass spectra using the program MSD Chemistry with the NIST MS library [21]. The peaks corresponding to nitrogen, methane and carbon dioxide as the original gas mixture were recorded at retention times under 2 minutes and thus they are not depicted in Figure 2.

The other peaks of the highest intensity in these chromatograms can be attributed to lower hydrocarbons and nitrile compounds. The dominant peak corresponds to hydrogen cyanide (HCN), the second dominant peak is acetylene (C_2H_2) and the third main product is acetonitrile (CH_3CN). Other abundant determined products were ethane (C_2H_6), ethylene (C_2H_4), cyanogen (C_2N_2), propenenitrile (C_2H_3CN), and propanenitrile (C_2H_5CN). A lot of nitriles, many hydrocarbons, and even aromatic compound, have been detected from the analysis of all obtained chromatogram. No oxygen containing compounds were detected because of our special high vacuum reactor preserved any oxygen contamination. The results for selected C_2 -hydrocarbons (ethane, ethylene and acetylene) and nitriles (hydrogen cyanide, acetonitrile and cyanogen) are shown in 1. The dominant hydrocarbon was acetylene and its amount increased nearly directly proportionally to the carbon dioxide concentration. Ethane and ethylene show the similar trend of relative intensity. Relative intensities of hydrogen cyanide,

acetonitrile and cyanogen as the main detected compounds are depicted on carbon dioxide concentration in the gas mixture again at both total gas flows. These compounds present various chemical structures with different number of carbon and nitrogen atoms.

A typical FTIR spectrum showing the products formed in the nitrogen discharge fed by 1% of CH_4 and 1% of CO_2 is shown in Figure 3. Similar spectra were observed for other $N_2:CH_4:CO_2$ ratios. Hydrogen cyanide (HCN) was found to be the most abundant product at wavenumbers of 1430 cm⁻¹ and of 720 cm⁻¹. It is in agreement with [17]. Ammonia (NH_3) was identified at 966 cm⁻¹ which was surprising because ammonia was not detected in previous experimental studies. The other major products were acetylene (C_2H_2) as well as carbon monoxide (CO) and water (H_2O). These products were recognized in all $N_2:CH_4:CO_2$ gas mixtures. The products concentrations are strongly dependent on the composition of the gas mixtures.

Relative quantifications of selected hydrocarbons were done in dependence on the methane concentration and gas mixture flow rate. The relative intensity was calculated as an area under the recorded peaks. Figures 4 and 5 shows dependences of the calculated relative hydrocarbon intensity on carbon dioxide additions and discharge current. Figure 4 shows the quantitative analysis of HCN (1430 cm⁻¹) and Figure 5 NH_3 (966 cm⁻¹) formed under different experimental conditions. The increase of the initial discharge current from 15 mA to 40 mA leads to increase in the product yield of this compound. The admixture of 1% CO_2 had little influence on HCN and NH_3 production. However, there is visible effect of CO_2 addition to nitrogen methane mixtures with 1% methane with the yield of HCN increasing with increasing CO_2 concentrations. This is in contrast to earlier study [22] that suggested that the kinetics of HCN formation slows down in presence of CO, showing an inhibiting role of CO on HCN formation.

4. Conclusion

The gaseous phase products formed in the atmospheric glow discharge fed by different mixtures of nitrogen plus methane (1 % and 3 %) and admixture of carbon dioxide (1, 2 and 3 %) were determined by in situ FTIR and GC-MS analysis. The discharge was operated in the flowing regime at different discharge currents at laboratory temperature. An in-situ FTIR technique for the exhaust gas phase sampling was successfully used for chemical analysis to deduce the gas composition in the $N_2:CH_4:CO_2$ reactive gas mixture mimics of Titan's atmosphere. Various nitrile compounds and hydrocarbons were observed in all experiments. HCN was identified as the major gas phase product in all of measurements. Others minor products detected were C_2H_2 , NH_3 , CO_2 , CO and also some nitrile oxides. These results are consistent with the Titan's atmospheric composition because the

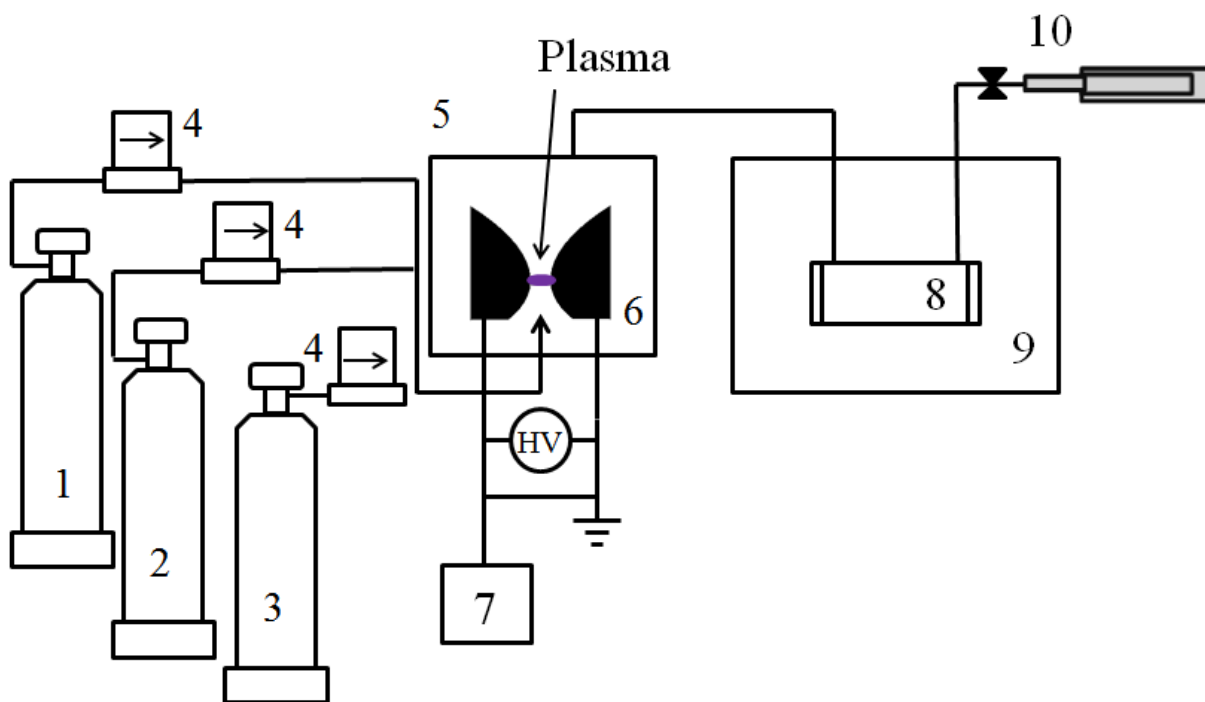


Figure 1. Experimental setup. 1- storage bottle of nitrogen, 2- storage bottle of methane, 3- storage bottle of carbon dioxide, 4- Bronkhorst controllers, 5- reactor body, 6- electrode system, 7- oscilloscope, 8- IR gas cell, 9- FTIR spectrometer, 10- cold trap.

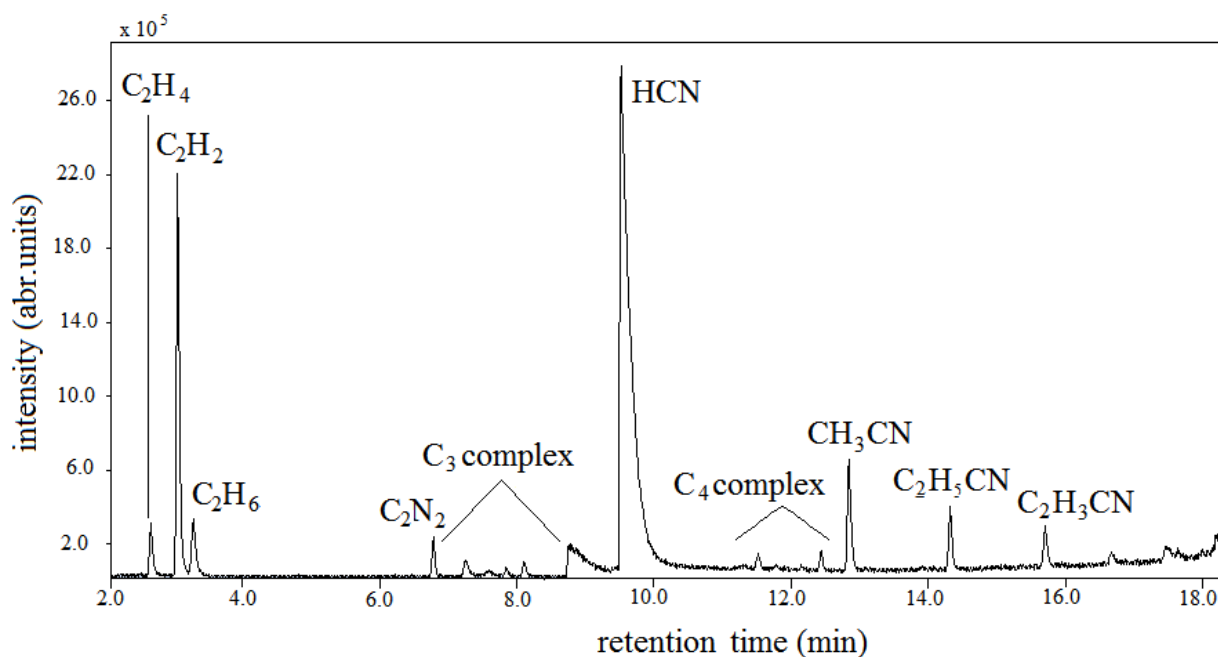


Figure 2. An example of exhaust gas chromatogram in 98 % N₂:1 % CH₄:1 % CO₂ gas mixture.

concentration of CO ₂ (%)	1% of CH ₄ concentration			3% of CH ₄ concentration		
	0	1	2	0	1	2
acetylene	1.45×10^6	1.72×10^6	2.12×10^6	1.79×10^6	2.77×10^6	3.33×10^6
ethene	1.94×10^5	2.63×10^5	3.02×10^5	2.69×10^5	3.19×10^5	3.24×10^5
ethane	4.35×10^4	5.39×10^4	7.04×10^4	5.36×10^5	6.19×10^5	7.44×10^5
hydrogen cyanide	8.87×10^6	1.82×10^7	2.26×10^7	2.89×10^7	3.43×10^7	5.08×10^7
acetonitrile	9.28×10^5	1.86×10^6	3.43×10^6	2.15×10^6	2.70×10^6	3.60×10^6
cyanogen	2.81×10^5	4.23×10^5	8.06×10^5	4.15×10^5	6.16×10^5	8.26×10^5

Table 1. The list of selected compounds from GC-MS analysis. The relative intensity was calculated as an area under the recorded peaks (arbitrary unit).

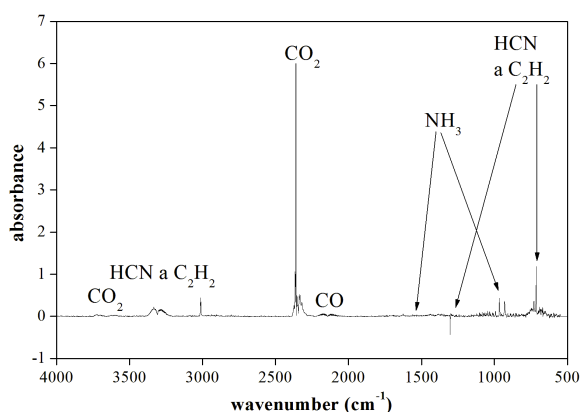


Figure 3. An example of IR spectrum in 98 % N₂:1 % CH₄:1% CO₂ gas mixture.

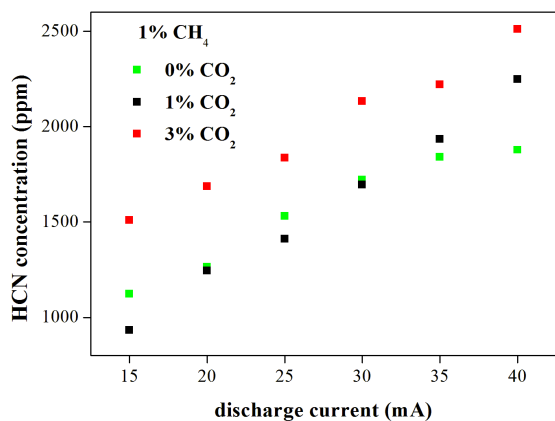


Figure 4. The dependence of hydrogen cyanide concentration on discharge current for different initial concentration of methane and carbon dioxide.

same compounds were detected during the Cassini-Huygens space mission. CO could have an effect on the atmospheric reactivity of Titan. The formation of organic molecules incorporating oxygen in gases could occur in the upper atmosphere of Titan where the dissociations of N₂ and CO₂ by VUV photons and magnetospheric electrons are possible. This fact clearly demonstrates that laboratory experiments can

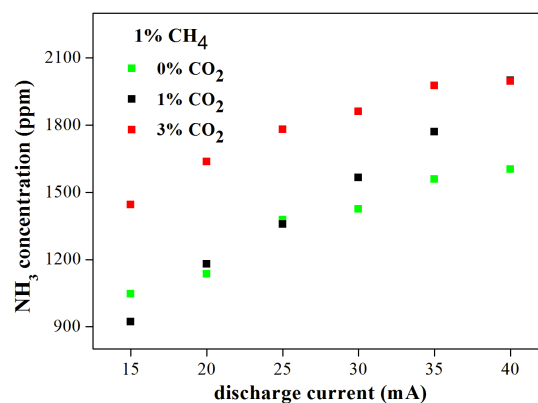


Figure 5. The dependence of ammonia concentration on discharge current for different initial concentration of methane and carbon dioxide.

be used for prediction of both the presence and possible concentrations of compounds which have not been detected, yet. These simple organics should be tracers of the chemical groups constituting the dusty products.

Acknowledgements

The research was supported by Czech Ministry of Education, Youth and Sports, projects No. COST CZ LD15011, within the collaboration of the COST Action TD 1308, CEEPUS network AT-0063.

References

- [1] C.A. Nixon. Detection of propene in Titan's stratosphere. *Astrophys J*, 776(1), 2013.
- [2] V.A. Krasnopolsky. Chemical composition of Titan's atmosphere and ionosphere: Observations and the photochemical model. *Icarus*, 236:83–91, 2014.
- [3] K.L. Aplin. Atmospheric electrification in the solar system. *Surveys in Geophysics*, 27(1):63–108, 2006.
- [4] S. Vinatier. Vertical abundance profiles of hydrocarbons in titan's atmosphere at 15 degrees s and 80 degrees n retrieved from CASSINI/CIRS spectra. *Icarus*, 188(1):120–138, 2007.
- [5] R. Navarro Gonzalez. Corona discharge of titan's troposphere. *Life Sciences: Complex Organics in Space*, pages 1121–1133, 1997.

- [6] M.L. Cable. Titan tholins: Simulating titan organic chemistry in the cassini-huygens era. *Chemical Reviews*, 112(3):1882–1909, 2012.
- [7] S.L. Miller. A production of amino acids under possible primitive earth conditions. *Science*, 117(3046):528–609, 1953.
- [8] G. Horvath. Methane decomposition leading to deposit formation in a dc positive ch₄-n₂ corona discharge. *Plasma Chemistry and Plasma Processing*, 31(2):327–335, 2011.
- [9] S.I. Ramirez. Organic chemistry induced by corona discharges in titan's troposphere: Laboratory simulations. *Space Life Sciences*, 36(2):274–280, 2005.
- [10] C. Szopa. Pampre: A dusty plasma experiment for titan's tholins production and study. *Planetary and Space Science*, 54(4):394–404, 2006.
- [11] E. Sciamma-O'Brien. The titan haze simulation experiment on cosmic: Probing titan's atmospheric chemistry at low temperature. *Icarus*, 243(0):325–336, 2014.
- [12] P. Lavvas. Aerosol growth in titan's ionosphere. *Proceedings of the National Academy of Sciences*, 110(8):2729–2734, 2013.
- [13] R. Navarro-Gonzalez. Production of hydrocarbons and nitriles by electrical processes in titan's atmosphere. *Space Life Sciences*, 27(2):271–282, 2001.
- [14] G. Horvath. Packed bed dbd discharge experiments in admixtures of n₂ and ch₄. *Plasma Chemistry and Plasma Processing*, 30(5):565–577, 2010.
- [15] J.M. Bernard. Experimental simulation of titan's atmosphere: Detection of ammonia and ethylene oxide. *Planetary and Space Science*, 51(14):1003–1011, 2003.
- [16] J.M. Bernard. Reflectance spectra and chemical structure of titan's tholins: Application to the analysis of cassini-huygens observations. *Icarus*, 185(1):301–307, 2006.
- [17] C.D. Pintassilgo. Methane decomposition and active nitrogen in a n₂-ch₄ glow discharge at low pressures. *Plasma Sources Science and Technology*, 8(3):463–478, 1999.
- [18] Y. Sekine. The role of organic haze in titan's atmospheric chemistry i. laboratory investigation on heterogeneous reaction of atomic hydrogen with titan tholin. *Icarus*, 194(1):186–200, 2008.
- [19] T. Gautier. Nitrile gas chemistry in titan's atmosphere. *Icarus*, 213(2):625–635, 2011.
- [20] H. Imanaka. Laboratory experiments of titan tholin formed in cold plasma at various pressures: Implications for nitrogen-containing polycyclic aromatic compounds in titan haze. *Icarus*, 168(2):344–366, 2004.
- [21] U.S. Department of Commerce. 2009 National institute of standards and technology.
- [22] B. Fleury. Influence of co on titan atmospheric reactivity. *Icarus*, 238(0):221–229, 2014.

The Influence of Admixtures on the Composition of Products by Nitrogen-Methane Atmospheric Glow Discharge

Torokova L.^{1,2}, Mazankova V.¹, Krcma F.¹, Mason N.J.², Matejcek S.³

¹Faculty of Chemistry, Brno University of Technology, Purkynova 119, 612 00, Brno, Czech Republic

²Department of Physics and Astronomy, Open University, Walton Hall, Milton Keynes MK7 6AA, UK

³Department of Experimental Physics, Comenius University, Mlynska dolina F-2, 842 48 Bratislava, Slovakia

This work extends our experimentally studies with simulation of Titan's atmosphere by atmospheric glow discharge. This work is devoted to estimate the influence of CO₂ and/or CO on reactivity in the Titan's atmosphere. The exploration of planetary atmosphere is being advanced by the exciting results of the Cassin-Huygens mission to Saturn and Titan, its most famous moon. Most of the studies were mainly interested in the reactivity of the N₂-CH₄ gaseous mixture and with the primary products of reactions, but the atmosphere of Titan also contains oxygenated volatile species.

Keywords: Titan's atmosphere, atmospheric glow discharge, FTIR spectroscopy

1 INTRODUCTION

Atmospheric pressure glow discharges are of significant interest for a wide range of applications such as pollution control, material processing or surface treatment. Among the many different types of atmospheric pressure discharges the DC glow discharges is one of the most deeply studied [1, 2]. The gliding arc configuration has been shown to be a good mimic of planetary atmospheres [3] being used to replicate physical and chemical conditions in Titan. Titan is the largest moon in Saturn's lunar system and the only one with a dense atmosphere-atmospheric pressure is approximately 1.5×10^5 Pa [4-6]. It is the only lunar body with a substantial containing significant quantities of methane (CH₄) and nitrogen (N₂) in its atmosphere [7]. Chemical processes in Titan's atmosphere are therefore able to create complex molecules containing C, N and H. This makes Titan our only planetary-scale laboratory for the synthesis of complex organics molecules [8]. In Titan's atmosphere, the dissociation of N₂ and CH₄ by solar ultraviolet radiation initiates chemical reactions that result in the formation of complex organic molecules.

The present work is focused on the experimental study of gaseous products produced in an atmospheric pressure glow discharge fed by

N₂-CH₄ gas mixtures with CH₄ concentrations in the range from 1 % to 4 % plus admixture of carbon dioxide (CO₂) from 1% to 4 %. The gaseous products were analyzed by Fourier-Transform-Infra-Red spectroscopy (FTIR).

2 EXPERIMENTAL APPARATUS

A simplified schematic drawing of the experimental set up is presented in Fig. 1. An atmospheric pressure DC glow discharge was created between two stainless steel electrodes separated by a 2 mm gap. The electrodes system had standard configuration of the gliding arc discharge but due to low applied power and low gas velocity the discharge is not moving along the electrodes. The discharge was formed in the stable abnormal glow regime with plasma channel of 1 mm in its diameter. The stainless steel vacuum chamber (volume of 1 litre) was evacuated by a rotary oil pump to maintain an oxygen free system. The discharge was operated with an applied power in range 4 to 15 W in pure nitrogen enriched by 1-4 % of CH₄ with admixture of 1-3% of CO₂ total flow rate of 200 sccm. The flow rates through the reactor for both methane and nitrogen were regulated using MKS mass flow controllers. The exhaust gas was analyzed in-situ by FTIR spectroscopy.

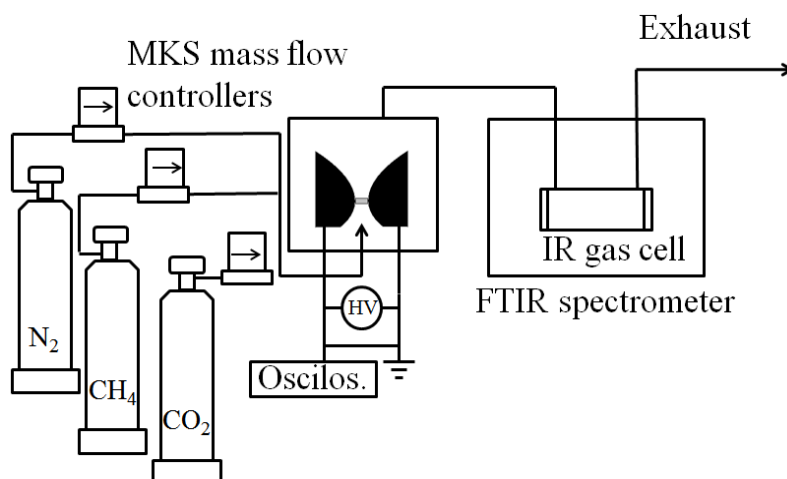


Fig.1: Schematic diagram of the experimental setup used for FTIR analysis of gaseous products of a DC glow discharge fed by various mixtures of N_2 - CH_4 - CO_2 .

3 RESULTS

A typical FTIR spectrum revealing the products formed in the nitrogen discharge fed by 2% of CH_4 and 1% of CO_2 is shown in Fig. 2. Similar spectra were observed for other N_2 - CH_4 - CO_2 molar ratios. The HITRAN spectral data individual absorption features was used for recognizing of specific compounds. Hydrogen cyanide (HCN) was found to be the most abundant product at wavenumbers of 1430 cm^{-1} and of 720 cm^{-1} . The other major

products were ammonia (NH_3) -966 cm^{-1} and acetylene (C_2H_2) -729 cm^{-1} as well as carbon monoxide (CO) and water. These products were recognized in all N_2 - CH_4 - CO_2 gas mixtures. The products concentrations are strongly depended on compositions of the gas mixture. Increasing the initial CH_4 concentration from 2% to 4% and also increasing admixture from 1% to 3% of CO_2 lead to increase in the products yield.

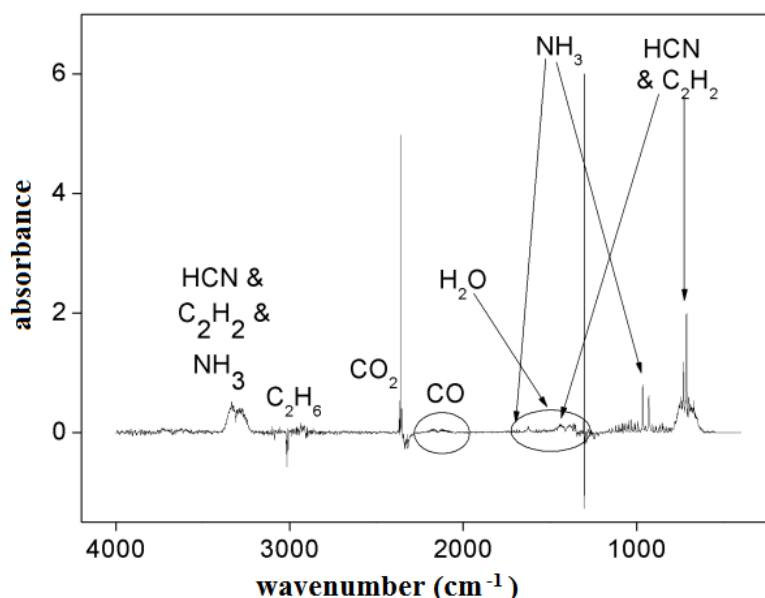


Fig.2: Sample spectrum of analysed products formed in a gas mixture 2% of CH_4 + 1% of CO_2 in N_2 .

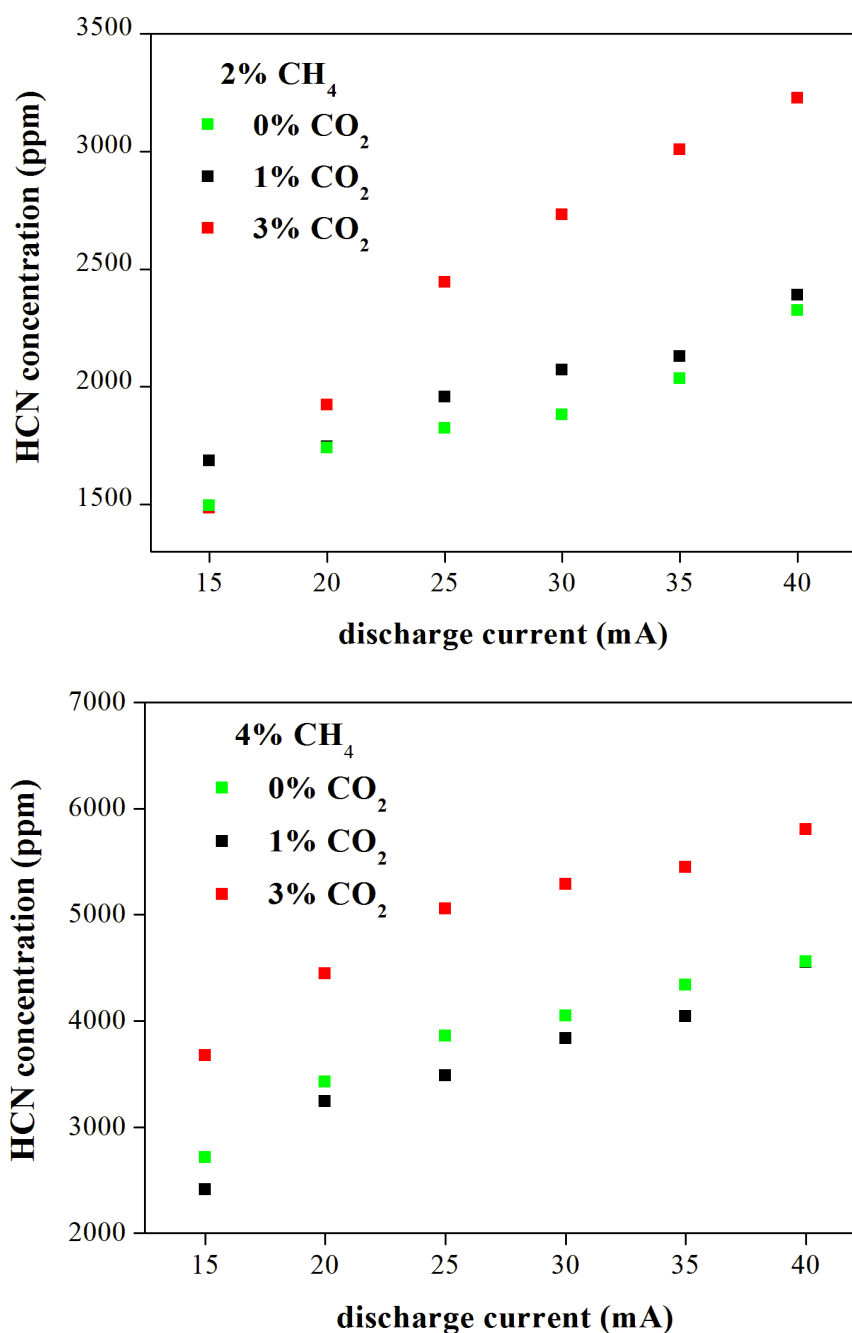


Fig.3: Concentration of hydrogen cyanide dependence on initial concentration of methane and also admixture of carbon dioxide.

Fig. 3 shows the quantitative analysis of HCN at 1430 cm^{-1} formed under different experimental conditions. Since these experiments have been carried out for different CH₄-N₂ mixture ratios and the same gas flow rates, the evolution of different product concentrations was found to depend strongly on the initial gas ratios. The dependence of product concentrations is strongly dependent on the different CH₄-N₂ gas mixtures. On the other hand it was proofed [9] that the kinetics of HCN formation

slows down in presence of CO, showing an inhibiting role of CO on HCN formation. In our experiments this influence was not recognize.

4 CONCLUSION

The gaseous phase products formed in the atmospheric glow discharge fed by different mixtures of N₂ plus CH₄ (2 % and 4 %) and admixture of CO₂ (1 and 3%) were determined by in situ FTIR analysis. The discharge was

operated in the flowing regime at different discharge currents at laboratory temperature. In situ FTIR technique for the exhaust gas phase sampling was successfully used for chemical analysis to deduce the gas composition in the N₂-CH₄-CO₂ reactive gas mixture mimics of Titan's atmosphere.

Various nitrile compounds and hydrocarbons were observed in all experiments. HCN was identified as the major gas phase product in all of measurements. Others minor products detected were C₂H₂, NH₃, CO₂, CO and also some nitrile oxides. These results are consistent with the Titan's atmospheric composition because the same compounds were detected during the Cassini-Huygens space mission. This fact clearly demonstrates that laboratory experiments can be used for prediction of both the presence and possible concentrations of compounds which have not been detected, yet. These simple organics should be tracers of the chemical groups constituting the dusty products.

Acknowledgements

This work has been supported by the EUROPLANET TNA2 and CEEPUS network AT-0063.

REFERENCES

- [1] Machala Z, Marode E, Laux C O, Kruger Ch, Journal of Advanced Oxidation Technologies 7 (2004) 133.
- [2] Kloc P, Wagner H E, Trunec D, Navratil Z, Fedoseev G, Journal of Physics D-Applied Physics 43 (2010) 34.
- [3] Torokova L, Watson J, Krcma F, Mazankova V, Mason N J, Horvath G, Matejcik S, Contributions to Plasma Physics 55 (2015) DOI 10.1002/ctpp.201400052 – in print.
- [4] Aplin K L, Surveys in Geophysics 27 (2006) 63.
- [5] Lavvas P, Yelle R V, Koskinen T, Bazin A, Vuitton V, Vigren E et al., Proceedings of the National Academy of Sciences of the United States of America 110 (2013) 2729.
- [6] Shebanits O, Wahlund J E, Mandt K, Agren K, Edberg N J T, Waite J H, Planetary and Space Science 84 (2013) 153.
- [7] Horst S M, Tolbert M A, Astrophysical Journal.
- [8] Jagota S, Kawai J, Deamer D, McKay C, Khare B, Beeler D, Planetary and Space Science. 103 (2014) 167.
- [9] Fleury B, Carrasco N, Gautier T, Mahjoub A, He J, Szopa C, et al., Influence of CO on Titan atmospheric reactivity, Icarus, 2014 8//;238(0):221-9.

CPP

Contributions to Plasma Physics

www.cpp-journal.org

Editors:

M. Bonitz, Kiel (Editor-in-Chief)
T. Klinger, Greifswald
K.-H. Spatschek, Düsseldorf

Associate Editors:

C. Franck
E. Kovacevic
A. v. Keudell

Managing Editors

D. Naujoks

Coordinating Editor

M. Dewitz

WILEY-VCH

REPRINT

Gas Chromatography Analysis of Discharge Products in N₂-CH₄ Gas Mixture at Atmospheric Pressure: Study of Mimic Titan's Atmosphere

L. Torokova^{1,2*}, J. Watson³, F. Krcma¹, V. Mazankova¹, N.J. Mason², G. Horvath^{2,4}, and S. Matejčík⁴

¹ Faculty of Chemistry, Brno University of Technology, Purkynova 118, 612 00 Brno, Czech Republic

² Department of Physics and Astronomy, Open University, Milton Keynes MK7 6AA, United Kingdom

³ Planetary and Space Sciences Research Institute, Open University, Milton Keynes MK7 6AA, United Kingdom

⁴ Department of Experimental Physics, Comenius University, Mlynska dolina F-2, 842 48 Bratislava, Slovakia

Received 19 August 2014, revised 22 December 2014, accepted 06 January 2015

Published online 25 March 2015

Key words Atmospheric pressure glow discharge, nitrogen-methane gas mixture, gas chromatography analysis.

In this paper, we report presence of various organic products formed in a flowing atmospheric glow discharge fed by gas mixture containing 1-5 % of methane in nitrogen, which mimics the Titan's atmosphere. Gaseous products from the discharge exhaust were analysed by Gas Chromatography with Mass Spectrometry (GC-MS). The experimental results revealed C₂H₂, HCN, and CH₃CN as the major products. Various hydrocarbons and nitriles were the other determined gaseous products. Whilst many of these compounds have been predicted and/or observed in the Titan atmosphere, the present plasma experiments provide evidence of both the chemical complexity of Titan atmospheric processes and the mechanisms by which larger species grow prior to form the dust that should cover much of the Titan's surface.

© 2015 WILEY-VCH Verlag GmbH & Co. KGaA, Weinheim

1 Introduction

Simple organic molecules play an important role in the formation of complex organics in planetary atmospheres. Recently, several lower hydrocarbons and nitriles have been confirmed in the atmosphere of Titan, the largest satellite of the Saturn. The first detailed information was brought by Voyager space mission in 1980. More important complex information about Titan atmosphere was obtained from Cassini-Huygens mission in 2005. Its atmosphere composition is principally nitrogen with 2-6 % methane and some trace gases as nitriles (HCN, HC₃N, HC₅N, and C₂N₂) and lower molecule hydrocarbons (C₂H₂, C₂H₄, C₂H₆, C₃H₈, C₃H₄) as well as hydrogen [1, 2]. These compounds can be produced by low power discharges in the methane clouds [3, 4] or by dissociation of nitrogen and methane either by solar induced photolysis, photodissociation or by electron impact. The same processes generate also charged particles that are transported through the atmospheric clouds. Neutralization of these charged particles leads to high power discharges like lightning within the clouds which can induce other chemical reactions in the troposphere [5]. Organic radicals produced by electron impact could also supply a significant fraction of Titan's haze and surface material [6]. Lightning activity is one of the most probable initiators of organic molecules formation on Titan lower atmosphere and has also been suggested as a mechanism for triggering the prebiotic chemistry on Earth [7], for which the lower atmosphere of Titan may be a good mimic [8-11]. The possibility of lightning on Titan is supported by theoretical models and observations of Titan's troposphere during the last decade, which indicate that methane droplets may suddenly condense and undergo vertical motions in the Titan's atmosphere [12].

Titan's chemical and physical properties are similar to the assumed prehistoric properties of the Earth. The Titan's tropospheric temperature is in such range that methane exists in three phases, like as water on the Earth.

* Corresponding author. E-mail: xctorokova@fch.vutbr.cz

Methane on Titan thus probably plays a role similar to that of water on Earth, and hydrologic cycles based on methane are possible [13-16]. The methane raindrops may evaporate before they reach the ground [6, 17]. The atmospheric temperature falls from its surface value of 94 K at the pressure of 1.5 bar to a minimum of 71 K at the height of 42 km and pressure of 0.128 bar at the tropopause. It is therefore impossible that nitrogen clouds can be formed in the Titan's atmosphere [5]. At low temperatures measured on the Titan surface (about 94 K), it is hard to imagine an origin of life [18]. The physical state of methane is liquid on the surface; between particles are Van der Waals intermolecular forces. The bigger particles in the atmosphere are formed by negatively charged organic aerosol covered with hydrocarbon dust [19].

Several theoretical models of the Titan's atmosphere were used, many of which consider three-body electron attachment to radicals or collisional charging of aerosols as the source of negatively charged species [5, 20]. Ionic chemistry is presented in [21] by a theoretical model with a scheme of reactions forming many interesting compounds on Titan (like HCN, C₂H₂, C₂H₄, C₃H₈, or C₆H₆).

Finally, the last approach to study the chemistry in the Titan's atmosphere is an experimental simulation in laboratories. Most of the experiments reproduce a gas mixture close to the Titan's atmosphere, or at least to a part of its atmosphere, and then supply energy into this gas mixture to induce chemical reactions. Different plasma discharges have been shown to be good mimics to a planetary atmosphere providing insights into both physical and chemical processes of such atmosphere. Various studies of electron-molecule and ion-molecule reactions in the planetary atmosphere were presented recently. Namely results obtained by corona discharge were presented in [9, 22], by DBD discharge in [23], by glow discharge in [24-26], by microwave discharge in [27], and by RF discharges in [10, 28, 29].

However, the mechanisms of such organic chemistry are still unclear. Several researchers used plasmas to simulate the Titan's atmosphere and generate solid aerosols (named tholins) [6, 30-32] that cause haze which covers the Titan's surface. In order to understand formation of these aerosols, it is necessary to explore the chemistry of such plasmas. Tholins are consisting mainly of polymeric sets of C_xH_yN_z compounds [33, 34].

The present work is focused on the experimental study of gaseous products produced in the atmospheric pressure glow discharge fed by a CH₄-N₂ gas mixture with CH₄ contents in the range from 1 % to 5 %. The gaseous products were measured qualitatively as well as quantitatively in dependence on different methane concentration in nitrogen by gas chromatography coupled with mass spectrometry. This study will help to understand the gaseous phase chemistry on Titan's atmosphere.

2 Experimental setup

2.1 Plasma reactor

The experimental setup schematic drawing is shown in Fig. 1. The special high vacuum stainless steel reactor was constructed for our experiments to prevent any oxygen contamination during the experiments.

Methane and nitrogen flows were automatically controlled by MKS mass flow controllers. The measurements were carried out at two total gas flows (100 sccm and 200 sccm) at atmospheric pressure and laboratory temperature. The discharge electrode system had the standard configuration of the gliding arc discharge. A pair of stainless steel electrodes was positioned in parallel at the reactor centre but created plasma was not gliding due to the low supplied energy as well as a low flow rate. The discharge was formed in the stable abnormal glow regime, and plasma was occurred between the electrodes at their shortest distance of 2 mm in the form of a plasma channel of 1 mm in its diameter. The reactor chamber volume was 0.5 l.

Electrical parameters were measured by a Tektronix two channel oscilloscope TDS2012. Applied high voltage was determined using a high voltage probe Tektronix P6015A, current was measured as a voltage drop on a 10 Ω ballast resistor. The discharge was supplied by a DC stabilized HV source. Discharge breakdown voltage was 5500 V, a stable plasma channel was operating at 400 V at current of 30 mA during all presented experiments. The measurements were performed for different CH₄-N₂ ratios in the range from 1 % to 5 % of methane in nitrogen (both gases having quoted purities of 99.995 %).

The reactor was cleaned before every change of experimental conditions, and the system was evacuated by a rotary oil pump down to base pressure of 1 Pa for one hour to obtain oxygen free conditions. The stable reaction gas mixture at the flow rate of 200 sccm was obtained within 20 min due to gas flow and reactor chamber volume;

40 min were needed at the flow rate of 100 sccm. The same times were applied after the discharge ignition to obtain stable conditions as it was confirmed recently by in situ PTR-MS measurements [35].

The exhaust gas was sampled using the cold trap technique. The liquid nitrogen stainless steel trap (diameter of 15 mm, length of 165 mm, the total volume of 116 cm³) was mounted at the outlet of the reactor, as it is shown in Fig. 1, as a side removable arm. The sampling time was 5 min and all gas products were subsequently analysed by GC-MS. The sampling efficiency closed to 100 % was confirmed by in situ FTIR done behind the sampling point (see description of experimental device given recently in [36]). Sampling time was adjusted based on preliminary experiments to avoid saturation at GC-MS measurements.

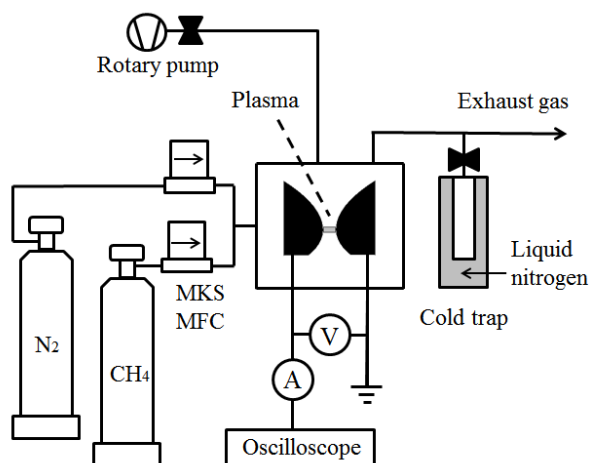


Fig. 1 Schematic diagram of the plasma experimental apparatus.

2.2 Analysis of gaseous products

GC-MS analysis of discharge exhaust gas was performed in all experiments. Gaseous samples immersed in liquid nitrogen trap were heated to the laboratory temperature and the resultant gas sample for GC-MS analysis was taken using a lock syringe just before being immediately analysed.

Before sample injection, a blank experiment was performed under the same analytical conditions. No specific contamination was detected in the blank except usual column releases. Only water traces were detected in the blank, which is present in the system all the time.

GC-MS analysis was carried out using an Agilent Technologies 6890 gas chromatograph coupled to a quadrupole mass spectrometer 5973. Separation was performed on a J & W GS-Q PLOT column (30 m length, 0.32 mm internal diameter) using helium flow of 2 sccm as the carrier gas. Injection was at a 5:1 split and injector temperature was 220 °C. The GC oven temperature was held for 2 min at 35 °C and then increased with the step of 10 °C min⁻¹ to 220 °C, whereas the final temperature was held for 5 min. The MS was operated in an electron impact (70 eV) mode and scanned between 12-120 amu at approximately 11 scans per second.

3 Results and discussion

3.1 Evolution of the gas products in the gas mixture

Three identified chromatograms given in Fig. 2a)-c) corresponding to three experiments at 1 %, 3 % and 5 % of CH₄ in N₂ are shown as typical examples. All the peaks have been identified using their retention time in the sequence and their mass spectra using the program MSD Chemistry with the NIST MS library [37]. The topological formulas of hydrogen cyanide compound and its experimental mass spectrum compared to theoretical one from NIST database are shown in Fig. 3. This comparison showed a good agreement between peaks at masses of 26, 27 and 28. This means the NIST database can be correctly used for the identification of all products.

The peaks corresponding to nitrogen and methane as the original gas mixture were recorded at retention times under 2 minutes and thus they are not depicted in Fig. 2. The other peaks of the highest intensity in these chromatograms can be attributed to lower hydrocarbons and nitrile compounds. The dominant peak corresponds to

hydrogen cyanide (HCN), the second dominant peak is acetylene (C_2H_2) and the third main product is acetonitrile (CH_3CN). Other abundant determined products were ethane (C_2H_6), ethylene (C_2H_4), cyanogen (C_2N_2), propenenitrile (C_2H_3CN), and propanenitrile (C_2H_5CN). Totally, more than 20 species (see in Table 1), including a lot of nitriles, many hydrocarbons, and even two aromatic compounds, have been detected from the analysis of all obtained chromatograms independently on the methane concentration.

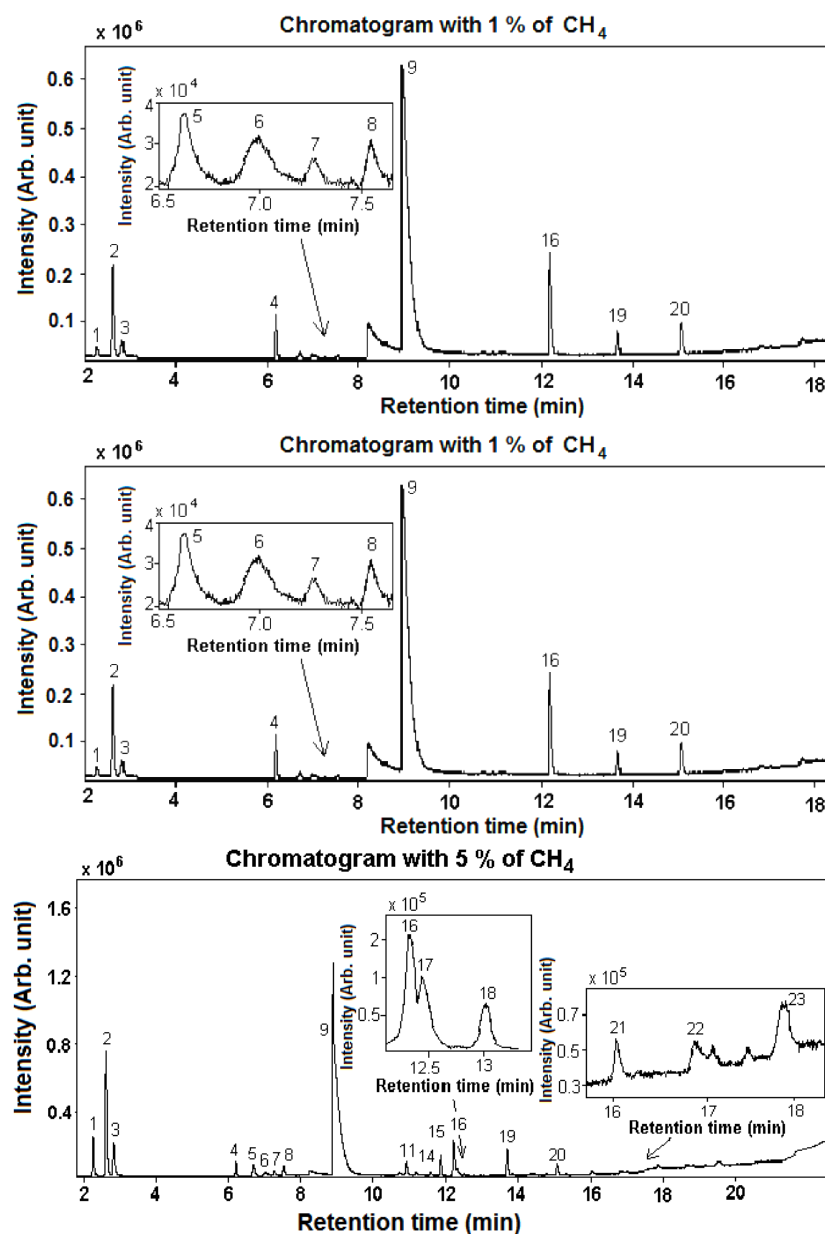


Fig. 2 Chromatograms from GC-MS analysis of gas samples trapped during experiments with 1 % -5 % of CH_4 in the gas mixture. Peaks are numbered according to Table 1. Minor peaks are shown in the immersed graphs.

The chromatograms for samples produced with 1 % and 3 % of CH_4 in the mixture seem to be similar, with just a small increase of the peak intensities. In contrary, new peaks can be observed in the chromatogram analysing exhaust gas in nitrogen with 5 % of CH_4 . These peaks were identified as hydrocarbons based on their retention time and their mass spectra. Hydrocarbons containing three carbon atoms (C_3 complex) are eluted as propene, propane, propyne and propadiene. C_4 hydrocarbons are identified as butene-3-yne, 1,3-butadiyne,

1,3-butadiene and the last is 1,2-butadiene. A small signals corresponding to heavier complex C_xH_yN compounds (like 2-propenenitrile, propanenitrile, 2-methylpropenenitrile and the last 2-methylpropanenitrile) were detected, too.

The higher hydrocarbons can be also detected for retention times longer than 16 min. Two aromatic compounds were detected as benzene and toluene in this case. As it was pointed above, the list of all determined gaseous compounds is given in Table 1. No oxygen containing compounds were detected because of our special high vacuum reactor preserved any oxygen contamination.

Besides gaseous discharge products, the formation of small amount of solids was detected, too. These deposits were observed at the electrode surfaces as well as on the discharge reactor bottom. The electrode deposits were analysed by X-ray photoelectron spectroscopy that confirmed their composition from nitrogen and carbon; it was impossible to carry out their full structure analysis because of their small amount and structural non-uniformity.

Table 1 The list of detected compounds

Detected compounds in our experiment	Formula	Peak classified in chromatogram	Retention time [min]	Detected in other lab. experiments
Aliphatic hydrocarbons				
Acetylene*	C_2H_2	2	2.631	[9, 24, 28, 38]
Ethylene*	C_2H_4	1	2.284	[9, 24, 28, 38]
Ethane*	C_2H_6	3	2.854	[9, 24, 28, 38]
Propene*	C_3H_6	5	6.587	[9, 28, 38, 39]
Propane*	C_3H_8	6	7.073	[9, 24, 28, 38, 39]
Propyne*	C_3H_4	7	7.305	[24, 28, 39]
1,2-Propadiene*	C_3H_4	8	7.566	[24, 28]
2-Butene	C_4H_8	10	10.658	[9, 28, 38, 39]
Butene-3-yne	C_4H_4	11	10.970	[28, 39]
2-Butyne	C_4H_6	13	11.398	[28, 39]
1,3-Butadiyne*	C_4H_2	14	11.525	[24, 28, 39]
1,3-Butadiene*	C_4H_6	15	11.880	[28]
1,2-Butadiene	C_4H_6	12, 17	11.192, 12.461	[28]
Cyclic compounds				
Benzene*	C_6H_6	22	16.885	[24, 28, 39]
Toluene*	C_7H_8	23	17.875	[39]
Nitriles				
Hydrogen cyanide*	HCN	9	8.982	[9, 24, 28, 38]
Acetonitrile*	CH_3CN	16	12.246	[24, 28, 39]
Cyanogen*	C_2N_2	4	6.228	[24, 28]
2-Propenenitrile*	C_2H_3CN	21	16.010	[28]
Propanenitrile*	C_2H_5CN	19	13.857	[9, 24, 28, 38]
2-Methylpropenenitrile	C_3H_5CN	20	15.153	
2-Methylpropanenitrile	C_3H_7CN	18	13.031	[9, 28, 38, 39]

* Detected in Titan's atmosphere [21, 40-43].

Compounds detected in Titan's atmosphere by the instruments on the board of the Cassini-Huygens mission are also marked by * in Table 1 [21, 40-43]. Besides them, some of lower molecule hydrocarbons as 2-butene, butane-3-yne, 2-butyne and 1,2-butadiene were detected in presented laboratory experiments, but not detected on Titan, yet. Moreover, two other nitriles (2-methylpropanenitrile and 2-methylpropenenitrile) were not detected on Titan, yet.

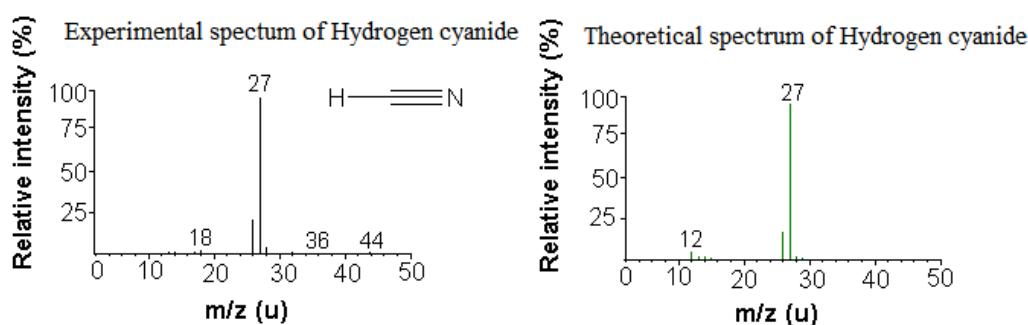


Fig. 3 Experimental (left) and theoretical (right) spectrum of hydrogen cyanide. The topological scheme of hydrogen cyanide is given in the left spectrum (NIST MS database [37]).

3.2 Relative quantifications of hydrocarbons

Relative quantifications of selected hydrocarbons were done in dependence on the methane concentration and gas mixture flow rate. The relative intensity was calculated as an area under the recorded peaks. Fig. 4 shows dependences of the calculated relative hydrocarbon intensity on methane additions for two different gas flow rates (100 and 200 sccm).

The results for selected C_2 -hydrocarbon compounds (ethane, ethylene and acetylene) are shown in Fig. 4-left. The dominant compound was acetylene and its amount increased nearly directly proportionally to the methane concentration. Ethane and ethylene show the similar trend of relative intensity but at the higher methane concentration their intensities are nearly independent.

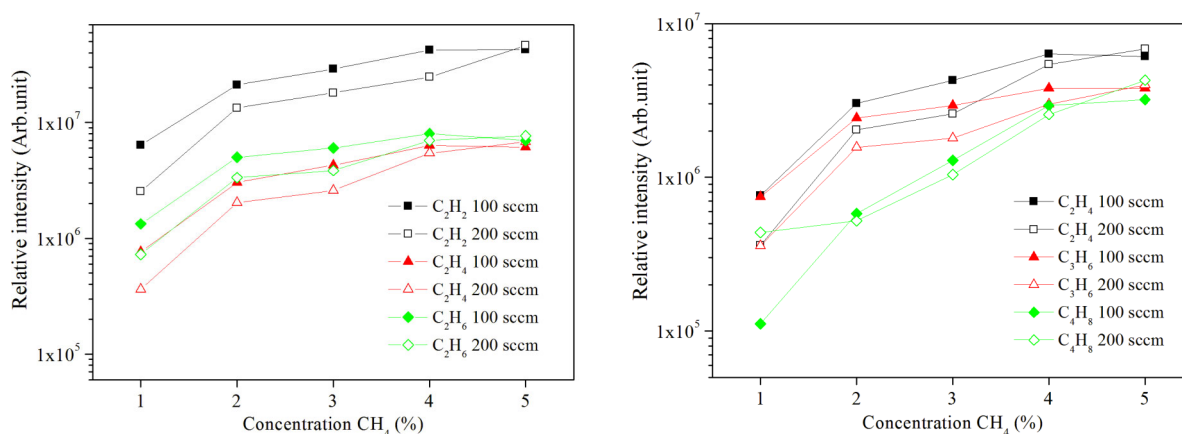


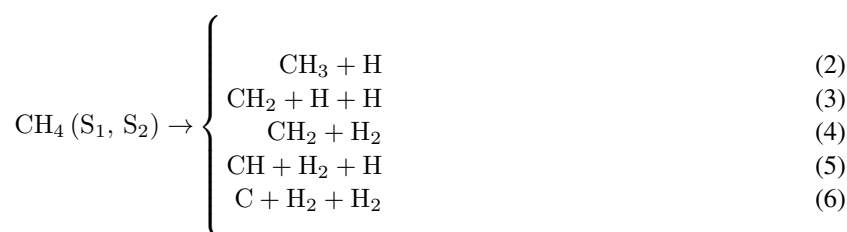
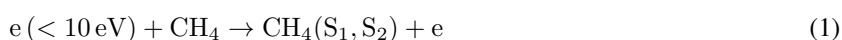
Fig. 4 The dependences of relative intensity on methane addition in nitrogen gas. Left: C_2 -hydrocarbons (ethane, acetylene and ethylene); right: C_2 , C_3 , C_4 hydrocarbons (ethylene, propene and 2-butene).

Dependences of relative intensity for selected C_2 , C_3 , C_4 hydrocarbon compounds (ethene, propene and 2-butene) are shown in Fig. 4-right. Relative intensities of these compounds are increasing with increasing the methane concentration in nitrogen gas mixture more strongly than in case of acetylene and they show no saturation. Their amounts are about two times higher at lower gas mixture flow rate (from 100 to 200 sccm). This means that residence time in discharge channel vicinity is a key parameter for the synthetic processes. This is in a good agreement with the experiments done in stationary systems where bigger molecules or even solid deposits and soot can be synthesized effectively [31]. A different result can be observed only in the case of the 5% methane in nitrogen mixture. The relative intensity of all determined products is higher for 100 sccm than for 200 sccm gas flow. It can be assumed that some other ways of synthesis could take place and various more complex species can be created under these conditions. Thus, formation of lower molecule compounds starts to increase while production of higher complicated compounds decreases as well as some dusty hydrocarbons on the electrodes.

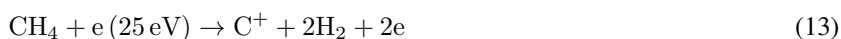
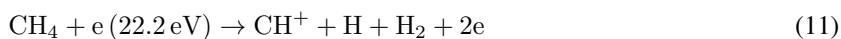
During the experiments with higher concentrations of methane the solid hydrocarbons were formed on the walls inside the reactor.

The quantity of solid hydrocarbons was increasing with the increasing of concentration of methane in nitrogen gas mixture.

The formation of various hydrocarbons is initiated by the methane dissociation. The dissociative potential of C-H bond of CH₄ is less than 4.6 eV. The excited methane S₁ (9.6 and 10.4 eV) and S₂ (11.7 eV) [44], which are formed by the electron-methane collisions, are so unstable that rapidly dissociate into radicals such as CH₃, CH₂, CH, C. The corresponding reactions are as follows [45-47]



The reactions (2) and (3) lead to rapid dissociation of CH₄. Also the reaction of charge transfer N₂⁺ + CH₄ → N₂ + CH₃⁺ + H whose rate coefficient is large contributes to dissociation of CH₄. The initial concentration of CH₄ can decrease down to 10 % [26, 48]. If the electron energy is higher than 12.75 eV, direct ionization of CH₄ by the following channels is possible [44, 49]:



The above plasma reactions might be dominant reactions for H₂ generation as well as for the formations of CH₄, CH₃, CH₂, CH radicals and CH₄⁺, CH₃⁺, CH₂⁺ ions. As it is shown in Table 1, small hydrocarbons (≤ C₄) such as ethane, ethylene, acetylene, propane, propylene, propyne, 1,2-propadiene, 2-butene, butane-3-yne, 2-butyne, 1,3-butadiene, 1,3-butadiene, 1,2-butadiene are produced by electron collision reactions and consequent recombination reactions of methyl radicals. The yield and generation rate of hydrocarbons are of the following relationship C₂H₂ > C₂H₄ > C₂H₆ > C₃H₆ > C₃H₈ > C₃H₄ > C₃H₄ > other C₄ hydrocarbons.

The formation of the observed hydrocarbon products is assigned to complex plasma chemistry. The most important role in the hydrocarbon productions could play methyl, hydrogen and also nitrogen radicals. During the electron-methane collisions, a large amount of hydrogen radicals can be produced by excited dissociation and direct ionization of CH₄. The hydrogen radicals can react with CH₄ producing CH₃ radical and CH₃ concentration increases. Also highly excited nitrogen molecules can produce CH₃ and CH₂ radicals by collisions with CH₄ and CH₃, respectively. Acetylene, as the dominate hydrocarbon detected by ex-situ GC-MS analysis, is than formed by reactions of two CH₂ radicals CH₂ + CH₂ → C₂H₂ + 2H. This reaction chain was found to be highly important [50]. The fast consumption of CH₂ radicals within the plasma could explain the lack of expected C₂H₄ and C₂H₆ in our chromatograms. Also the reactions leading to formation of C₂H₄ and C₂H₆ have lower rate coefficients than the above mentioned reaction leading to acetylene formation [47]. This could explain lower concentrations of C₂H₄ and C₂H₆.

Our experimental results are in good agreement with the results from kinetic model presented in [49]. We could not detect any heavier compounds because the used GC column was optimized for lower molecule (max. C₆ or C₇) compounds detection (J & W GS-Q PLOT column). We have also detected two aromatic compounds benzene and toluene. These aromatic compounds are less abundant than it was reported in other laboratory experiments [22, 38].

3.3 Relative quantifications of nitro-compounds

The relative abundances of selected nitro-compounds are given in Fig. 5. Relative intensities of hydrogen cyanide, acetonitrile and propanenitrile as the main detected compounds are depicted on methane concentration in the gas mixture again at both total gas flows. These compounds present various chemical structures with different number of carbon atoms.

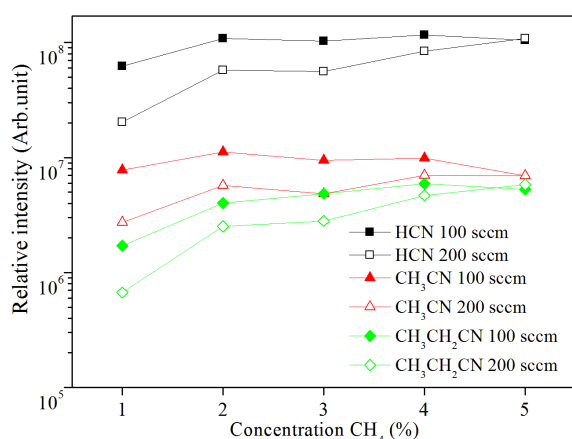
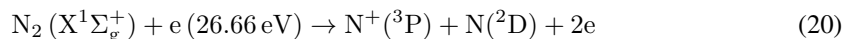
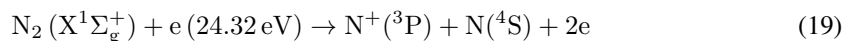
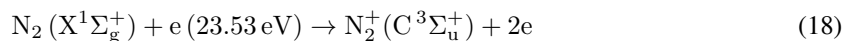
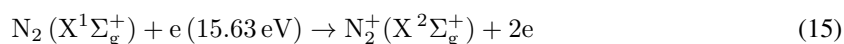
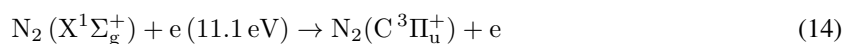


Fig. 5 The dependencies of relative intensity of hydrogen cyanide, acetonitrile and propanenitrile on methane addition in nitrogen gas.

The most dominant nitrile product was hydrogen cyanide in all cases. The profiles of all dependencies are similar with a rapid concentration increase between 1 % and 2 % of methane; abundances of hydrogen cyanide and acetonitrile are nearly independent at the higher methane concentrations. We can also observe different values at 5 % of methane in gas mixture as it was discussed before in the case of hydrocarbons. Relative intensities of nitro-compounds are increasing with increasing the methane concentration in nitrogen gas mixture and also with decreasing of the gas flow. The values are higher for 100 sccm than for 200 sccm in all experiments.

Since nitrogen is dominant component in our gas mixture, its reactions as electron impact excitation, ionization and dissociation also has a significant role in the reaction kinetics. Excitation, dissociation and ionization of N₂ molecule are described by following reactions [51]:



The population of N₂(C³Π_u) states (upper level of the detected second positive system) is mainly due to direct electron impact excitation from the ground state X¹Σ_g⁺ [52, 53]. This is a result of the collision with electrons via reaction (14), whose energy is above the excitation threshold (11.1 eV). Reaction (17) is responsible for the electron impact excitation of N₂ molecule from neutral ground state to N₂⁺(B²Σ_u) excited state, which is the upper level of the detected first negative system. Usually, the direct electron impact processes of high energy

threshold are less important in atmospheric pressure discharges but in our case they must be taken into the account due to a high intensity of local electric field near the shaped electrode surface. Moreover, the excited N_2 states can also induce CH_4 dissociation [10, 54]. Thus electrons are the primary initiators of the organic chemistry induced by the discharge.

The various nitriles formation (not only HCN, CH_3CN and C_2H_5CN presented in Fig. 5) is assigned to a complex plasma-physical chemistry. Situation is very similar as in the case of hydrocarbons. Hydrogen cyanide formation can be described by the direct reaction $CH_3 + N \rightarrow HCN + H_2$ or/and indirect by a two-step process $CH_3 + N \rightarrow H_2CN + H$; $H_2CN + N \rightarrow HCN + NH$ through a highly unstable intermediate product, H_2CN [10]. As it is shown in Table 1, nitriles such as hydrogen cyanide, acetonitrile, propanenitrile, propenenitrile, cyanogen, 2-methylpropenenitrile and 2-methylpropanenitrile are produced by electron collision reaction and recombination reaction of methyl radicals. The yield and generation rate of nitriles are of the following relationship $HCN > CH_3CN > C_2H_5CN > C_2H_3CN > C_2N_2 > C_3H_5CN > C_3H_7CN$.

The dissociation energies of N_2 , CH and CN bonds play an important role in the mechanisms of other nitrile compounds production. Knowledge of the nitriles chemistry is still to be improved. The main detected nitrile compounds were molecular structures with nitrile groups ($-CN$), amino groups ($-NH_2$, $-NH-$, and $-N<$), and/or imino groups ($-C=N-$) in our experiments. HCN, CH_3CN and C_2H_5CN have been previously detected in Titan's upper stratosphere. This suggests that the molecules identified in the upper atmosphere can be precursors of the aerosols and that knowledge of their abundance is crucial to the understanding of aerosol chemical formation pathways [12, 55]. Also in this case, there is a lot of data for the two body reactions [28, 56, 57] but such reactions play only a minor role at the atmospheric pressure.

It can be noted that ammonia was not detected in these experiments, however it was found in our previous experiments with in situ Fourier Transform Infrared spectroscopy (FTIR) products determination [36]. The explanation for this lack of NH_3 is the use of the stainless steel cold trap for the sorption of products from the reactor. Ammonia is known to be adsorbed on the stainless steel walls, thus it could be lost during the transfer to the GC-MS analysis. Another possible explanation is that ammonia could heterogeneously react with other compounds forming another nitro compounds in the liquid nitrogen trap.

The best agreement of our experimental results on nitro-compounds was obtained with the study [28].

4 Conclusions

The gas phase products formed in the atmospheric glow discharge fed by different mixtures of methane in nitrogen (from 1% to 5% of CH_4) were determined by GC-MS analysis. The discharge was operated in the flowing regime at laboratory temperature. The cold trap technique for the exhaust gas sampling was successfully used for chemical analysis to deduce the gas composition in the N_2 - CH_4 reactive gas mixture mimics of Titan's atmosphere.

Various hydrocarbon and nitrile compounds were observed in all experiments. The main hydrocarbons detected in our experimental setup were ethane, acetylene, ethene, propene, and 2-butene. The yields of these compounds are such as follows: $C_2H_2 > C_3H_6 > C_4H_8 > C_2H_6 > C_2H_4$. Acetylene is dominating hydrocarbon in our type of the discharge.

The yields of some nitrile compounds are such as follows: $HCN > CH_3CN > C_2H_5CN$. Hydrogen cyanide was dominating nitrile compound in our type of the discharge. This compound was also detected in large amounts in the Titan's atmosphere. We have also detected other nitriles such as acetonitrile, cyanogen, 2-propenenitrile, and propanenitrile. The results of our experiment are consistent with the Titan's atmospheric composition because the same compounds were detected during the Cassini-Huygens space mission. This fact clearly demonstrates that laboratory experiments, at least these which allow nitrogen dissociation, can be complementary used for prediction of both the presence and possible concentrations of compounds which have not been detected, yet. These simple organics should be tracers of the chemical groups constituting the tholins.

During the presented experiment, more than twenty compounds were detected. A few of them had never been detected in experimental simulations before, but they were expected since they had been observed in the Titan's atmosphere. The processes leading to the hydrocarbons formation were explained in many experimental and theoretical studies, based on bimolecular reactions that are dominant under low pressure conditions. The nitriles gas chemistry is still mostly unknown, and nitriles are often ignored in the Titan's atmospheric models

even though we know them both from observations and from computational models that they could be present in large amounts. Atmospheric pressure conditions could play an important role in the chemical processes of hydrocarbons and also nitriles because of high probability of three body reactions or clusters formation. The formation mechanisms of compounds detected on the Titan could be explained by two step reactions between some important intermediates. These molecules including nitrogen are also interesting in exobiology since they are known for their reactivity and as precursors of amino acids.

Acknowledgements This work has been supported by the ESF COST Actions CM0805 and EUROPLANET TNA2 and CEEPUS network AT-0063..

References

- [1] C.A. Nixon, D.E. Jennings, B. Bezard, S. Vinatier, N.A. Teanby, K. Sung K, et al., *Astrophysical Journal Letters* **776**, 14 (2013).
- [2] V.A. Krasnopolsky, *Icarus* **236**, 83 (2014).
- [3] K. L. Apli, *Surveys in Geophysics* **27**, 63 (2006).
- [4] S. Vinatier, B. Bezard, T. Fouchet, N.A. Teanby, R. de Kok, P.G.J. Irwin, et al., *Icarus* **188**, 120 (2007).
- [5] R. Navarro Gonzalez, S.I. Ramirez, *Life Sciences: Complex Organics in Space*, p. 1121-1133 (1997).
- [6] M.L. Cable, S.M. Horst, R. Hodyss, P.M. Beauchamp, M.A. Smith, P.A. Willis, *Chemical Reviews* **112**, 1882 (2012).
- [7] S.L. Miller, *Science* **117**, 528 (1953).
- [8] G. Horvath, M. Zahoran, N.J. Mason, S. Matejcik, *Plasma Chemistry and Plasma Processing* **31**, 327 (2011).
- [9] S.I. Ramirez, R. Navarro-Gonzalez, P. Coll, F. Raulin, *Space Life Sciences: Astrobiology: Steps toward Origin of Life and Titan before Cassini* **36**, 274 (2005).
- [10] C. Szopa, G. Cernogora, L. Boufendi, J. Correia, P. Coll, *Planetary and Space Science* **54**, 394 (2006).
- [11] E. Sciamma-O'Brien, C.L. Ricketts, F. Salama, *Icarus* **243**, 325 (2014).
- [12] P. Lavvas, R.V. Yelle, T. Koskinen, A. Bazin, V. Vuitton, E. Vigren, et al., *Proceedings of the National Academy of Sciences of the United States of America* **110**, 2729 (2013).
- [13] S.J. Desch, W.J. Borucki, C.T. Russell, A. Bar-Nun, *Reports on Progress in Physics* **65**, 955 (2002).
- [14] H. Lammer, T. Tokano, G. Fischer, W. Stumtner, G.J. Molina-Cuberos, K. Schwingenschuh, et al., *Planetary and Space Science* **49**, 561 (2001).
- [15] B. Bézard, *Icarus* **242**, 64 (2014).
- [16] E. Lellouch, B. Bezard, F.M. Flasar, S. Vinatier, R. Achterberg, C.A. Nixon, et al., *Icarus* **231**, 323 (2014).
- [17] T. Tokano, G.J. Molina-Cuberos, H. Lallmer, W. Stumtner, *Planetary and Space Science* **49**, 539 (2001).
- [18] K. Plankensteiner, H. Reiner, B.M. Rode, T. Mikoviny, A. Wisthaler, A. Hansel et al., *Icarus* **187**, 616 (2007).
- [19] K. Rinnert, *Journal of Geophysical Research-Atmospheres*. **90**(ND4), 6225 (1985).
- [20] D.M. Hunten, *Nature* **443**, 669 (2006).
- [21] V. Vuitton, R.V. Yelle, M.J. McEwan, *Icarus* **191**, 722 (2007).
- [22] R. Navarro-Gonzalez, S.I. Ramirez, J.G. de la Rosa, P. Coll, F. Raulin, *Space Life Sciences: Life in the Solar System: Prebiotic Chemistry, Chirality and Space Biology*, **27**, 271 (2001).
- [23] G. Horvath, N.J. Mason, L. Polachova, M. Zahoran, L. Moravsky, S. Matejcik, *Plasma Chemistry and Plasma Processing* **30**, 565 (2010).
- [24] J.M. Bernard, P. Coll, A. Coustenis, F. Raulin, *Planetary and Space Science* **51**, 1003 (2003).
- [25] J.M. Bernard, E. Quirico, O. Brissaud, G. Montagnac, B. Reynard, P. McMillan, et al., *Icarus* **185**, 301 (2006).
- [26] C.D. Pintassilgo, J. Loureiro, G. Cernogora, M. Touzeau, *Plasma Sources Science & Technology* **8**, 463 (1999).
- [27] Y. Sekine, H. Imanaka, T. Matsui, B.N. Khare, E.L.O. Bakes, C.P. McKay, et al. *Icarus* **194**, 186 (2008).
- [28] T. Gautier, N. Carrasco, A. Buch, C. Szopa, E. Sciamma-O'Brien, G. Cernogora, *Icarus* **213**, 625 (2011).
- [29] H. Imanaka, B.N. Khare, J.E. Elsila, E.L.O. Bakes, C.P. McKay, D.P. Cruikshank et al. *Icarus* **168**, 344 (2004).
- [30] H. Imanaka, M.A. Smith, *Geophysical Research Letters* **34**, 2 (2007).
- [31] N. Carrasco, T. Gautier, E.T. Es-sebbar, P. Pernot, G. Cernogora, *Icarus* **219**, 230 (2012).
- [32] H.J. Cleaves, C. Neish, M.P. Callahan, E. Parker, F.M. Fernandez, J.P. Dworkin, *Icarus* **237**, 182 (2014).
- [33] A. Somogyi, CH. Oh, M.A. Smith, J.I. Lunine, *Journal of the American Society for Mass Spectrometry* **16**, 850 (2005).
- [34] M.J. Nguyen, F. Raulin, P. Coll, S. Derenne, C. Szopa, G. Cernogora et al., *Advances in Space Research* **42**, 48 (2008).
- [35] L. Torokova, V. Mazankova, F. Krcma, N.J. Mason, S. Matejcik, HAKONE 2014, Zinnowitz, Germany, P2-03-06 (2014).
- [36] G. Horvath, F. Krcma, L. Polachova, K. Klohnova, N.J. Mason, M. Zahoran et al., *European Physical Journal-Applied Physics* **53**, (1) (2011).
- [37] T. Shimanouchi, *Molecular Vibrational Frequencies*, cited; <http://webbook.nist.gov/chemistry/>
- [38] S.I. Ramirez, R. Navarro-Gonzalez, P. Coll, F. Raulin, *Space Life Sciences: Life in the Solar System: Prebiotic Chemistry, Chirality and Space Biology* **27**, 261 (2001).

- [39] B.N. Tran, J.C. Joseph, M. Force, R.G. Briggs, V. Vuitton, J.P. Ferris, *Icarus* **177**, 106 (2005).
- [40] J. Cui, R.V. Yelle, V. Vuitton, J.H. Waite, W.T. Kasprzak, D.A. Gell et al., *Icarus* **200**, 581 (2009).
- [41] P.P. Lavvas, A. Coustenis, I.M. Vardavas, *Planetary and Space Science* **56**, 67 (2008).
- [42] I.P. Robertson, T.E. Cravens, J.H. Waite, R.V. Yelle, V. Vuitton, A.J. Coates et al., *Planetary and Space Science* **57**, 1834 (2009).
- [43] J.H. Waite, D.T. Young, T.E. Cravens, A.J. Coates, F.J. Crary, B. Magee et al., *Science*. **316**, 870 (2007).
- [44] M.D. Bai, Z.T. Zhang, X.Y. Bai, H.H. Gao, *Plasma Chemistry and Plasma Processing* **28**, 405 (2008).
- [45] A. Oumghar, J.C. Legrand, A.M. Damiy, N. Turillon, R.I. Benaim, *Plasma Chemistry and Plasma Processing* **14**, 229 (1994).
- [46] A. Oumghar, J.C. Legrand, A.M. Damiy, *Plasma Chemistry and Plasma Processing* **15**, 87 (1995).
- [47] J.C. Legrand, A.M. Damiy, R. Hrach, V. Hrachova, *Vacuum* **52**, 27 (1999).
- [48] C.D. Pintassilgo, J. Loureiro, *Advances in Space Research* **46**, 657 (2010).
- [49] M.D. Bai, Z.T. Zhang, X.Y. Bai, W. Ning, *IEEE Transactions on Plasma Science* **31**, 1285 (2003).
- [50] J.C. Legrand, A.M. Damiy, R. Hrach, V. Hrachova, *Vacuum* **50**, 491 (1998).
- [51] S.F. Yoon, K.H. Tan, Ahm. J. Rusli, *Journal of Applied Physics* **91**, 40 (2002).
- [52] F. Debal, M. Wautelet, J. Bretagne, J.P. Dauchot, M. Hecq, *Plasma Sources Science & Technology* **9**, 152 (2000).
- [53] Z.L. Petrovic, F. Tochikubo, S. Kakuta, T. Makabe, *Journal of Applied Physics*, **73**, 2163 (1993).
- [54] Y.L. Yung, M. Allen, J.P. Pinto, *Astrophysical Journal Supplement Series* **55**, 465 (1984).
- [55] Z. Peng, N. Carrasco, P. Pernot, *GeoResJ.* **3**, 33 (2014).
- [56] J.C. Legrand, A.M. Damiy, R. Hrach, V. Hrachova **37**, 521 (1997).
- [57] E. Hebrard, M. Dobrijevic, Y. Benilan, F. Raulin, *Planetary and Space Science*, **55** 1470 (2007).

EPJ AP

Applied Physics

EPJ.org
your physics journal

Eur. Phys. J. Appl. Phys. (2015) 71: 20806

DOI: 10.1051/epjap/2015150072

Atmospheric pressure glow discharge generated in nitrogen-methane gas mixture: PTR-MS analyzes of the exhaust gas

Lucie Torokova, Vera Mazankova, Frantisek Krcma, Nigel J. Mason, and Stefan Matejcik

 edp sciences

The title "The European Physical Journal" is a joint property
of EDP Sciences, Società Italiana di Fisica (SIF) and Springer

Atmospheric pressure glow discharge generated in nitrogen-methane gas mixture: PTR-MS analyzes of the exhaust gas[★]

Lucie Torokova^{1,2,a}, Vera Mazankova¹, Frantisek Krcma¹, Nigel J. Mason², and Stefan Matejcik³

¹ Faculty of Chemistry, Brno University of Technology, Purkynova 118, 612 00 Brno, Czech Republic

² Department of Physical Science, Open University, Walton Hall, Milton Keynes MK7 6AA, UK

³ Department of Experimental Physics, Comenius University, Mlynska dolina F-2, 842 48 Bratislava, Slovakia

Received: 5 February 2015 / Received in final form: 2 April 2015 / Accepted: 17 April 2015

Published online: 15 July 2015 – © EDP Sciences 2015

Abstract. This paper reports the results of an extensive study of with the in situ mass spectrometry analysis of gaseous phase species produced by an atmospheric plasma glow discharge in N₂-CH₄ gas mixtures (with methane concentrations ranging from 1% to 4%). The products are studied using proton-transfer-reaction mass spectrometry (PTR-MS). HCN and CH₃CN are identified as the main gaseous products. Hydrazine, methanimine, methyldiazene, ethylamine, cyclohexadiene, pyrazineacetylene, ethylene, propyne and propene are identified as minor compounds. All the detected compounds and their relative abundances are determined with respect to the experimental conditions (gas composition and applied power). The same molecules were observed by the Cassini-Huygens probe in Titan's atmosphere (which has same N₂-CH₄ gas mixtures). Such, experiments show that the formation of such complex organics in atmospheres containing C, N and H, like that of Titan, could be a source of prebiotic molecules.

1 Introduction

Atmospheric pressure glow discharges are of significant interest for a wide range of applications such as pollution control, material processing or surface treatment. Among the many different types of atmospheric pressure discharges the DC glow discharges is one of the most deeply studied [1,2]. The gliding arc configuration has been shown to be a good mimic of planetary atmospheres [3] being used to replicate physical and chemical conditions in Titan. Titan is the largest moon in Saturn's lunar system and the only one with a dense atmosphere (atmospheric pressure is approximately 1.5×10^5 Pa) and thus it has been a subject of interest to astronomers and planetary scientists for more than a century particularly since its atmospheric conditions are thought to resemble those conditions on the Earth several billion years ago [4–6]. It is the only lunar body with a substantial containing significant quantities of carbon (CH₄) and nitrogen (N₂) in its atmosphere [7–9]. Chemical processes in Titan's atmosphere are therefore able to create complex molecules containing C, N and H. This makes Titan our only

planetary-scale laboratory for the synthesis of complex organics molecules [10]. In Titan's atmosphere, the dissociation of N₂ and CH₄ by solar ultraviolet radiation initiates chemical reactions that result in the formation of complex organic molecules. The aggregation and heterogeneous chemistry of these molecules produces the aerosols responsible for Titan's orange colour and thick haze layers.

The recent (and on-going) study of Titan by the Cassini-Huygens space mission has revealed its atmosphere contains a rich cocktail are nitriles (HCN, HC₃N, HC₅N, C₂N₂) all believed to be formed as a result of dissociation of nitrogen and methane either by solar induced photolysis or by electron impact [5, 11, 12] and a large number of hydrocarbons (C₂H₂, C₂H₄, C₂H₆, C₃H₈, C₃H₄) [11, 13, 14].

In order to induce a nitrogenous chemistry and to study electron-molecule and ion-molecule reactions in planetary atmospheres, experiments have been developed using different plasma discharges (dielectric barrier discharge, gliding arc or corona discharges) to produce the energy delivered to Titan's atmosphere that can induce the aforementioned chemistry [15–22] demonstrating that various complex compounds can be formed, for example the higher hydrocarbons, nitriles or even amino acids.

The present work is focused on the experimental study of gaseous products produced in an atmospheric pressure glow discharge fed by N₂-CH₄ gas mixtures with CH₄ concentrations in the range from 1% to 4%.

^a e-mail: xctorokova@fch.vutbr.cz

[★] Contribution to the topical issue “The 14th International Symposium on High Pressure Low Temperature Plasma Chemistry (HAKONE XIV)”, edited by Nicolas Gherardi, Ronny Brandenburg and Lars Stollenwerk

These concentrations are typical of those in Titan's middle and lower atmosphere where pressure may actually exceed those of Earth. The gaseous products were measured qualitatively as well as quantitatively for different methane concentrations in nitrogen by proton-transfer-reaction mass spectrometry.

2 Experimental apparatus

A simplified schematic drawing of the experimental set up is presented in Figure 1. An atmospheric pressure DC glow discharge was created between two stainless steel electrodes separated by a 2 mm gap. The electrodes system had standard configuration of the gliding arc discharge but due to low applied power and low gas velocity the discharge is not moving along the electrodes. The discharge was formed in the stable abnormal glow regime with plasma channel of 1 mm in its diameter. The stainless steel vacuum chamber (volume of 1 L) was evacuated by a rotary oil pump to maintain an oxygen free system. The discharge was operated with an applied power in range 4–15 W in pure nitrogen enriched by 1–4% of CH₄ with total flow rate of 200 sccm. The flow rates through the reactor for both methane and nitrogen were regulated using MKS mass flow controllers. The exhaust gas was analysed in-situ by PTR-MS using H₃O⁺ ions. This technique allows very fast analysis of compounds with proton affinity higher than, 165 kcal/mol without any sampling, separation and with little fragmentation of the analysed species. Unfortunately, this method is very difficult to use for the absolute measurements due to difficulty in making a detailed calibration of the feed gases. Thus the presented results are only relative. Moreover, it is nearly impossible to distinguish different isomers so further (complementary) experiments using GC-MS are necessary.

3 Results

The first sets of experiments present stability analysis of gas phase products. Typical result for acetonitrile is shown in Figure 2. There is a distinct time evolution in the formation of acetonitrile recorded over 1000 scans lasting some 2 h. The first part is before the discharge ignition. It represents stabilization before measurement and it takes 70 scans. The second part takes place just after the discharge ignition and takes 200 scans during which there is a rapid increase in acetonitrile relative intensity during 20 scans, then the intensity decreases to 6.5×10^{-8} arb. unit. After this, the relative intensity is nearly constant. There is a small deviation at 600 scans which could be result of product saturation. The same dependencies were obtained for other gas products.

According to stability experiments, the PTR spectra were analysed in range 240–700 scans. Representative PTR-MS spectra for the gas-phase products formed in a plasma discharge driven by a 40 mA current, operating at laboratory temperature, in a 200 sccm gas flow, and at atmospheric pressure for 1% of methane (a) and 4% of methane in nitrogen (b) are shown in Figure 3.

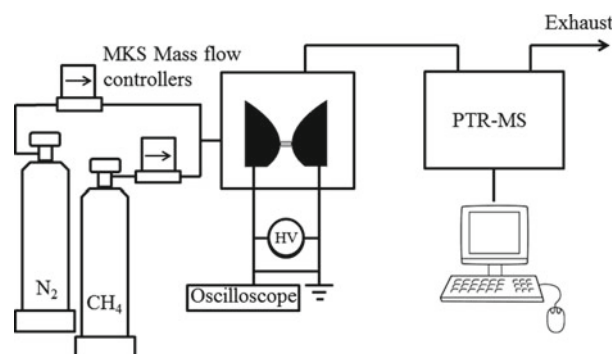


Fig. 1. Schematic diagram of the experimental setup used for PTR-MS analysis of gaseous products of a DC glow discharge fed by various mixtures of N₂-CH₄.

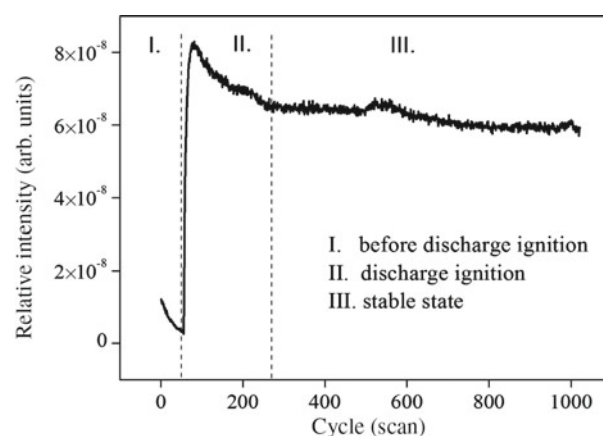


Fig. 2. The time response on the PTR-MS detector system, results for acetonitrile.

The spectra appear to be similar with just a small increase in the peak intensities between 21 and 60 protonated mass. In contrary, a higher intensity of some peaks and some new peaks in the spectra with mass higher than 60 protonated mass can be observed in spectra with 4% of methane.

A higher methane concentration in nitrogen leads to the production of higher molecular weight compounds. So new peaks with higher protonated mass were observed in spectra with 4% CH₄, see Figure 3b. Different ways of synthesis could take place and various complex species can be created under these conditions. Moreover, the solid hydrocarbons were formed on the walls inside the reactor as well as at electrodes during the experiments with higher concentration of methane. The quantity of solid hydrocarbons was seen to increase with increasing methane concentration. These deposits have not been analysed under the presented study.

The main product compounds with their protonated masses are listed in Table 1. The product compounds can be divided into two groups (i) nitrile compounds and (ii) hydrocarbons. The peaks at masses 21 and 37 are not listed there because they correspond to D₂HO⁺, and H₃O⁺-H₂O ions originating in the ionization source [23]. Small amounts of hydrocarbons in the form of acetylene,

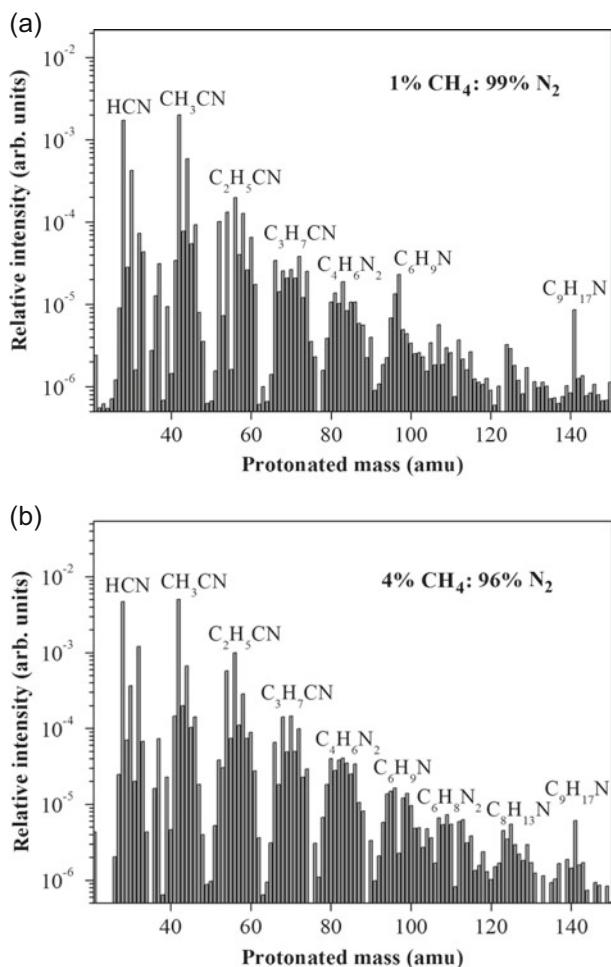


Fig. 3. PTR-MS spectra of the gas-phase products from the reaction of 1% of CH_4 in N_2 (a) and 4% of CH_4 in N_2 (b) gas mixture, flow rate 200 sccm and current 40 mA.

ethylene, propyne, propene, 2-butene and cyclohexadiene were detected. Observation of these species is in agreement with our previous experiments as well as other publications [3,24].

The major products are nitrile compounds. Hydrogen cyanide HCN (proton. mass = 28) and acetonitrile CH_3CN (proton. mass = 42) are the two major products but other nitrile compounds detected are methanimine, methylamine, hydrazine, ethenamine, methyldiazene, ethylamine, propionitrile, propenenitrile, proparylamine, 2-propanamine, butanenitrile, 4-methyl-pyrazole, 2,5-dimethyl-pyrazole and nonanenitrile. Ammonia (protonated mass is 18) was not observed because the molecular mass is lower than 21 that is the lowest limit for used PTR-MS analytical device.

A quantitative analysis of hydrogen cyanide and acetonitrile under different experimental conditions are given in Figures 4 and 5. These concentrations depend on the discharge current for different methane concentrations in the gas mixtures. Nevertheless the profiles are similar for concentrations between 1% and 4% of methane indeed abundances of hydrogen cyanide and acetonitrile are nearly independent at the higher methane concentrations. The relative intensities of these two selected nitro-compounds decrease with increasing methane concentration in nitrogen gas mixture. The trends of dependencies are similar for all cases, but there is small increasing of intensity (between 25 and 30 mA). It is probably due to experimental uncertainty, because only one measurement was performed.

The formation of various other nitriles (not only HCN and CH_3CN) is assigned to a complex plasma-physical chemistry. Hydrogen cyanide formation can be described by the direct reaction:

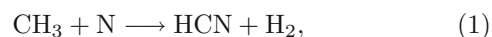


Table 1. The main determined compounds by PTR-MS.

Detected compounds	Formula	Proton. mass	Detected compounds	Formula	Proton. mass
Acetylene	C_2H_2	27	Propionitrile	C_2HCN	52
Hydrogen cyanide	HCN	28	Propenenitrile	$\text{C}_2\text{H}_3\text{CN}$	54
Ethylene	C_2H_4	29	Proparylamine	$\text{C}_3\text{H}_3\text{NH}_2$	56
Methanimine	CH_3N	30	Propanenitrile	$\text{C}_2\text{H}_5\text{CN}$	56
Amino-methyl	CH_2NH_2	31	Vinylimine	$\text{C}_3\text{H}_3\text{NH}_2$	56
Diimine	H_2N_2	31	2-Butene	C_4H_8	57
Methylamine	CH_5N	32	2-Methylpropene	C_4H_8	57
Hydrazine	H_4N_2	33	Cyclopropylamine	$\text{C}_3\text{H}_5\text{NH}_2$	58
Propyne	C_3H_4	41	2-Propanimine	$\text{C}_3\text{H}_6\text{NH}$	58
1,2-Propadiene	C_3H_4	41	Dimethyl-diazene	$\text{CH}_3\text{N}_2\text{CH}_3$	59
Acetonitrile	CH_3CN	42	Propanamine	$\text{C}_3\text{H}_7\text{NH}_2$	60
Isocyano-methane	$\text{C}_2\text{H}_3\text{N}$	42	Butanenitrile	$\text{C}_3\text{H}_7\text{CN}$	70
Cyclopropane	C_3H_6	43	Cyclohexadiene	C_6H_8	81
Propene	C_3H_6	43	Pyrazine	$\text{C}_4\text{H}_4\text{N}_2$	81
Cyanamide	H_2NCN	43	4-Methyl-pyrazole	$\text{C}_4\text{H}_6\text{N}_2$	83
Ethenamine	$\text{C}_2\text{H}_3\text{NH}_2$	44	Pyridinamine	$\text{C}_5\text{H}_6\text{N}_2$	95
Methyldiazene	$\text{CH}_3\text{N}_2\text{H}$	45	Pyrazole-2,5-dimethyl	$\text{C}_6\text{H}_9\text{N}$	96
Ethylamine	$\text{C}_2\text{H}_5\text{NH}_2$	46	Benzendiamine	$\text{C}_6\text{H}_8\text{N}_2$	124
Methylhydrazine	$\text{CH}_3\text{N}_2\text{H}_3$	47	Nonanenitrile	$\text{C}_9\text{H}_{17}\text{N}$	140

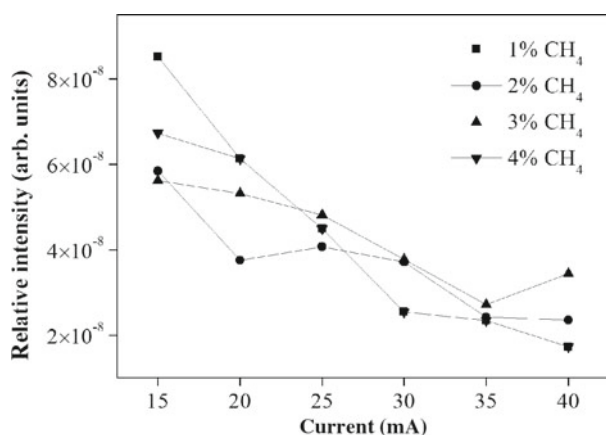


Fig. 4. The dependence of hydrogen cyanide concentrations on discharge current and composition of the gas mixture 1%–4% of methane in nitrogen.

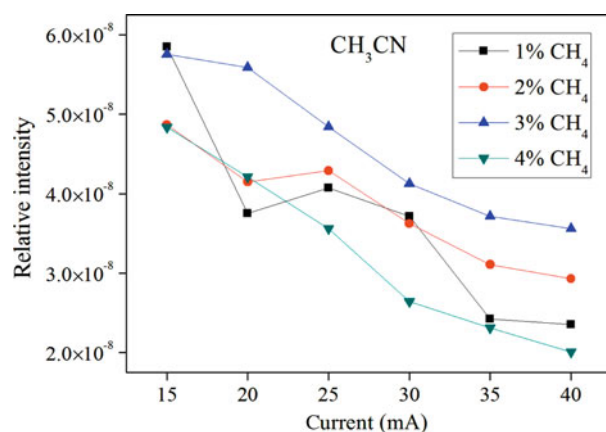
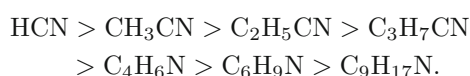


Fig. 5. The dependence of acetonitrile concentrations on discharge current and composition of the gas mixture 1%–4% of methane in nitrogen.

or/and indirect by a two-step process



through a highly unstable intermediate product H_2CN [17]. As it is shown in Table 1, nitriles such as hydrogen cyanide, methanimine, methylamine, hydrazine, acetonitrile, ethenamine, methyl diazene, ethylamine, propionitrile, propenenitrile, propylamine, 2-propanamine, butanenitrile, 4-methyl-pyrazole, 2,5-dimethyl-pyrazole and nonanenitrile are produced by electron collision reaction and consequent recombination reaction of cyano-groups. The yield and generation rate of nitriles are of the following relationship:



The dissociation energies of N_2 , CH and CN bonds play an important role in the mechanisms of other nitrile compounds production. Knowledge of the nitriles chemistry

has still to be improved. The main detected nitrile compounds were molecular structures with nitrile groups ($-\text{CN}$), amino groups ($-\text{NH}_2$, $-\text{NH}-$, and $-\text{N}<$), and/or imino groups ($-\text{C}=\text{N}-$) in our experiments. HCN , CH_3CN and $\text{C}_2\text{H}_5\text{CN}$ have been previously detected in Titan's upper stratosphere, too [5,12,25]. This suggests that the molecules identified in the upper atmosphere can be precursors of the aerosols and that knowledge of their abundance is crucial to the understanding of aerosol chemical formation pathways [5,26]. The overall chemistry is very complicated and unfortunately there is little available data for the bimolecular reactions [27–29]. In the case of atmospheric pressure discharges, these reactions play minor role, only, and more intermediate complexes are formed and thus three body reactions (or indirect reactions with formation of intermediate complexes) are more probable. Data for these reactions are unfortunately very rare.

4 Conclusion

The gaseous phase products formed in the atmospheric glow discharge fed by different mixtures of methane in nitrogen (from 1% to 4%) were determined by in situ PTR-MS analysis. The discharge was operated in the flowing regime at different discharge currents (from 15 up to 40 mA) at laboratory temperature. In situ PTR-MS technique for the exhaust gas phase sampling was successfully used for chemical analysis to deduce the gas composition in the N_2 - CH_4 reactive gas mixture mimics of Titan's atmosphere.

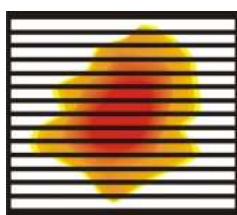
Various nitrile compounds and hydrocarbons were observed in all experiments. HCN and CH_3CN were identified as the two major gas phase products with different methane admixtures between 1% and 4%. Small yields of various hydrocarbons were also detected in our experiments. These results are consistent with the Titan's atmospheric composition because the same compounds were detected during the Cassini-Huygens space mission. This fact clearly demonstrates that laboratory experiments can be used for prediction of both the presence and possible concentrations of compounds which have not been detected, yet. These simple organics should be tracers of the chemical groups constituting the dusty products.

The nitriles gas chemistry is still mostly unknown, and nitriles are often ignored in the Titan's atmospheric models even though we know them from direct observations, laboratory mimic experiments and computational models suggest they could be present in large amounts. Atmospheric pressure conditions could play an important role in the chemical processes of hydrocarbons and also nitriles because of high probability of three body reactions or clusters formation. The formation mechanisms of compounds detected on the Titan could be explained by two step reactions between some important intermediates. These molecules including nitrogen are also interesting in exobiology since they are known for their reactivity and as precursors of amino acids.

This work has been supported by the ESF COST Actions CM0805, EUROPLANET TNA2 and CEEPUS network AT-0063.

References

1. Z. Machala, E. Marode, C.O. Laux, Ch. Kruger, *Journal of Advanced Oxidation Technologies* **7**, 133 (2004)
2. P. Kloc, H.E. Wagner, D. Trunec, Z. Navratil, G. Fedoseev, *J. Phys. D: Appl. Phys.* **43**, 34 (2010)
3. L. Torokova, J. Watson, F. Krcma, V. Mazankova, N.J. Mason, G. Horvath, S. Matejcek, *Contrib. Plasma Phys.* **55** (2015), DOI: 10.1002/ctpp.201400052 (in press)
4. K.L. Aplin, *Surv. Geophys.* **27**, 63 (2006)
5. P. Lavvas et al., *Proc. Natl. Acad. Sci. USA* **110**, 2729 (2013)
6. O. Shebanits, J.E. Wahlund, K. Mandt, K. Agren, N.J.T. Edberg, J.H. Waite, *Planet. Space Sci.* **84**, 153 (2013)
7. S.M. Horst, M.A. Tolbert, *Astrophys. J.* **781**, 53 (2014)
8. C.A. Nixon et al., *Astrophys. J. Lett.* **776**, L14 (2013)
9. H.B. Niemann et al., *Nature* **438**, 779 (2005)
10. S. Jagota, J. Kawai, D. Deamer, C. McKay, B. Khare, D. Beeler, *Planet. Space Sci.* **103**, 167 (2014)
11. S. Vinatier et al., *Icarus* **188**, 120 (2007)
12. B.N. Tran, M. Force, R.G. Briggs, J.P. Ferris, P. Persans, J.J. Chera, *Icarus* **193**, 224 (2008)
13. B.N. Tran, J.C. Joseph, M. Force, R.G. Briggs, V. Vuitton, J.P. Ferris, *Icarus* **177**, 106 (2005)
14. A. Coustenis et al., *Exp. Astron.* **23**, 893 (2009)
15. J.M. Bernard et al., *Icarus* **185**, 301 (2006)
16. C.D. Pintassilgo, J. Loureiro, G. Cernogora, M. Touzeau, *Plasma Source. Sci. Technol.* **8**, 463 (1999)
17. C. Szopa, G. Cernogora, L. Boufendi, J.J. Correia, P. Coll, *Planet. Space Sci.* **54**, 394 (2006)
18. H. Imanaka et al., *Icarus* **168**, 344 (2004)
19. Y. Sekine et al., *Icarus* **194**, 186 (2008)
20. P. Coll, D. Coscia, M.C. Gazeau, E. Devanssay, J.C. Guillemin, F. Raulin, *Prebiotic Chemistry in Space* **16**, 93 (1995)
21. C. Ponnampuruma, F. Woeller, *Nature* **203**, 272 (1964)
22. R. Navarro Gonzalez, S.I. Ramirez, *Life Sciences: Complex Organics in Space. Book Series: Advances in Space Research-Series* **19**, 1121 (1997)
23. T. Shimanouchi, *Molecular Vibrational Frequencies*. Available from: <http://webbook.nist.gov/chemistry/>
24. G. Horvath et al., *Eur. Phys. J. Appl. Phys.* **53**, 11001 (2011)
25. S. Vinatier et al., *Icarus* **205**, 559 (2010)
26. Z. Peng, N. Carrasco, P. Pernot, *GeoResJ.* **3**, 33 (2014)
27. T. Gautier, N. Carrasco, A. Buch, C. Szopa, E. Sciamma-O'Brien, G. Cernogora, *Icarus* **213**, 625 (2011)
28. J.C. Legrand, A.M. Diamy, R. Hrach, V. Hrachova, *Contrib. Plasma Phys.* **37**, 521 (1997)
29. E. Hebrard, M. Dobrijevic, Y. Benilan, F. Raulin, *Planet. Space Sci.* **55**, 1470 (2007)



HAKONE XV

15th High Pressure Low Temperature Plasma Chemistry Symposium

September 11-16, 2016, Brno, Czech Republic

STUDY OF O₂ AND O₃ REACTIONS WITH ELECTRODE SURFACE IN OZONIZER

David Trunec¹, Věra Mazánková², Jana Mierna², Ivana Manduchová², František Krčma²
¹*Department of Physical Electronics, Masaryk University, Kotlářská 2, Brno, Czech Republic*
²*Institute of Physical and Applied Chemistry, Brno University of Technology, Purkyňova 118,
Brno, Czech Republic*

E-mail: trunec@physics.muni.cz

In this contribution the study of O₂ and O₃ reactions with electrode surface in an ozonizer is presented. The electrode surfaces in ozonizer were treated in the discharge with pure (99.9999%) oxygen for long time. Then the discharge was switched off and pure oxygen or oxygen with ozone reacted with treated electrodes for different time periods. Then the ozone concentration at the ozonizer output was measured by the absorption spectroscopy. It was found that the molecular oxygen reacts with oxygen atoms adsorbed on electrode surfaces producing ozone. On the other hand the ozone concentration in switched off ozonizer stays constant for long time.

1 Introduction

The plasma surface interactions are of considerable importance for a wealth of discharge phenomena. The surface oxidation on Pyrex of NO into NO₂ by adsorbed O atoms was studied by Guaitella et al. [1]. The surface recombination of oxygen atoms in O₂ plasma was studied by Lopaev et al. [2]. It has been also observed that the ozone concentration in high purity (99.99995%) oxygen-fed ozonizers decreases from the initial level to almost zero during several hours. This phenomenon is known as Ozone Zero Phenomenon [3]. This phenomenon is probably caused by surface processes at ozonizer electrodes. Explanation of this phenomenon can bring deeper insight into surface processes in ozonizer and it is also important for the models of ozone production in dielectric barrier discharges. Marinov et al. [4] also directly observed ozone formation on SiO₂ surfaces in oxygen discharges.

2 Experimental

A cylindrical ozonizer was used in this study. Outer electrode was made of stainless steel and it was maintained at earth potential. The internal diameter of the outer electrode was 24 mm. The outer electrode was covered by alumina dielectric, which was 2.85 mm thick. The inner cylinder is a high-voltage electrode and it was made of stainless steel. The external diameter of the inner electrode was 17 mm. The discharge gap was 0.65 mm. The length of the ozonizer was 240 mm. The water flowed trough outer electrode, the water temperature was controlled to be constant during the experiments. Extremely high-grade oxygen of 99.9999% was led into the ozonizer through the mass flow controller, the oxygen flow was set to 2 l/min. The ozone produced in the ozonizer was led to absorption cell, where the ozone concentration was measured using absorption spectroscopy.

3 Results and Discussion

In the first set of experiments the discharge in pure oxygen in ozonizer was burning for 5 min, then the discharge was switched off and the ozonizer was flowed by argon for 3 min. After this the ozonizer was flowed by oxygen for 1 min and then the ozonizer filled by oxygen was closed at the input and at the output by the valves for the reaction time t_r . After the elapse of time t_r the oxygen flow through ozonizer was restored and the concentration of produced ozone flowing through absorption cell was measured. The measured ozone concentrations are shown for different reaction time t_r in Fig. 1. The ozone amounts calculated from these time dependences are shown in Fig. 2. The amount of produced ozone increases with time t_r , at short times the amount of ozone increases quickly, at reaction times longer than 2 min the amount of ozone increases slowly.

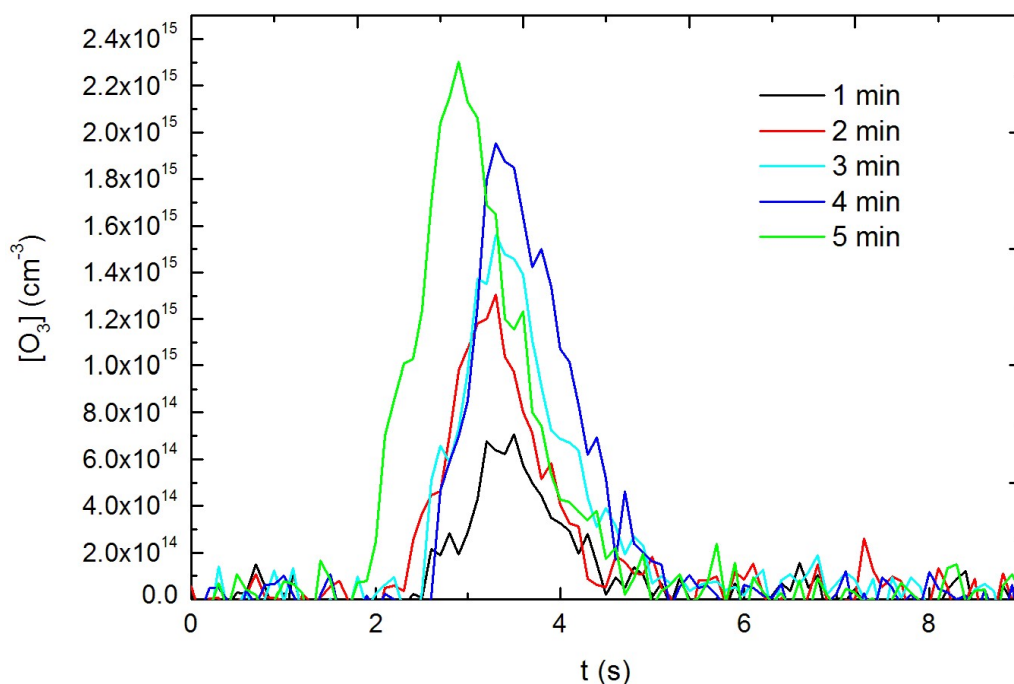


Fig. 1: The time dependences of ozone concentration in absorption cell for different reaction time t_r .

In the second set of experiments the discharge in pure oxygen in ozonizer was burning again for 5 min, then the ozonizer filled by oxygen with ozone was closed at the input and at the output by the valves simultaneously with switching of the discharge. After the elapse of time t_r the oxygen flow through ozonizer was restored and the concentration of ozone flowing through absorption cell was measured. The measured concentrations of ozone are shown in Fig. 3. It can be seen from this figure that ozone concentration in the ozonizer does not decrease with time t_r .

In the third set of experiments the mixture of 95% oxygen and 5% of nitrogen was used as working gas for the discharge in ozonizer. The discharge in this mixture was burning for 5 min. Then the discharge was switched off, the ozonizer was flowed by oxygen for 1 min and then the ozonizer filled by oxygen was closed at the input and at the output by the valves for the time t_r . The results of these experiments are shown again in Fig. 2. The dependence of created ozone amount versus reaction time t_r shows again two slopes – steeper one at short

times t_r and gradual one at longer times. Surprisingly amounts of created ozone are higher than the ozone amounts in the case of pure oxygen discharge.

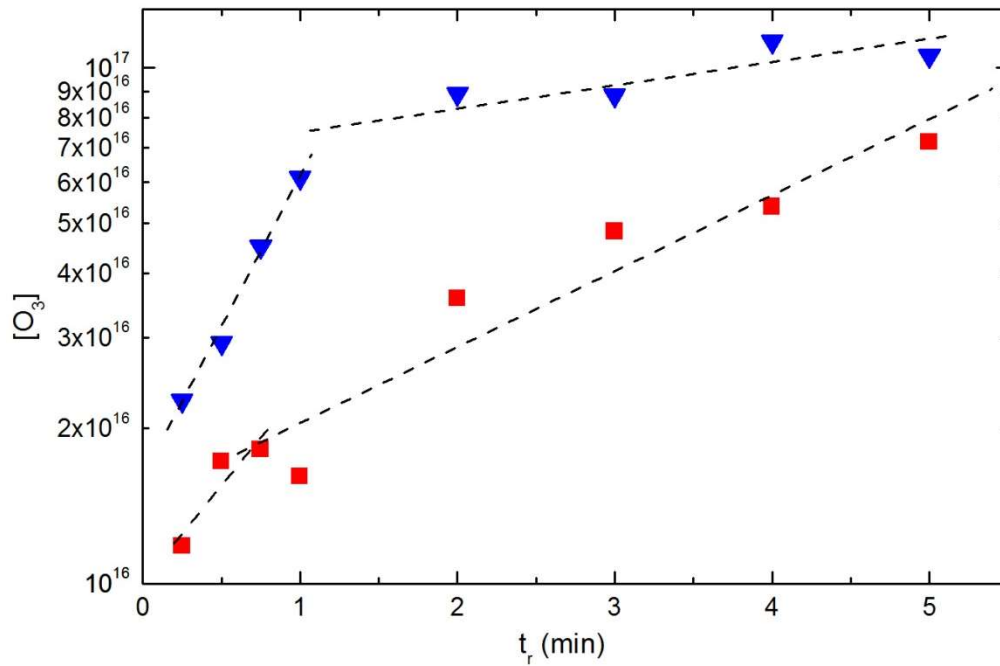


Fig. 2: The dependence of ozone amount on reaction time t_r . Squares – first set of experiments, pure oxygen discharge; triangles – third set of experiments, discharge in the mixture of 95% oxygen and 5% nitrogen.

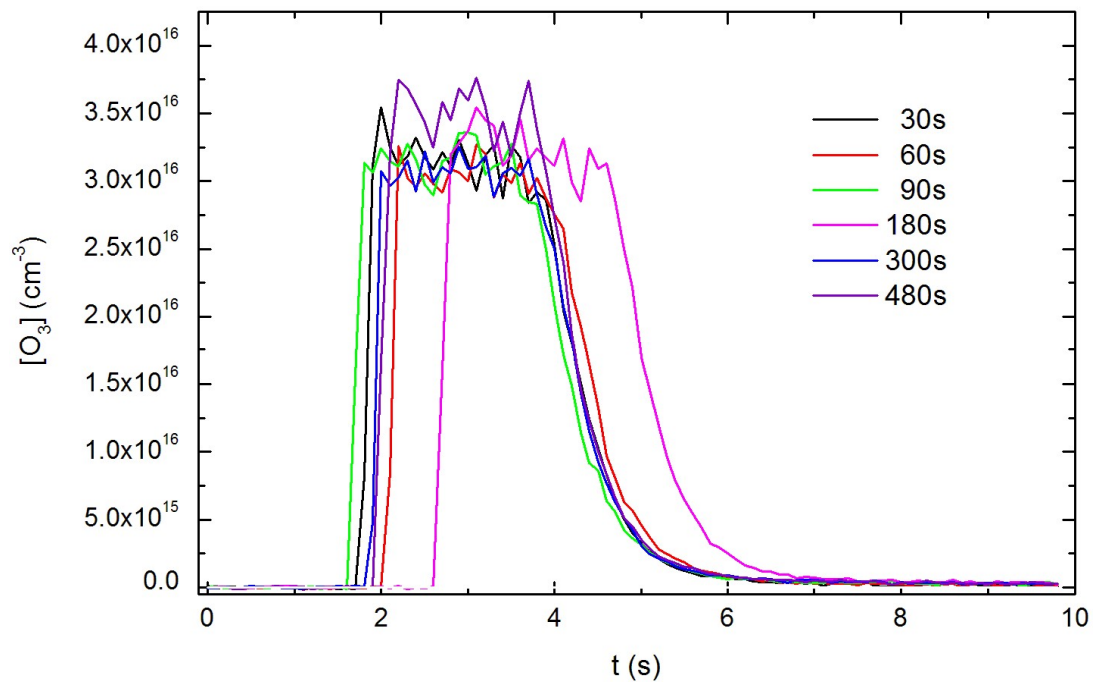


Fig. 3: The time dependence of ozone concentration in absorption cell at second set of experiments.

4 Conclusion

The experiments proved the creation of ozone on electrode surfaces which were treated in oxygen or oxygen/nitrogen DBD discharge. The measured time dependence of produced amount of ozone has two slopes, steeper one at shorter times and gradual one at longer times. This suggests that there is also a process in which the ozone is destroyed or the number of active sites with absorbed oxygen atoms on electrode surface decreases significantly.

5 Acknowledgement

This research has been supported by the Czech Science Foundation under contract GA13-24635S, by the project CZ.1.05/2.1.00/03.0086 funded by European Regional Development Fund, by project LO1411 (NPU I) funded by Ministry of Education Youth and Sports of Czech Republic and by the Technology Agency of the Czech Republic under contract TA03010098.

References

1. O. Guaitella, M. Hübner, S. Welzel, D. Marinov, J. Röpcke and A. Rousseau, *Plasma Sources Sci. Technol.* 19, 045026 (2010)
2. D. V. Lopaev, E. M. Malykhin and S. M. Zyryanov, *J. Phys. D: Appl. Phys.* 44, 015202 (2011)
3. M. Taguchi, Y. Ochiai, R. Kawagoe, Y. Kato, K. Teranishi, S. Suzuki and H. Itoh, in *HAKONE XII Proceedings*, 2009, p. 291
4. D. Marinov, O. Guaitella, J. P. Booth and A. Rousseau, *J. Phys. D: Appl. Phys.* 46, 032001 (2013)

Atmospheric pressure barrier discharge at high temperature: Diagnostics and carbon nanotubes deposition

M. Eliáš, P. Kloc, O. Jašek, V. Mazánková, D. Trunec, R. Hrdý, and L. Zajíčková

Citation: [Journal of Applied Physics](#) **117**, 103301 (2015); doi: 10.1063/1.4914062

View online: <http://dx.doi.org/10.1063/1.4914062>

View Table of Contents: <http://scitation.aip.org/content/aip/journal/jap/117/10?ver=pdfcov>

Published by the [AIP Publishing](#)

Articles you may be interested in

[Simulation of stationary glow patterns in dielectric barrier discharges at atmospheric pressure](#)

Phys. Plasmas **21**, 123503 (2014); 10.1063/1.4903460

[Columnar discharge mode between parallel dielectric barrier electrodes in atmospheric pressure helium](#)

Phys. Plasmas **21**, 013503 (2014); 10.1063/1.4861608

[A dielectric-barrier discharge enhanced plasma brush array at atmospheric pressure](#)

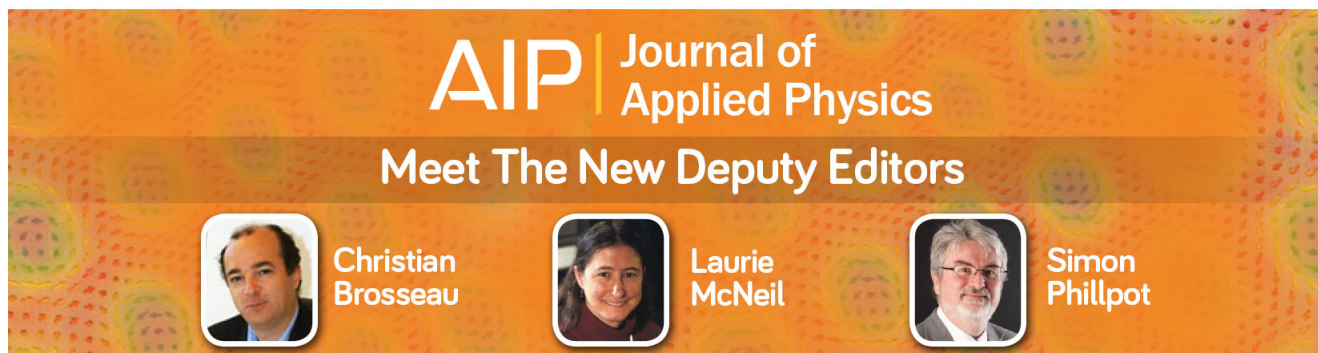
Appl. Phys. Lett. **103**, 033519 (2013); 10.1063/1.4816061

[Numerical simulation of operation modes in atmospheric pressure uniform barrier discharge excited by a saw-tooth voltage](#)

Phys. Plasmas **19**, 083505 (2012); 10.1063/1.4745653

[A large gap of radio frequency dielectric barrier atmospheric pressure glow discharge](#)

Appl. Phys. Lett. **96**, 041502 (2010); 10.1063/1.3299010

A promotional banner for the Journal of Applied Physics. It features the AIP logo and the text 'Journal of Applied Physics' at the top. Below this, it says 'Meet The New Deputy Editors'. Three circular portraits of the new deputy editors are shown: Christian Brosseau, Laurie McNeil, and Simon Phillpot, each with their name written below their portrait.

AIP | Journal of Applied Physics

Meet The New Deputy Editors

 Christian Brosseau

 Laurie McNeil

 Simon Phillpot

Atmospheric pressure barrier discharge at high temperature: Diagnostics and carbon nanotubes deposition

M. Eliáš,^{1,2} P. Kloc,¹ O. Jašek,^{1,2} V. Mazánková,² D. Trunec,^{1,a)} R. Hrdý,^{3,4}
 and L. Zajíčková^{1,2}

¹Department of Physical Electronics, Faculty of Science, Masaryk University, Kottlářská 2, 611 37 Brno, Czech Republic

²CEITEC – Central European Institute of Technology, Masaryk University, Kamenice 753/5, 625 00 Brno, Czech Republic

³CEITEC, Brno University of Technology, Technická 3058/10, 616 00 Brno, Czech Republic

⁴Department of Microelectronics, Faculty of Electrical Engineering and Communication, Brno University of Technology, Technická 3058/10, 616 00 Brno, Czech Republic

(Received 5 December 2014; accepted 22 February 2015; published online 9 March 2015)

Atmospheric pressure dielectric barrier discharge (DBD) in Ar/H₂ gas feed with C₂H₂ or CH₄ admixture was studied at room and high temperature of 680 °C by plasma diagnostics (electrical measurements, fast camera imaging, and optical emission spectroscopy). It was shown that filamentary DBD in pure Ar or Ar/H₂ can be converted into homogeneous discharge by an acetylene admixture. Fast intensified charge-coupled device (ICCD) camera proved that this homogeneous discharge is an atmospheric pressure glow discharge (APGD) at room temperature whereas at high temperature the discharge mode switches at every half-period between APGD and atmospheric pressure Townsend discharge. The high temperature discharges (610–710 °C) in Ar/H₂/C₂H₂ and Ar/H₂/CH₄ were also investigated with respect to a surface bound deposition of carbon nanotubes using 5 nm thick iron layer as a catalyst. CNTs were deposited without any dedicated catalyst pretreatment phase. The quality of CNTs, namely, their density, vertical alignment, and width of the diameter distribution, was better for the C₂H₂ gas feed and higher temperatures.

© 2015 AIP Publishing LLC. [<http://dx.doi.org/10.1063/1.4914062>]

I. INTRODUCTION

Dielectric barrier discharges (DBDs) burning at atmospheric pressure in a filamentary form have been known for more than a century and they are widely used in industrial applications such as ozone generation, pollution control, high power CO₂ lasers, ultraviolet excimer lamps, excimer based mercury-free fluorescent lamps, flat large-area plasma displays, and surface treatment.¹ It was reported, in the late seventies and eighties, that DBD discharges can be operated also in a homogeneous mode using helium as a dilution gas.^{2,3} This discovery brought further motivation for fundamental research of DBDs and opened new possibilities for atmospheric pressure plasma processing.

The stabilization of homogeneous DBDs requires suppression of streamer formation in which the structure and material of electrodes, the frequency of power supply and/or the gas mixture play important role. Influence of the gas mixture on the ignition of either filamentary or homogeneous form of DBD can be relatively easily studied and it is of high importance for plasma processing at atmospheric pressure. Besides helium, the homogeneous DBD was obtained in neon⁴ but utilization of either He or Ne is not suitable for industrial applications. Although the homogeneous DBD cannot be obtained in pure argon without a specially structured electrode,^{5,6} Okazaki and her colleagues showed that a small amount of certain hydrocarbons can lead to the

stabilization of homogeneous DBD in Ar.⁷ Additionally, the homogeneous DBD was also observed and studied in argon with ammonia admixture^{8,9} and in nitrogen.¹⁰

The physical principles behind the formation of homogeneous DBDs were investigated by Massines *et al.* in He, Ar/NH₃, and N₂.^{11,12} It was shown that during the current increase the discharge transits from a non-self-sustained discharge to a Townsend discharge and then to a subnormal glow discharge in He and Ar/NH₃ and, therefore, can be called atmospheric pressure glow discharge (APGD). However, in N₂ the glow regime cannot be achieved and the discharge is classified as an atmospheric pressure Townsend-like discharge (APTD). The advantage of plasma homogeneity in case of APGD or APTD was proved, for example, by plasma enhanced chemical vapor deposition (PECVD) of silicon oxide thin films from organosilicon reactants mixed either with He^{13,14} or N₂,^{15–17} respectively.

Filamentary DBDs in methane and acetylene containing gas feeds were used to deposit amorphous hydrogenated carbon films (a-C:H) with the hardness up to 10 GPa^{18,19} but Bugaev *et al.* found that the films had significant quantity of defects due to a filamentary nature of the discharge.¹⁸ Jiang *et al.* deposited amorphous carbon structures by DBD in an Ar/C₂H₂ mixture and observed that the discharge burns first several minutes in the homogeneous mode.²⁰ Kodama *et al.* deposited a-C:H films in homogeneous DBD burning in pure acetylene at 9 kHz.²¹ Good barrier properties of the films proved that hydrocarbon DBD in homogeneous mode can produce compact and pinhole free a-C:H films.

^{a)}Author to whom correspondence should be addressed. Electronic mail: trunec@physics.muni.cz

APGD at 125 kHz in the mixture of He/H₂/CH₄ was investigated for the deposition of carbon nanotubes (CNTs) using Ni films, 20 nm in thickness, as catalyst and temperature range of 500–600 °C.²² The nanotubes were multi-walled and high percentage of helium was used to stabilize the homogeneous DBD because filamentary DBD did not yield clearly developed CNTs. A dedicated experiment showed that even at the temperature of 700 °C the CNTs grew only at the temporary cathode of APGD because it is surrounded by a plasmachemically active region resembling cathode and negative glows of low pressure glow discharges.²³ Further improvement was achieved in He/H₂/CH₄ atmospheric pressure radio frequency (13.56 MHz) discharge (APRFD) due to its quasi-continuous nature. The advantages of APRFD combined with an advanced preparation of catalytic nanoparticles resulted in the synthesis of single-walled CNTs at 700 °C.^{23,24}

This work aims to investigate DBD discharges at 6.8 kHz in argon mixed with hydrocarbon gases, namely, in Ar/H₂/C₂H₂ and Ar/H₂/CH₄ gas feeds. Unlike the previous studies helium was not used as the working gas. It is focused on the discharges at high temperature 610–710 °C because such conditions are suitable for the synthesis of nanostructured materials such as carbon nanotubes, nanowalls, and graphene. The plasma diagnostics help to compare effect of hydrocarbon admixture and temperature on the DBD mode. Besides diagnostics of DBD by using electrical measurement, fast ICCD camera, and optical emission spectroscopy, the surface bound growth of carbon nanotubes was investigated in the both gas feeds using a vacuum-evaporated iron thin film as catalyst.

II. EXPERIMENTAL DETAILS

The experiments were carried out in a metallic discharge reactor with the dimensions 500 mm × 500 mm × 500 mm. The discharge burned between two planar metal electrodes covered by dielectrics, see Fig. 1. The bottom electrode was grounded,

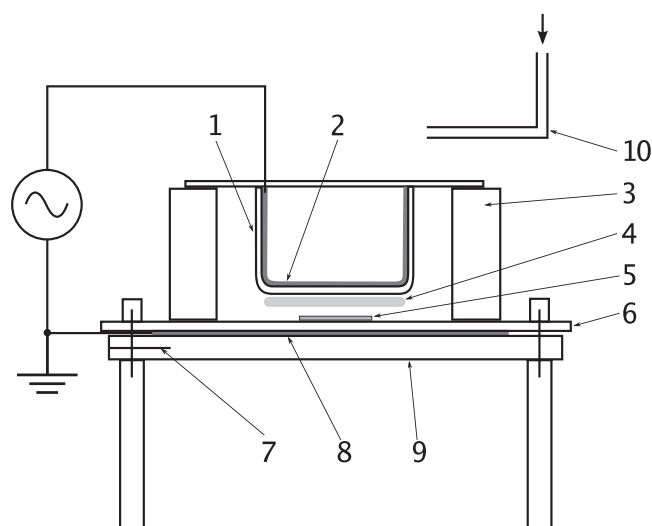


FIG. 1. Electrode configuration. 1—Simax glass dielectric, 2—upper electrode, 3—distance pillar, 4—discharge, 5—substrate, 6—AlN dielectric, 7—thermocouple, 8—bottom electrode, 9—heater, 10—gas inlet.

the upper electrode was connected to the high voltage power supply. The upper circular electrode, 36 mm in diameter, was covered with a Simax glass plate, 1.8 mm in thickness. The bottom circular electrode, 40 mm in diameter, was covered with an aluminium nitride plate 50 mm × 70 mm × 0.6 mm. The bottom electrode was attached to the Boralectric[®] heater. The heater temperature, measured by a thermocouple, could be elevated up to 750 °C. The distance between the bottom and top electrodes was 1.75 mm. The gas inlet was located 30 mm above the electrode system. This place represented a suitable location of gas inlet near the electrode system and it does not disturb the gas flow between the electrodes. The gas outlet was located 100 mm below the electrode system. The substrates for deposition of CNTs were silicon pieces, 15 mm × 10 mm × 0.5 mm, covered by a thermal oxide film with the thickness of 300 nm. Iron catalyst layer, 4.7 nm in thickness, was vacuum evaporated on the top. The as-prepared substrates were placed on the bottom electrode. The temperature of substrate and the temperature of the dielectrics on upper electrode was measured by a thermocouple before discharge was ignited. It was found the substrate temperature is about 40 °C lower than the heater temperature and the temperature of upper electrode dielectrics is about 250 °C lower than the heater temperature.

Before starting the experiments, the discharge chamber was pumped down to 20 Pa and then filled with the investigated gas mixture up to the pressure of 101 kPa. In case of experiments at elevated temperature, the heater temperature was set to 300 °C for the filling period of 5 min. After reaching the pressure of 101 kPa, the substrate temperature was increased to a desired value from the range of 610–710 °C and the discharge was ignited. The argon (Ar) flow rate of 7 slm was mixed with acetylene (C₂H₂) or methane (CH₄) flow of 15 sccm. Optionally, 100 sccm of hydrogen was added. Atmospheric pressure during the deposition was maintained by a slight pumping. A high voltage power supply with the frequency of 6.8 kHz and applied voltage 0.8–4.0 kV (peak-to-peak) was used for the discharge generation.

Jobin Yvon FHR 1000 spectrometer with a CCD detector (focal length 1 m, grating 2400 gr mm⁻¹) was used for optical spectroscopy in the UV/VIS spectral range (300–750 nm). The optical spectra from weakly glowing discharges were obtained using a lens with diameter of 7 cm attached to the side window and focusing light from the discharge to the input of the optical fiber. The measured spectra were identified using Spectrum Analyzer program.^{25,26} Temporally and spatially resolved discharge emission was recorded without a spectral resolution with the intensified charge-coupled device (ICCD) camera PI-MAX1024RB-25-FG-43 (Princeton Instruments), controlled by the ST-133 controller and working in an imaging mode. The camera was synchronized with the applied voltage. The exposure time was 80 μs, i.e., one half-period of applied voltage, or 5 μs. In the case of 5 μs exposure time a sequence of images covering the entire period of applied voltage was recorded by varying the delay from selected trigger voltage. Due to long unload time, the obtained images were recorded at different half-periods. The images shown in Sec. III always present the discharge at maximum light intensity which occurs at different times in the half-

period due to randomness of discharge appearance. The applied voltage and discharge current were recorded by the digital oscilloscope HP 54820 A Infinium (500 MHz, 2 GS/s). A high-voltage probe Tektronix P6015A connected to the upper electrode, and a resistor placed between the bottom electrode and ground, was used to measure the applied voltage and the discharge current, respectively. The Raman spectra of CNTs were obtained with the Renishaw in Via spectrometer using argon laser (514.5 nm). The laser spot diameter and beam intensity were approximately $2\ \mu\text{m}$ and $2\ \text{mW}$, respectively. The scanning electron microscopy (SEM) imaging of the CNT deposits was performed with Tescan MIRA II LMU microscope equipped with Oxford Instruments Energy Dispersive Microanalysis (EDS/EDX) and AZTEC Software or with FEI MAGELAN 400 microscope. The samples of nanostructures prepared by positive replication technique were also imaged with a Philips CM12 STEM transmission electron microscope (TEM).

III. RESULTS AND DISCUSSION

A. Discharge diagnostics at room temperature

Influence of the hydrocarbon admixture on the properties of DBD discharges in Ar or Ar/H₂ was at first studied at room temperature, i.e., without external heating of the bottom electrode. The voltage necessary for discharge ignition was significantly reduced by a small admixture of C₂H₂ and stayed low up to the maximum studied C₂H₂ concentration of 1.7% (see Fig. 2). It was caused by the Penning ionization of acetylene molecules by argon metastables. The same study performed for the Ar/CH₄/H₂ mixture showed that the ignition voltage was not decreased by the addition of CH₄. The reason can be seen in different values of the ionization potential of hydrocarbon molecules. The Penning ionization of C₂H₂ in Ar is possible because C₂H₂ ionization potential is 11.40 eV and the energy of argon 1s₅ metastable is 11.55 eV. The ionization potential of CH₄ is 12.61 eV and, therefore, the Penning ionization cannot take place.

Influence of hydrogen on the ignition voltage can be seen from the comparison of Ar/C₂H₂ and Ar/C₂H₂/H₂ gas

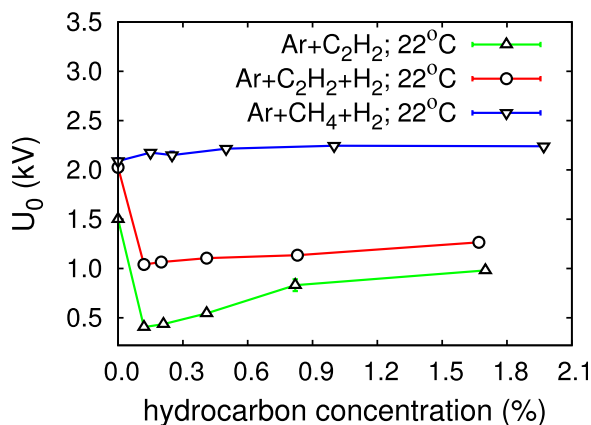


FIG. 2. The dependence of ignition voltage U_0 on the concentration of acetylene or methane added to Ar or Ar/H₂. The discharge was operated at room temperature 22 °C. Argon and hydrogen flow rates were 7 slm and 100 sccm, respectively.

feeds in Fig. 2. In Ar/H₂ mixture, the electrons lose energy in inelastic collisions with hydrogen molecules at low electron energies, thus causing an increase of the ignition voltage from 1.5 to 2.0 kV. Addition of C₂H₂ to Ar/H₂ caused an abrupt decrease of the ignition voltage similarly as without H₂ in the mixture. The rate constants for the reaction of 1s₅ Ar metastable with C₂H₂ and H₂ at 300 K are 56×10^{-11} and $6.6 \times 10^{-11}\ \text{cm}^3\ \text{s}^{-1}$, respectively.²⁷ Therefore, eight times more H₂ than C₂H₂ can be added and still the collisions of argon metastables with acetylene will prevail over the quenching of argon metastables by hydrogen. Indeed, a deep decrease of ignition voltage was observed after acetylene addition even at the presence of hydrogen.

The discharge current in Ar or gas mixtures with CH₄ consisted of sharp peaks corresponding to the filamentary DBD, see Figs. 3(a) and 3(b). In the discharge in pure Ar and at the ignition voltage, the discharge current consisted of one sharp peak (width of several μs). In rare cases the single peak was replaced by two consecutive peaks with approximately half amplitude. Higher applied voltage leads to the development of multiple current peaks per half period. The current of the discharge ignited in the mixtures with C₂H₂ had the form of broad peaks superimposed by many smaller and shorter peaks, see Fig. 3(c). It indicated that the discharge had the form of homogeneous APGD but it did not burn in the whole discharge gap at the same time. The ionization of acetylene by argon metastables leads to the formation of APGD. This effect was a little bit disturbed when H₂

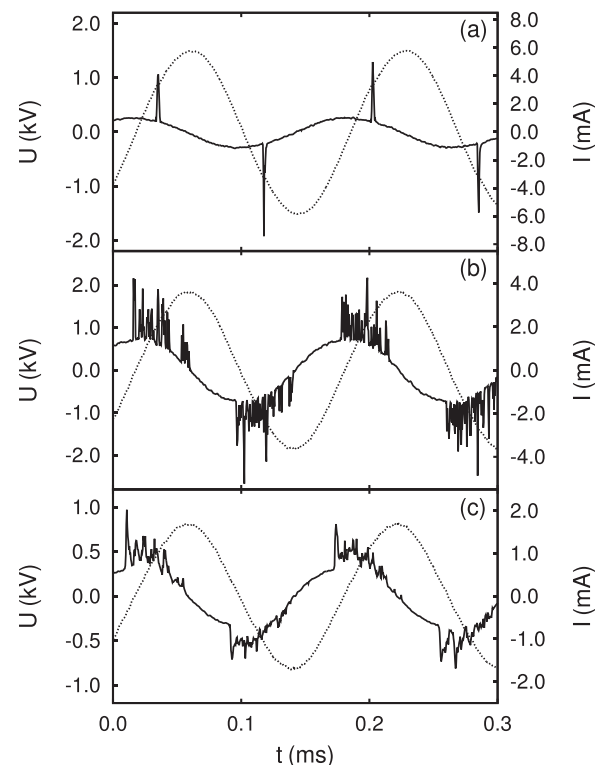


FIG. 3. The time dependence of applied voltage (dotted line) and discharge current (full line) at room temperature for (a) DBD in pure Ar, (b) DBD in Ar/CH₄, and (c) APGD in Ar/C₂H₂. The concentration of CH₄ or C₂H₂ in Ar was 0.41 vol. %. Discharges were operated slightly above the ignition voltage in particular gas mixture.

was added to the mixture as seen from the comparison of current measurements in Figs. 3(c) and 4(b).

The DBD in Ar/C₂H₂ mixture has similar behavior as DBD in Ar/NH₃ mixture.^{9,28} The DBD in Ar/NH₃ mixture was identified as the APGD.²⁹ However, the discharge current in the DBD in Ar/NH₃ mixture has the form of several sharp peaks instead one broad peak under some experimental conditions and it was assumed that this phenomenon could be explained by the presence of impurities in used argon gas.²⁸ This could be also the explanation for observed discharge currents in DBD in Ar/C₂H₂ mixture.

The results from the electrical measurements were confirmed by images taken with the fast ICCD camera over one half-period, i.e., 80 μs, and with shorter exposure time of 5 μs, as shown in Figs. 5 and 6, respectively. The images in Figs. 5(a) and 5(b) document the filamentary structure of Ar and Ar/CH₄ discharges. The images Figs. 5(c) and 5(d) of the discharges in Ar/C₂H₂ and Ar/C₂H₂/H₂ revealed the existence of a luminous layer at instantaneous cathode, identifying these discharges as APGD. Similar behavior was observed during both polarities of applied voltage. The images with shorter exposition time showed that APGD with C₂H₂ did not cover the whole electrode area, see Fig. 6.

B. Discharge diagnostics at high temperature

If the bottom electrode was heated up to 680 °C the ignition voltage decreases due to the decrease of neutral gas

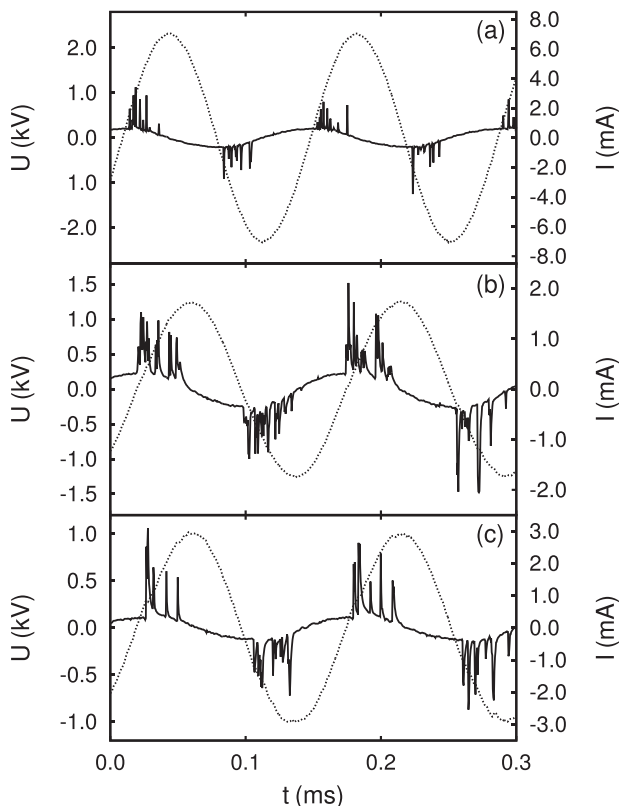


FIG. 4. The time dependence of applied voltage (dotted line) and discharge current (full line) for (a) DBD in Ar/CH₄/H₂ at 22 °C, (b) APGD Ar/C₂H₂/H₂ at 22 °C, and (c) APGD Ar/C₂H₂/H₂ at 680 °C. The concentration of CH₄ or C₂H₂ in Ar/H₂ was 0.41 vol. %. Discharges were operated slightly above the ignition voltage in particular gas mixture.

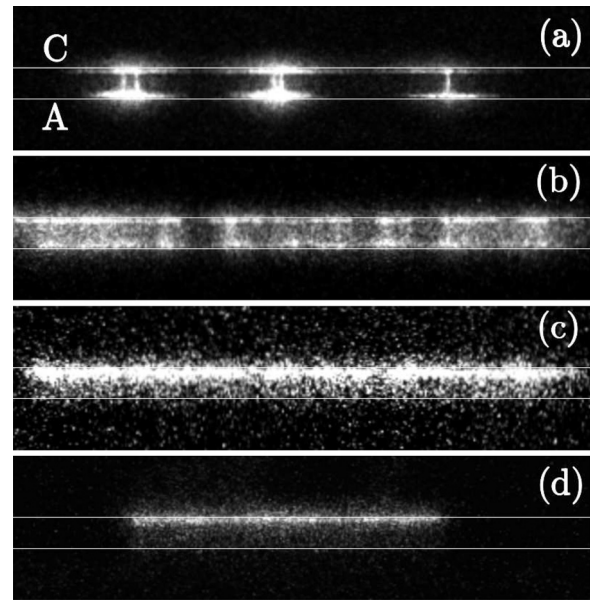


FIG. 5. ICCD images of discharges at room temperature with 80 μs (one half-period) exposure time: (a) filamentary DBD in Ar, (b) filamentary DBD in Ar/CH₄, (c) APGD in Ar/C₂H₂, and (d) APGD in Ar/C₂H₂/H₂. The concentration of CH₄ or C₂H₂ was 0.41 vol. %. Horizontal lines indicate the dielectric surfaces and the upper electrode is the instantaneous cathode in all images.

concentration (i.e., argon and hydrogen concentration), see Fig. 7. An additional decrease of the ignition voltage can be seen after acetylene addition. However, at high temperature this decrease is not as significant as at room temperature.

Imaging of the discharge at the temperature of 680 °C showed that heating of the bottom electrode had profound effect on the discharge structure, see Fig. 8. Since the upper electrode was not heated the discharge burned in different modes in subsequent half-periods of the applied voltage. If the instantaneous cathode was the upper cold electrode, the emitted light integrated over a discharge half-period of 80 μs was homogeneously distributed in the discharge gap, see Fig. 8(a). However, a short exposure time of 5 μs revealed that the intensity at the instantaneous cathode was slightly higher, see Fig. 8(c). So the recorded homogeneous light in Fig. 8(a) was rather an exceptional case. Therefore, the discharge mode can still be called APGD mode, although it is not so clearly seen as at room temperature. The ICCD

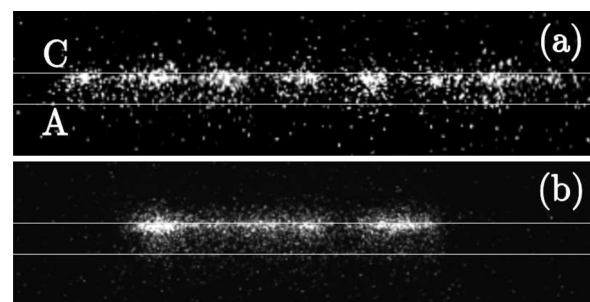


FIG. 6. ICCD images of APGD discharges at room temperature with short exposure time of 5 μs: (a) APGD in Ar/C₂H₂, (b) Ar/H₂/C₂H₂. The concentration of C₂H₂ was 0.41 vol. %. Horizontal lines indicate the dielectric surfaces and the upper electrode is the instantaneous cathode in all images.

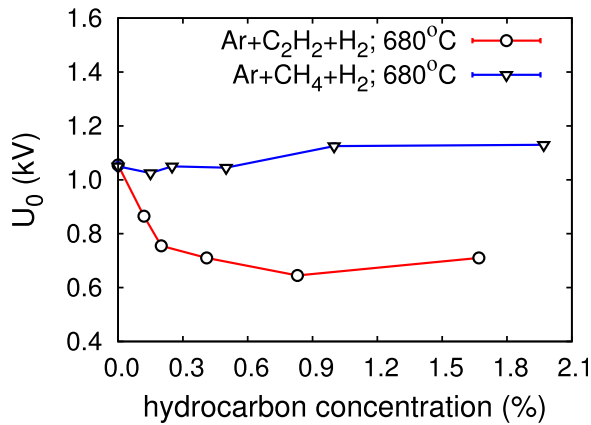


FIG. 7. The ignition voltage U_0 in dependence on the concentration of acetylene or methane added to Ar/H₂ for the temperature of bottom electrode 680°C. Argon and hydrogen flow rates were 7 slm and 100 sccm, respectively.

images of discharge at 410°C (not shown here) confirmed more clearly the APGD discharge mode, i.e., higher intensity at instantaneous cathode, if the cathode was cold but a systematic study of discharges at different elevated temperatures was not performed. The current at this half-period, i.e., for negative voltage, had similar character as for room temperature, see Fig. 4(c).

If the instantaneous cathode was the bottom heated electrode, only luminous layer at the instantaneous anode was visible, see Figs. 8(b) and 8(d). It indicated that the discharge was Townsend-like discharge (APTD). In this case the electron concentration had to be lower than in case of the APGD at room temperature and the electric field in the discharge gap was not influenced by a space charge. The current at this half-period is composed from several peaks, similar as for APGD, but the peaks are less frequent and wider, see Fig.

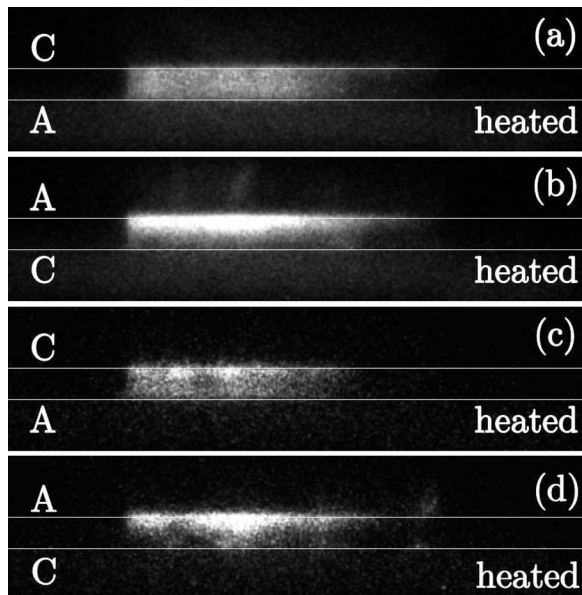


FIG. 8. ICCD images of APGD in Ar/C₂H₂/H₂ with 0.41 vol. % admixture of C₂H₂ and bottom electrode heated to 680°C: (a) 80 μs (one half-period), instantaneous cathode at upper electrode, (b) 80 μs (one half-period), cathode at bottom electrode, (c) 5 μs, cathode at upper electrode, and (d) 5 μs, cathode at bottom electrode. Horizontal lines indicate the dielectric surfaces.

4(c). The conditions for the formation of different discharge modes in subsequent half-periods will be discussed in Sec. III C.

Optical emission spectra of DBD in Ar, Ar/C₂H₂, and Ar/C₂H₂/H₂ were recorded through a glass window in the spectral range 350–750 nm. The second positive system of N₂ ($C^3\Pi \rightarrow B^3\Pi$) was detected in all the mixtures owing to a presence of air impurities. It was represented by several bands but the most intensive band 0–0 at 337.7 nm was missing due to decreased transmittance of the window. Therefore, the first visible N₂ band was 0–1 at 357.7 nm. The low transmittance of the glass window in UV prevented to evaluate the presence of OH impurities because their emission band lies at 306 nm.

The C₂ Swan system and CH bands were observed after the addition of acetylene to the gas feed. The optical emission spectra of the discharges at low and high temperatures are compared in Fig. 9 for Ar/C₂H₂/H₂. A vertical shift of the spectra recorded at the high temperature was caused by a thermal radiation of the heated electrode. The Swan system of C₂ ($d^3\Pi_g \rightarrow a^3\Pi_u$) was located between 450 and 620 nm. The most intensive transitions, 0–0 at 516.5 nm, 1–0 at 473.7 nm, 0–1 at 563.6 nm, and 1–2 at 558.6 nm, were easily distinguished. Altogether, 15 separate bands were assigned to the Swan system of C₂. Additionally, one CH emission band was associated with the 0–0 transition of 430 nm band ($^2\Delta \rightarrow ^2\Pi$).⁴⁰

C. Discussion of discharge conditions at high temperature

The different discharge behavior in subsequent half-periods can be explained as follows. The thermal conductivity of argon does not change significantly in the range of temperatures considered, so the gas temperature changes linearly from heated electrode to non-heated electrode. The spatial profile of neutral gas density can be then calculated from the equation of state for an ideal gas at constant pressure. The different values of gas density influence the values of reduced electric field, the values of electron and ion mobilities and the values of Townsend coefficient.

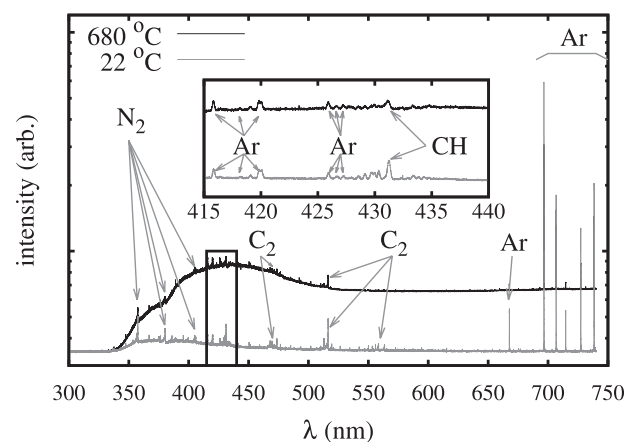


FIG. 9. Optical emission spectra of APGD in Ar/C₂H₂/H₂ (0.41 vol. % of C₂H₂ and 1.4 vol. % of H₂) without and with heating of the bottom electrode.

The transition from Townsend discharge to glow discharge causes the distortion of initially homogeneous electric field. To calculate the electric field $E(x)$ in the discharge gap, the approximation of the charge density distribution obtained in the assumption $E(x) = \text{const.}$ is taken.³⁰ The ion current density $j_+(x)$ in the Townsend discharge in the case of non-homogeneous gas density is given by formula

$$j_+(x) = j \left(1 - \exp \left(- \int_0^d \alpha(x') dx' + \int_0^x \alpha(x') dx' \right) \right), \quad (1)$$

where j is the total current density, α is the Townsend coefficient, and d is the discharge gap width. The x axis points from the cathode to the anode. The discharge gap at Townsend discharge is almost entirely positively charged, i.e., $n_+ \gg n_e$ ^{30,32} (n_+ is the concentration of positive ions, n_e is the electron concentration). Also the ion current density j_+ much exceeds the electron current density j_e over a large part of the discharge gap, except the small part of gap at anode.³⁰ Then current density $j \approx j_+$ and $n_+(x) = j_+(x)/(e\mu_+(x)E)$, μ_+ is the positive ion mobility. However, the electric field in the discharge gap is not distorted, because the charge density is low. As j increases, the ion concentration increases and the electric field in the discharge gap begins to decrease at the anode. The spatial profile of electric field is determined by the equation

$$\frac{dE(x)}{dx} = \frac{e}{\epsilon_0} n_+. \quad (2)$$

In the DBD discharge in the mixture Ar/H₂/C₂H₂ at atmospheric pressure primary ions Ar⁺ are quickly converted to Ar₂⁺ molecular ions, these argon ions react with hydrogen producing H₂⁺ and H₃⁺ ions.³¹ Also some hydrocarbon ions originated from acetylene are present in the discharge. The mobility of Ar₂⁺ molecular ions increases with increasing neutral gas temperature,³³ the mobilities, and their temperature dependence of other above mentioned ions are not known, however, the mobilities of molecular ions in argon usually increase with increasing temperature.³³

In our experiment, the amplitudes of current peaks in both half-periods have almost the same value. If the temporary cathode is the heated electrode, the neutral gas concentration at the cathode is lower than the neutral gas density at the anode (non-heated electrode). Also, the ion mobility at the cathode is higher, because the ion mobility is inversely proportional to neutral gas density and because the ion mobilities of above mentioned ions increase with temperature. Then the ion concentration in cathode region is lower and thus the distortion of electric field is lower, see Figs. 10 and 11. The discharge remains in Townsend mode. The profiles in these figures were calculated for the gap voltage $U_{\text{gap}} = 0.7 \text{ kV}$ and total current density $j = 1.5 \text{ A m}^{-2}$, which are values typical for the studied discharge. The values for the Townsend coefficient for argon and for Ar₂⁺ mobility in argon were taken from literature.^{33,34}

In opposite case, the temporary anode is the heated electrode, the major part of ions is far away from the anode and their concentration is not affected, the distortion of electric

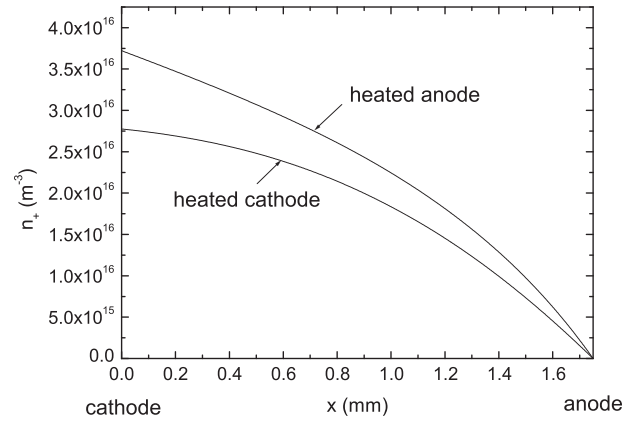


FIG. 10. Spatial profiles of ion concentration in the discharge gap.

field is higher as in previous case (at the same discharge current), see Fig. 11. The distortion of electric field depends on current density j , if the current density increases to the value of $j = 2.2 \text{ A m}^{-2}$, the electric field at the anode reaches zero (see the dashed line in Fig. 11) and the discharge transits to glow mode. However, at this value of j the model loses its validity, because the initial assumption ($E(x) = \text{const.}$) is not more valid. If the temporary cathode is the bottom electrode at our experiment, the current density at the cathode is lower due to the asymmetry of electrodes. Moreover, as can be seen in Fig. 8, the discharge in glow mode is localized in columns with smaller diameter than the discharge in Townsend mode which gives higher current density in glow mode. So the higher n_+ at the non-heated temporary cathode and the higher current density j lead to the discharge transition to the glow mode.

The temperature of dielectric at electrodes also influences the thermodesorption frequency ν_e

$$\nu_e = \nu_{e0} \exp \left(- \frac{E_{\text{ads}}}{kT_w} \right), \quad (3)$$

where ν_{e0} is the frequency of oscillations for an electron near an adsorption site, E_{ads} is the electron binding energy, k is the Boltzmann constant, and T_w is the wall temperature. The values $E_{\text{ads}} \approx 0.8 \text{ eV}$ and $\nu_{e0} \approx 4 \times 10^{15} \text{ s}^{-1}$ were considered in previous study.³⁵ Then the desorption current from

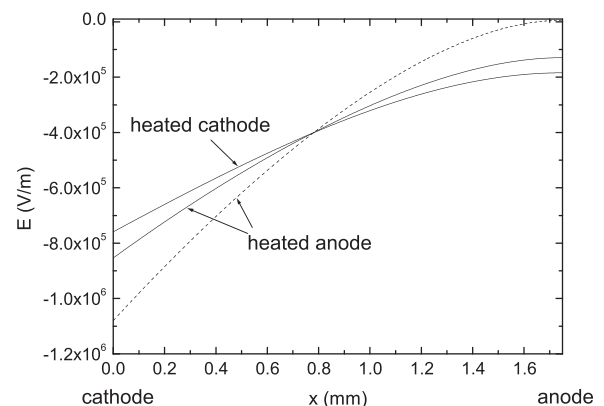


FIG. 11. Profiles of electric field in the discharge gap. Full lines- $j = 1.5 \text{ A m}^{-2}$, dashed line- $j = 2.2 \text{ A m}^{-2}$.

the heated electrode (with the temperature of 710 °C) is $25 \times$ higher than the desorption current from non-heated electrode (with the temperature of 460 °C). So when the heated electrode is the temporary cathode, higher desorption current can also sustain homogeneous Townsend discharge.

Similarly, the modes of DBD burning in Ar/NH₃ mixture were studied also for excitation voltage frequencies ranging from 50 kHz to 9 MHz.³⁶ It was found that the discharge was an APGD at frequencies up to 200 kHz. For frequencies higher than 250 kHz, the discharge changed to Townsend discharge. This change was explained also by the decrease of ion concentration close to cathode up to the point where their concentration was too low to generate the cathode fall.

D. Carbon nanotubes deposition

The growth of CNTs was investigated in Ar/C₂H₂/H₂ and Ar/CH₄/H₂ discharges on the Si substrates covered by barrier oxide layer and top iron film as described in Sec. II. Hydrogen played an important role in suppressing the formation of amorphous carbon on the electrodes and in the improvement of the quality of CNTs. Without hydrogen, large amount of amorphous carbon was generated by deposition process, especially in the case of C₂H₂. Without the discharge and substrate heated to 710 °C, the CNT growth was not observed in case of CH₄ mixture and only very poorly aligned CNTs were grown using C₂H₂ mixture. In following paragraphs, the growth of CNTs using Ar/C₂H₂/H₂ and Ar/CH₄/H₂ discharges is discussed.

The deposition did not include any dedicated process of the iron thin film restructuring into nanoparticles besides the substrate heating to 300 °C during 5 min of chamber filling with the deposition (hydrocarbon) mixture. The growth of

CNTs by CVD methods requires the presence of catalytic nanoparticles. If the catalyst is initially prepared in the form of thin film on a substrate, the restructuring into nanoparticles is often obtained by heating the film in N₂, H₂, or NH₃ atmosphere.³⁷ It was shown that for the CNT growth in microwave plasma torch a separate plasma treatment step leading to creation of thin metallic film into NPs was not necessary and that this process is an integral part of the CNTs synthesis.^{38,39} The present work showed that when using DBD it can be also omitted.

The substrate temperature was varied from 610 to 710 °C (maximum achievable temperature in the setup) and the microstructure of the material deposited in DBD fed by 0.2% mixture of C₂H₂ and CH₄ in Ar/H₂ was compared by TEM. The TEM micrographs in Fig. 12 clearly showed that at both temperatures, 610 and 710 °C, the deposit in Ar/C₂H₂/H₂ DBD exhibited much higher order of nanostructuring. The carbon material deposited from Ar/CH₄/H₂ DBD at 610 °C was amorphous without any hints of ordering (Fig. 12(c)) whereas using C₂H₂ the hollow structure of carbon nanotubes was observed together with some amorphous impurities (Fig. 12(a)). The best results were achieved using the temperature of 710 °C. The sample deposited in Ar/CH₄/H₂ mixture showed highly disordered carbon nanofiber (CNF) structures with the diameter of 80 nm (Fig. 12(d)). The analysis of TEM micrographs revealed that the sample deposited in Ar/C₂H₂/H₂ mixture consisted of multi-walled carbon nanotubes with the diameters ranging from 15 to 30 nm and wall thicknesses from 3 to 7 nm. From the wall thickness and assumed distance of 0.34 nm between each carbon layer, it was concluded that the wall of deposited carbon nanotubes consists of up to 20 carbon layers.

Darker spots in TEM micrographs can be attributed to the iron catalytic particles but they can be also caused by a

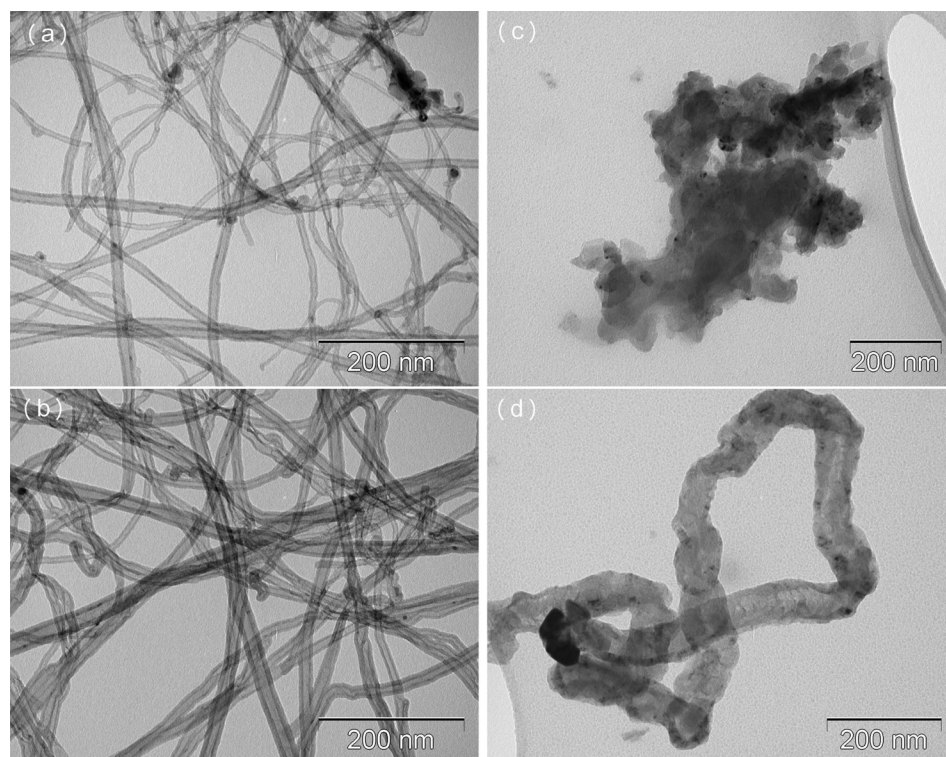


FIG. 12. TEM micrograph of the carbon nanostructures deposited from (a), (b) 0.2% of C₂H₂ in Ar/C₂H₂/H₂ mixture and (c), (d) 0.2% of CH₄ in Ar/CH₄/H₂ mixture. The substrate temperature was 610 °C for (a) and (c) and 710 °C for (b) and (d) images. The micrographs were made using Philips CM12 microscope.

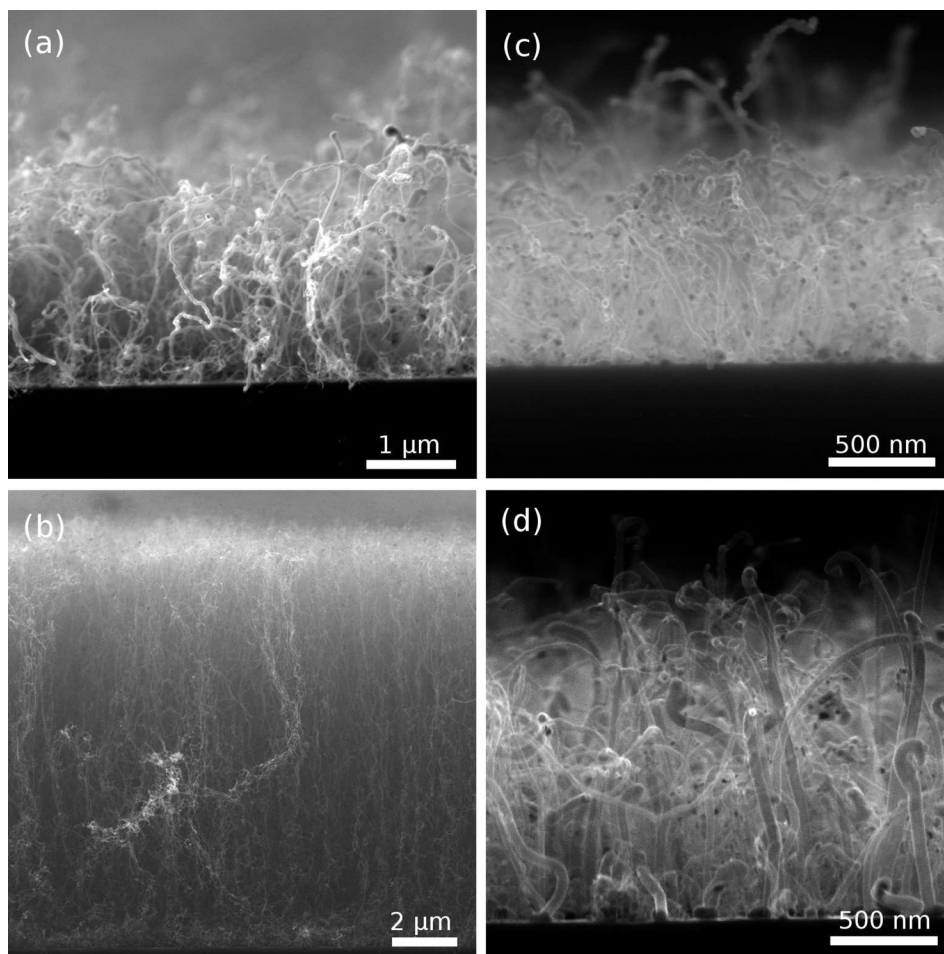


FIG. 13. Cross sectional SEM micrographs of deposited carbon nanostructures for (a) 0.1%, (b) 0.2% of C_2H_2 in $Ar/C_2H_2/H_2$ APG discharges, and (c) 0.2%, (d) 0.4% of CH_4 in $Ar/CH_4/H_2$ DBD discharges. The substrate temperature was $710^\circ C$. The micrographs were made using TESCAN LYRA microscope.

different contrast of graphitic structures, places with overlapping structures or thicker amorphous carbon material. The latter two possibilities hide the interpretation of catalyst incorporation especially in the case of CH_4 mixtures. Based on the current understanding of the carbon nanotube growth, the catalytic nanoparticles are assumed to be of a similar size as the nanotube diameter. It holds for the C_2H_2 deposits. The size and shape of iron particles incorporated into CH_4 deposits were sometimes difficult to assess but in many cases it was clear that the particles were much larger than for C_2H_2 and it led to larger diameter of CNFs. The EDS mapping confirmed that in both the mixtures iron nanoparticles are distributed over all the sample and the amount of iron is very low (C 37.5 wt. %, Fe 0.3 ± 0.02 wt. % at 1σ) compared to the substrate background (Si 47.0 wt. %, O 15.2 wt. %) and the EDS detection limit of 0.1 wt. %. The scan was done with small beam size (5 nm) to give smaller interaction volume and substrate background but nevertheless the influence of the background was substantial.

The SEM micrographs for 0.2% hydrocarbon mixtures confirmed the results from TEM. In the $Ar/CH_4/H_2$ gas mixture, the carbon nanostructures deposited at $710^\circ C$ were curled CNFs shown in Fig. 13(c). For $Ar/C_2H_2/H_2$ mixture, the deposited carbon nanostructures at $710^\circ C$ were well aligned multi-walled CNTs (Fig. 13(b)) but at $610^\circ C$ a higher amount of amorphous carbon and worse alignment were observed.

Additional SEM study was performed to access the dependence of CNTs growth on hydrocarbon flow rate and type of the gas. The cross sectional SEM images of carbon nanostructures deposited at $710^\circ C$ with 0.1% and 0.2% of C_2H_2 or 0.2% and 0.4% of CH_4 in Ar/H_2 are compared in Fig. 13. The same rows of Fig. 13 compare the nanostructures deposited with the same amount of carbon delivered into the discharge, i.e., doubled CH_4 flow rate as compared to C_2H_2 . The images revealed that the growth rate was higher in C_2H_2 mixtures being about 870 nm/min for $Ar/C_2H_2/H_2$ and only 110 nm/min for $Ar/CH_4/H_2$ at the higher carbon delivery rate. For the higher C_2H_2 flow rate, the density of CNTs was higher, leading to a better alignment, and the growth rate increased. The growth rate of CNFs from $Ar/CH_4/H_2$ DBD increased for the higher CH_4 flow rate but their density remained similar. The growth rate in C_2H_2 mixture was determined also for the deposition time decreased from 15 to 5 min. The observed growth rate was similar (1070 nm/min) as for the 15 min deposition.

The mixtures with C_2H_2 and CH_4 differed in the amount of hydrogen atoms and its higher amount in case of CH_4 could explain the lower CNT growth rate due to a removal of accessible free carbon leading to growth of amorphous carbon and poisoning of the catalyst. However, the increased hydrogen content in the gas mixture did not result in a better quality of CNTs. In general these results are in agreement with the work of Nozaki *et al.*,⁴¹ where C_2H_2 was identified

as the principal precursor for the carbon nanotube growth even in the mixtures with CH_4 only. It should be noticed that CH_4 can be used for the synthesis of dense carbon nanotubes at higher temperature of the deposition (around 1000°C) or in a different plasma source such as atmospheric pressure plasma torch.⁴²

The average diameters of CNTs from 0.1% and 0.2% of C_2H_2 in Ar/H_2 were 21 ± 4 and 15.5 ± 0.6 nm, whereas 0.2% and 0.4% of CH_4 in Ar/H_2 resulted in CNFs with 35 ± 3 and 34 ± 2 nm in diameter, respectively. There is a difference between the nanostructure diameters determined from SEM and TEM analysis. This difference can be caused by TEM sample preparation, by its selectivity and by the inaccuracy of the measurement from TEM and SEM micrographs.

The influence of the DBD discharge mode (filamentary or homogeneous) on the deposited layer of CNTs/CNFs was observed macroscopically. Large holes observed in the layers made in the $\text{Ar}/\text{CH}_4/\text{H}_2$ mixture were attributed to the high amount of filaments in the discharge. In the $\text{Ar}/\text{C}_2\text{H}_2/\text{H}_2$ mixture, the CNTs layer homogeneously covered the whole area with the catalyst and no large discontinuities in the layer structure were observed. The CNTs layer height was uniform on the whole substrate, only some lower CNTs density areas with the diameter of the hundreds of nanometers randomly distributed over the substrate were observed. The CNTs height in these areas was also lower. These areas covered around 20% of all substrate area and they could be attributed to the discharge influence (occasionally occurring filaments).

According to Raman spectroscopy, all the deposited CNTs were solely multi-walled. Features belonging to single-walled CNTs, i.e., radial breathing modes (RBM) in the range of $100\text{--}250\text{ cm}^{-1}$ and splitting of G peak,⁴⁶ were not observed. Raman spectra showed two intense peaks typical for graphite-like materials, the so-called G and D bands.⁴³ The D band observed at $1342\text{--}1352\text{ cm}^{-1}$ was induced by the presence of defects in the structure of CNTs.⁴⁴ The G band, assigned to the in-plane vibration of carbon atoms, was observed at $1580\text{--}1590\text{ cm}^{-1}$. Its asymmetry towards higher wavenumbers was caused by the presence of the third small peak, D' band at 1620 cm^{-1} , that is typical for defective graphite-like materials.^{45,46}

Raman spectra of carbon nanostructures deposited from C_2H_2 ($T = 610^\circ\text{C}$, $T = 710^\circ\text{C}$) and CH_4 mixtures ($T = 710^\circ\text{C}$) are compared in Fig. 14. The intensity of D band was always higher than the intensity of G band in case of CNFs grown from CH_4 . It corresponds to SEM micrographs in Fig. 13 that show more defective structure of CNFs from CH_4 . Additionally, the D' band is quite well resolved for the most defective CNFs (Fig. 13(c)) deposited from 0.2% CH_4 but only very poorly resolved for CNTs deposited with C_2H_2 . The ratio of peak integrated intensity of D and G bands was 1.7 for $T = 610^\circ\text{C}$ and 1.0 for $T = 710^\circ\text{C}$ for C_2H_2 mixture. The second order peaks at 2450 , 2695 , and 2941 cm^{-1} were also identified in the spectra. With increasing temperature the intensity of 2695 cm^{-1} band increased while the intensity of 2941 cm^{-1} band decreased.

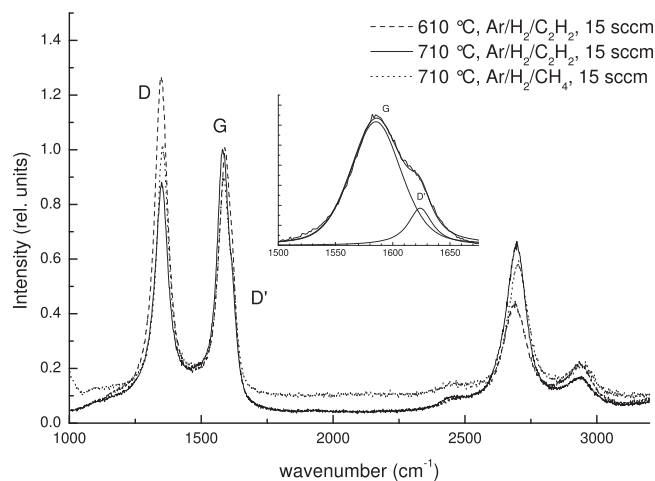


FIG. 14. Raman spectra of deposits from APG discharge in $\text{Ar}/\text{C}_2\text{H}_2/\text{H}_2$ (0.2% of C_2H_2) at the substrate temperature 610 and 710°C and filamentary DBDs in $\text{Ar}/\text{CH}_4/\text{H}_2$ (0.2% of CH_4) at the substrate temperature 710°C . Details of G band fitting shown for 0.2% of CH_4 in $\text{Ar}/\text{CH}_4/\text{H}_2$.

The intense peak at 522 cm^{-1} (not shown in graph) was assigned to the silicon substrate. It was a prominent feature in the spectra of the samples deposited from CH_4 whereas in the case of dense CNTs grown from C_2H_2 it was very weak or not detected at all. Thus, a low density of carbon nanofibers observed by SEM was also confirmed by Raman spectroscopy.

IV. CONCLUSION

Diagnostics of $\text{Ar}/\text{C}_2\text{H}_2$ and Ar/CH_4 DBD discharges at room temperature suggested that Penning ionization, taking place in C_2H_2 mixtures, is significant process that changes the character of the discharge concerning the ignition voltage and discharge homogeneity even when hydrogen is added. It was proved that the discharge in $\text{Ar}/\text{C}_2\text{H}_2$ and $\text{Ar}/\text{C}_2\text{H}_2/\text{H}_2$ has character of APGD whereas CH_4 mixture resulted in a filamentary DBD. The discharges in hydrocarbon mixtures with Ar and H_2 were investigated also at elevated temperature of the bottom electrode with the aim to grow surface bound CNTs. Fast ICCD camera of DBD in $\text{Ar}/\text{C}_2\text{H}_2/\text{H}_2$ mixture revealed that the discharge mode switches at every half-period between APGD and atmospheric pressure Townsend discharge due to increased temperature of the instantaneous cathode. The growth of CNTs on silicon with barrier thermal SiO_2 layer and 5 nm thick iron catalytic film was performed in Ar/H_2 mixed with various percentages of C_2H_2 or CH_4 at different temperatures from 610 to 710°C . The deposition did not include any dedicated process of iron catalyst restructuring into nanoparticles and did not use helium as working gas. Carbon nanotubes grown from C_2H_2 were multi-walled exhibiting two intense Raman peaks, G and D bands, typical for graphite-like materials, whereas only carbon nanofibers were grown from CH_4 . The average diameter of CNTs grown from C_2H_2 was lower and the growth rate was higher as compared to the growth of carbon nanofibers from CH_4 at the same carbon delivery rate. Moreover, Raman signal

from Si substrate and SEM micrographs showed that carbon nanofibers grown from CH₄ have lower density compared to CNTs grown from C₂H₂. It can be associated to higher amount of hydrogen in CH₄ and/or filamentary nature of CH₄-based DBDs.

ACKNOWLEDGMENTS

The present work was supported by the Czech Science Foundation under contracts P205/10/1374 and 13-24635S, by the Projects “R&D center for low-cost plasma and nanotechnology surface modifications” (CZ.1.05/2.1.00/03.0086) and “CEITEC-Central European Institute of Technology” (CZ.1.05/1.1.00/02.0068) funded by European Regional Development Fund and by the Project LO1411 (NPU I) funded by Ministry of Education, Youth and Sports of Czech Republic. We would like to thank Dušan Hemzal for Raman measurements. P.K. would like to thank for support to the Project “Excellent young scientists on BUT” (CZ.1.07/2.3.00/30.0039).

- ¹U. Kogelschatz, *Plasma Chem. Plasma Process.* **23**, 1 (2003).
- ²K. G. Donohoe and T. Wydeven, *J. Appl. Polym. Sci.* **23**, 2591 (1979).
- ³S. Kanazawa, M. Kogoma, T. Moriwaki, and S. Okazaki, *J. Phys. D: Appl. Phys.* **21**, 838 (1988).
- ⁴D. Trunec, A. Brablec, and J. Buchta, *J. Phys. D: Appl. Phys.* **34**, 1697 (2001).
- ⁵M. Kogoma and S. Okazaki, *J. Phys. D: Appl. Phys.* **27**, 1985 (1994).
- ⁶S. Okazaki, M. Kogoma, M. Uehara, and Y. Kimura, *J. Phys. D: Appl. Phys.* **26**, 889 (1993).
- ⁷N. Kanda, M. Kogoma, H. Jinno, H. Uchiyama, and S. Okazaki, in *Proceedings of the 10th International Symposium on Plasma Chemistry (Bochum)* (1991), Vol. 3, pp. 2–20.
- ⁸A. Fateev, F. Leipold, Y. Kusano, B. Stenum, E. Tsakadze, and H. Bindslev, *Plasma Process. Polym.* **2**, 193 (2005).
- ⁹P. Kloc, H.-E. Wagner, D. Trunec, Z. Navrátil, and G. Fedoseev, *J. Phys. D: Appl. Phys.* **43**, 345205 (2010).
- ¹⁰N. Gherardi, G. Gouda, E. Gat, A. Ricard, and F. Massines, *Plasma Sources Sci. Technol.* **9**, 340 (2000).
- ¹¹F. Massines, P. Segur, N. Gherardi, C. Khamphanb, and A. Ricard, *Surf. Coat. Technol.* **174–175**, 8 (2003).
- ¹²F. Massines, N. Gherardi, N. Naude, and P. Segur, *Plasma Phys. Controlled Fusion* **47**, B577 (2005).
- ¹³Y. Sawada, S. Ogawa, and M. Kogoma, *J. Phys. D: Appl. Phys.* **28**, 1661 (1995).
- ¹⁴R. Foest, F. Adler, F. Sigeneger, and M. Schmidt, *Surf. Coat. Technol.* **163–164**, 323 (2003).
- ¹⁵N. Gherardi, S. Martin, and F. Massines, *J. Phys. D: Appl. Phys.* **33**, L104 (2000).
- ¹⁶D. Trunec, Z. Navrátil, P. Sřahel, L. Zajičková, V. Buršíková, and J. Čech, *J. Phys. D: Appl. Phys.* **37**, 2112 (2004).
- ¹⁷D. Trunec, L. Zajičková, V. Buršíková, F. Studnička, P. Sřahel, V. Prysiaznyh, V. Peřina, J. Houdková, Z. Navrátil, and D. Franta, *J. Phys. D: Appl. Phys.* **43**, 225403 (2010).
- ¹⁸S. P. Bugaev, A. D. Korotaev, K. V. Oskomov, and N. S. Sochugov, *Surf. Coat. Technol.* **96**, 123 (1997).
- ¹⁹D. Liu, S. Yu, T. Ma, Z. Song, and X. Yang, *Jpn. J. Appl. Phys.* **39**, 3359 (2000).
- ²⁰N. Jiang, S. F. Qian, L. Wang, and H. X. Zhang, *Thin Solid Films* **390**, 119 (2001).
- ²¹H. Kodama, A. Shirakura, A. Hotta, and T. Suzuki, *Surf. Coat. Technol.* **201**, 913 (2006).
- ²²T. Nozaki, Y. Kimura, and K. Okazaki, *J. Phys. D: Appl. Phys.* **35**, 2779 (2002).
- ²³T. Nozaki and K. Okazaki, *Plasma Process. Polym.* **5**, 300 (2008).
- ²⁴T. Nozaki, K. Ohnishi, K. Okazaki, and U. Kortshagen, *Carbon* **45**, 364 (2007).
- ²⁵Z. Navrátil, D. Trunec, R. Smid, and L. Lazar, *Czech. J. Phys.* **56**, B944 (2006).
- ²⁶See <http://www.physics.muni.cz/~zdenek/span/> for Spectrum Analyzer program Home page.
- ²⁷J. E. Velazco, J. H. Kolts, and D. W. Setser, *J. Chem. Phys.* **69**, 4357 (1978).
- ²⁸P. Kloc, Ph.D. thesis, Masaryk University, Brno, 2012.
- ²⁹F. Massines, N. Gherardi, N. Naude, and P. Segur, *Eur. Phys. J. Appl. Phys.* **47**, 22805 (2009).
- ³⁰Y. P. Raizer, *Gas Discharge Physics* (Springer, 1997).
- ³¹D. L. Albritton, *At. Data Nucl. Data Tables* **22**, 1 (1978).
- ³²R. Brandenburg, Z. Navrátil, J. Jansky, P. Sřahel, D. Trunec, and H.-E. Wagner, *J. Phys. D: Appl. Phys.* **42**, 085208 (2009).
- ³³H. W. Ellis, R. Y. Pai, E. W. McDaniel, E. A. Mason, and L. A. Viehland, *At. Data Nucl. Data Tables* **17**, 177 (1976).
- ³⁴J. Dutton, *J. Phys. Chem. Ref. Data* **4**, 577 (1975).
- ³⁵Y. B. Golubovskii, V. A. Maiorov, J. Behnke, and J. F. Behnke, *J. Phys. D: Appl. Phys.* **35**, 751 (2002).
- ³⁶R. Bazinette, R. Subileau, J. Paillol, and F. Massines, *Plasma Sources Sci. Technol.* **23**, 035008 (2014).
- ³⁷L. Zajičková, O. Jašek, M. Eliáš, P. Synek, L. Lazar, O. Schneeweiss, and R. Hanzliková, *Pure Appl. Chem.* **82**, 1259 (2010).
- ³⁸O. Jašek, M. Eliáš, L. Zajičková, V. Kudrle, M. Bublan, J. Matejková, A. Rek, J. Buršík, and M. Kadleciková, *Mater. Sci. Eng. C* **26**, 1189 (2006).
- ³⁹L. Zajičková, M. Eliáš, O. Jašek, Z. Kucerová, P. Synek, J. Matejková, M. Kadleciková, M. Klementová, J. Buršík, and A. Vojacková, *Plasma Process. Polym.* **4**, S245 (2007).
- ⁴⁰R. W. B. Pearse and A. G. Gaydon, *The Identification of Molecular Spectra* (Chapmann & Hall Ltd., 1950).
- ⁴¹T. Nozaki, S. Yoshida, T. Karatsu, and K. Okazaki, *J. Phys. D: Appl. Phys.* **44**, 174007 (2011).
- ⁴²O. Jašek, M. Eliáš, L. Zajičková, Z. Kucerová, J. Matejková, A. Rek, and J. Buršík, *J. Phys. Chem. Solids* **68**, 738 (2007).
- ⁴³M. S. Dresselhaus, G. Dresselhaus, R. Saito, and A. Jorio, *Phys. Rep.* **409**, 47 (2005).
- ⁴⁴K. Jeet, V. K. Jindal, L. M. Bharadwaj, D. K. Avasthi, and K. J. Dharamvir, *Appl. Phys.* **108**, 034302 (2010).
- ⁴⁵M. Souza, A. Jorio, C. Fantini, B. R. A. Neves, M. A. Pimenta, R. Saito, A. Ismach, E. Joselevich, V. W. Brar, Ge. G. Samsonidze, G. Dresselhaus, and M. S. Dresselhaus, *Phys. Rev. B* **69**, 241403(R) (2004).
- ⁴⁶A. Jorio, M. A. Pimenta, A. G. Souza Filho, R. Saito, G. Dresselhaus, and M. S. Dresselhaus, *New J. Phys.* **5**, 139 (2003).



Low pressure plasmachemical processing of multi-walled carbon nanotubes for the production of polyurethane composite films with improved mechanical properties

Lenka Zajíčková^{a,b,*}, Marek Eliáš^{a,b}, Vilma Buršíková^{a,b}, Zuzana Studýnková^b, Věra Mazánková^b, Miroslav Michlíček^{a,b}, Jana Houdková^c

^a Plasma Technologies, CEITEC – Central European Institute of Technology, Masaryk University, Kotlářská, 2, Brno 61137, Czech Republic

^b Department of Physical Electronics, Faculty of Science, Masaryk University, Kotlářská 2, Brno 61137, Czech Republic

^c Institute of Physics, Academy of Sciences of the Czech Republic, Cukrovarnická 10, Prague 162 53, Czech Republic

ARTICLE INFO

Available online 19 December 2012

Keywords:

Plasma functionalization
CCP
Carbon nanotubes
Polyurethane composites
XPS
FTIR
Depth sensing indentation

ABSTRACT

Multiwalled carbon nanotubes (CNTs) were modified in low pressure capacitively coupled discharges (13.56 and 27.12 MHz) in Ar/NH₃ and oxygen-containing gas mixtures. A direct functionalization by nitrogen groups was not possible but 1–3 percentage of carbon–oxygen bonds increased with the total oxygen content on the expenses of sp²C almost independently on the plasma conditions. The plasma modified CNTs were used as fillers for polyurethane (PU) composites prepared by in situ polymerization. The composites were investigated by depth sensing indentation that revealed the existence of surface harder layer caused probably by different polymerization process in the bulk and at the surface that was in a contact with air. The significant improvement of the hardness and elastic modulus was observed when plasma-modified CNTs with high amount of oxygen were added to PU. It also improved the creep resistance of the PU, whereas the ability to recover from a deformation, i.e. anelastic recovery, did not change much.

© 2012 Elsevier B.V. All rights reserved.

1. Introduction

Polyurethane (PU) is a versatile polymer [1–3] that can be tailored to desired applications choosing carefully the reactants, their ratio and their synthesis procedure [4]. Different combinations of strength, ductility, biodegradability or hardness can be achieved with the proper formulation and preparation. Nevertheless, there are still some properties such as thermal stability, electrical and thermal conductivity, stiffness or stress recovery, which could be improved with the addition of carbon nanotubes (CNTs).

Polymer composites filled by CNTs are in the center of interest because they represent a class of materials with multifunctional applications. The idea behind preparation of these composites seems to copy engineered structure of polymers reinforced by carbon or glass microfibers, i.e. a soft matrix (polymer) encapsulating a stiffer, high aspect ratio, load-bearing filler. However, CNTs are entirely different from traditional fibers because their dimensions and mechanical flexibility are similar to the polymer chains used as composite matrices [5] and there are fundamental differences between the interaction behavior of the composite constituents in conventional composites and nanocomposites [6].

The CNTs have excellent mechanical and electrical properties over the microfibers. The tensile strength of multi-walled CNTs (MWCNTs)

was reported at approximately 150 GPa by Lu et al. [7] and, even though recent measurements by nanostressing stage located within a scanning electron microscope showed that the tensile strength of outermost MWCNTs layer was 11–63 GPa [8], it is still higher than 6 GPa of the highest-strength carbon microfibers. The MWCNTs, having Young's modulus 0.8–1.3 TPa [7,9,10], are also stiffer than e. g. carbon fibers, which have Young's modulus of up to 750 GPa [11]. The most striking difference is, however, the combination of high flexibility and strength with high stiffness, a property that is absent in graphite fibers [10].

The MWCNTs exhibit the dominating metallic or semimetallic nature while small band gap was reported and attributed to presence of defects or an electric contact barrier [12]. Because of their very low energy dissipation, nanotubes carry tremendous current densities, higher than 100 MA/cm², which may be compared to current densities of tens of kA/cm² for superconducting wires [11]. The thermal conductivities of CNTs are highly anisotropic, diamond-like over the length of the tube and insulating in the transverse direction [13].

The above mentioned MWCNT properties initiated a high amount of research work on the applications of their polymer composites. It comprises nanocomposites prepared for improvement of the strength and durability [14], thermal stability [3,14], electromagnetic interference shielding [15,16], biochemical and sensoric applications [17] etc. However, the polymer composites filled with CNTs do not yet fulfill the expectations. The CNTs form aggregates that are difficult to disperse on the nanoscale level. Chemical inertness of the CNTs causes problems with their fixation to the polymer matrix. Covalent attachment of functional groups to CNTs is one of the critical steps for the

* Corresponding author at: Plasma Technologies, CEITEC – Central European Institute of Technology, Masaryk University, Kotlářská 2, Brno 61137, Czech Republic.

E-mail address: lenkaz@physics.muni.cz (L. Zajíčková).

application of CNTs in nanocomposites where it should ensure better dispersion of CNTs and increase binding ability to the matrix [5].

The application of CNTs in nanocomposites requires development of effective and environmentally friendly method for CNTs functionalization. In many applications, plasma processing of materials appears to be an advantageous alternative to conventional chemical methods. However, plasmachemical approaches used for these purposes are less studied and understood. The low pressure plasma processes were extensively investigated for the functionalization of various materials. About 400 papers on low pressure plasma functionalization or treatment of CNTs have been published during last 5 years but there are only few studies in which plasma modified CNTs (pmCNTs) were used as fillers in polymer composites. In this work the MWCNTs were modified in low pressure capacitively coupled discharges using two excitation frequencies and various gas mixtures. The plasma conditions were compared not only with respect to the incorporation of oxygen or nitrogen functional groups but also regarding the performance of pmCNTs as polyurethane filler that should improve composite mechanical properties.

2. Experimental details

2.1. Materials

The MWCNTs were purchased from the Nanocyl as Nanocyl-3100 and Nanocyl-3150 (research grade series). According to the datasheet provided by the supplier, the CNTs were prepared by catalytic chemical vapor deposition (CCVD) and purified to 95%, the rest being metal oxides. Their average diameter was 9.5 nm and the length 1.5 μm or below 1 μm for 3100/3101 and 315X ($X=1-3$) grades, respectively. The TEM micrograph of Nanocyl-3150 is in Fig. 1. Commercially functionalized MWCNTs from Nanocyl, Nanocyl-3101 and Nanocyl-315X grades, were used for the reference purposes. Their expected functional groups are listed in Table 1.

The polyurethane was prepared by in situ polymerization from polyol (AXAPUR U100X), isocyanate (U7012) and solvent thinner (U6002) supplied by Colorlak a. s. The antistatic agent Atmer™ 163 (synthetic ethoxylated amine) was purchased from Croda Polymer Additives.

2.2. Plasma modification of CNTs

The Nanocyl-3100 and Nanocyl-3150 MWCNTs were modified in low pressure capacitively coupled plasma (CCP) discharges operating at two different frequencies, 13.56 or 27.12 MHz. The corresponding applied RF power was 15 and 45 W, respectively. The CCP reactor

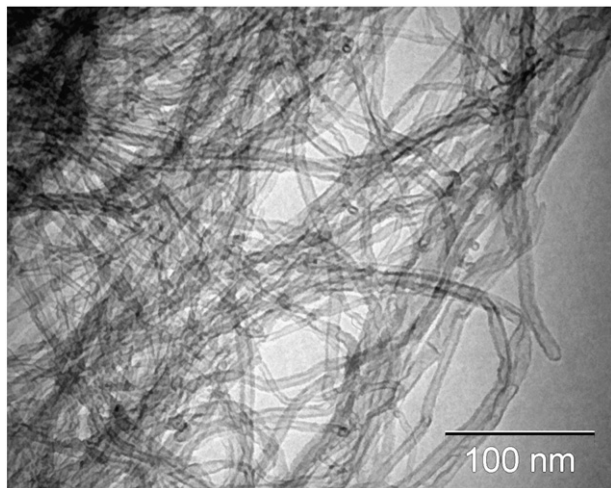


Fig. 1. TEM micrograph of Nanocyl-3150 MWCNTs.

Table 1

Overview of used Nanocyl research grade CNTs together with their XPS elemental analysis.

Grade number	Functionalization	Oxygen (%)	Nitrogen (%)
3100	Pristine	1.2–1.8	0
3150	Pristine	1.2–1.7	0
3101	COOH	6.3	0
3151	COOH	4.7	0
3152	OH	1.1	0
3153	NH ₂	0.6	0.3

was a horizontally mounted glass tube, 8 cm in diameter, closed by two aluminum electrodes (Fig. 2). The perforated grounded electrode enabled gas feeding whereas perforated RF electrode was used to pump the reactor by a rotary pump. The distance between the grounded and RF electrodes was 18.5 cm. Different gas mixtures, summarized in Table 2, were tested at the total pressure of 100 and 180 Pa for 13.56 and 27.12 MHz, respectively. The flow rates of gases were regulated by electronic flow controllers Hastings, whereas flow rates of water and ethanol vapors were set by a needle valve. For each experimental run, the reactor was loaded with 50 mg of CNT powder distributed on the glass tube along the distance of 50 mm. The thickness of the powder layer in the reactor was below 1 mm. The treatment time ranged from 30 to 180 min. However, the process was interrupted at half of the treatment time in order to mix the CNTs and thereby obtain more homogeneous treatment.

2.3. Preparation of PU and PU/CNTs composites

The preparation of PU/CNTs composites consisted of the following steps:

- (i) polyol, solvent thinner, MWCNTs and antistatic agent were weighed out and stirred well manually,
- (ii) the mixture was ultrasonicated for 60 min at temperature of 300 K together with glass beads added for better separation and mixing of CNTs,
- (iii) isocyanate was stirred into the mixture,
- (iv) the final mixture was sucked up with syringe and poured onto a glass substrate (100 × 100 mm) enclosed in a frame,
- (v) homogeneously spread and carefully leveled liquid composite was dried in air at laboratory temperature of 300 K for 48 h.

Polyol, isocyanate and solvent thinner were used, according to the recipe of the producer, in the weight ratio of 7:2:1. The MWCNTs and the antistatic agent for improved dispersion of MWCNTs were added in the amount of 0.1 wt.% and 0.2 wt.% of final composite, respectively. Control samples of pure PU were prepared using the same procedure but omitting the MWCNTs and the antistatic agent.

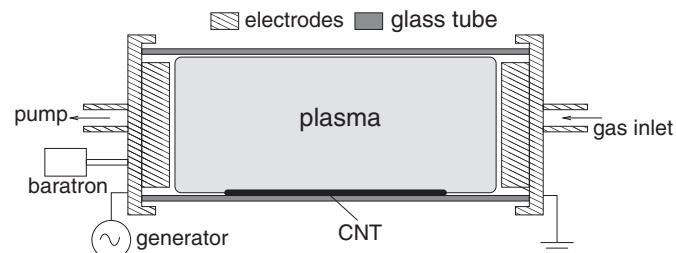


Fig. 2. Schematic drawing of capacitively coupled plasma (CCP) discharge used for modification of CNTs.

Table 2

Summary of plasma conditions used for modification of 3100-Nanocyl CNTs together with elemental analysis of plasma modified CNTs as determined by XPS.

Sample	Gas mixture	Flow rates (sccm)	Pressure (Pa)	Frequency (MHz)	Power (W)	Time (min)	C (%)	O (%)	N (%)	S (%)
CNTF12	Ar/O ₂	15/5	100	13.56	15	60	79.9	17.0	1.4	1.6
CNTF09	Ar/H ₂ O	15/5	100	13.56	15	60	83.4	13.5	1.5	1.6
CNTF18	Ar/C ₂ H ₆ O	15/5	100	13.56	15	120	81.5	12.8	3.3	2.5
CNTF19	O ₂ /C ₂ H ₆ O	5/15	100	13.56	15	180	74.8	21.4	1.6	2.2
FU14	Ar/O ₂	20/5	180	27.12	45	30	78.9	20.4	0.7	0
FU16	Ar/H ₂ O	20/5	180	27.12	45	30	90.7	9.3	0	0
FU17	Ar/CO ₂	20/5	180	27.12	45	30	80.2	19.8	0	0
FU12	Ar/NH ₃	20/5	180	27.12	45	60	96.1	4.4	0	0

2.4. Characterization of CNTs and PU/CNTs composites

CNT powder was analyzed by X-ray photoelectron spectroscopy (XPS). The analyses were carried out on ADES-400 VG Scientific spectrometer using Mg K_α line (1253.6 eV). Quantitative atomic composition was calculated from the spectra measured at the pass energy of 100 eV. The chemical bonding was assessed by investigation of the chemical shifts of C1s and O1s signals measured with the pass energies of 20 and 100 eV, respectively. The resolution at these conditions was 0.8 and 1.2 eV, respectively. The spectra were deconvoluted using XPS Peak Fit 4.1 after subtraction of Shirley-type background by Lorentzian–Gaussian profiles (20% of Lorentzian). Transmittance Fourier transform infrared spectroscopy (FTIR) was performed on the pellets prepared by pressing the mixture of KBr and CNT powder. The measurements (50 scans) were carried out on Vertex 80v Bruker spectrometer in the spectral range 370–4000 cm⁻¹ with the resolution of 4 cm⁻¹.

A Fischerscope H100 depth sensing indentation (DSI) tester with Vickers and Berkovich indenters was used to study the indentation response of composites on glass substrates. Several different testing conditions were used in order to find the optimum procedure that suppressed the influence of the time dependent indentation response of CNT-filled PU composites. The loading period of 20 s was followed by a hold time of 60 s, an unloading period of 1 or 5 s and finished after holding the minimum load for 20 or 60 s. The testing conditions are demonstrated for pure PU on glass substrate in Fig. 3. The tests were carried out at several different maximum indentation loads in order to study the mechanical properties of the composite/substrate system from near the composite surface up to the composite/substrate interface. The applied load varied from 1 to 1000 mN.

The mechanical quantities HM, H_{pl} , Y defined below were obtained from the measurements at such load at which the indentation depth was much less than one tenth of the composite thickness, i.e. the influence of the substrate was negligible. The Martens hardness, HM, is defined for Vickers and Berkovich indenters as the maximum applied load, L_{max} divided by the maximum contact area $A_{max}(h_{max})$:

$$HM = \frac{L_{max}}{A_{max}(h)} = \frac{L_{max}}{\alpha h_{max}^2} \quad (1)$$

where h_{max} is the maximum indentation depth and $\alpha=26.43$. The Martens hardness is sometimes referred as the universal hardness. The plastic hardness is defined as the maximum applied load, L_{max} , divided by the contact area A_c remained after unloading

$$H_{pl} = \frac{L_{max}}{\alpha h_r^2} \quad (2)$$

where h_r is the remaining plastic depth. The elastic modulus, Y , is calculated from the slope of tangent of an unloading curve:

$$Y = \frac{E}{1-\nu^2} = \frac{1}{\frac{1}{E_r} - \frac{1-\nu_i}{E_i}} \quad (3)$$

where E is the Young's modulus of the tested material, E_i is the Young's modulus of the indenter (1141 GPa for diamond), ν_i is the Poisson's ratio of the indenter (0.07 for diamond) and ν is the Poisson's ratio of the tested sample. The reduced modulus, E_r , is determined from unloading curve as

$$E_r = \frac{\sqrt{\pi}S}{2\sqrt{A_p}}, \quad S = \left. \frac{dL}{dh} \right|_{h_{max}} \quad (4)$$

where S is the so-called contact stiffness, A_p is the remained projected contact area and h is the indentation depth for the applied load L .

In order to study the inhomogeneities in the samples an additional quantity, the so-called differential hardness,

$$DH = \frac{\partial L}{26.43\partial(h^2)} \quad (5)$$

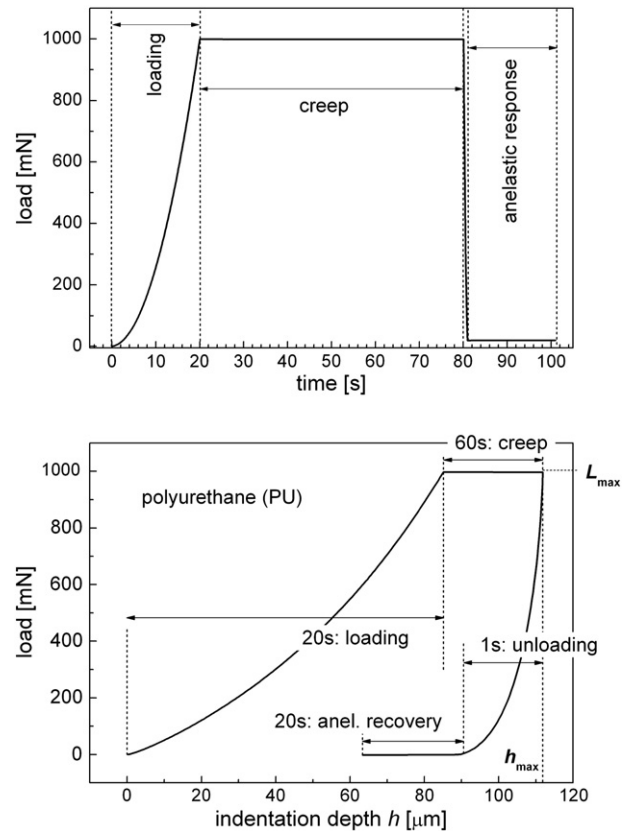


Fig. 3. Example of loading–unloading conditions (top) used for indentation tests of PU composites. Bottom figure shows corresponding relation between applied load and indentation depth for pure PU on glass substrate.

was used. This quantity visualizes the response of the material to a small change in the load for a given depth. It is very sensitive to any defects, abrupt or gradual changes in the tested materials and, therefore, it is very useful for the testing of composite materials.

3. Results and discussion

3.1. Commercial CNTs

Two types of Nanocyl research grade CNTs, 3100 and 3150, contained both a small amount of oxygen (1.2–1.8%) that can be attributed to the purification process and adsorption of water. Their XPS C1s signal had a similar shape that was fitted by three Gauss-Lorentzian peaks. The width of the peaks, except the main peak, was fixed at 1.3 eV in order to decrease the correlation among fitting parameters and ensure consistent comparison between pristine CNTs and various CNTs modifications. The main carbon peak was found at the binding energy 284.4 eV. Its position corresponded very well to the sp^2 carbon atoms obtained for graphite [18] or CNTs [19,20]. The second peak at 285.4 eV was assigned to sp^3 carbons [19,20] and the peak at 286.4 eV corresponded to carbons bonded to a single oxygen atom, i.e. C-O functional groups. The percentages of their areas were 81.5, 14.0 and 4.4%, respectively.

The commercially functionalized CNTs from Nanocyl, 3101 CNTs-COOH, 3151 CNTs-COOH, 3152 CNTs-NH₂ and 3153 CNTs-OH, were investigated for the comparison with pristine and, namely, plasma modified CNTs. Their elemental composition determined by XPS is summarized in Table 1. The grades with COOH groups contained higher percentage of oxygen than pristine CNTs, 4.7–6.3%. The amount of oxygen in the grade with OH groups was as low as 1.1%. The high-resolution C1s signal of CNTs-COOH extended to higher binding energies. It was fitted by six peaks with the positions 284.4, 285.4, 286.5, 287.7, 289.4 and 291.6 eV (Fig. 4) that correspond to

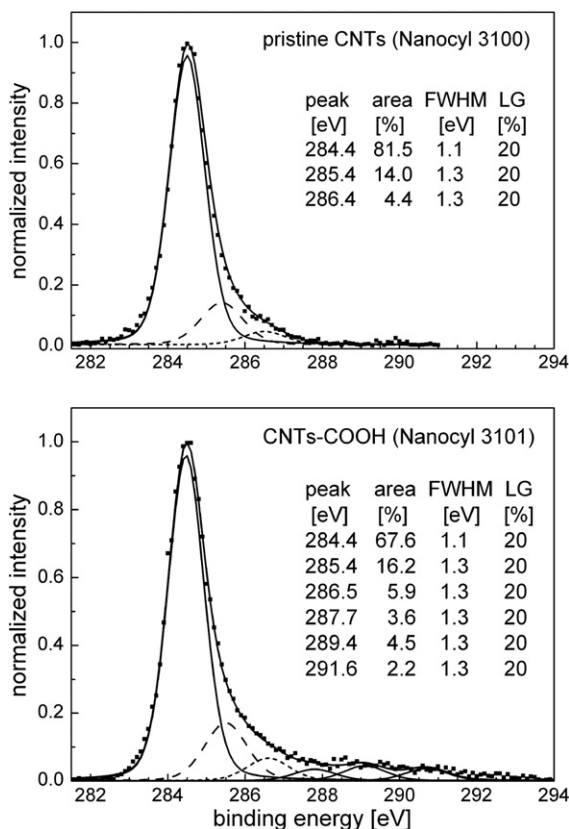


Fig. 4. Fit of C1s XPS signal for two types of Nanocyl CNTs, pristine 3100 and -COOH functionalized 3101.

the sp^2 carbon, sp^3 carbon and carbon with one, two, three or four bonds to oxygen atoms, respectively, because electronegative oxygen atoms induce a positive charge on a carbon atom [21]. The carbon-oxygen bonds at 286.5 eV can be assigned to ether group -C-O-C- or hydroxyl group -C-OH as in alcohol or phenol. The peak at 287.7 eV represents carbonyl group -C=O as in ketone and aldehyde, the peak at 289.4 eV arises due to carboxyl group -C(=O)OH or a carbonyl adjacent to an ether linkage -C(=O)O- as in ester. The last very weak peak at 291.6 eV can be associated with carbon in highly electronegative environment -O-C(=O)O- [19].

The commercial functionalization of CNTs was also investigated by IR spectroscopy of KBr/CNTs pellets. The amount of CNTs in the pellets influenced the appearance of the absorption bands. If it was too low the characteristic absorption peaks were hardly visible, whereas for too high amount of CNTs the peaks became too broad to distinguish fine changes. The IR transmittances of pristine 3150 and functionalized 3151–3153 CNTs, corrected for a tilted background, are compared in Fig. 5 for the KBr/CNTs pellets with 50–70% transmittance at 900 cm^{-1} , whereas the pellet transmittance was below 10% in our previous work [22]. Two distinct IR absorption bands at 1555–1580 and 1120–1180 cm^{-1} were detected in all the CNTs samples, including pristine and plasma modified 3100 CNTs (Figs. 5 and 6).

The absorption band at 1555–1580 cm^{-1} is usually observed in CNTs samples and assigned to -C=C- stretching, i.e. CNT skeletal motion [23–27]. This assignment is in agreement with a general observation of stretching in aromatic compounds at 1580 and 1600 cm^{-1} that become more IR active after the substitution of benzene ring [28]. The position of this peak at about 1560 cm^{-1} for 3150 CNTs shifted to higher wavenumbers for 3151–3153 CNTs. Other absorption peaks related to ring stretching could appear as a double peak at 1450 and 1500 cm^{-1} and, on ring substitution, as a peak at 1010 cm^{-1} [28]. These peaks were not detected in the pristine CNTs but a weak peak at 1020 cm^{-1} appeared for CNTs-COOH and -OH. The assignment of the peak at 1464 cm^{-1} observed in functionalized CNTs is not quite clear. Besides the ring stretching it can be associated with methyl anti-symmetric and methylene deformation vibrations (1460 cm^{-1}) or in-plane bending in alcohols R-OH (1410 cm^{-1}).

A questionable point is the assignment of the absorption in the range 1120–1180 cm^{-1} . Some authors associate it with the CNT skeletal motion [27,29], C-C asymmetric stretching [26], C-C-O ring stretching [20,26], stretching of C-O bond present in ethers, esters, alcohols, and phenols groups [20,30,31] or even C-N groups [32]. A double peak structure similar as observed for 3150 CNTs was reported by Zhang et al. [25] in single-walled CNTs (SWCNTs) prepared by CVD but without a clear explanation. The double peak 1120 and 1145 cm^{-1} became broader and weaker with the functionalization as seen in Fig. 5. Additionally,

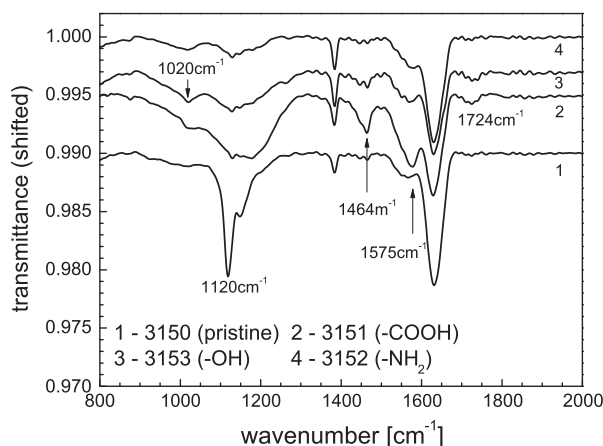


Fig. 5. IR transmittance of KBr pellets with Nanocyl CNTs corrected for tilted background and shifted with respect to each other.

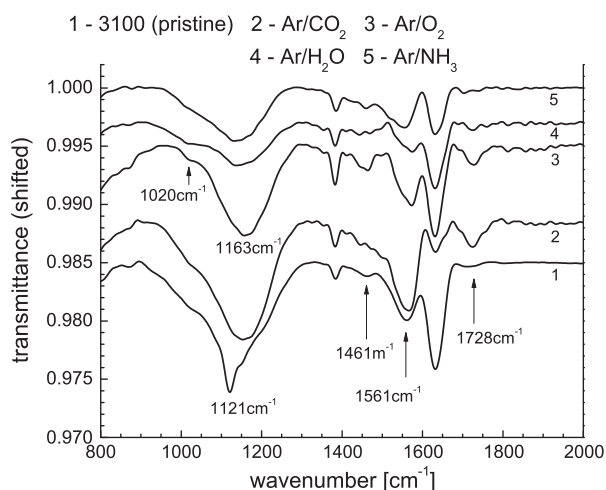


Fig. 6. IR transmittance of KBr pellets with CNTs modified in 27.12 MHz discharges. The measured transmittances were corrected for tilted background and shifted with respect to each other.

the CNTs-COOH/OH samples exhibited clear presence of carbonyl groups as a peak at 1720 cm^{-1} .

Other peaks shown in Fig. 5 are not reliable for assessment of CNTs modifications. The peak at 1384 cm^{-1} can be caused by an oil contamination from hydraulic press. The peak at 1630 cm^{-1} , that is sometimes discussed as stretching of carboxyl group [30] or C=C stretching [32], cannot be taken into consideration because it can be caused by water absorbed in KBr or in CNTs. From the same reasons, the absorption peaks in the region of high wavenumbers $2900\text{--}3600\text{ cm}^{-1}$ are not of importance. The stretching hydrocarbon peaks around 3000 cm^{-1} can be caused by oil contamination and strong absorption at 3450 cm^{-1} by presence of water.

3.2. Plasma modification of CNTs

The 3100 CNTs grades were modified in low pressure CCP of several gas mixtures containing either oxygen or nitrogen. The first set of experiments was performed in 13.56 MHz discharge. In this case the power was limited to 15 W because local microdischarges appeared in perforations of the RF showerhead electrode at higher powers. The second set of plasma treatment was carried out in the double frequency discharges, 27.12 MHz, which could be homogeneously ignited even at higher powers.

The XPS elemental analysis of the first set of samples showed the presence of small amount of sulfur, 1.6–2.5% (Table 2). This contamination arose probably from the vacuum rubber sealing that was partially in contact with plasma because it diminished after the sealing replacement.

The Ar/NH₃ plasma treatment seems to be very ineffective in the initiation of reactions at inert CNT surface because it did not result in a detectable amount of nitrogen and produced the lowest percentage of oxygen (Table 2). Nitrogen in the amount of 1.4–3.3% was detected in CNTs treated in 13.56 MHz discharges and a smaller amount of 0.7% was found for 27.12 MHz Ar/O₂ discharge. It could occur due to a presence of air impurities in the plasma reactor. However, the nitrogen bands in optical emission spectra of these discharges were very weak compared to the discharges fed by nitrogen-containing gas, namely Ar/NH₃ discharge, in which the incorporation of nitrogen groups was not detected at all. Therefore, it is suggested that nitrogen incorporation was caused by synergistic effect of CNT plasma oxidation followed by exposure to air and/or synergistic effect of the plasma oxidation in the presence of nitrogen impurities in the discharge. The confirmation of any of these hypotheses requires further investigation.

The comparison of high-resolution C1s signal of the CCP-modified CNTs in Fig. 7 reveals the differences in the high energy range correlated with the oxygen content in CNTs. The high-oxygen-content samples Ar/O₂, Ar/CO₂ and O₂/C₂H₆O had the signal at 287.6 eV, corresponding to carbonyl group, slightly higher than CNTs-COOH. The signal at this energy for the CNTs modified in Ar/H₂O discharges was similar to CNTs-COOH and lower for the other low-oxygen-content samples. Accordingly, the C1s signal was fitted by 3–6 peaks which area percentages are shown in Fig. 8 in dependence on the total oxygen content. The peak related to sp²C (284.4 eV) decreased almost monotonously with increasing percentage of oxygen in CNTs mainly due to increase of the peaks assigned to carbon–oxygen bonds. A clear exception is the Nanocyl 3101 CNTs-COOH sample because it exhibited relatively high percentage of carbon–oxygen bonds with respect to the total amount of oxygen. The amount of sp³C (285.4 eV) stayed almost constant. The amount of -C-O- (286.5 eV) bonds increased from 4% to 7% for oxygen percentage 4–18% and further increase to 9% was observed for the CNTs with the highest oxygen content. The carbon atoms with two (-C=O) or three (-COO-) bonds to oxygen atoms appeared for the CNTs modified in Ar/H₂O plasmas and their percentage further increased for the discharges containing O₂ or CO₂.

The oxygen O1s signal was measured with lower resolution than C1s because of its relative weak intensity. Anyway, its comparison was very interesting because it varied significantly over the CCP-modified CNTs as shown in Fig. 9. Most of the samples exhibited the profile similar to O₂/C₂H₆O conditions (CNTF19), i.e. the peak positioned at 532.5 eV with a slight asymmetry towards higher binding energies. Its fitting by five Gauss–Lorentzian peaks is shown in Fig. 9. The positions of the peaks correspond to oxygen double bonded to carbon in ester R-C(=O)-O-C- (531.9 eV), oxygen double bonded to carbon in acid anhydride R-C(=O)-O-C(=O)- or carboxyl HO-C=O (532.6 eV), single bonded O-C as in hydroxyl, phenol, ester or acid anhydride

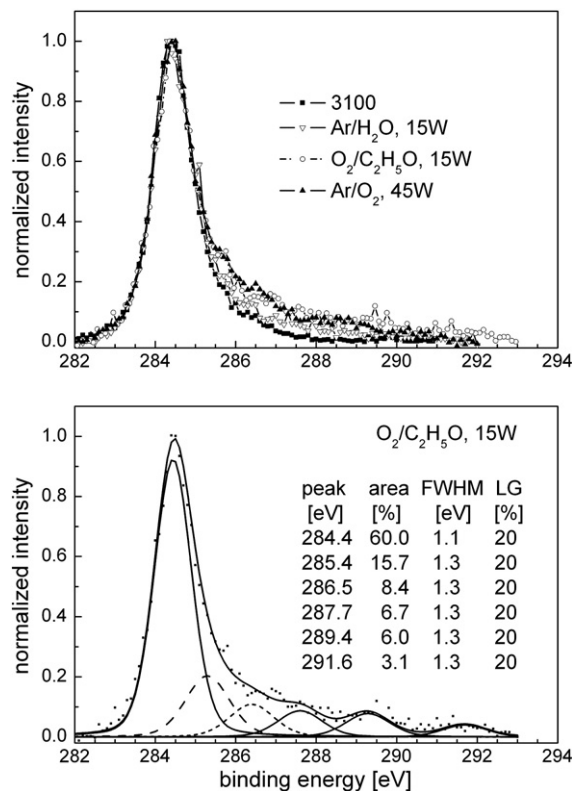


Fig. 7. Comparison of C1s XPS signal of pristine 3100 CNTs and three selected plasma modified CNTs (top). Bottom graph demonstrates the fit of C1s signal for plasma modified CNTs with high-oxygen-percentage (plasma conditions: O₂/C₂H₆O, 13.56 MHz, 15 W in this example).

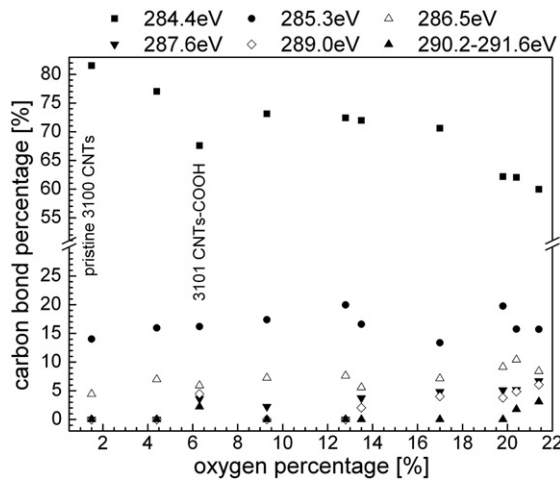


Fig. 8. Dependence of carbon bond percentages on oxygen content in pristine 3100, COOH-functionalized 3101 and CCP-modified 3100 CNTs.

(533.7 eV), single bonded O–C in carboxyl HO–C=O (534.6 eV) and oxygen in water (535.8 eV) [20]. The peak of adsorbed water at 535.8 eV was the strongest for two samples with total oxygen content below 10%, i.e. Ar/NH₃ and Ar/H₂O in 45 W discharge. These samples had also relatively high peak at 534.6 eV. Both these peaks caused a significant signal increase at higher binding energies as showed on the example of FU16 (Ar/H₂O, 45 W) in Fig. 9. The O1s signal of the sample FU14 (Ar/O₂, 45 W) exhibited a shift to lower BE and required,

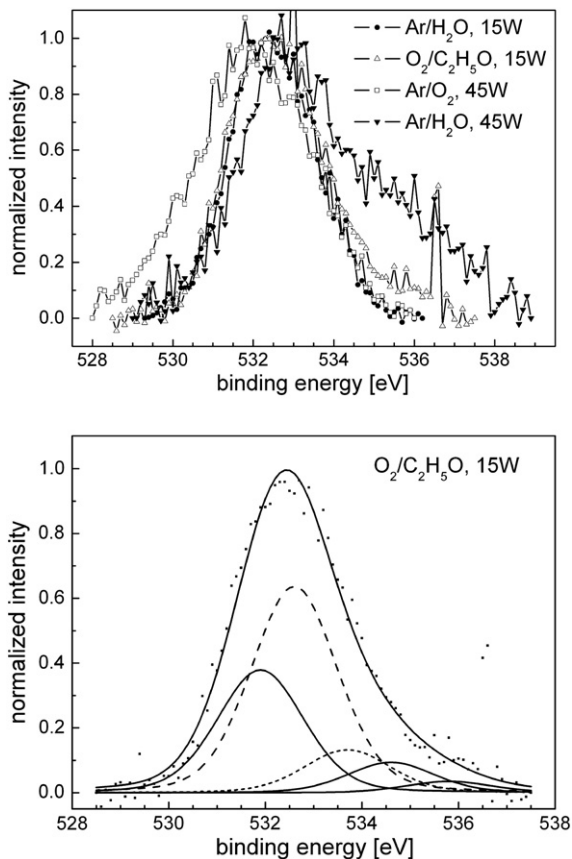


Fig. 9. Comparison of O1s XPS signal (top) of four plasma modified CNTs selected to show major differences in the position and shape of measured O1s peaks. The fitting of O1s signal (bottom) is demonstrated for the sample treated in O₂/C₂H₅O, 13.56 MHz and 15 W discharge.

therefore, additional peak at 531 eV that can be attributed to oxygen bonded in carbonyl R–C=O groups.

Infrared spectroscopy confirmed modification of CNTs chemical structure in plasma similarly as commercial chemical modification. The position of the peak observed in pristine CNTs at 1561 cm⁻¹ shifted slightly with the plasma modifications, towards lower wavenumber of 1555 cm⁻¹ for Ar/NH₃ and towards higher wavenumbers, 1566 cm⁻¹ for Ar/CO₂ and 1574 cm⁻¹ for Ar/H₂O and Ar/O₂. The absorption band at around 1130 cm⁻¹ modified its shape from the sharp structure with two distinguished peaks at 1120 and 1145 cm⁻¹ to a broad band. Additionally, the absorption at 1020 cm⁻¹ became more visible. Besides that, a clear carbonyl peak at 1726–1728 cm⁻¹ appeared for the pmCNTs that required high energy peaks for the fitting of the C1s XPS signals.

3.3. Polyurethane composites filled with CNTs

The SEM micrograph of PU filled by 0.1 wt.% of pristine CNTs is given in Fig. 10. Although the composites looked reasonably uniform with bare eyes the SEM study revealed areas with almost no CNTs and areas with CNT aggregations. These aggregations were well distributed throughout the whole sample leading to the homogeneous look. The SEM micrograph in Fig. 10 was taken at the place of aggregation. The dispersion of commercially and plasma modified CNTs in polyol mixture was much easier than in case of pristine CNTs. The effect of CNT modifications on mechanical properties of PU/CNTs composites was tested for all commercially modified CNTs and CNTs modified in 13.56 MHz discharges. The indentation tests of nanocomposites and their evaluation were carried out carefully by keeping in mind the following possible problems:

- nonuniformity of nanocomposites due to a nonuniform CNT distribution,
- inhomogeneity perpendicular to the substrate due to the existence of a harder surface layer,
- time dependent material response due to viscoelastic-plastic behaviour of polyurethane.

The effect of composite nonuniformity on the averaged mechanical properties was excluded by analysis of indentation imprints and curves of differential hardness. The defect in the composite can be clearly identified from indentation tests as an abrupt jump in the depth dependence of the differential hardness defined by Eq. (5). It is demonstrated for the composites filled with CNTs modified in Ar/O₂ plasma at top of Fig. 11. In this graph, one selected measurement without a defect is compared to three measurements close to defects. The inspection of indentation

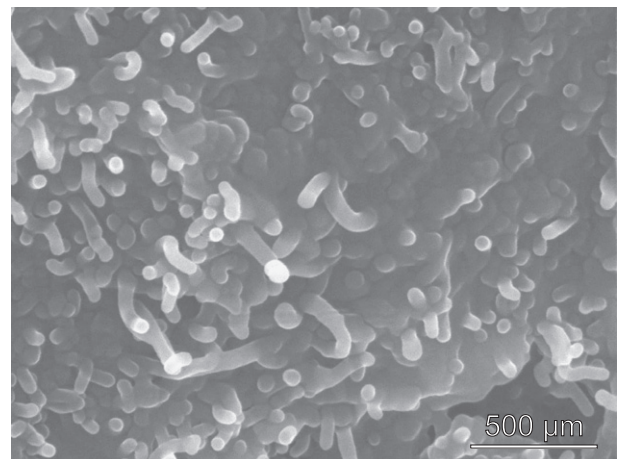


Fig. 10. SEM micrograph of PU filled with 0.1 wt.% of pristine CNTs taken at the place of CNT aggregation.

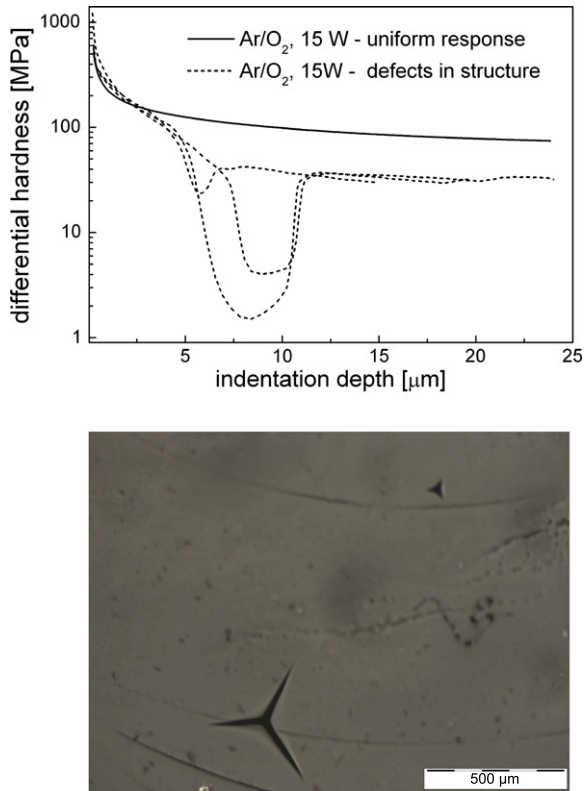


Fig. 11. Differential hardness (top) selected to show defects in the composites encountered during indentation and micrograph (bottom) of two indentation imprints made at the same maximum load $L_{\text{max}} = 100$ mN but once close to the defect (left imprint).

imprints by optical microscope allows to correlate the observed jumps in DH data with irregular shapes of imprints as shown at bottom of Fig. 11. The measurements were repeated at least $16\times$ at various places and maximum loads and the measurements closed to the defects were omitted from the statistical analysis.

The depth dependences of differential hardness (Fig. 11) or Martens hardness (Fig. 12) for 250 μm thick PU or PU/CNTs films revealed a significantly increased hardness of subsurface region of about 5 μm thick. Therefore, the hardness values in the depth range 10–50 μm were used for the determination of PU or PU/CNTs bulk hardnesses. The thickness of the polymer films ensured that, in this depth range, the values were not yet influenced by the glass substrate having the hardness of 7 GPa. One order of magnitude different hardness of the surface layer was probably caused by a different process of polymerization in contact with air than in the bulk material. It is interesting to notice

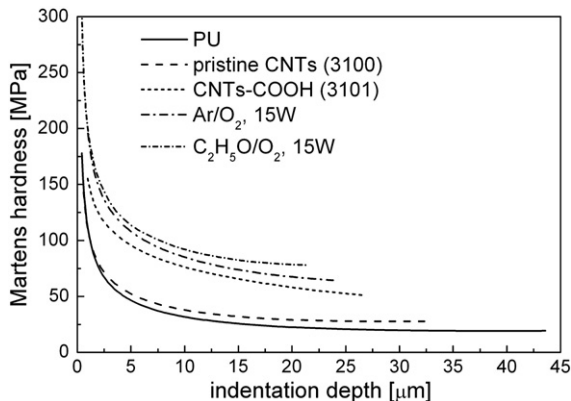


Fig. 12. Martens hardness for pure PU and PU/CNTs composites in dependence on indentation depth.

that the mechanical properties were more homogeneous in thinner polymer films. In this case the difference between the surface and bulk mechanical properties were weaker but not negligible. Therefore, when studying mechanical properties, it was necessary to compare the composites to the matrix of corresponding thickness. In order to compare HM and H_{pl} for different samples as in Fig. 12 and Table 3, the analyses were carried out on the polymer films with the thickness of 250 μm .

The most often reported results on the mechanical properties of PU/CNTs composite were obtained by standard testing methodology such as tensile tests, dynamic mechanical analysis, creep and recovery tests. The quantities obtained using these tests, i.e. Young's modulus, loss modulus, tensile strength, elongation at break, creep and recovery strains, are representative for the bulk properties of tested samples. Several authors referred improvement of bulk PU mechanical properties when CNTs were added [3,14,33–35]. Jia et al. studied PU composites with 3 wt.% of MWCNTs by tensile tests and observed an increase of modulus by 16% for pristine MWCNTs and by 24% for ozone-functionalized MWCNTs as compared to pure PU [35]. Jung et al. showed that modulus of pure PU was increased by 123 or 180% if PU composites contained 4 wt.% of pristine or H₂SO₄/HNO₃-modified MWCNTs, respectively [33]. Buffa et al. investigated PU composites with different percentages of SWCNTs and observed that Young's modulus was improved by 33% for 1 wt.% of either pristine or chemically functionalized SWCNTs [34]. An increased percentage of SWCNTs further improved the modulus mainly for the functionalized SWCNTs. Ryszkowska et al. showed, on the other hand, a slight decrease of modulus for PU filled with 0.1 wt.% of MWCNTs that was attributed to the change of polymerization process in the presence of CNTs and a CNT agglomeration [36].

Compared to the bulk tests the indentation tests have advantage of a local method that can distinguish the effect of a surface layer, nonuniformity due to inhomogeneous dispersion of filler or failures in filler-matrix bonding. These effects are averaged in the bulk tests and, therefore, the results are hard to compare. Moreover, the differences in experimental results can be explained by a different quality of CNTs, different procedure of composite preparation and different CNT dispersion in polymer matrix. Yusoh et al. observed by nanoindentation that hardness and modulus increased by 50 and 5%, respectively, when 1 wt.% of pristine MWCNTs was mixed into PU matrix [37,38]. Using the same percentage of pristine MWCNTs, we have observed increase of plastic hardness H_{pl} by 36% and modulus Y by 50%.

As seen from previously reported results a modification of CNTs can further improve the mechanical parameters of composites but it certainly depends on many parameters including the type and extend of the modification. Our previously published results showed that 3100 CNTs modified in Ar/O₂ plasma increased Martens hardness HM, plastic hardness H_{pl} and elastic modulus Y by 300, 560 and 200%, respectively, as compared to pure PU [22]. These composites exhibited a better performance also in comparison to PU filled with CNTs-COOH or CNTs modified in Ar/H₂O because their mechanical parameters HM, H_{pl} and Y increased by only 120, 170% and 210, 280% and 10, 100%, respectively. Table 3 summarizes the absolute values of mechanical parameters together with the results on a composite filled with CNTs modified in O₂/C₂H₅O plasma. The O₂/C₂H₅O plasma treatment resulted in the highest amount of oxygen in pmCNTs (Table 2). The composite had similar H_{pl} as the composite with Ar/O₂ modified CNTs but HM and Y were slightly lower. It is interesting to notice that these two modifications differed by the relative amount of carbon with four bonds to oxygen atoms as found by XPS (Fig. 8).

The testing conditions of composites took into account the influence of time dependent polyurethane response as shown in Fig. 3. Fig. 13 demonstrates that the composites exhibited significant time dependent plastic deformation (creep) and also some time dependent anelastic deformation ("backcreep") after unloading period. It can be seen from Table 3 that creep resistance CR of the composites

Table 3
Mechanical properties of nanocomposites assessed by depth sensing indentation. Polyurethane was filled by Nanocyl 3100 pristine CNTs, 3101 CNTs-COOH and 3100 CNTs modified in 13.56 MHz discharges.

Sample	HM [MPa]	H_{pl} [MPa]	Y [GPa]	CR [%]	ANR [%]	Y_1 [GPa]	η_1 [GPa s]	η_2 [10 GPa s]
Pure PU	23 ± 1	11 ± 2	1.0 ± 0.1	57 ± 2	−21 ± 1	1.5 ± 0.1	0.15 ± 0.03	5.6 ± 0.5
# 3100 Pristine	28 ± 1	15 ± 2	1.5 ± 0.2	40 ± 3	−20 ± 3	2.2 ± 0.1	0.22 ± 0.03	11 ± 1
# 3101 COOH	51 ± 3	34 ± 3	1.1 ± 0.1	38 ± 2	−33 ± 1	4.5 ± 0.5	0.57 ± 0.07	21 ± 1
# 3100 Ar/H ₂ O, 15 W	63 ± 7	42 ± 7	2.0 ± 0.2	34 ± 8	−23 ± 2	6.5 ± 0.5	1.0 ± 0.1	43 ± 3
# 3100 Ar/O ₂ , 15 W	91 ± 9	73 ± 7	3.0 ± 0.5	22 ± 3	−25 ± 4	13 ± 1	1.7 ± 0.4	80 ± 5
# 3100 O ₂ /C ₂ H ₅ O, 15 W	71 ± 2	79 ± 7	2.2 ± 0.2	21 ± 2	−33 ± 1	11 ± 1	1.6 ± 0.3	79 ± 4

was significantly improved for both the composites filled by CNTs with high amount of oxygen. The ability of PU to recover from a deformation, i.e. its anelastic recovery ANR, did not change much for PU/CNTs composites and did show any clear dependence on the type of CNTs.

The time dependent mechanical properties of the composites were analyzed using three empirical mechanical models (Kelvin–Voigt, Voigt, Maxwell–Voigt). The four-element Maxwell–Voigt model, considering the Maxwell and Voigt elements in series, revealed to be most suitable for the description of experimental data. Within this model, a time dependence of indentation depth h at the constant load L can be described according to formula [39]

$$h^2(t) = CL \left[\frac{1}{Y} + \frac{1}{Y_1} \left(1 - \exp\left(-t \frac{Y_1}{\eta_1}\right) \right) + \frac{t}{\eta_2} \right] \quad (6)$$

where C is the constant describing geometry of the indenter, η_1 and η_2 are the viscosity terms quantifying the time-dependent property of tested composite, Y_1 is the elastic parameter of the spring element in parallel to the dash-pot η_1 (the Voigt element) and Y is the elastic parameter of the spring in series to the Voigt element and the dash-pot

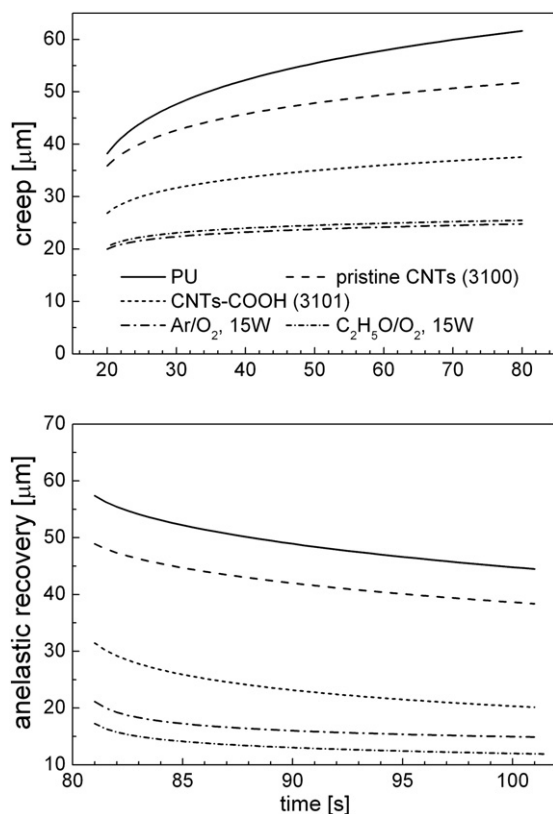


Fig. 13. Anelastic recovery and creep for pure PU and PU/CNTs composites prepared on glass.

η_2 . The parameter Y has the meaning of the elastic modulus of the composite that was determined from loading–unloading hysteresis using Eq. (3). The other three parameters, Y_1 , η_1 and η_2 , were determined by fitting the creep data using Marquart–Levenberg method. Their values are summarized in Table 3. The elastic parameter Y_1 followed the trend of the elastic modulus Y and the viscosity terms $\eta_{1,2}$ showed increased resistance to plastic flow for O₂/C₂H₅O and Ar/O₂ modified CNTs.

4. Conclusion

The MWCNTs were modified in low pressure capacitively coupled discharges ignited at 13.56 and 27.12 MHz in various oxygen-containing gas mixtures and in Ar/NH₃. It was found that the attachment of nitrogen containing functional groups to MWCNTs was not possible in Ar/NH₃ discharge but some nitrogen was attached after the treatments in oxidizing plasmas, probably due to a synergistic effect of plasma oxidation and reaction of the oxidized CNT surface with air. The maximum oxygen content of 17–21%, as measured by XPS was achieved in Ar/O₂, Ar/CO₂ and O₂/C₂H₅O discharges, whereas oxygen content in Nanocyl CNTs-COOH was 5–6%. Almost independently on plasma conditions the percentage of carbon–oxygen bonds increased with the total oxygen content on the expenses of sp²C. The Nanocyl CNTs-COOH contained more C=O and –C(=O)– bonds for the given oxygen content but the high-oxygen-content pmCNTs had the amount of carbon–oxygen bonds even higher.

The MWCNTs modified in 13.56 MHz discharges were used as fillers for PU composites prepared by in situ polymerization. The composites were tested for the changes of their mechanical properties by depth sensing indentation method. These tests were complicated by the existence of surface harder layer caused probably by different polymerization process in the bulk material and at the surface that was in a contact with air. When compared composites with the same thickness of 250 μm the significant improvement of the hardness and elastic modulus was observed for the pmCNTs with high amount of oxygen. The plasma modification of CNTs also improved the creep resistance of the PU, whereas the ability to recover from a deformation, i.e. anelastic recovery, did not change much.

Acknowledgments

This work was supported by the projects ‘CEITEC – Central European Institute of Technology’ (CZ.1.05/1.1.00/02.0068) and ‘R&D Center for Low-Cost Plasma and Nanotechnology Surface Modifications’ (CZ.1.05/2.1.00/03.0086) from European Regional Development Funds, by the project P205/10/1374 of the Czech Science Foundation and by the EU Seventh Framework Programme under the ‘Capacities’ specific programme (Contract No. 286154–SYLICA).

References

- [1] C. Hepburn, Polyurethane elastomers, 2nd edition Elsevier Science, 1992.
- [2] S. Gogolewski, Colloid Polym. Sci. 267 (9) (1989) 757.
- [3] H. Xia, M. Song, Soft Matter 1 (2005) 386.

- [4] C. Prisacariu, Polyurethane Elastomers: From Morphology to Mechanical Aspects, Springer, 2011.
- [5] P.M. Ajayan, J.M. Tour, Nature 447 (7148) (2007) 1066.
- [6] M. Rahmat, P. Hubert, Compos. Sci. Technol. 72 (2011) 72.
- [7] J. Lu, J. Han, Int. J. High Speed Electron. Syst. 9 (1998) 101.
- [8] M.-F. Yu, O. Lourie, M. Dyer, K. Moloni, T. Kelly, R. Ruoff, Science 287 (2000) 637.
- [9] E. Wong, P. Sheehan, C. Lieber, Science 277 (1997) 1971.
- [10] J.P. Salvetat, J.M. Bonnard, N.H. Thomson, A.J. Kulik, L. Forro, W. Benoit, L. Zupiroli, Appl. Phys. A 69 (1999) 255.
- [11] O. Breuer, U. Sundararaj, Polym. Compos. 25 (2004) 630.
- [12] In: M. Meyyappan (Ed.), Carbon Nanotubes, Science and Applications, CRC Press, Boca Raton, 2005.
- [13] E. Barrera, JOM J. Miner. Met. Mater. Soc. 52 (2000) 38.
- [14] J. Xiong, Z. Zheng, X. Qin, M. Li, H. Li, X. Wang, Carbon 44 (2006) 2701.
- [15] H. Kim, K. Kim, S. Lee, J. Joo, H. Yoon, S. Cho, S. Lyu, C. Lee, Curr. Appl. Phys. 4 (2004) 577.
- [16] Y. Yang, R. Gupta, K. Dudley, R. Lawrence, Nano Lett. 5 (2005) 3131.
- [17] C. Dhand, S.K. Arya, M. Datta, B. Malhotra, Anal. Biochem. 383 (2008) 194.
- [18] J. Moulder, W. Stickle, P. Sobol, K.D. Bomben, Handbook of X-ray Photoelectron Spectroscopy, Perkin-Elmer Co., Eden Prairie, MN, 1992.
- [19] T. Okpalugo, P. Papakonstantinou, H. Murphy, J. McLaughlin, N. Brown, Carbon 43 (1) (2005) 153.
- [20] L. Stobinski, B. Lesiak, J. Zemek, P. Jiricek, S. Biniak, G. Trykowski, J. Alloy. Compd. 505 (2010) 379.
- [21] H. Ago, T. Kugler, F. Cacialli, W.R. Salaneck, M. Shaffer, A. Windle, R. Friend, J. Phys. Chem. B 103 (1999) 8116.
- [22] L. Zajíčková, Z. Kučerová, V. Buršíková, M. Eliáš, J. Houdková, P. Synek, H. Maršíková, O. Jašek, Plasma Process. Polym. 6 (2009) S864.
- [23] M.S.P. Shaffer, X. Fan, A. Windle, Carbon 36 (1998) 1603.
- [24] W. Zhao, C. Song, J. Zheng, B. Liu, T. Viswanathan, J. Phys. Chem. B 106 (2002) 293.
- [25] J. Zhang, H. Zou, Q. Qing, Y. Yang, Q. Li, Z. Liu, X. Guo, Z. Du, J. Phys. Chem. B 107 (2003) 3712.
- [26] Y. Liu, L. Gao, Carbon 43 (1) (2005) 47.
- [27] Z.-M. Dang, L. Wang, L.-P. Zhang, J. Nanomater. (2006) 1, (Article ID 83583).
- [28] D. Mayo, F.A. Miller, R.W. Hannah, in: Course Notes on the Interpretation of Infra-red and Raman Spectra, Wiley-Interscience, 2004, p. 108.
- [29] M. Schaffer, X. Fan, A.H. Windle, Carbon 11 (1998) 1603.
- [30] V. Antolín-Cerón, S. Gómez-Salazar, M. Rabelero, V. Soto, G. Luna-Bárcenas, I. Katime, S. Nuño-Donlucas, Polym. Compos. 33 (2012) 562.
- [31] S. Girei, S. Thomas, M. Atieh, S. Mezghani, K. adn Bandyopadhyay, A. Al-Juhani, J. Thermoplast. Compos. Mater. 25 (2012) 333.
- [32] L. Chen, H. Xie, W. Yu, J. Mater. Sci. 47 (2012) 5590.
- [33] Y.C. Jung, N.G. Sahoo, J.W. Cho, Macromol. Rapid Commun. 27 (2006) 126.
- [34] F. Buffa, G.A. Abraham, B.P. Grady, D. Resasco, J. Polym. Sci. B Polym. Phys. 45 (2007) 490.
- [35] Y. Jia, Z.M. Jiang, X.L. Gong, Z. Zhang, Express Polym. Lett. 6 (9) (2012) 750.
- [36] J. Ryszkowska, M. Jurczyk-Kowalska, T. Szymborski, K.J. Kurzydowski, Phys. E 39 (2007) 124.
- [37] K. Yusoh, M. Song, World J. Eng. 11 (Suppl. 1) (2011) 1293.
- [38] K. Yusoh, Subsurface and bulk mechanical properties of polyurethane nanocomposite films, Ph.D. thesis, Loughborough University, Leicestershire, UK, 2010. URL <http://hdl.handle.net/2134/6313>
- [39] A. Fischer-Cripps, Mater. Sci. Eng., A 385 (2004) 74.